Modelling Cell Cycle Entrainment during Cortical Brain Development

Duncan Barrack, BSc.

Thesis submitted to the University of Nottingham
for the degree of Doctor of Philosophy

May 2010

Abstract

Radial glial cells play an important role during embryonic development in mammals. They are not only important for neural production but help to organise the architecture of the neocortex. Glial cells proliferate during the development of the brain in the embryo, before differentiating to produce neurons at a rate which increases towards the end of embryonic brain development. Glial cells communicate via Adenosine tri-phosphate (ATP) mediated calcium waves, which may have the effect of locally synchronising cell cycles, so that clusters of cells proliferate together, shedding cells in uniform sheets. Hence radial glial cells are not only responsible for the production of most neocortical neurons but also contribute to the architecture of the brain. It has been argued that human developmental disorders which are associated with cortical malfunctions such as infantile epilepsies and mental retardation may involve defects in neuronal production and/or architecture and mathematical modelling may shed some light upon these disorders.

This thesis investigates, among other things, the conditions under which radial glial cells' cell cycles become 'phase locked', radial glia proliferation and stochastic effects. There are various models for the cell cycle and for intracellular calcium dynamics. As part of our work, we marry two such models to form a model which incorporates the effect of calcium on the cell cycle of a single radial glial cell. Furthermore, with this achieved we consider populations of cells which communicate with each other via the secretion of ATP.

Through bifurcation analysis, direct numerical simulation and the application of the theory of weakly coupled oscillators, we investigate and compare the behaviour of two models which differ from each other in the time during the cell cycle at which ATP is released. Our results from this suggest that cell cycle synchronisation is highly dependent upon the timing of ATP release. This in turn suggests that a malfunction in the timing of ATP release may be responsible for some cortical development disorders. We also show how the increase in radial glia proliferation may mostly be down to radial glial cells' ability to recruit quiescent cells onto the cell cycle. Furthermore, we consider models with an additive noise term and through the application of numerical techniques show that noise acts to advance the onset of oscillatory type solutions in both models. We build upon these results and show as a proof of concept how noise may act to enhance radial glia proliferation.

Contents

Acknowledgements **1**

1 Introduction and Literature Review **2**

1.1 The Cell Cycle 5

1.1.1 Duration of the Cell Cycle Phases 6

1.1.2 Key Cell Cycle Proteins 6

1.2 The Developing Neocortex 6

1.3 Calcium's Effect on the Cell Cycle 10

1.3.1 Nature of the Cell Divisions in the Neocortex 13

1.4 Coupling Calcium to the Cell Cycle 15

1.5 Cell Cycle Models 15

1.5.1 Tyson and Novak's Model 17

1.5.2 Obeyesekere's and Zimmerman's Model 22

1.6 A Model Incorporating Calcium 28

1.6.1 Adapting Dupont's Model 35

1.7 Models of Calcium Release 35

1.7.1 Li and Rinzel's Model 37

1.7.2 Fink *et al*'s Model 38

1.8 Bennett *et al*'s Astrocyte Model 41

1.8.1 Intercellular Communication between Several Astrocytes 44

1.9 Conclusions . . . 47
1.10 Thesis Structure . . . 51

2 Coupled Calcium and Cell Cycle Dynamics **53**
2.1 Introduction . . . 53
2.2 Model Formulation . . . 53
2.2.1 Choice of Parameter Values . . . 58
2.3 Single Cell Simulations . . . 66
2.4 Reduction of the Model . . . 73
2.5 Single Cell Analysis . . . 76
2.5.1 Bifurcation Analysis . . . 76
2.6 Weak Coupling Theory . . . 80
2.6.1 Phase . . . 80
2.6.2 Phase Locking, Synchronisation and the Theory of Weakly Coupled Oscillators . . . 81
2.7 Two Cell Analysis . . . 83
2.7.1 Cyclin D Dependent ATP Release . . . 83
2.7.2 R_s Dependent ATP Release . . . 95
2.8 Conclusions and Further work . . . 101

3 Several Cells in 1D and 2D **103**
3.1 Introduction . . . 103
3.2 Theory of Weakly Coupled Oscillators . . . 105
3.3 Analysis in 1D and 2D . . . 109
3.3.1 Cyclin D Dependent ATP Release . . . 109
3.3.2 R_s Dependent ATP Release . . . 113
3.4 Synchrony Measures . . . 114
3.5 One Dimensional Simulations . . . 118

3.5.1 Cyclin D Dependent ATP Release . . . 119
3.5.2 R_s Dependent ATP Release . . . 128
3.6 Two Dimensional Simulations . . . 135
3.6.1 Cyclin D Dependent ATP Release . . . 139
3.6.2 R_s Dependent ATP Release . . . 139
3.7 Conclusions and Further work . . . 144

4 Recruitment by Driving Cells **147**
4.1 Introduction . . . 147
4.2 Bifurcation Analysis . . . 148
4.2.1 Cyclin D Dependent ATP Release . . . 148
4.2.2 R_s Dependent ATP Release . . . 152
4.3 Duration of Near Synchronous Entrainment . . . 161
4.3.1 Cyclin D Dependent ATP Release . . . 161
4.3.2 R_s Dependent ATP Release . . . 168
4.4 Several Cells . . . 178
4.4.1 Cyclin D Dependent ATP Release . . . 178
4.4.2 R_s Dependent ATP Release . . . 183
4.5 Conclusions and Further Work . . . 184

5 A Role for Noise? **189**
5.1 Introduction . . . 189
5.2 The Stochastic Model . . . 190
5.3 Numerical Techniques and Considerations . . . 191
5.3.1 Method of Integration . . . 191
5.3.2 Bifurcation Analysis . . . 192
5.4 Single Cell Bifurcation Analysis . . . 194
5.4.1 Cyclin D Dependent ATP Release . . . 194

5.4.2 R_s Dependent ATP Release 197
5.5 Two Cell Bifurcation Analysis 199
5.5.1 Cyclin D Dependent ATP Release 200
5.5.2 R_s Dependent ATP Release 208
5.6 Simulations of Larger Systems 215
5.6.1 Cyclin D Dependent ATP Release 216
5.6.2 R_s Dependent ATP Release 216
5.7 Conclusions and Further Work 219

6 Discussion **225**

Bibliography **239**

Acknowledgements

First and foremost, I would like to thank my supervisors Markus Owen and Rüdiger Thul for their time, expertise and limitless patience. I would also like to thank Stephen Coombes for helping me to get to grips with the theory of weakly coupled oscillators. My thanks also to Dave Parkin, for his ability to solve all of my IT problems almost instantly and to the Schools support staff, who helped in numerous ways.

My special thanks to my girlfriend Becca, for being prepared to be seen in public with me despite the fact I was doing a maths PhD and to my mum, dad and sister who have supported me throughout.

Finally, I wish to thank the postgraduates and members of staff for the times spent "discussing Wittgenstein over a game of backgammon" in the C9 coffee room. You know who you are.

Chapter 1

Introduction

Radial glial cells play an important role during the embryonic development of the mammalian brain. They are a transient cell, only present in the mammalian brain for a brief period during embryonic development, when they give rise to neurons [63] and in doing so play a major role in the development of the six layered structure known as the neocortex, shown in Figure 1.1. Initially glial cells divide symmetrically, with a parent cell producing two daughter radial glial cells. Further into neurogenesis, glial cells divide asymmetrically; a parent cell produces one radial glial cell and another cell that differentiates to become a neuron [56, 58]. Towards the end of neurogenesis most cell divisions are of a symmetric nature, but this time the two cells that are produced both differentiate to become neurons [86]. This process is illustrated in Figure 1.2.

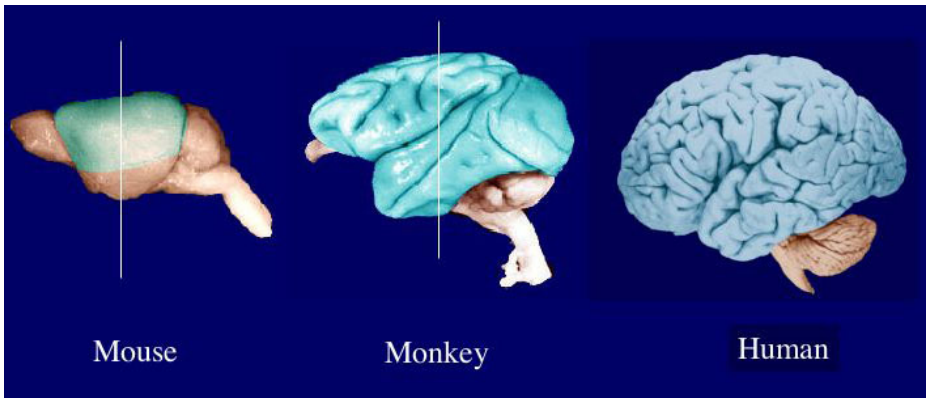

Figure 1.1: Graphic showing the neocortex (coloured blue), the thin layered structure surrounding the brain of three different mammals. Reproduced from http://www.nibb.ac.jp/brish/Gallery/cortexE.html. Visited October 2009.

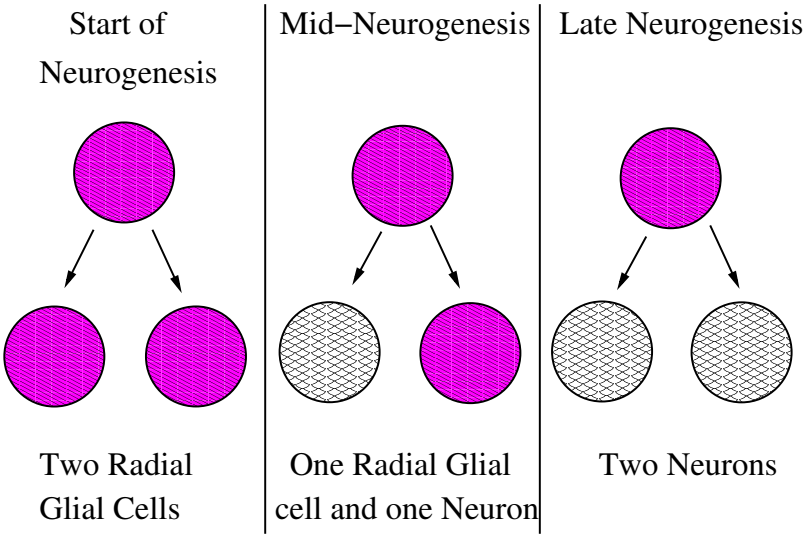

Figure 1.2: Schematic illustrating the nature of cell divisions during neurogenesis

The intercellular signalling mechanisms that coordinate radial glial cell proliferation are not well understood. Recently a novel mechanism has been found that regulates radial glial cell proliferation via calcium waves which propagate through the ventricular zone of the embryonic brain [93]. The ventricular zone is an area next to the ventricles which are in turn enclosed within the neocortex. The location of the ventricles within the brain is shown in Figure 1.3. Wave induced elevations in intracellular calcium may then help drive cells through the division cycle. Moreover, cell division can provide a stimulus for further wave propagation.

Calcium waves are initiated by the release of Adenosine triphosphate (ATP), facilitated through the opening of hemichannels. A hemichannel is an 'undocked' gap junction. Gap junctions are a type of cell junction in which the cell membranes of 'docked' cells each contain a channel that allows the passage of ions and small molecules between the two cells' cytoplasms. A cell which has an 'undocked' gap junction channel, (i.e. a hemichannel) lacks another cell with which to dock its cell membrane to. This then allows communication between the cells cytoplasm and extracellular space. An illustration of a gap junction, or two 'docked' hemichannels can be seen in Figure 1.4.

It has been shown that calcium is required for a cell to enter a certain phase of the cell cycle, and can act to recruit a cell in a rest or quiescent state onto the cell cycle

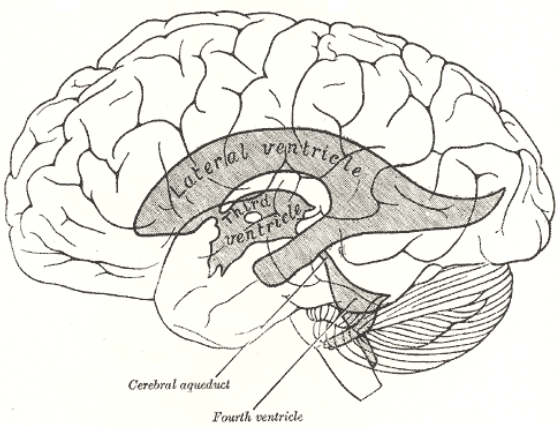

Figure 1.3: Graphical illustration of the location of the ventricles within the fully developed brain. Reproduced from http://en.wikipedia.org/wiki/Ventricular_system. Visited October 2009.

[7, 9, 95]. Weissman *et al* showed that calcium was responsible for increased radial glia proliferation and they postulate that this was as a consequence of ATP mediated calcium waves inducing cells to complete part of the cell cycle more quickly and recruiting quiescent cells onto the cell cycle. They further postulate that the calcium signalling mechanism enables the synchronisation of the cell cycles of clusters of radial glial cells [93].

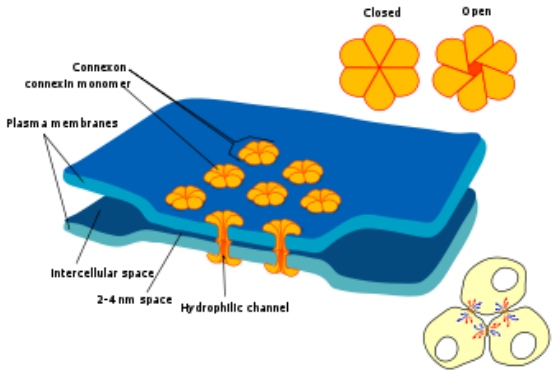

Figure 1.4: Graphical illustration of a number of gap junctions, each of which is comprised of two 'docked' hemichannels or connexons. Reproduced with permission from http://en.wikipedia.org/wiki/Gap_junction. Visited October 2009.

1.1 The Cell Cycle

In order to gain an understanding of how and when calcium affects the cell cycle of radial glial cells as well as when in the cell cycle ATP is released from radial glial cells, it is important to consider the cell cycle itself in detail. The cell cycle can be broken down into several phases which are illustrated in Figure 1.5. G_1 phase is the period of greatest growth for most cells. It is when a cell pauses during G_1 phase that it enters the quiescent state, G_0. Whether G_0 is distinct from G_1 phase or just a name for cells 'stuck' in this phase is currently an open question. G_1 is followed by S phase, during which DNA replication or synthesis occurs, producing chromosomes consisting of two sister chromatids, contained within the centromere. G_2, which can last up to 5 hours, follows S phase. It is during G_2 phase that the cell prepares for mitosis.

Mitosis (M phase) is the final phase of the cell cycle. M phase can be broken down into yet more phases. Metaphase is the phase in which the chromosomes align. It is succeeded by anaphase, where the chromosomes separate, with the chromatids moving to opposite poles of the cell. At this point, the cell is prepared for telophase, where new nuclear envelopes form around the now separated chromatids. It is shortly after this that the parent cell separates into two daughter cells, signalling the end of mitosis and the completion of the cell cycle.

Although traditionally the cell cycle is subdivided into these four phases (G_1, S, G_2 and M), it has been argued [90] that the process is best understood by considering two 'states', the G_1 state and the S-G_2-M state. With this interpretation, we must consider two irreversible transitions, the 'start' transition taking us from the G_1 state to the S-G_2-M state and the 'finish' from the S-G_2-M state to the G_1 state. At 'start' the cell is committed to entering S phase, a commitment that is irreversible. Similarly, at 'finish', the cell is committed to entering anaphase from metaphase. Again this is an irreversible process.

The cell cycle is controlled by a large number of biochemical regulators including Cyclins and Cyclin dependent kinases (Cdks). Cdks phosphorylate target proteins when paired up with their respective Cyclin partners. In phosphorylating a protein, a Cdk/Cyclin complex will have the effect of altering the activity of the protein. There are usually a constant amount of Cdks during the cell cycle and consequently Cdk activity is highly dependent

upon the availability of their Cyclin partners. Cyclins are produced and degraded as needed during the cell cycle. Once paired to form Cdk/Cyclin complexes, the complexes will first migrate into the cell nucleus and then phosphorylate various target proteins and alter their activity. These target proteins facilitate cell cycle events such as DNA replication, chromosome condensation as well as all other events which are part of the cell cycle.

1.1.1 Duration of the Cell Cycle Phases

Although, the total duration of the cell cycle depends upon the type of cell in question, G_1 phase is the longest phase. Typically, cells remaining in G_1 for nearly half of the cell cycle [1]. Cells will generally take between a fifth and a quarter of the total cell cycle period to complete S phase [1]. G_2 phase lasts approximately one sixth of the total period [1]. M phase is the shortest phase, lasting for about one tenth of the total cell cycle period [1].

1.1.2 Key Cell Cycle Proteins

In the mammalian cell cycle, Cyclin D concentrations are high during G_1 phase, before dropping off during S phase [13, 81, 96]. Late G_1 phase is associated with high concentrations of Cyclin E [20, 44].

M phase is brought to an end by the activation of the anaphase promoting complex (APC), which is itself made up of several different proteins. This allows the cell to re-enter G_1 phase and once again embark on the cell cycle.

1.2 Radial Glial cells in the Developing Neocortex

Weissman *et al* [93] claim that the empirical evidence points towards a calcium signalling mechanism between cortical radial glial cells. Their results show that ATP mediated calcium waves propagate through the ventricular zone of the embryonic cortex. Recent work shows that clusters of radial glial cells' gap junctions have a propensity to form hemichannels in G_1 or S phase of the cell cycle [10, 34, 93]. Weissman *et al* claim that it is at this

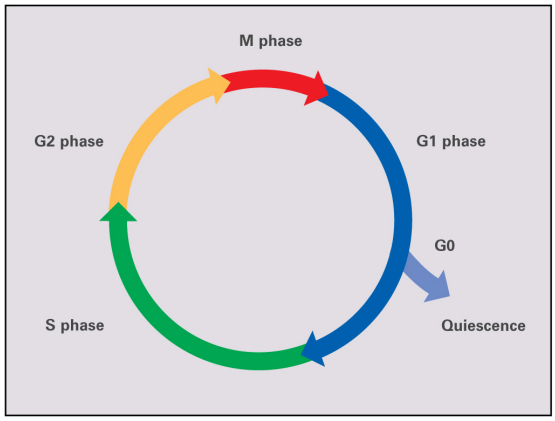

Figure 1.5: Graphical illustration showing the phases of the the cell cycle. G_0 quiescence. G_1 Gap 1. S DNA synthesis. G_2 Gap 2. M mitosis. Reproduced from http://images.nigms.nih.gov. Visited October 2009.

time that ATP is released [93]. Furthermore they show that ATP leads to inositol 1,4,5-triphosphate (IP_3) mediated calcium release from the internal stores of the radial glial cells. It has been shown that an increase in intracellular calcium can induce resting cells in G_0 phase to re-enter the cell cycle and can also induce a cell to enter S phase from G_1 phase [7, 9, 95]. Berridge [7, 9] and Weissman *et al* believe that calcium is also required for entry into M phase of the cell cycle [93]. However recent findings by Kahl and Beauman suggest that the role of calcium at this stage in the cell cycle may not be as crucial as once thought [3, 45, 46]. Figure 1.6 illustrates how the cell cycle is likely to be affected by calcium in radial glial cells and the point during the cell cycle that hemichannels form.

As mentioned previously, Weissman *et al* speculate that calcium waves may be the mechanism by which the cell cycles of a cluster of radial glial cells synchronise (i.e. go through each phase of the cell cycle at the same time). This would lead to daughter cells, which are created from proliferation, being shed in uniform sheets. They suggest that a 'recruiting' cell in late G_1 or S phase of the cell cycle may induce neighbouring cells into S phase, synchronising the cell cycles of the cluster of cells in the process. This process is illustrated in Figure 1.7. Furthermore, Weissman *et al* go on to speculate that calcium waves would have the ultimate effect of increasing the rate at which neurons are produced. Cells that were sluggishly approaching S phase will be induced into it by an increase in intracellular calcium. Indeed, without this boost, some cells may enter G_0, rather than continue cycling.

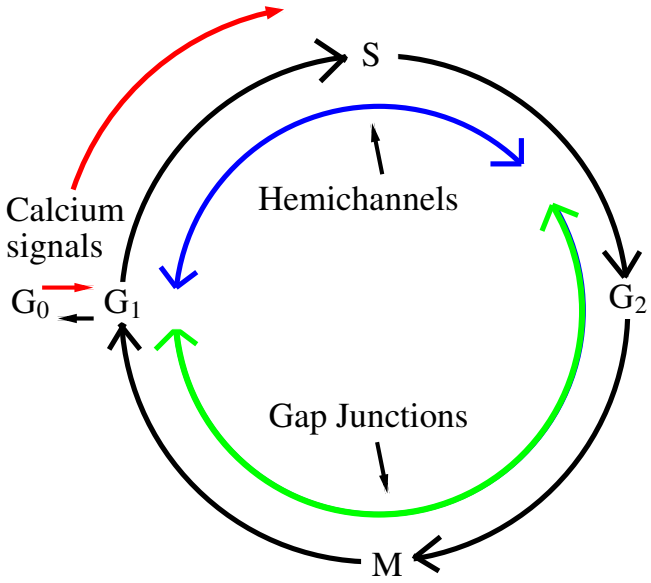

Figure 1.6: Graphical illustration of likely effect of Calcium on the cell cycle. The schematic illustrates that calcium signals have the effect of inducing a cell to enter S phase from G_1 phase as well as inducing a cell in the quiescent G_0 phase onto the cell cycle. The schematic also shows at which point during the cell cycle hemichannels form from gap junctions, at which point it is claimed ATP is released. It has been claimed that calcium may affect other phases of the cell cycle (see text for details), however these particular effects are not illustrated in this schematic.

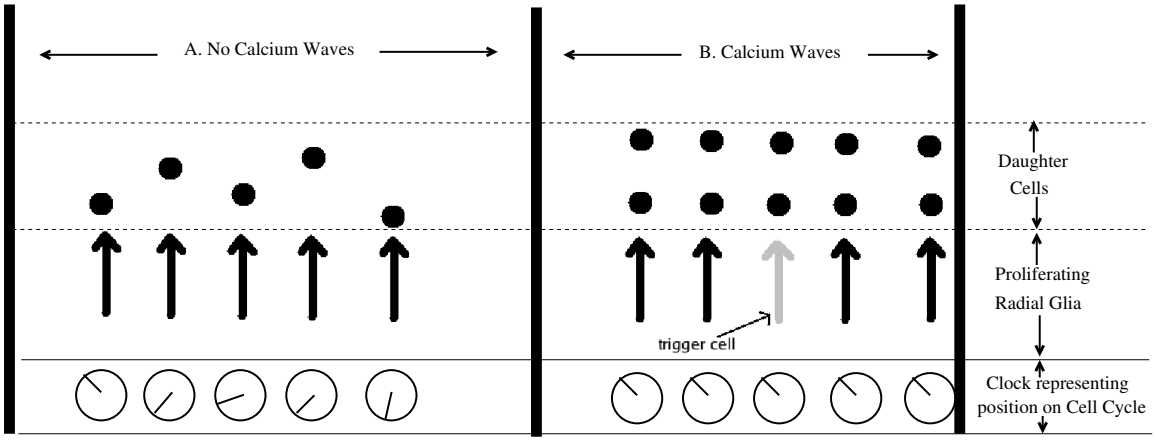

Figure 1.7: Schematic illustrating how radial glial cells may recruit neighbouring cells so that clusters of cells cycle in synchrony. Two scenarios are illustrated, (A); without calcium present and (B); with calcium waves . In (A), cells proliferate in an asynchronous manner (represented by the position of the clock hands), with some cells entering the quiescent G_0 state instead of continuing or embarking upon the cell cycle. (B) with calcium waves; cycling cells are recruited by a trigger cell (coloured grey), which initiates an ATP mediated calcium wave. The trigger cell, when in G_1 or S phase, has the effect of synchronising the cell cycles of the cluster of cells in which it resides (represented by the position of the clock hands), leading to the shedding of daughter cells in uniform sheets. ATP mediated calcium waves may lead, in turn to an increase in overall proliferation. Figure adapted from [93].

The claim that this mechanism may lead to an increase in cortical proliferations is supported by experimental evidence. Weissman *et al* investigated the effect of introducing the ATP receptor antagonist suramin for a period of one hour during day 16 of embryonic development. Suramin, in preventing a cell's ATP receptor functioning properly, should have the effect of disrupting calcium waves and cell proliferation. Weissman *et al* showed that when the $P2Y_1$ ATP receptor was inhibited, cells did not exhibit an increase in internal calcium [93], strongly suggesting that the downstream target of bound ATP is the release of calcium from internal stores. With suramin present, the developing rat neocortex on day 16 of development contained 54.7 % $\pm$ 4.1% of the density of radial glial cells incorporating BrdU (the chemical label used to detect DNA synthesis) that it contained on the same day of development in the control case, reflecting the decreased entry into S phase of the glial cells. Neural production peaks during day 16 of the development of the rat. Day 16 corresponds to the fourth day of neurogenesis of the rat (mid-neurogenesis in Figure 1.2), which is complete after 6-7 days [2, 12]. Weissman *et al*'s discovery that ATP mediated calcium waves lead to increased neural density is not surprising considering that there is a large body of evidence suggesting calcium is responsible for increasing proliferation of many cell types [8, 9] and that the ATP signalling pathway has been shown to have the effect of increasing the proliferation rate of a number of different cells including glia [59] and neurol progenitor cells [77, 91].

1.3 Calcium's Effect on the Cell Cycle

It is clear that in order to successfully model radial glial cell communication and proliferation, we must get a better handle on how exactly calcium affects the cell cycle. Until recently, the effect calcium has on the various proteins involved within the cell cycle and indeed the mechanism by which calcium affects these proteins has been given little attention. Recent work by Kahl [45, 46] and Beauman [3] has gone some way to address this issue.

The intracellular receptor for Ca^{2+} is calmodulin (CaM) and as such CaM is the means by which Ca^{2+} influences the cell cycle. Ca^{2+}/CaM-dependent Kinases (CaMK) are a group of protein kinases (enzymes that play an important role in intracellular pathways) that are regulated by phosphorylation. CaMK's are activated by Ca^{2+}/calmodulin complexes.

There is some discrepancy in the literature as to which cell cycle proteins are affected by CaMKs and how such effects are mediated. Several authors have conducted studies on several different cell types in order to get to the bottom of the issue.

KN-93 is a well known inhibitor of CaMK activity and through its application to NIH 3T3 cells (mouse fibroblast cells), Morris *et al* showed that it can induce cell cycle arrest in late G_1 phase [60]. They concluded that this was due to a reduction in levels of Cyclin D, thus preventing the formation of Cdk4/Cyclin D complexes which are integral to the progression from G_1 to S phase of the cell cycle.

Kahl *et al* conducted similar experiments but this time on WI-38 cells (human fibroblast cells originating from the lungs) with slightly different results [45, 46]. Upon KN-93 treatment, WI-38 cells underwent G_1 phase arrest in keeping with Morris *et al*'s results. However, unlike with the NIH 3T3 case, normal levels of Cyclin D were detected, leading to the formation of Cdk4/Cyclin D dimers which then migrated to the nucleus of the cell. However, these dimers were not active. Kahl *et al* then produced mutant versions of both CaMKI and CaMKII (two different types of CaMKs). These mutants had the effect of inhibiting their respective CaMK's enzymatic activity. It was discovered through this process, that CaMKI and not CaMKII was responsible for G_1 phase arrest, suggesting that CaMKI plays an important role in activating Cdk4/Cyclin D complexes during G_1 phase of the cell cycle. The precise mechanism by which it achieves this however remains to be established. This suggests that CaMKI's effect on the cell cycle could be modelled phenomenologically. *In vitro* experiments seem to suggest that CaMKI does not phosphorylate any proteins involved directly with the regulation of Cdk4 or Cyclin D [46]. This is not surprising considering CaMKI resides in the cytoplasm, while once Cdk4/Cyclin D dimers form they migrate into the cell nucleus. Kahl *et al* suggest that CaMKI has the effect of regulating the subcellular localisation of a protein or proteins involved in regulating the activity of Cyclin D/Cdk4 dimers [45, 46]. Perhaps this is achieved by allowing a protein, normally present in the cytoplasm, to enter into the nucleus where it can promote Cdk4/Cyclin D activity, for example. Despite this gap in knowledge, there is a consensus in the literature that calcium has the affect of promoting the activation of Cyclin D/Cdk4 dimers, facilitating a cell's entry into S phase from G_1 phase of the cell cycle and inducing quiescent cells in G_0 to embark upon the cell cycle.

Weissman *et al* also argue that Ca^{2+} may be required for a cell to enter M-phase of the cell cycle. Both Patel *et al* [67] and Beaumann *et al* [3] investigated the role Ca^{2+} plays in M-phase or mitotic progression, by investigating its roles in the G_2/M transition. Patel *et al* showed that CaMKII and not CaMKI played a role in the G_2/M transition [67]. Their *in vitro* experiments on HeLa cells (a cell line derived from cervical cancer cells) showed that CaMKII phosphorylated inactive Cdc25, marginally increasing its activity, suggesting that CaMKII is one of a number of Cdc25C kinases in cells. Active Cdc25 removes the inhibition from the protein kinase Cdc2 [67]. In relieving Cdc2 inhibition, Cyclin B/Cdc2 complexes are able to form, allowing the cell to undergo the transition from G_2 to M phase. According to Patel's results Ca^{2+} mediated by CaMKII appears to play a small role in helping to facilitate the G_2/M transition.

Beauman *et al* conducted a similar experiment, again on HeLa cells yet came to different conclusions [3]. They claim that CaMKII expression had the effect of delaying a cells entry in to mitosis, contradicting Patel's results. The precise mechanism by which CaMKII achieved this was not discovered. They noticed that Cyclin B1 expression increased with increased levels of active CaMKII, which is in line with Patel *et al*'s results. This led them to conclude that as Cyclin B is required for entry into mitosis, CaMKII must inhibit mitotic entry by some other means. One possible mechanism that they propose is through interfering with DNA synthesis. They also speculate that CaMKII may regulate wee 1 kinase (a protein kinase that inhibits the activity of a Cyclin/Cdk complex) and through this inhibit Cdc2 activation. It is therefore unclear whether calcium, through CaMKII, actually facilitates or hinders the G_2/M transition. Either way, calcium's effect on this part of the cell cycle appears to be rather limited and consequently we do not consider it when forming our model in Chapter 2.

Other signal transduction pathways affect radial glia behaviour. For example, it has been discovered that delta-notch signalling plays a role in determining radial glia cell fate [28, 36]. However, we neglect delta-notch signalling when developing our mathematical model in this thesis. Instead, we focus upon ATP mediated calcium release within radial glia, which has been shown to be the dominant mechanism controlling cell proliferation. It is suspected that this mechanism also acts to promote cell cycle synchronisation [93].

1.3.1 Nature of the Cell Divisions in the Neocortex

As mentioned above, neurons produced from differentiated radial glial cells are not produced at a uniform rate throughout embryonic neurogenesis. In order to explore this phenomenon, it is first of all important to outline the different types of cell divisions that lead to the creation of daughter cells upon the completion of the cell cycle.

Symmetric division: This is the event whereby two cells produced from a cell division have the same cell fate. For dividing radial glial cell, symmetric division can take the form of both daughters being radial glial cells, or both daughters being cells that differentiate into neurons.

Asymmetric division: This is the event when one daughter cell's fate is different to that of the other after cell division. With regard to radial glial cells, this is the case when one daughter cell is a radial glial cell and the other differentiates into a neuron.

Process by which neurons are produced by radial glial cells

Malatesta *et al* claim that radial glial cells give rise to neurons via asymmetric division [58]. Although this is true, it does not provide us with the full story as some of these neurons, particularly towards the end of neurological development are produced via symmetric divisions, whereby a glial cell divides and yields two neurons as daughter cells [86, 93].

In their paper, Takahashi *et al* publish various results which show the proportions of different cell types resulting from cell divisions during neurogenesis [86]. They take mice and record the proportion of cells (represented by 'Q') in the pseudostratified ventricular epithelium (PVE) that leave the cell cycle and become neurons and those that continue on the cell cycle (represented by 'P'). The PVE is the area that lines the ventricles of the developing brain and as such makes up part of the ventricular zone. The location of the ventricles within the fully developed brain are shown in Figure 1.3. Although it is not explicitly stated in their paper, the population of P cells is the population of radial glial cells [40]. The beginning of neurogenesis is signalled when Q rises above 0, i.e. when neurons are first produced and ends when P=0, i.e when radial glial cell proliferation ceases. With regard to mice, the period of neurogenesis lasts around 11 cell cycles, with Q=0.5 after 8 cycles and ≈ 0.8 after ten cell cycles. The evolution of these proportions can be seen in Figure 1.8.

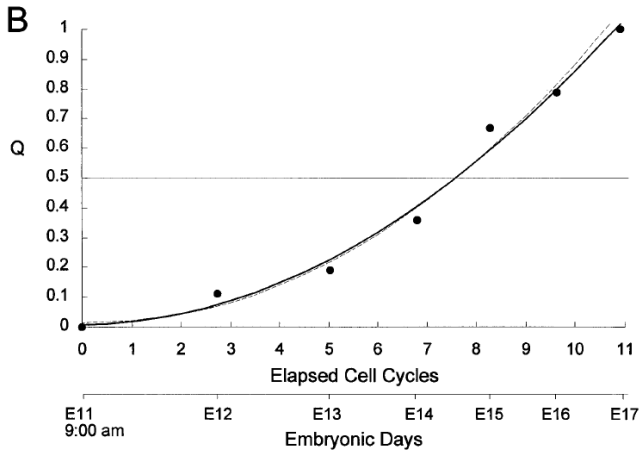

Figure 1.8: Graph illustrating the evolution of the proportion of different cell types during neurogenesis. Q represents the proportion of neurons and P the proportion of neural progenitor cells (P=1-Q). Experimentally determined values for Q are denoted by solid circles. The solid curve was produced by Takahashi et al using a least squares curvilinear fit to the experimental data. The dashed curve was produced by Takahashi et al, using a least squares curvilinear fit to the experimental data, but disregarding the data point at the origin. Graph reproduced from [86].

Although Takahashi *et al* do not provide experimental data as to the exact nature of the division during neurogenesis, i.e. the proportion of symmetric and asymmetric divisions, they do produce a model which predicts such proportions [86]. They claim that this model compares favourably with results obtained by Chenn and McDonnell *et al* [14]. Chenn and McDonnell discovered that towards the beginning of embryonic neurogenesis, most cell divisions are symmetric, with two neural progenitor (radial glial cells) produced. Towards the middle of embryonic neurogenesis, most cell divisions are asymmetric, with one neural progenitor cell (radial glial cell) and one cell that differentiates into a neuron being produced. It is at this stage during neurogenesis that neural production peaks [2, 86]. Finally, towards the end of embryonic neurogenesis, most cell divisions are symmetric, with two cells who differentiate into neurons being produced. Their results are shown in Figure 1.8.

1.4 Coupling Calcium to the Cell Cycle

We are now in a position to consider the coupling between the cell cycle and calcium in a single radial glial cell in more detail. Figure 1.9 illustrates the biological mechanisms that lead to the release of calcium and its effect on the cell cycle. In referring to Figure 1.9 we can see that once a radial glial cell's P_{2Y} receptor binds ATP, a chain of events is set off which eventually leads to a release of calcium from a cell's endoplasmic reticulum. When ATP binds to a radial glial cell's surface P_{2Y} receptor it initiates a guanine nucleotide binding protein (G-protein) cascade. G-proteins are a family of messenger proteins that regulate cellular processes. This regulation is achieved via a molecular 'switch', whereby G-proteins exchange guanosine diphosphate (GDP) for guanosine triphosphate (GTP). The particular cellular process that is 'switched' on by a G-protein cascade with regard to a radial glial cell is the production IP_3. IP_3 has the effect of liberating calcium from internal stores. Calcium then has the effect of increasing Cyclin D/Cdk activity which can induce the cell to enter S phase from G_1-phase, or re-embark on the cell cycle if the cell is in G_0 phase. Figure 1.9 also shows that ATP is released by the cell via hemichannels which form around G_1-S phase of the cell cycle.

As mentioned earlier, it has been proposed that ATP mediated calcium waves have the effect of locally synchronising the cell cycles of radial glial cells as well as increasing overall proliferation. This is the phenomenon that we intend to investigate through mathematical modelling. We introduce our model in Chapter 2. Before doing so, we need to consider relevant mathematical models for the cell cycle, calcium dynamics and intercellular communication via ATP.

1.5 Cell Cycle Models

It is clear that any attempt to model the biological processes outlined above will require a mathematical model for the cell cycle. Several models of the cell cycle have been produced, both deterministic [19, 30, 66, 89, 90] and stochastic [84, 98]. We focus upon deterministic models in this thesis.

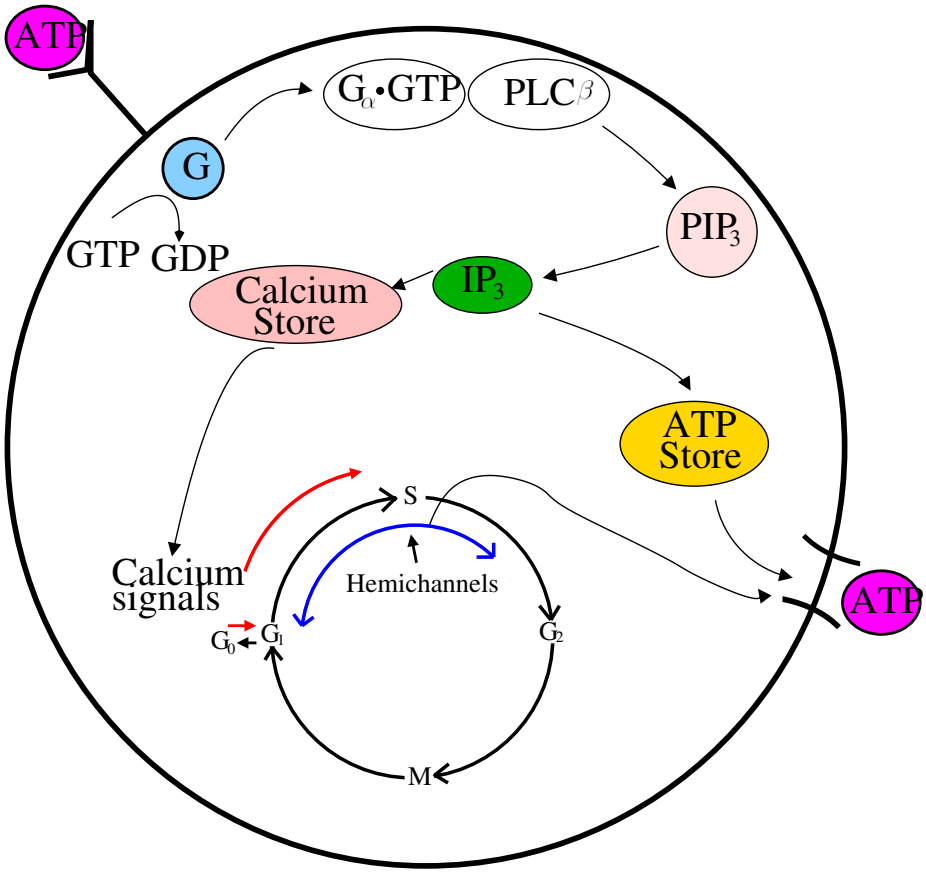

Figure 1.9: Schematic illustrating how calcium is coupled to the cell cycle of a radial glial cell. Bound ATP leads to a G-protein cascade which in turn leads to the production of IP_3. IP_3 allows for the release of ATP and facilities the liberation of calcium from internal stores. The free calcium then has the effect of inducing a cell to enter S phase from G_1 and/or driving a cell in G_0 onto the cell cycle. During G_1 or S phase a cell's hemichannels open up facilitating the release of ATP into extracellular space.

1.5.1 Tyson and Novak's Model

Perhaps the most well known deterministic models are a series of models due to Tyson and Novak [89, 90]. In their most basic model of yeast cells, Tyson *et al* consider the dynamics of Cyclin B, the cell mass, the Anaphase Promoting Complex (APC) and its subunits to form a four dimensional model. In their model, Cdks are assumed to be readily available throughout the cell cycle and form active Cyclin B/Cdk complexes (X in the model) when Cyclin B becomes available. Similarly, APC is assumed to be in abundant supply and binds to Cdh1 to form active APC/Cdh1 complexes (Y in the model) when Cdh1 is produced. Tyson and Novak also consider a protein called Cdc20 (a subunit of APC, given by A) and the cell mass (m) in their model. Active Cyclin B/Cdk complexes act to increase Cdc20 activity and suppress Cdh1/APC activity. In turn, Cdc20 acts to promote Cdh1/APC, which in turn degrades Cyclin B. Tyson *et al* argue that the cell cycle is best subdivided into two states, the G_1 state and the $S-G_2-M$ state. The former is characterised by high Cdh1/APC activity while the latter by high Cyclin B/Cdk activity and low Cdh1/APC activity. Their model is given by

$$\frac{dX}{dt} = k_1 - (k_2' + k_2''Y)X, \tag{1.1}$$

$$\frac{dY}{dt} = \frac{(k_3' + k_3''A)(1-Y)}{J_3 + 1 - Y} - \frac{k_4 mXY}{J_4 + Y}, \tag{1.2}$$

$$\frac{dA}{dt} = k_5' + k_5'' \frac{(mX)^n}{J_5^n + (mX)^n} - k_6 A, \tag{1.3}$$

$$\frac{dm}{dt} = m\mu(1 - \frac{m}{m_*}). \tag{1.4}$$

In this model, k's are rate constants and J's Michaelis constants. In equation (1.1), k_1 provides the synthesis rate and the $(k_2' + k_2''Y)X$ expression represents the degradation of Cyclin B/Cdk dimers (X). The dynamics of APC/Cdh1 (Y) are governed by equation (1.2). From the $\frac{(k_3'+k_3''A)(1-Y)}{J_3+1-Y}$ expression in equation (1.2), it can be seen that Cdh1/APC (Y) activation not only depends upon its own concentration $(1-Y)$, but also the variable A. A's (Cdc20's) dynamics are described by equation (1.3) and it is activated by Cyclin B/Cdk (modelled by the mX expression in equation (1.3)) at maximal rate k_5''.

The mX term which appears in equations (1.2) and (1.3) and contributes to Cdh1/APC

(Y) degradation and Cdc20 (A) activation, represents the 'intranuclear concentration' of Cyclin B/Cdk (X) dimers. Essentially, as the cell grows throughout the cell cycle and its mass m increases so do the number of ribosomes. Ribosomes can be regarded as the factories of the cells and their function is to build proteins including the Cyclins. Therefore, as the number of ribosomes increases, the amount of proteins produced increases. Once formed Cyclin B/Cdk dimers migrate into the nucleus. During the growth process, the size of the nucleus remains constant and hence the concentration of the protein Cyclin B/Cdk will increase within the nucleus.

m, whose dynamics are described by equation (1.4) represents the mass of the cell, with μ the cell growth rate. In their model, Tyson and Novak normalise the parameters such that the cell mass and concentrations are dimensionless and rate constants have dimensions min^{-1}. A schematic of the biochemical reactions that model this process is shown in Figure 1.10 and a summary of the parameters used in Tyson *et al*'s model is given in Table 1.1.

If we consider the full model (system (1.1)-(1.4)), Tyson *et al* add a condition to ensure that solution trajectories do not tend towards a stable fixed point, but instead can oscillate. When X falls below a certain value, the end of the cell cycle is signalled (i.e. M phase is complete) and $m \rightarrow \frac{m}{2}$, signalling that the cell has divided into two daughter cells. The cell then returns to G_1 phase and the whole system begins anew, with the cell irreversibly progressing towards S phase. A simulation of system (1.1)-(1.4) can be seen in Figure 1.11.

Figure 1.11 shows how the variables in Tyson *et al*'s model evolve, modelling the cell cycle of the budding yeast cell in the process. When the mass is low (i.e. the cell is just beginning the cell cycle), Cyclin/Cdk concentration is low too, as one would expect when the cell is in G_1 phase. As the cell grows and begins to progress towards S phase, it can be seen that Cyclin B/Cdk (X) activity begins to rise, which is associated with a rise in Cdh1/APC activity (Y). This is what one would expect when approaching the $S - G_2 - M$ state. It is at this point that Cdc20 is activated, which in turn activates Cdh1/APC at anaphase. As levels of Cdh1/APC peak, the concentration of Cyclin/Cdk begins to fall, until Cyclin/Cdk concentration falls below 0.1, signalling the end of mitosis and the cell cycle.

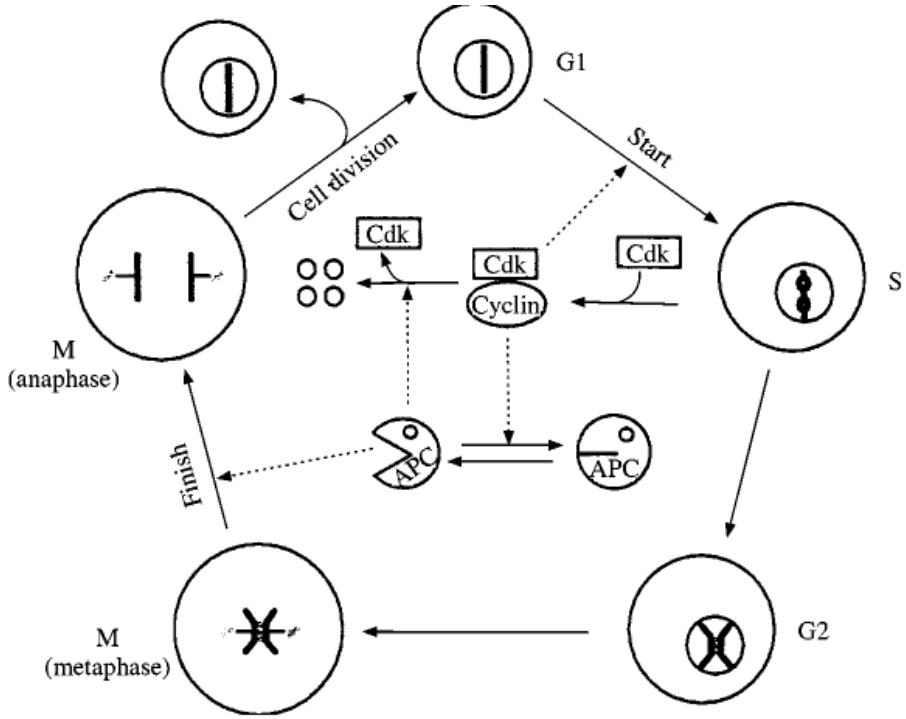

Figure 1.10: Schematic illustrating the how the various proteins that Tyson *et al* are concerned with interact during the cell cycle. Reproduced from [89] with permission from Elsevier.

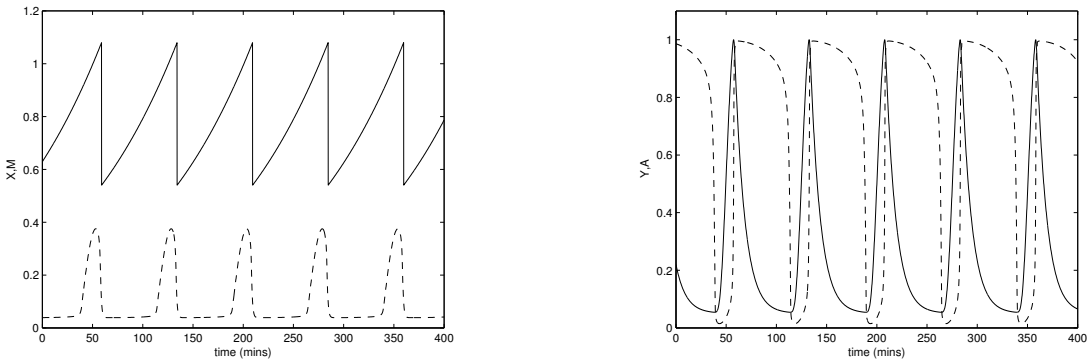

Figure 1.11: Oscillations of X (average concentration of Cyclin B/Cdk),Y (average concentration of Cdh1/APC), A (Cdc20), and M (the cell mass) for Tyson and Novak's model of the yeast cell cycle. The cell mass and all protein concentrations are dimensionless. Results obtained by numerically integrating equations (1.1)-(1.4) using the Runge Kutta method of integration. Key:- solid line corresponds to m, dashed curve to X in the left hand plot; solid line corresponds to A, dashed curve to Y, in the right hand plot. Parameter values: $k_1 = 0.04\ \text{min}^{-1}, k_2' = 0.04\ \text{min}^{-1}, k_2'' = 1\ \text{min}^{-1}, k_3''' = 1\ \text{min}^{-1}, k_3' = 1\ \text{min}^{-1}, k_3'' = 10\ \text{min}^{-1}, k_4' = 2\ \text{min}^{-1}, k_4 = 35\ \text{min}^{-1}, k_5' = 0.005\ \text{min}^{-1}, k_5'' = 0.2\ \text{min}^{-1}, k_6 = 0.1\ \text{min}^{-1}, J_3 = 0.04, J_4 = 0.04, J_5 = 0.3, n = 4, \mu = 0.01\ \text{min}^{-1}, m_\star = 10.$

Table 1.1: Description of parameters used in Tyson and Novak's model

Parameter	Unit	
k_1	min^{-1}	Cyclin B synthesis rate
k_2'	min^{-1}	Cyclin B degradation rate
k_2''	min^{-1}	Rate at which APC/Cdh1 degrades Cyclin B
k_3'	min^{-1}	Maximal rate at which Cdh1 is synthesised
k_3''	min^{-1}	Maximal rate at which Cdh1 is synthesised by Cdc20
k_4	min^{-1}	Maximal rate at which Cdh1 is degraded by Cyclin B
k_5'	min^{-1}	Cdc20 synthesis rate
k_5''	min^{-1}	Maximal rate at which Cdc20 is synthesised by Cyclin B
k_6	min^{-1}	Rate at which Cdc20 is degraded
J_3	dimensionless	Michaelis constant
J_4	dimensionless	Michaelis constant
J_5	dimensionless	Michaelis constant
n	dimensionless	Hill coefficient
μ	min^{-1}	Cell growth rate
$m_\star$	dimensionless	Maximum cell mass

Suitability of using Tyson and Novak's model in a radial glial cell model

Tyson and Novak's model is unsuitable for our purposes as firstly their minimal model does not include Cyclin D, one of the cell cycle molecules thought to be responsible for calcium modulation of the cell cycle. A later model of theirs for the mammalian cell cycle does incorporate Cyclin D [64], yet this is a large model with 17 ODEs and as such will be computationally very expensive to simulate. This would be particularly problematic when considering clusters of a large number of coupled cells. Secondly, the discontinuous nature of mass in both of Tyson *et al*'s models presents problems with regards to analysing the models. Bifurcation analysis would be difficult for example, as the numerical techniques would have great difficulty resolving the discontinuities. In addition to this, it would be extremely difficult to apply techniques that explore 'phase locking' of coupled oscillators, which we intend to employ later, if the variables of model are not all continuous.

1.5.2 Obeyesekere's and Zimmerman's Model

A five dimensional system for the mammalian cell cycle, incorporating Cyclin D has been proposed by Obeyesekere and Zimmerman in which all variables are continuous [66]. Obeyesekere *et al* are mainly concerned with G_1 phase of the cell cycle and as such include within their model many of the proteins involved with this phase in particular, such as Cyclin D, Cyclin E and retinoblastoma tumour suppressor protein.

As with the Tyson and Novak model, Cdks are assumed to be available in abundance in Obeyesekere *et al*'s model and as soon as Cyclins are produced they immediately bind to their respective Cdk partners and form active Cyclin/Cdk complexes; Cyclin D binds with Cdk4 and Cyclin E binds with Cdk2. In their model, active Cyclin D (D in the model) is synthesised at maximum rate a_d and Cyclin E (represented by E), initiates Cyclin D's degradation at rate d_D. Obeyesekere *et al* also make Cyclin D production dependent upon growth factors (GF in the model). Growth factors bind to receptors on the cell membrane, whereupon they initiate a chain of events, eventually leading to the production of cell cycle proteins within the cell. Free unphosphorylated retinoblastoma tumour suppressor protein (RB, R in the model) forms complexes with the E2F transcription factor (E2F's total concentration is given by $\ominus$ in the model). Like the Cdks, the concentrations of RB and E2F are assumed to be constant throughout the cell cycle. When RB exists in its free unphosphorylated form (R), it forms RB/E2F complexes (R_s) at rate p_s. E2F acts to promote a number of genes involved with DNA synthesis and as such helps to drive the cell towards S phase of the cell cycle. However, it is inert when bound to RB. Active Cyclin D/Cdk4 (D) and Cyclin E/Cdk2 (E) complexes phosphorylate RB bound to E2F (with parameters p_D, q_D and p_E, q_E respectively) and in the process release E2F. Free E2F ($R_s - \ominus$), liberated from RB, then acts to promote Cyclin E (E) production at maximal rate a_f. It is assumed that the reduction in RB/E2F complexes (R_s) is proportional to the amount of free E2F ($R_s - \ominus$) and hence the total E2F ($\ominus$) will never fall below the concentration of bound RB/E2F complexes (R_s) in the model. Free E2F in concert with Cyclin E initiates S phase of the cell cycle.

Obeyesekere *et al* also consider a variable, which they refer to as the 'cell progression indicator' (CPI, denoted by X in the model). It does not represent any one protein but allows Obeyesekere *et al* to model S, G_2 and M phase of the cell cycle with one variable.

As such the CPI indirectly represents the kinases, phosphatases and proteases responsible for driving the cell through S, G_2 and M phase. In the model, the CPI dephosphorylates RB (with parameters p_X, q_X), degrades Cyclin E (at rate d_E) and degrades its self (at rate d_X). For a detailed discussion of these processes see [65]. Figure 1.12 shows how the various proteins that Obeyesekere *et al* model interact with each other and in Table 1.2 we provide a summary of the variables and parameter values used in their model. Obeyesekere *et al*'s model, which describes the concentrations of five compounds, D (Active Cyclin D/Cdk4 complexes), E (Active Cyclin E/Cdk2 complexes), R (free unphosphorylated RB), R_s (E2F sequestered by RB) and X (the CPI) is given by

$$\frac{dD}{dt} = a_d\left(\frac{kGF}{1+kGF}\right) - d_D E D, \tag{1.5}$$

$$\frac{dE}{dt} = a_E(1 + a_f(\ominus - R_s)) - d_E X E, \tag{1.6}$$

$$\frac{dR}{dt} = \frac{p_X(R_T - R_s - R)X}{q_X + (R_T - R_s - R) + X} - p_s(\ominus - R_s)R, \tag{1.7}$$

$$\frac{dR_s}{dt} = p_s(\ominus - R_s)R - \frac{p_D R_s D}{q_D + R_s + D} - \frac{p_E R_s E}{q_E + R_s + E}, \tag{1.8}$$

$$\frac{dX}{dt} = a_X E + f(\ominus - R_s) + gX^2 E - d_X X. \tag{1.9}$$

The inclusion of the 'cell progression indicator' X perhaps makes Obeyesekere's model less biologically comprehensive but does mean that the number of ODEs are kept to a minimum. System (1.5) - (1.9) can be numerically integrated to give the results shown in Figure 1.13.

Figure 1.13 shows how Cyclin D and E oscillate in a continuous manner as the cell progresses through the cycle. As mentioned above, calcium has the effect of increasing the concentration of active Cyclin D/Cdk4 complexes [45, 46, 79]. In a phenomenological model incorporating the effect of calcium on the cell cycle, it would therefore seem natural to allow calcium to affect the Cyclin D synthesis rate. As mentioned above, calcium can have the effect of inducing quiescent cells onto the cell cycle [7, 9]. Additionally, increased Cyclin D/Cdk4 shortens the duration of G_1 in different cell types leading to an overall reduction in the period of the cell cycle [55, 72, 74]. Therefore in modelling calcium's effect on the cell cycle, one would look for a cell cycle model where an increase in the Cyclin D synthesis rate

Table 1.2: Description of variables and parameters used in Obeyesekere's and Zimmerman's Model

Term	
D	Concentration of active Cyclin D/Cdk4 complexes
E	Concentration of active Cyclin E/Cdk2 complexes
R	Concentration of free unphosphorylated RB
R_s	Concentration of E2F sequestered by RB
X	Cell progression indicator
a_d	Maximum Cyclin D synthesis rate
GF	Growth Factors
k	Efficiency of Growth Factor signal transduction pathway
d_D	Rate at which active Cyclin E/Cdk2 degrades Cyclin D
a_E	E2F independent Cyclin E synthesis rate
a_f	E2F dependent Cyclin E synthesis rate
$\ominus$	Total concentration of E2F
p_X	Maximal rate at which the CPI dephosphorylates RB
q_X	Michaelis constant
d_E	Rate at which the CPI degrades Cyclin E
p_s	Rate at which free unphosphorylated RB sequesters E2F
p_D	Maximum rate at which active Cyclin D/Cdk4 phosphorylates RB
q_D	Michaelis constant
p_E	Maximum rate at which active Cyclin E/Cdk2 phosphorylates RB
q_E	Michaelis constant
a_X	Rate of Cyclin E/Cdk2 dependnet CPI production
f	Rate of free E2F dependnet CPI production
g	CPI autocatalytic reaction rate
d_X	CPI degradation rate
R_T	Total RB

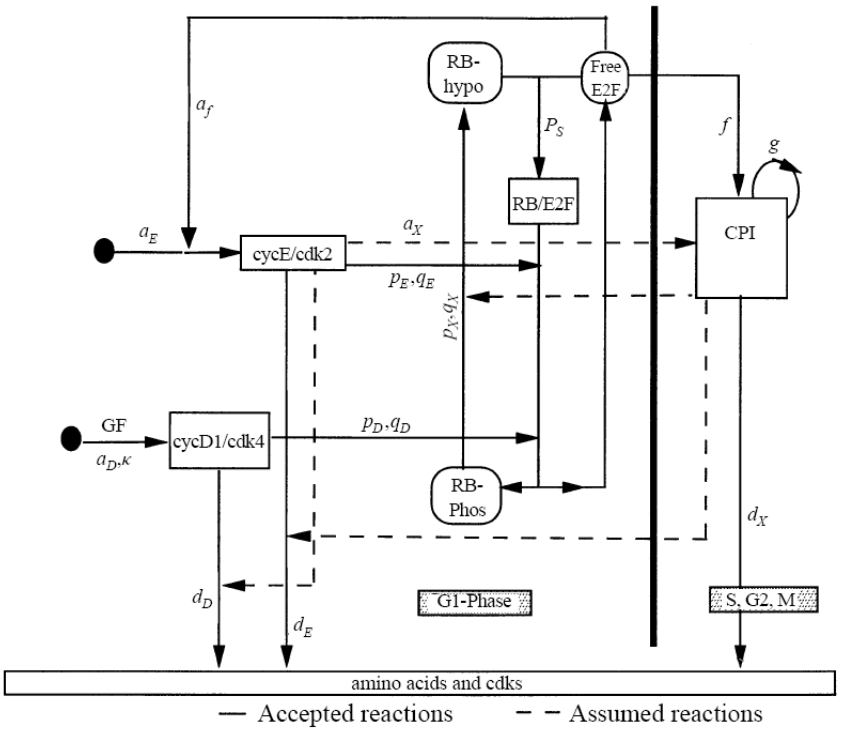

Figure 1.12: Schematic illustrating how cell cycle proteins modelled by Obeyesekere *et al* interact. Reproduced from [66] with permission from Springer Science and Business Media.

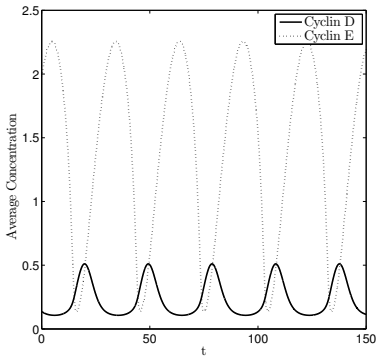

Figure 1.13: Oscillations of D (Cyclin D concentration) and E (Cyclin E) obtained by numerically integrating equations (1.5)-(1.9) using the 4^{th} order Runge Kutta method of integration in Matlab. All units are dimensionless. Parameter values:- $a_D = 0.4, a_E = 0.16, a_X = 0.08, k = 0.05, q_D = 0.6, q_E = 0.6, q_X = 0.8, f = 0.2, g = 0.528, p_s = 0.6, p_D = 0.48, p_E = 0.096, p_X = 0.48, d_D = 0.4, d_E = 0.2, d_X = 1.04, a_f = 0.9, R_t = 2.5, \ominus = 1.5$ and $GF = 6.3$. Initial conditions: $D(0) = 0.1376, E(0) = 1.9833, R(0) = 0.2897, R_s(0) = 1.0297$ and $X(0) = 0.3053$.

can induce a dormant cell into an oscillatory regime and also reduce the period of oscillation of a cell already oscillating. 'a_D' from equation (1.5) provides the Cyclin D synthesis rate of the Obeyesekere *et al* model. Bifurcation diagrams of Obeyesekere *et al*'s model with 'a_D' as the control parameter are shown in Figure 1.14.

By referring to Figure 1.14 it is clear that a branch of low amplitude limit cycle solutions is created via a Hopf bifurcation point at $a_d \approx 0.409957$. The stability of this branch is then lost via a saddle node bifurcation of limit cycle solutions before being regained via another saddle node bifurcation at $a_d \approx 0.3952941$. This time however the limit cycle solutions are of a far higher amplitude. It can also be seen that an increase in the Cyclin D synthesis rate a_d (which is calcium's downstream target) leads to a reduction in the period of the cell cycle.

Overexpression of Cyclin D in rat-2 fibroblast cells (a cell line derived from the connective tissue of the rat) resulted in a decrease in G_1 phase duration of $\approx$ 2-3 hours depending upon the degree of overexpression [72]. This resulted in a total reduction in the period of the cell cycle of rat-2 cells of $\approx$ 6.67 - 10 %. Overexpression of Cyclin D in NIH 3T3 cells (a mouse embryonic fibroblast cell line) resulted in the shortening of G_1 phase of the

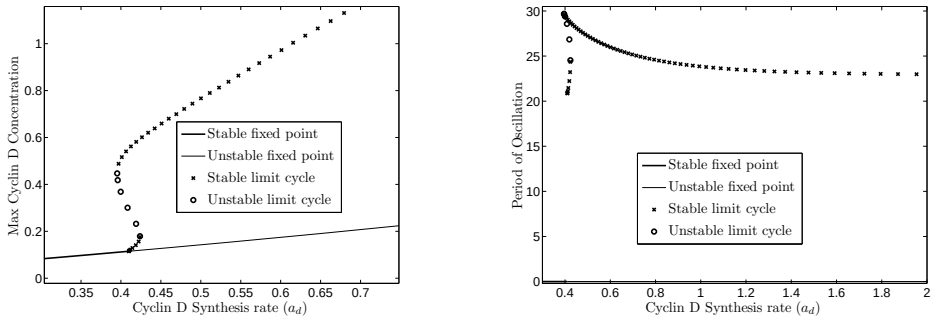

Figure 1.14: Bifurcation diagrams showing how the Cyclin D synthesis rate given by a_D affects Cyclin D concentration and the period of the cell cycle. $a_E = 0.16, a_X = 0.08, k = 0.05, q_D = 0.6, q_E = 0.6, q_X = 0.8, f = 0.2, g = 0.528, p_s = 0.6, p_D = 0.48, p_E = 0.096, p_X = 0.48, d_D = 0.4, d_E = 0.2, d_X = 1.04, a_f = 0.9, R_t = 2.5, \ominus = 1.5, GF = 6.3$ and a_D as shown. Diagrams computed using AUTO within XPP.

cell cycle of around 2 hours, corresponding to a decrease in the duration of the cell cycle of around 11.63 % [55]. In Obeyesekere *et al*'s model increasing the parameter controlling the Cyclin D synthesis rate a_d from 0.41 to 0.6 brings about a reduction in the period of the cell cycle of $\approx 10.72\%$, while an increase to 0.8 brings about a decrease in period of $\approx$ 15.60%. These values are very similar to those calculated in the biological literature. In this sense, it would seem that Obeyesekere *et al*'s model is a good candidate when considering a phenomenological model for calcium's affect on the cell cycle in radial glial cells.

Furthermore, the stable fixed point below the Hopf bifurcation point and the lower branch of stable limit cycle solutions are interpreted by Obeyesekere *et al* as the G_0 quiescent state of the cell cycle [66]. If a cell lies on this stable fixed point, a sufficiently large increase in the Cyclin D synthesis rate a_d would drive it onto the branch of limit cycle solutions. This increase could be brought about by calcium and raises the possibility that it is by this process that calcium's effect of driving a cell from the G_0 state into G_1 could be modelled. This later observation further supports the argument that Obeyesekere *et al*'s model is a suitable candidate for our purposes.

1.6 A Model Incorporating Calcium's Effect on Metaphase II Arrest in Meiosis

Dupont investigates the effect of calcium via CaMKII on metaphase II of meiosis II [18]. Meiosis is a different process to mitosis and occurs in eukaryotic life cycles involving sexual reproduction. Unlike the mitotic process which continues for a number of cycles, meiosis occurs only once and consequently it can not be said to engage in a cell cycle, even though it leads to the creation of daughter cells. Despite this, the start of the meiotic cycle is identical to that of the mitotic cell cycle and it is for these reasons that we study Dupont's model here. Like mitosis, in meiosis a cell enters G_1 phase, followed by entry into S and then G_2 phase. It is during the next phase of the cell cycle that meiosis differs from the mitotic cell cycle. A cell undergoing meiosis then enters into meiosis I, where one diploid (a cell with two sets of chromosomes) divides into two haploid cells (with one set of chromosomes each). The cell then progresses on to meiosis II where the two haploids divide again by separation of sister chromatids producing four haploids in all, each with half of the original cells chromosomes. Meiosis II can be subdivided into prophase II, metaphase II, anaphase II and finally telophase II. It is metaphase II of meiosis II that Dupont focuses upon, when the cell is in a state of arrest and can only be activated by fertilisation with another haploid cell of opposite gender, producing a diploid cell. This arrest is characterised by high levels of Cyclin B and active Cdc2, as well as high levels of cytostatic factor (CSF) which prevents the degradation of Cyclin. CSF, by preventing Cyclin degradation, prevents the cell from proceeding to anaphase II of meiosis II. Fertilisation triggers a train of Ca^{2+} spikes which have the effect of inhibiting CSF activity and also that of Cdc2. It is important here to note that Cdc2 inhibition occurs before CSF inhibition. This leads Dupont to make several assumptions in the mathematical model as we shall see below.

The Mathematical Model

Dupont intially considers Goldbeter's model for the mitotic cell cycle [30], with the intention of adapting it to incorporate the effect of calcium on meiosis. In his model, Golbeter considers the concentration of Cyclin B (C in the model), the fraction of active Cdc2 (M) and the fraction of active APC (X). Cdc2 is used interchangeably with Cdk2 in the literature and exists in its active form when bound to Cyclin B. Active Cdc2 therefore is

nothing more than the Cyclin B/Cdk2 complexes that we have encountered previously. In the model, Cyclin B is synthesised at rate v_i and degraded by the fraction of active APC (X) at maximal rate v_d. Inactive Cdc2 ($1-M$) is activated at maximal rate V_{M1} by Cyclin B (C). Inactive APC ($1-X$) is activated at maximal rate V_{M3}, by the fraction of active Cdc2 (M). k_d provides the degradation rate of Cyclin B (C) in the model. V_2 and V_4 provide the maximal rates of Cdc2 and APC inactivation respectively. Goldbeter's model of the mitotic cell cycle is as follows:

$$\frac{dC}{dt} = v_i - v_d X \frac{C}{K_d + C} - k_d C, \tag{1.10}$$

$$\frac{dM}{dt} = V_{M1} \frac{C}{K_c + C} \frac{1-M}{K_1 + 1 - M} - V_2 \frac{M}{K_2 + M}, \tag{1.11}$$

$$\frac{dX}{dt} = V_{M3} M \frac{1-X}{K_3 + 1 - X} - V_4 \frac{X}{K_4 + X}. \tag{1.12}$$

In a number of ways, Goldbeter's model is similar to Tyson's and Novak's model which we studied earlier in the chapter. Both models include a term for Cyclin B and APC for example, although Goldbeter has in mind the amphibian cell cycle when forming his model and Tyson *et al* the cell cycle of budding yeast. In Tyson's and Novak's model, Cdks are assumed to be in abundance and as soon as Cyclin B is produced it binds to Cdk2. This is not the case for Goldbeter's model however, where C, whose dynamics are described by equation (1.10) represents free Cyclin B and Cyclin B/Cdk2 complexes are represented by M (equation 1.11).

Tyson and Novak also include a term for the mass of the cell, while Goldbeter does not. The reset condition imposed upon the mass term in Tyson's and Novak's model drives the oscillations in their system, while oscillations in Goldbeter's model come about due to the presence of limit cycle solutions in the underlying dynamics of the system. In this dynamical sense, Goldbeter's model has more in common with Obeyesekere *et al*'s model, as in Obeyesekere *et al*'s model oscillations arise as a result of limit cycle solutions present in the underlying dynamics of the system as well. This is where the similarities with Obeyesekere *et al*'s model end however. The proteins considered in Obeyesekere *et al*'s model for the mammalian cell cycle differ from the proteins modelled by Tyson *et al* and Goldbeter, reflecting the different class of animal that the different authors consider when developing their respective models.

Numerically integrating Goldbeter's model for the cell cycle (system (1.10)-(1.12)) leads to the results illustrated in Figure 1.15.

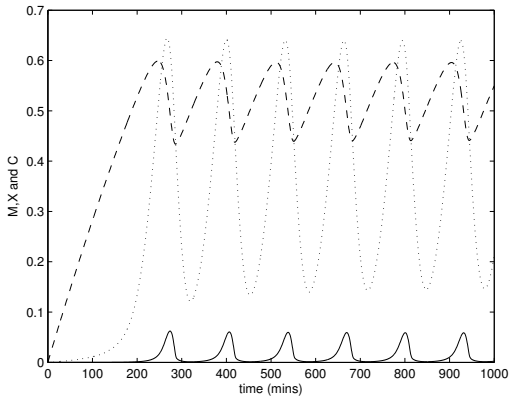

Figure 1.15: Graph showing oscillations of Cyclin B, fraction of active Cdc2 and fraction of active APC of the model for the mitotic cell cycle, obtained by numerically integrating system (1.10)-(1.12) using a fourth order Runge Kutta method. Key:- dotted lines correspond to M (fraction of active Cdc2), dashed to C (Cyclin B) and solid line to X (fraction of active APC). The concentration of Cyclin B is of dimension μM. Fractions of active Cdc2 (M) and active APC (X) are dimensionless. Parameter values: $v_1 = 0.003\,\mu\text{Mmin}^{-1}, v_d = 0.18\,\mu\text{Mmin}^{-1}, K_d = 0.05\,\mu\text{M}, k_d = 0.0012\,\text{min}^{-1}, V_{M1} = 0.36\,\text{min}^{-1}, K_c = 0.5\,\mu\text{M}, V_2 = 0.186\text{min}^{-1}, V_{M3} = 0.072\text{min}^{-1}, V_4 = 0.048\text{min}^{-1}, K_1 = K_2 = K_3 = K_4 = 0.005$.

As mentioned above, metaphase II of meiosis II is characterised by high levels of Cyclin B and active Cdc2 as well as low levels of APC. This situation is modelled using equations (1.10)-(1.12) in Figure 1.16, where it can be seen that Cdc2 (M) and Cyclin B (C) concentrations are high as is the case during metaphase II arrest of the process of meiosis.

Dupont adds a further five equations to the above three in order to model the effect calcium has on relieving the cell from Metaphase II arrest of meiosis II. The full system is given by equations (1.10) and (1.11) together with the following set of ODEs

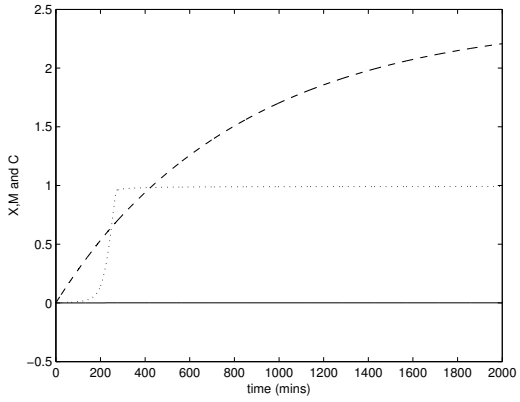

Figure 1.16: Results of modelling metaphase II arrest. It can be seen that towards the end of the period of integration, concentrations of active Cdc2 (M, dotted line) and Cyclin B (C, dashed line) are high and active APC (X, solid line) are low. This is characteristic of metaphase II arrest. The concentration of Cyclin B is of dimension μM. Fractions of active Cdc2 (M) and active APC (X) are dimensionless. Results obtained by numerically integrating equations (1.10)-(1.12) using a fourth order Runge Kutta method. Parameter values as in Figure 1.15 except for $V_{M3} = 0.0045\ \text{min}^{-1}$.

$$\frac{dW}{dt} = V_{M5}\frac{Z^4}{K_A^4 + Z^4}\frac{1-W}{K_5+1-W} - V_6\frac{W}{K_6+W}, \tag{1.13}$$

$$\frac{dS}{dt} = V_7\frac{1-S}{K_7+1-S} - V_{M8}W\frac{S}{K_8+S}, \tag{1.14}$$

$$\frac{dQ}{dt} = V_{M10}(1-S)^4\frac{1-Q}{K_{10}+1-Q} - V_{11}\frac{Q}{K_{11}+Q}, \tag{1.15}$$

$$\frac{dQ_2}{dt} = V_{M12}Q\frac{1-Q_2}{K_{12}+1-Q_2} - V_{13}\frac{Q_2}{K_{13}+Q_2}, \tag{1.16}$$

$$\frac{dCSF}{dt} = -V_{M9}Q_2\frac{CSF}{K_9+CSF} - k_9 CSF. \tag{1.17}$$

Equation (1.12) in the model for mitotic cell cycle now becomes

$$\frac{dX}{dt} = V'_{M3}M\frac{K_i^4}{K_i^4+CSF^4}\frac{1-X}{K_3+1-X} - V'_{M4}S\frac{X}{K_4+X}. \tag{1.18}$$

The evolution of the fraction of active CaMKII is given by W in equation (1.13). The Hill function $\frac{Z^4}{K_A^4+Z^4}$ in equation (1.13) accounts for the way in which Ca^{2+} activates CaMKII (W). Hence Z represents the level of Ca^{2+} and in Dupont's model its behaviour is described

by the following piecewise linear ODE:

$$\frac{\mathrm{d}Z}{dt} = \begin{cases} -0.230258509Z & t < 240 \\ 0 & t > 240 \end{cases} \tag{1.19}$$

with the condition that Z resets to 1 once it falls below 0.1, provided $t < 240$ min. These conditions model the spiking nature of the calcium oscillations as well as the transient nature of the spikes.

In Table 1.3 with summarise the variables used in Dupont's model and in Table 1.4 the parameters. Figure 1.17 shows how the proteins Dupont considers in her model interact and serves as a useful reference point in the subsequent discussion on Dupont's model. As mentioned above, CSF is inactivated well after Cdc2. It is with this in mind that Dupont introduces the terms S, Q and Q_2 whose behaviour is given by equations (1.14), (1.15) and (1.16) respectively. S represents a 'mediator' protein substrate in its unphosphorylated form whose existence is postulated by Dupont. S facilitates CaMKII's activation of APC, which in turn leads to the de-activation of Cdc2. In order to achieve this CaMKII phosphorylates S into its inactive form ($-V_{M8}W$ from equation (1.14)) and in doing so nullifies the effects of S inhibition upon APC (modelled by the $-V'_{M4}S$ term in equation (1.18)). CaMKII through S also has the effect of decreasing the activity of CSF via two more postulated proteins proteins Q and Q_2, whose dynamics are represented by equations (1.15) and (1.16) respectively. The behaviour of active CSF is given by CSF in equation (1.17) with the '$-V_{M9}Q_2$' term corresponding to its is de-activation by CaMKII via the '$S - Q - Q_2$' pathway. The reason for postulating these two further proteins is to provide a time delay in the system to ensure that a decrease in Cdc2 activity (facilitated by an increase in APC activity) will precede a decrease in CSF activity. However, introducing these postulated proteins S, Q and Q_2 makes Dupont's model less biologically rigorous than perhaps it could be. The system (1.10), (1.11), (1.13)-(1.19) can be numerically integrated to model the resumption of the the meiotic process upon fertilisation from metaphase II arrest of meiosis II. Results of these simulations are shown in Figure 1.18.

Figure 1.18 reveals that calcium spikes of a sufficient intensity and lasting a duration of 240 mins are sufficient to reduce the levels of Cyclin B sufficiently to relieve the cell from

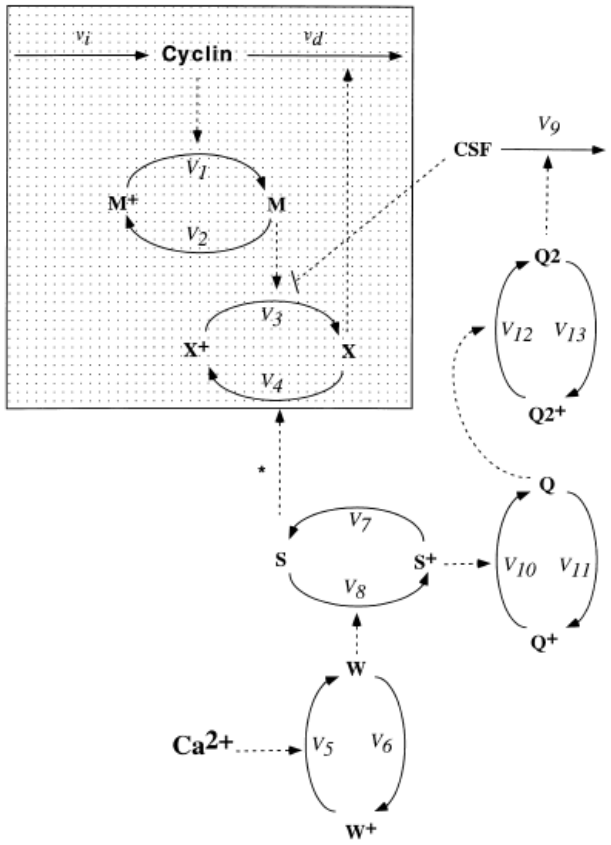

Figure 1.17: Schematic illustrating how the various proteins interact with each other in Dupont's model. Dashed arrows indicate activations, dashed lines terminated with hyphens indicate inhibition. C stands for Cyclin B while M and X represent active Cdc2 and APC respectively. W stands for CaMKII. $^+$ indicates the active form of protein. Reproduced from [18] with permission from Elsevier.

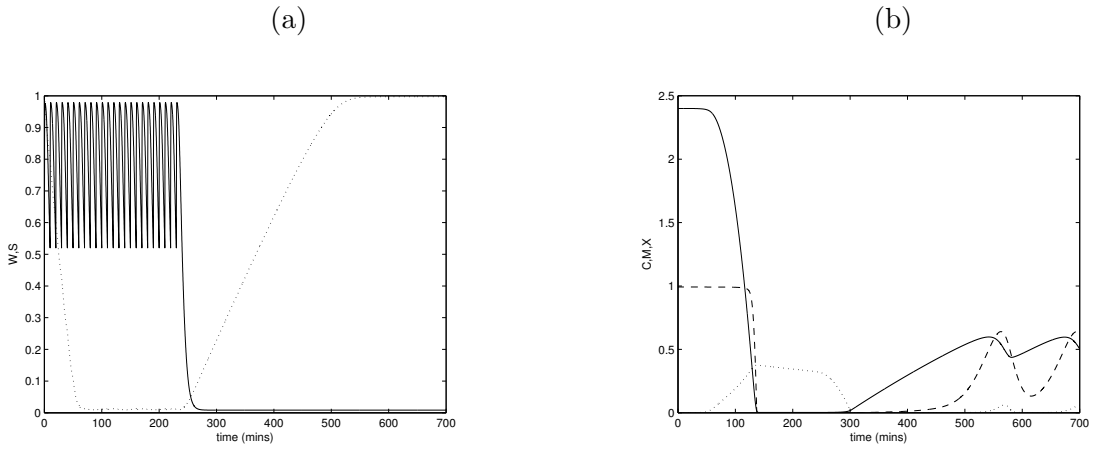

Figure 1.18: Simulation of the full model given by the system (1.10), (1.11), (1.13)-(1.19) for the resumption of meiosis after metapahse II. Key:- solid lines correspond to W (fraction of active CaMKII), dotted lines to S (the mediator protein) in (a). Solid lines correspond to C (Cyclin B), dotted lines to X (APC) and dashed lines to M (fraction of active Cdc2) in (b). It can be seen in (a), that at $t \approx 500$ mins, the majority of CaMKII exists in its active form ($W \to 1$). Active CaMKII acts to lift the cell from metaphase II arrest by inducing mitotic oscillations in the cell (evidenced by the oscillatory behaviour of the cell cycle variables C, M and X, which begins at $t \approx 500$ mins in (b)). The concentration of Cyclin B is of dimension μM. Fractions of active Cdc2 (M), active APC (X), active CaMKII (W) and active mediator protein S are dimensionless. Parameter values as per Figure 1.15 with $V'_{M3} = 0.072\,\text{min}^{-1}, V_{M4'} = 0.048\,\text{min}^{-1}, K_i = 0.5\,\mu\text{M}, V_{M5} = 8\,\text{min}^{-1}, V_6 = 0.2\ \text{min}^{-1}, K_5 = K_6 = 1, K_A = 0.7\ \mu\text{M}, V_7 = 0.0045\ \text{min}^{-1}, V_{M8} = 0.03\ \text{min}^{-1}, K_7 = K_8 = 0.05, V_{M9} = 0.015\ \mu\text{Mmin}^{-1}, K_9 = 0.5, k_9 = 0.0001\text{min}^{-1}, V_{M10} = 0.2\text{min}^{-1}, V_{11} = 0.14\text{min}^{-1}, V_{M12} = 0.02\text{min}^{-1}, V_{13} = 0.014\ \text{min}^{-1}, K_{10} = K_{11} = K_{12} = K_{13} = 0.01$. Results obtained using a fourth order Runge Kutta method of integration.

Table 1.3: Description of variables used in Dupont's model

Variable	Unit	
C	μM	Concentration of active Cyclin B
M	dimensionless	Fraction of active Cdc2
X	dimensionless	Fraction of active APC
W	dimensionless	Fraction of active CaMKII
S	dimensionless	Fraction of active mediator protein S
Q	dimensionless	Fraction of active mediator protein Q
Q_2	dimensionless	Fraction of active mediator protein Q_2
CSF	μM	Concentration of cytostatic factor
Z	μM	Concentration of calcium

metaphase II arrest. The cell is then free to proceed onto the mitotic cell cycle which is evidenced by the oscillations in the cell cycle variables seen in the second plot in Figure 1.18.

1.6.1 Can Dupont's Model be Utilised to Account for Calcium's Effect in Inducing a Cell to Enter S phase of the Mitotic Cell Cycle?

Dupont's model deals with the effect of calcium on meiosis, while our project is concerned with calcium's effect on the mitotic cell cycle. In meiosis calcium effects CaMKII, while in the mitotic cell cycle calcium predominantly affects CaMKI. Dupont does not incorporate CaMKI into her model. Hence it would seem unlikely that Dupont's model could be easily adapted into a model incorporating the effect of calcium on mitosis. Furthermore, Goldbeter's model for the cell cycle [30] which Dupont utilises, does not contain a Cyclin D term, the very protein affected by calcium during the mitotic cell cycle. All of this suggests that neither Dupont's model nor Golbeter's model for the cell cycle are suitable for building a model incorporating the effect of calcium on the mitotic cell cycle. In summary Obeyesekere *et al*'s model seems to be the most suitable for our purposes.

1.7 Models of Calcium Release

We will also need to consider models of calcium release from within cells. Although Dupont achieves this through a piecewise linear ODE, calcium release in her model is prescribed

Table 1.4: Description of parameters used in Dupont's model

Parameter	Unit	
v_i	μMmin^{-1}	Cyclin B synthesis rate
v_d	min^{-1}	Maximal rate at which APC degrades Cyclin B
K_d	μM	Michaelis constant
k_d	min^{-1}	Cyclin B degradation rate
V_{M1}	min^{-1}	Maximal rate at which inactive Cdc2 is activated by Cyclin B
K_c	μM	Michaelis constant
K_1	dimensionless	Michaelis constant
V_2	dimensionless	Maximal rate at which Cdc2 is inactivated
K_2	dimensionless	Michaelis constant
V_{M5}	min^{-1}	Maximal rate at which inactive CaMKII is activated by calcium
K_A	μM	Threshold constant of CaMKII activation by calcium
K_5	dimensionless	Michaelis constant
V_6	min^{-1}	Maximal rate of CaMKII inactivation
K_6	dimensionless	Michaelis constant
V_7	min^{-1}	Maximal rate at which inactive S is activated
K_7	dimensionless	Michaelis constant
V_{M8}	min^{-1}	Maximal rate at which active S is inactivated by active CaMKII
K_8	dimensionless	Michaelis constant
V_{M10}	min^{-1}	Maximal rate of activation of Q by inactive S
K_{10}	dimensionless	Michaelis constant
V_{11}	min^{-1}	Maximal rate of inactivation of Q
K_{11}	dimensionless	Michaelis constant
V_{M12}	min^{-1}	Maximal rate of activation of inactive Q_2 by active Q
K_{12}	dimensionless	Michaelis constant
V_{13}	min^{-1}	Maximal rate of inactivation of Q_2
K_{13}	dimensionless	Michaelis constant
V_{M9}	μMmin^{-1}	Maximal rate at which Q_2 inactivates CSF
K_9	μM	Michaelis constant
k_9	min^{-1}	Rate at which CSF is inactivated
V'_{M3}	min^{-1}	Maximal rate at which inactive APC is activated
K_i	μM	Term characterising the inhibition of APC by CSF
K_3	dimensionless	Michaelis constant
V'_{M4}	min^{-1}	Maximal rate at which APC is inactivated by S

and much research has gone into mechanistic modelling of calcium release. We consider two of these models in detail in this section.

1.7.1 Li and Rinzel's Model

Li and Rinzel [90] developed a simplified model for the release of calcium from internal stores based on the high dimensional model produced by De Young and Keizer [97]. Li and Rinzel consider a closed cell and consequently focus only upon the intracellular mechanisms of calcium release. These mechanisms are illustrated in the schematic in Figure 1.19.

In their model, $[Ca^{2+}]$ represents free cytosolic calcium, which is released from the cell's internal stores located in the endoplasmic reticulum (ER) of the cell. In the model, calcium residing in the ER is $[Ca^{2+}]_{ER}$ and total calcium, both cytosolic and ER, is denoted by C_t. Cytosolic calcium (which is released at rate $\frac{f_i}{V_i}$ from the ER) depends upon the flux of calcium release from internal stores (J_{ER}^{out}) and the flux that refills the internal stores from free calcium in the cytosol (J_{ER}^{in}). For a detailed description on how Li and Rinzel derive J_{ER}^{out} and J_{ER}^{in} from De Young and Keizer's model, see [54]. J_{ER}^{out} depends upon calcium leaked from the internal stores into the cytosol (L) and also the concentration of IP_3 (represented by $[IP_3]$), which acts to stimulate calcium release from internal stores. Furthermore, J_{ER}^{out} depends upon a 'gating' variable (h), representing the fraction of channels which are not inactivated by calcium and hence available to open upon IP_3 activation. The system of ODEs below constitute Li and Rinzel's model

$$\frac{d[Ca^{2+}]}{dt} = \frac{f_i}{V_i}(J_{ER}^{out} - J_{ER}^{in}), \tag{1.20}$$

$$\frac{dh}{dt} = A[K_d - ([Ca^{2+}] + K_d)h], \tag{1.21}$$

$$J_{ER}^{out} = \left[L + \frac{P_{IP3R}[IP_3]^3[Ca^{2+}]^3h^3}{([IP_3] + K_i)^3([Ca^{2+}] + K_a)^3}\right]([Ca^{2+}]_{ER} - [Ca^{2+}]), \tag{1.22}$$

$$J_{ER}^{in} = \frac{V_{SERCA}[Ca^{2+}]^2}{[Ca^{2+}]^2 + K_{SERCA}^2}, \tag{1.23}$$

$$[Ca^{2+}]_{ER} = \frac{C_t - [Ca^{2+}]}{\sigma}. \tag{1.24}$$

A simulation of system (1.20)-(1.24), together with its bifurcation diagram which shows

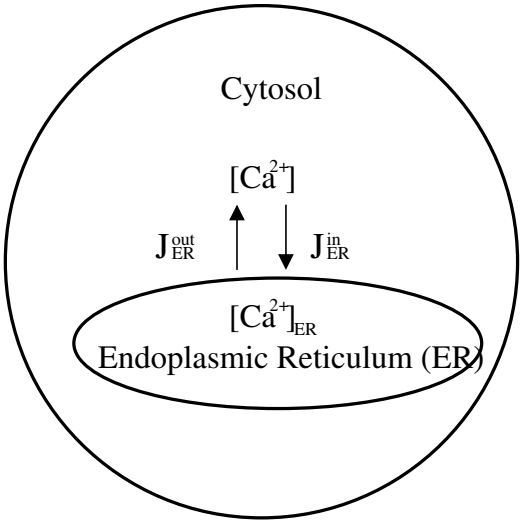

Figure 1.19: Schematic showing the mechanism that leads to calcium release from a cell's internal stores. J_{ER}^{out} accounts for the release of calcium into the cytosol from internal stores, while J_{ER}^{in} accounts for the refilling of internal stores from the cytosol.

which values for IP_3 give rise to calcium oscillations can be seen in Figure 1.20

Figure 1.20 reveals that Li and Rinzel's model of calcium release captures the temporal oscillatory behaviour of cytosolic calcium that has been observed in many different cell types [8, 87, 88].

1.7.2 Fink *et al*'s Model

Fink *et al* have used experimentally determined parameter values to help them form a model of calcium release [27]. Their model is identical to Li and Rinzel's model except for a change of parameters and a slight difference in the construction of equations (1.22) - (1.24). Fink *et al* argue that with these changes in parameter values, their model agrees well when compared to experiments conducted on A7r5 cells (a smooth muscle cell line). However, with these changes the calcium dynamics in Fink *et al*'s model are qualitatively different to that of Li and Rinzel's. The bifurcation points that lead to limit cycles which are present in Li and Rinzel's model are lost in Fink *et al*'s model for the parameter values in [27]. Fink *et al*'s model is given by the system of equations below

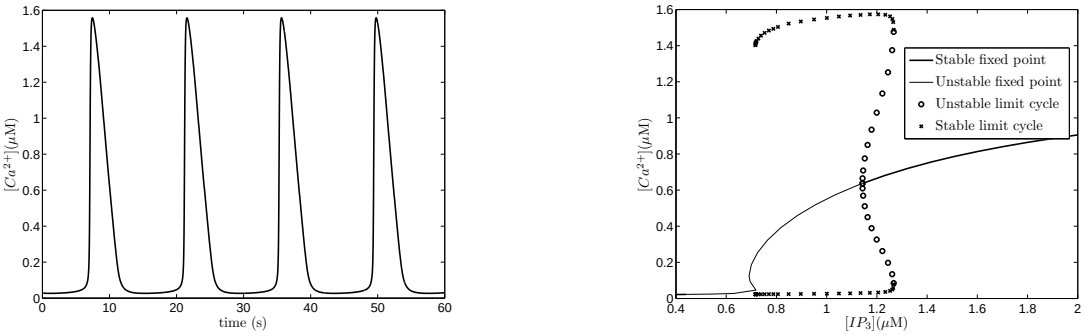

Figure 1.20: Diagram showing calcium oscillations resulting from the numerical integration of system (1.20)-(1.24) and bifurcation diagram showing which values for $[IP_3]$ give rise to calcium oscillations. Parameter values: $f_i = 0.01, V_i = 4\text{pL}, L = 0.37\text{pLs}^{-1}, P_{IP3R} = 26640\text{pLs}^{-1}, K_i = 1\mu\text{M}, K_a = 0.4\mu\text{M}, V_{SERCA} = 400\text{Mols}^{-1}, K_{SERCA} = 0.2\mu\text{M}, A = 0.5\text{s}^{-1}, K_d = 0.4\mu\text{M}, \sigma = 0.185, C_t = 2\mu\text{M}, [IP_3] = 1\mu\text{M}$ and as indicated in the second plot. Initial conditions for first plot were $[Ca^{2+}](0) = 0.028128\mu\text{M}$ and $h(0) = 0.638334$. The first plot was calculated using a fourth order Runge Kutta method, while the bifurcation diagram was calculated using AUTO within XPP.

$$\frac{d[Ca^{2+}]}{dt} = \beta(J_{ip3} - J_{pump} + J_{leak}), \tag{1.25}$$

$$J_{IP3} = J_{max}\left[\left(\frac{[IP_3]}{[IP_3]+K_I}\right)\left(\frac{[Ca^{2+}]}{[Ca^{2+}]+K_{act}}\right)h\right]^3\left[1-\frac{[Ca^{2+}]}{[Ca^{2+}]_{ER}}\right], \tag{1.26}$$

$$\frac{dh}{dt} = k_{on}[K_{inh} - ([Ca^{2+}]+K_{inh})h], \tag{1.27}$$

$$J_{pump} = V_{max}\frac{[Ca^{2+}]^2}{[Ca^{2+}]^2+K_P^2}, \tag{1.28}$$

$$J_{leak} = P_L\left(1-\frac{[Ca^{2+}]}{[Ca^{2+}]_{ER}}\right). \tag{1.29}$$

It can be seen by comparing equations (1.23) and (1.28), that J_{pump} in the Fink *et al* model is identical in form to J_{ER}^{in} in the Li and Rinzel model. Also, although it is not apparent initially it can be seen from equations (1.22), (1.26) and (1.29) that $J_{ER^{out}} = J_{IP3} + J_{leak}$, with a change of parameter values. This later observation becomes more apparent when one substitutes equation (1.24) into equation (1.22) to give the expression

below

$$J_{ER}^{out} = \left[L + \frac{P_{IP3R}[IP_3]^3[Ca^{2+}]^3h^3}{([IP_3]+K_i)^3([Ca^{2+}]+K_a)^3}\right]\left(\frac{C_t-[Ca^{2+}]}{\sigma} - [Ca^{2+}]\right). \tag{1.30}$$

which after factorisation becomes the equation below

$$J_{ER}^{out} = \left[\frac{LC_t}{\sigma} + \frac{P_{IP3R}C_t[IP_3]^3[Ca^{2+}]^3h^3}{\sigma([IP_3]+K_i)^3([Ca^{2+}]+K_a)^3}\right]\left(1 - [Ca^{2+}](\frac{1}{C_t}+\sigma)\right). \tag{1.31}$$

It can now be seen from equation (1.31), (1.26) and (1.29) that $J_{ER^{out}} = J_{IP3} + J_{leak}$, with a change of parameter values. The differences in the parameter values used in Fink *et al*'s and Li and Rinzel's model are given in Table 1.5.

Table 1.5: Table showing how the parameter values in Li and Rinzel's and Fink *et al*'s model differ. Values that differ shown in red.

Parameter in Li and Rinzel	Parameter in Fink *et al*	Value in Li and Rinzel	Value in Fink *et al*
$\frac{1}{\frac{1}{C_t}+\sigma}$	$[Ca^{2+}]_{ER}$	400	400
$\frac{LC_t}{\sigma}$	P_L	4	0.0804
$\frac{f_i}{v_i}$	β	0.0025	0.0804
$\frac{P_{IP3R}C_t}{\sigma}$	J_{max}	288000	2880
k_i	K_I	1.0	0.03
K_a	K_{act}	0.4	0.17
A	K_{on}	0.5	8
K_d	K_{inh}	0.4	0.1
V_{SERCA}	V_{max}	400	5.85
K_{SERCA}	K_p	0.2	0.24

Simulating system (1.25)-(1.29) leads to the results in Figure 1.21. Fink *et al* argue that these results agree favourably with those observed experimentally in A7r5 cells. This allows them to use the mathematical model to predict how calcium release is dependent upon the IP_3 dynamics of A7r5 cells, something which they argue is very difficult to achieve experimentally [27].

From Figure 1.21, it can be seen that despite having the same concentration for $[IP_3]$ as in the simulations for the Li and Rinzel model, calcium in Fink *et al*'s model does not oscillate, unlike in Li and Rinzel's model. If we are to model the excitable, oscillatory

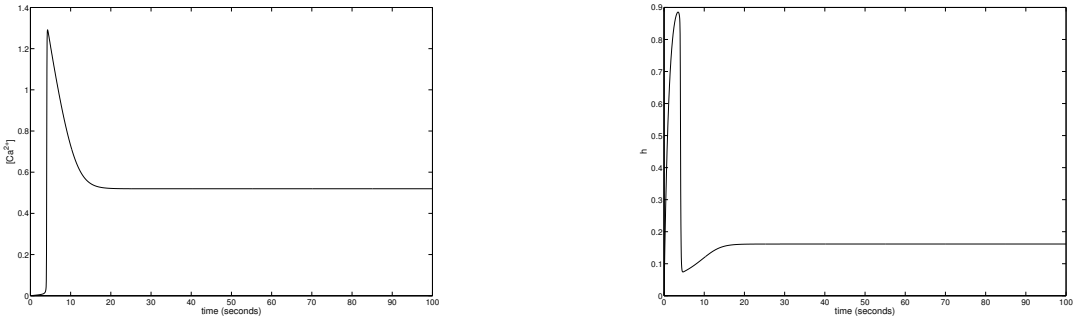

Figure 1.21: Simulations of system (1.25)-(1.29), illustrating how calcium is released from a cell's internal stores when the cell is exposed to a sustained amount of IP_3. The parameter values are $\beta = 0.0244, K_I = 0.03\mu M, K_{act} = 0.17\mu M, [Ca^{2+}]_{ER} = 400\mu M, k_{on} = 8.0\mu M^{-1}s^{-1}, K_{inh} = 0.1\mu M, V_{max} = 5.85\mu Ms^{-1}, K_P = 0.24\mu M, P_L = 0.67739936\mu Ms^{-1}, [IP_3] = 1.0\mu M$. The initial conditions were $[Ca^{2+}](0) = 0\mu M$ and $h(0) = 0\mu M$. A Fourth order Runge Kutta method was used to obtain the results.

behaviour of calcium as observed experimentally in cortical cells in our model therefore, it would make more sense to use Li and Rinzel's parameter values, rather than Fink *et al*'s.

1.8 Bennett *et al*'s Model of Calcium Waves in Networks of Astrocytes

With Obeyesekere *et al*'s cell cycle model and Li and Rinzel's model of calcium release, we are almost in a position to form a model coupling the calcium dynamics and cell cycle dynamics of radial glial cells. However, we still have not considered a model for the process by which ATP leads to calcium release from a cell's internal stores. Bennett *et al* have produced a model for a network of astrocytes (another type of brain cell, closely related to radial glia [35]) which communicate with each other via calcium waves, in order to investigate the nature of these propagating calcium waves [5]. Radial glial cells exhibit molecular and cellular characteristics of astrocytes [35]. Indeed the signal transduction pathway that leads to calcium release as a result of ATP binding described by Weissman *et al* [93] is identical to the signal transduction pathway that leads to calcium release as a result of ATP binding in astrocytes, as described by Bennett *et al*. This suggests that Bennett *et al*'s model could be a suitable candidate for use in our model. As we have already outlined in Section 1.4 the signal transduction pathway that leads to calcium release from ATP

binding, we do not discuss it again here. Instead, the reader who wishes to refresh their memory is directed to Figure 1.22.

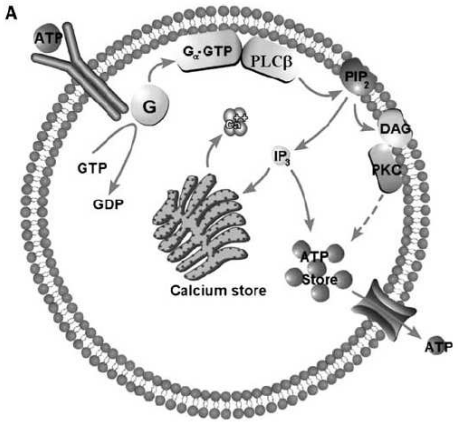

Figure 1.22: Schematic diagram of the steps from ATP receptor activation to Calcium release from the internal store. ATP binds to the cell's receptor which sets off a G-protein cascade ultimately leading to the production of IP_3. IP_3 then leads to the release of Ca^{2+} by allowing the opening ion channels within the cell's endoplasmic reticulum. Figure reproduced from [5] with permission from Elsevier.

In Bennett *et al*'s model, the proportion of G-protein activated by ATP, assuming fast binding kinetics is given by G^*. It is assumed that G-protein activation is dependent upon the fraction of bound receptors (ρ) and also the ratio of activities of unbound receptors (δ). δ allows for G-protein activation in the absence of bound ATP receptors. The concentration of IP_3 (which is assumed to be created on the inner walls of the cell, before diffusing towards the centre of the cell) is represented by $[IP_3]$ in the model. It is synthesised at rate r_h^* by active G-protein and degraded at rate K_{deg}. Bennett *et al* assume that the release of extracellular ATP ($[ATP]$) is dependent upon IP_3, although the precise mechanism of ATP release is not known [5]. They argue that replacing the dependence of ATP release upon IP_3 with the proportion of active G-protein (G^*), or the concentration of intra-cellular ATP (χ) gives essentially the same qualitative results [5]. The intracellular ATP store (χ) in the model is depleted at rate K_{loss} and its inclusion in the model ensures that once ATP stores are emptied, ATP release will cease. Initially $\chi = 1$ in simulations, representing a fully stocked ATP store. In the model, ATP is only released if IP_3 concentration is higher than a minimum concentration ($[IP_3] > [IP_3]_{min}$). This ensures small amounts of ATP are not

amplified and do not lead to a propagating wave.

Bennett *et al* use Fink *et al*'s model (system (1.25)-(1.29)) and parameter values for calcium release within astrocytes. As in Fink *et al*'s model, in Bennett *et al*'s model $[Ca^{2+}]$ gives the concentration of free cytosolic calcium. It is dependent upon the flux of calcium from the ER to the cytosol (J_{leak} and J_{IP3}) and the flux of calcium from the cytosol into the ER (J_{pump}). Bennett *et al*'s model for a lane of astrocytes is represented by the following equations

$$G^* = \frac{\rho + \delta}{K_G + \rho + \delta}, \tag{1.32}$$

$$\rho = \frac{[ATP]}{K_R + [ATP]}, \tag{1.33}$$

$$\frac{\partial [IP_3]}{\partial t} = D_{IP}\nabla^2[IP_3] + r_h^* G^* - K_{deg}[IP_3], \tag{1.34}$$

$$\frac{\partial [ATP]}{\partial t} = D_{ATP}\nabla^2[ATP] + H([IP_3] - [IP_3]_{min})V_{ATP}\chi\frac{[IP_3] - [IP_3]_{min}}{K_{rel} + [IP_3]} - V_{deg}\frac{[ATP]}{K_{deg} + [ATP]}, \tag{1.35}$$

$$\frac{d\chi}{dt} = -H([IP_3] - [IP_3]_{min})K_{loss}\chi(t)\frac{[IP_3] - [IP_3]_{min}}{K_{rel} + [IP_3]}, \tag{1.36}$$

$$\frac{d[Ca^{2+}]}{dt} = \beta(J_{IP3} - J_{pump} + J_{leak}), \tag{1.37}$$

$$J_{IP3} = J_{max}\left[\left(\frac{[IP_3]}{[IP_3] + K_I}\right)\left(\frac{[Ca^{2+}]}{[Ca^{2+}] + K_{act}}\right)h\right]^3\left[1 - \frac{[Ca^{2+}]}{[Ca^{2+}]_{ER}}\right], \tag{1.38}$$

$$\frac{dh}{dt} = k_{on}[K_{inh} - ([Ca^{2+}] + K_{inh})h], \tag{1.39}$$

$$J_{pump} = V_{max}\frac{[Ca^{2+}]^2}{[Ca^{2+}]^2 + K_P^2}, \tag{1.40}$$

$$J_{leak} = P_L\left(1 - \frac{[Ca^{2+}]}{[Ca^{2+}]_{ER}}\right), \tag{1.41}$$

$$H(x) = \begin{cases} 0 & \text{if } x \leq 0, \\ 1 & \text{else.} \end{cases} \tag{1.42}$$

It is illuminating at this point to focus upon how calcium release resulting from ATP binding is described mathematically. The ratio of bound receptors to total ATP receptors is given by ρ whose dynamics are governed by equation (1.33). Bound receptors then lead to G-protein activation as can be seen from equation (1.32) which governs the proportion of active G-protein (G^*). This in turn leads to production of IP_3 at rate r_h^*, as can be seen

from the $r_h^* G_*$ term in equation (1.34) governing the IP_3 dynamics. IP_3 then allows for the release of ATP at rate V_{ATP} ($H([IP_3] - [IP_3]_{min}) V_{ATP} \chi \frac{[IP_3]-[IP_3]_{min}}{K_{rel}+[IP_3]}$ from equation (1.35)) and the release of calcium from internal stores ($\frac{[IP_3]}{[IP_3]+K_I}$ in equation (1.38)).

Although Bennett *et al* regard cells as 3D cubes and therefore consider IP_3 diffusion within a cell, we shall assume spatial homogeneous distributions within each cell, and ignore the $D_{IP}\nabla^2[IP_3]$ term from equation (1.34), reducing the PDE to an ODE. This makes coding up Bennett *et al*'s model a simpler task and also means that numerically solving the system will be computationally less expensive. We sumarise the variables and parameters used in Bennett *et al*'s model in Tables 1.6 and 1.7. Simulations, ignoring IP_3 diffusion, for one cell subjected to an initiating ATP pulse of 10 μM can be seen in Figure 1.23. These results show that exposure of a single astrocyte to an ATP pulse leads to a fast increase in IP_3. This increase is accompanied with an increase of calcium, albeit with a time lag.

Table 1.6: Description of variables used in Bennett *et al*'s model

Variable	Unit	
G^*	dimensionless	Proportion of activated G-protein
ρ	dimensionless	Ratio of bound to unbound P2Y receptors
$[IP_3]$	μM	Concentration of IP_3
$[ATP]$	μM	Concentration of extra-cellular ATP
χ	dimensionless	Intra-cellular ATP concentration normalised to 1
$[Ca^{2+}]$	μM	Concentration of calcium released from internal stores
J_{IP3}	μMs^{-1}	Flux of calcium from the ER to the cytosol
h	dimensionless	Gating variable
J_{pump}	μMs^{-1}	Flux of calcium from the cytosol to the ER
J_{leak}	μMs^{-1}	Term accounting for calcium leaked into the cytosol from the ER

1.8.1 Intercellular Communication between Several Astrocytes

Bennett *et al* go on to consider calcium release in a lane of astrocytes. It is important to note Bennett *et al* consider each cell to be a cube of side 25 μm [5]. For simplicity, it is easier to regard these cells as points and this is the approach we intend to pursue with regard to our overall project. Hence in simulating Bennett *et al*'s model over a spatial domain,

Table 1.7: Description of parameters used in Bennett *et al*'s model

Parameter	Unit	
δ	dimensionless	Ratio of activities of the unbound and bound receptors
K_G	dimensionless	Term equal to the G-protein deactivation rate
		divided by the G-protein activation rate
K_R	μM	Effective dissassociation constant for P2Y receptor ATP binding
r_h^*	μMs^{-1}	IP_3 production rate
K_{deg}	s^{-1}	IP_3 degradation rate
D_{ATP}	$\mu\text{m}^2\text{s}^{-1}$	ATP diffusion coefficient
$[IP_3]_{min}$	μM	Minimum IP_3 concentration which must be reached
		to allow for ATP release
V_{ATP}	$\mu\text{M}\mu\text{m}^{-2}\text{s}^{-1}$	ATP production rate
K_{rel}	μM	Michaelis constant
V_{deg}	μMs^{-1}	Maximal ATP degradation rate
K_{deg}	μM	Michaelis constant
K_{loss}	s^{-1}	Depletion rate parameter
β	dimensionless	Calcium buffering parameter
J_{max}	μMs^{-1}	Maximum channel current
K_I	μM	Michaelis constant
K_{act}	μM	Michaelis constant
$[Ca^{2+}]_{ER}$	μM	Calcium concentration in ER
k_{on}	μMs^{-1}	IP_3 channel kinetic parameter
K_{inh}	μM	IP_3 channel kinetic parameter
V_{max}	μMs^{-1}	Maximum pumping rate of calcium into the ER
K_P	μM	Pump dissociation constant
P_L	μMs^{-1}	Calcium leak rate from ER

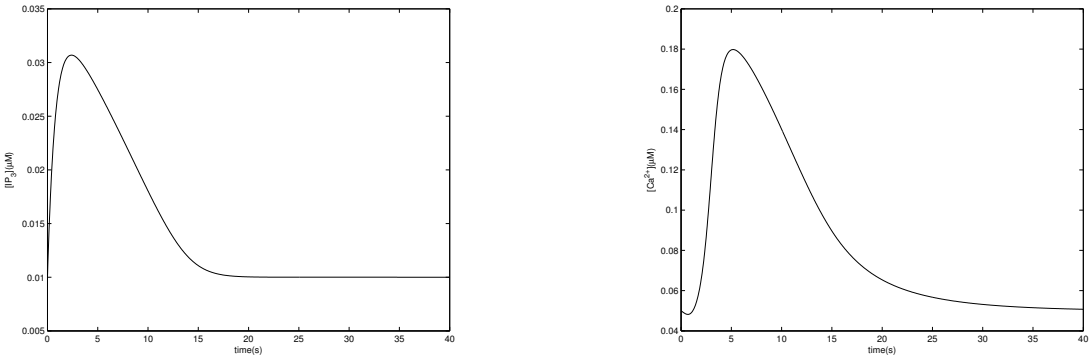

Figure 1.23: Simulation of system (1.32)-(1.42), for a single cell. Parameter values given by $K_{deg} = 1.25s^{-1}, K_a = 0.017\text{s}^{-1}, K_d = 0.15\text{s}^{-1}, r_h^* = 1\mu\text{mols}^{-1}, V_{ATP} = 300\text{s}^{-1}, K_{rel} = 10\mu\text{M}, [IP_3]_{min} = 0.012\mu\text{M}, k_{loss} = 30\text{s}^{-1}, D_{ATP} = 300\mu\text{m}^2\text{s}^{-1}, J_{max} = 2880\mu\text{M}s^{-1}, K_I = 0.03\mu\text{M}, K_{act} = 0.17\mu\text{M}, k_{on} = 8\mu\text{Ms}^{-1}, K_{inh} = 0.1\mu\text{M}, [Ca_{ER}^{2+}] = 400\mu\text{M}, V_{max} = 5.85\mu\text{Ms}^{-1}, K_p = 0.24\mu\text{M}, \beta = 0.0244, K_R = 25, V_{deg} = 0.35\text{s}^{-1}, \delta = 0.0013992$ and $P_L = 0.08665\mu\text{M}s^{-1}$ Initial conditions were $[ATP](0) = 10\mu\text{M}, \chi(0) = 1\mu\text{M}, [IP_3](0) = 0.01\mu\text{M}, [Ca^{2+}](0) = 0.05\mu\text{M}, h(0) = 0$ and $[IP_3](0) = 0.01\mu\text{M}$. Results obtained by using a fourth order Runge Kutta method of integration.

cells are regarded as point sources. This presents some problems with regard to obtaining the qualitative and quantitative results Bennett *et al* reach when simulating the system for several cells. The cell walls are impermeable to ATP, hence when considering diffusion of ATP, ATP will diffuse around cells but will not diffuse into the intracellular space. If we consider cells as points, there is nothing preventing ATP from diffusing throughout the entirety of the spatial domain. These two processes are illustrated in Figure 1.24. When regarding cells as 'point sources' therefore, we will effectively be dealing with a different intercellular space. There will also be differences with regard to ATP uptake and IP_3 production in the cells. Consequently, it is necessary to 'adjust' various parameters such as the ATP release and degradation rates (V_{ATP} and V_{deg} respectively) and the IP_3 production rate (r_*^h), in order that the results of our simulations are qualitatively and quantitatively similar to Bennett *et al*'s results. Simulating system (1.32)-(1.42), disregarding intra-cellular IP_3 diffusion for 19 astrocytes in one spatial dimension leads to the results illustrated in Figures 1.25 and 1.26.

From Figures 1.25 and 1.26 we can see that an initiating pulse of ATP, introduced at the centre of a lane of astrocytes leads to a wave of ATP which propagates throughout the spatial domain. This wave is shortly followed by a propagating calcium wave. These results agree very well with Bennett *et al*'s results for a similar parameter regime [5].

1.9 Conclusions

In this chapter we have introduced the biology of our project, focussing on Weissman *et al*'s paper [93]. In this paper Weissman *et al* show that a calcium signalling mechanism is likely to be responsible for an increase in the proliferation of radial glia during embryonic development and hypothesise that the same mechanism may lead to the synchronisation of cell cycles of clusters of radial glia. Additionally, through reviewing the biological literatue we have identified the salient biological features that will need to be considered in formulating a mathematical model for the coupling between the cell cycle dynamics and calcium dynamics of radial glial cells. For example, we identified that calcium has the downstream effect of promoting Cyclin D activity and therefore ideally we would incorporate a cell cycle model into our model which includes a term for Cyclin D. Furthermore, in this chapter we have reviewed a number of mathematical models for the cell cycle, two models for IP_3 induced calcium release and Bennett *et al*'s model of calcium waves in networks of astrocytes,

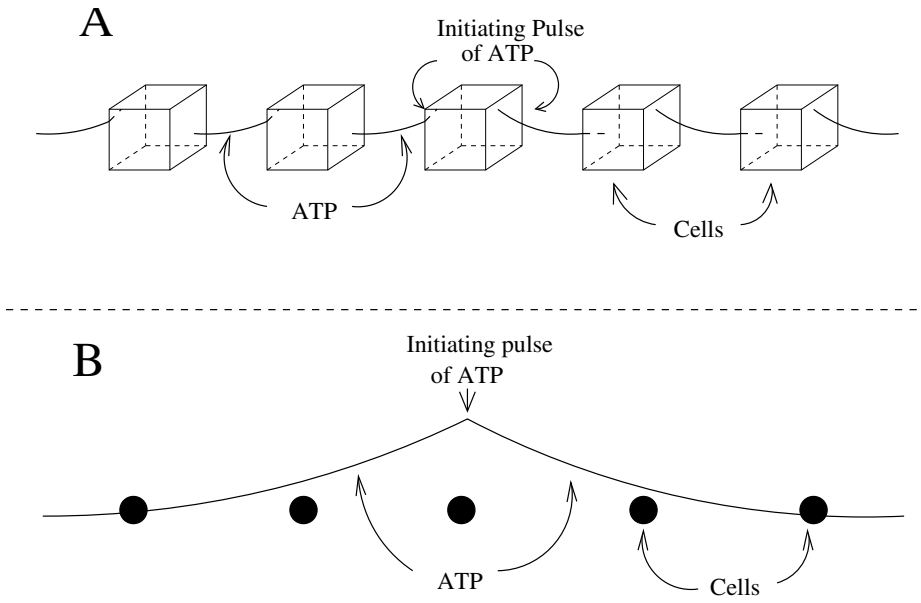

Figure 1.24: Diagram illustrating the differences between treating astrocyte cells as cubes and regarding them as points when considering ATP diffusion. In A, cells take the form of cubes and it can be seen that ATP diffusing from the initiating pulse does not penetrate cell walls. ATP binds to cell surface receptors, leading via a G-protein cascade to the production of IP_3 on the inside of the cell walls, in turn leading to the autocrine release of more ATP at the cell walls. IP_3 also diffuses into the middle of the cell, leading to the release of calcium from internal stores. If we look at B, where cells are modelled as point sources, the effective intercellular space is different. ATP is free to diffuse throughout the whole spatial domain. In this case ATP binding, IP_3 production and ATP autocrine release all occur at the centre of the cell.

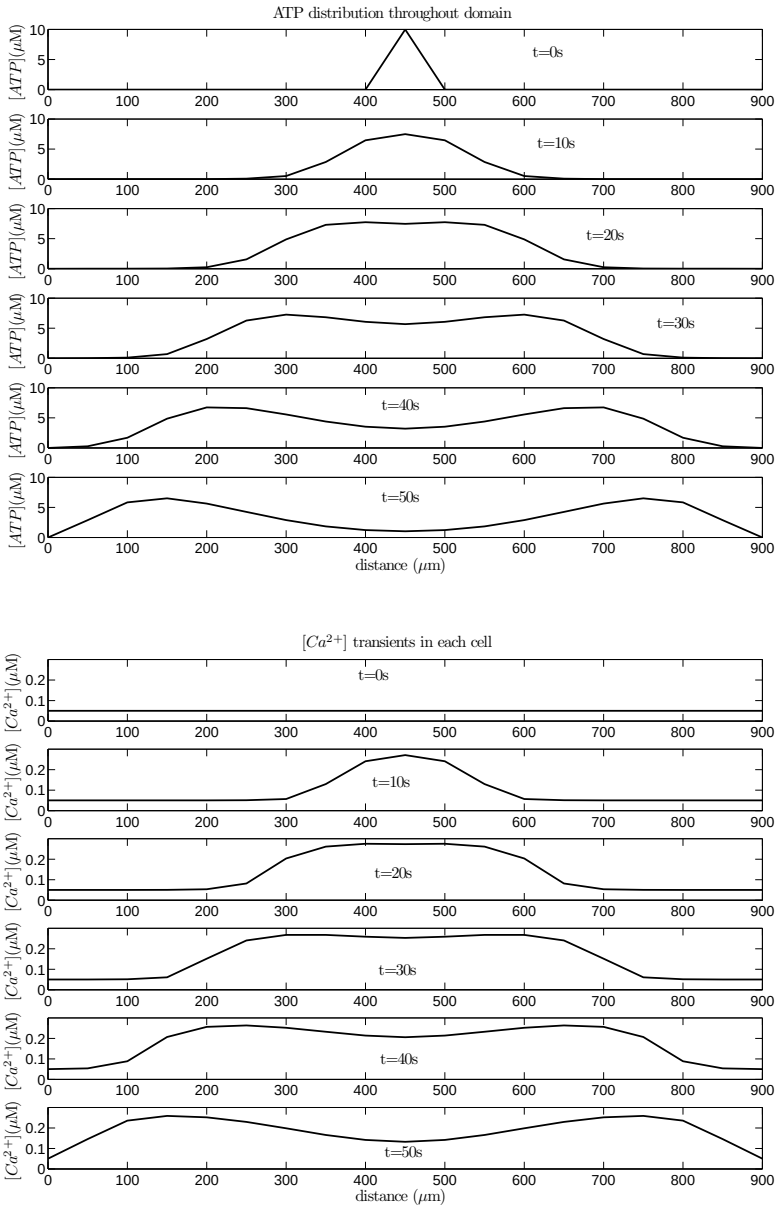

Figure 1.25: Simulations of system (1.32)-(1.42), disregarding intra-cellular IP_3 diffusion. Results show the evolution of the propagating ATP and Calcium waves throughout the spatial domain when an initiating pulse of $10\mu M$ of ATP is introduced around the cell in the middle of the lattice at t=0. Parameter values and initial conditions as for Figure 1.23 except for $[ATP](0) = 0$ for all cells except for the cell in the middle of the spatial lattice. Equation (1.35) was solved numerically using the method of lines, with a mesh interval of $50\mu m$. Results obtained using a fourth order Runge Kutta method of integration and Dirichlet boundary conditions of $ATP = 0$ at all boundaries.

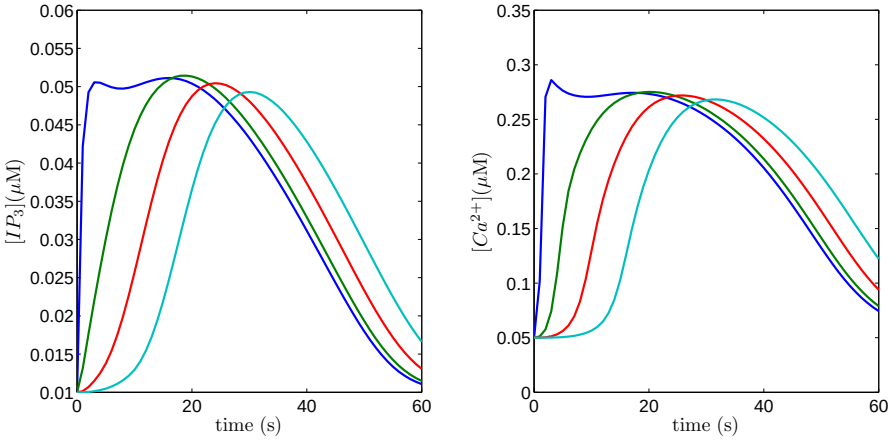

Figure 1.26: Simulations of system (1.32)-(1.42), disregarding intra-cellular IP_3 diffusion. Results show the evolution of IP_3 production and calcium release within cells 10-13 (with cell 1 being the left most cell in the lattice) when an initiating pulse of 10μM of ATP is introduced around the cell in the middle of the lattice at t=0. Parameter values and initial conditions as for Figure 1.23 except for $[ATP](0) = 0$ for all cells except for the cell in the middle of the spatial lattice. Equation (1.35) was solved numerically using the method of lines, with a mesh interval of 50μm. Results obtained using a fourth order Runge Kutta method of integration and Dirichlet boundary conditions of $ATP = 0$ at all boundaries.

accessing the suitability of each for our purposes.

In summary we identified Obeyesekere *et al*'s cell cycle model as being the most suitable cell cycle model to incorporate into our model for a number of reasons. It has a term for Cyclin D and an increase in Cyclin D activity in Obeyesekere *et al*'s model results in a modest reduction in the period of the cell cycle, in keeping with the results for many cell types in the biological literature. Furthermore, it is a relatively low dimensional model which means that simulations of many cell systems are unlikely to prove as computationally expensive as if we used a higher dimensional model. Its relatively low dimension coupled with the fact that it is a temporally continuous model means that it should not be too difficult to analyse using numerical continuation. Bennett *et al*'s model for ATP mediated calcium release in lanes of astrocytes is likely to be suitable to use to model ATP mediated calcium release in radial glial cells, as radial glia and astrocytes are molecularly very similar. With all this in mind therefore, we decided to use Obeyesekere *et al*'s cell cycle model and Bennett *et al*'s model for ATP mediated calcium release to form the basis for our model for the coupling between the calcium and cell cycle dynamics in radial glial cells.

1.10 Thesis Structure

In chapter 2, we discuss the formulation of two models which couple the cell cycle dynamics to the calcium dynamics in radial glial cells. In the first model, ATP release is modelled as occurring during mid G_1 phase and in the second it occurs at the G_1/S transition. We then, via bifurcation analysis study the dynamics of both models for a single cell. With this achieved, we study the dynamics of both models for two cell systems by applying the theory of weakly coupled oscillators, bifurcation analysis and direct numerical simulation. In particular, we investigate the conditions which lead to synchronous phase locked solutions and other phase locked solutions for both models.

In chapter 3, we build upon our results from chapter 2 and investigate phase locked behaviour in systems of several cells. We achieve this through the application of the theory of weakly coupled oscillators, but mainly via direct numerical simulation. The results from this chapter form the first major result of the thesis and suggest that ATP released at the G_1/S phase transition is more likely to lead to synchronous behaviour than ATP released

during mid G_1 phase.

We, in chapter 4, via bifurcation analysis and direct numerical simulation, investigate the ability of cycling cells to recruit quiescent cells onto the cell cycle. Our analysis reveals that phase locked solutions can not be guaranteed in the short term, suggesting the transient behaviour may have more of an impact during neurogenesis. Both models suggest that cycling radial glia can successfully recruit quiescent cells within the period of neurogenesis. However, our results indicate that the model where ATP is released during the G_1/S phase transition is more successful at entraining quiescent cells onto the cell cycle in a synchronous manner.

In chapter 5, we introduce models for coupled cell cycle and calcium dynamics with an additive noise term. Using a numerical ensemble prediction system, we show that noise acts to advance the onset of oscillatory solutions in one and two cell systems. This result suggests that noise may play an important regulatory role during neurogenesis.

Chapter 2

Coupled Calcium and Cell Cycle Dynamics in One and Two Cells

2.1 Introduction

In this chapter we introduce two models for the coupling between the calcium dynamics and cell cycle dynamics in radial glial cells. As it is not clear from the literature as to exactly when hemichannels form (they form some time during G_1 phase and the beginning S phase [10, 34, 93]), allowing for the release of ATP, we consider two models. In our first model, we consider ATP release as occurring during mid G_1 phase. In the second, we consider ATP release during the G_1/S phase transition. Through bifurcation analysis and direct simulation of a system modelling a single cell, we show that both models capture the salient biological features of radial glial cells. These features include the release of ATP from hemichannels, as well as the effect calcium has on the cell cycle of radial glial cells. Through applying bifurcation theory, weakly coupled non-linear oscillator theory and via direct simulation we then investigate the behaviour of two coupled cells. In particular we consider for each model, how the existence and stability of phase locked solutions depends upon different parameter regimes.

2.2 Coupling the Cell Cycle and Calcium Dynamics

We couple Obeyesekere et *al*'s model of the mammalian cell cycle [65] (system (1.5)-(1.9) in chapter 1) to Li and Rinzel's model of calcium release [90] (system (1.20)-(1.24) in chapter 1) and Bennett *et al*'s model of ATP mediated calcium release in astrocytes [90] (system (1.32)-(1.41) in chapter 1) to form two phenomenological models of the coupling of the

calcium dynamics to the cell cycle dynamics of radial glial cells. Obeyesekere *et al*'s model for the cell cycle of cells indexed by i is given by

$$\frac{dD_i}{dt} = a_d\left(\frac{kGF}{1+kGF}\right) - d_D E_i D_i, \tag{2.1}$$

$$\frac{dE_i}{dt} = a_E(1 + a_f(\ominus - R_{si})) - d_E X_i E_i, \tag{2.2}$$

$$\frac{dR_i}{dt} = \frac{p_X(R_T - R_{si} - R_i)X_i}{q_X + (R_T - R_{si} - R_i) + X_i} - p_s(\ominus - R_{si})R_i, \tag{2.3}$$

$$\frac{dR_{si}}{dt} = p_s(\ominus - R_{si})R - \frac{p_D R_{si} D_i}{q_D + R_{si} + d} - \frac{p_E R_{si} E_i}{q_E + R_{si} + E_i}, \tag{2.4}$$

$$\frac{dX_i}{dt} = a_X E_i + f(\ominus - R_{si}) + gX_i^2 E_i - d_X X_i. \tag{2.5}$$

As mentioned in the introduction, calcium has the downstream effect of increasing Cyclin D activity. We model this by coupling calcium to the Cyclin D synthesis rate term a_{di} from equation (2.1) to give

$$a_{di} = a_d' + \gamma([Ca^{2+}]_i - [Ca^{2+}]_b). \tag{2.6}$$

Equation (2.6) ensures that a_{di}, the Cyclin D synthesis rate in cell i, is an increasing function of calcium in that cell. γ is the strength of the coupling and $[Ca^{2+}]_b$ is a basal concentration of calcium in the cell, which ensures that only calcium transients above the basal concentration will affect Cyclin D production in our model (we set $[Ca^{2+}]_b$, so that it is never larger than $[Ca^{2+}]_i$).

We model IP_3 dependent calcium release from internal stores using Li and Rinzel's model which was discussed in Section 1.7.1 of the previous chapter. Their model is given by

$$\frac{d[Ca^{2+}]_i}{dt} = t_s(\beta(J_{IP3i} - J_{pumpi} + J_{leaki})), \tag{2.7}$$

$$\frac{dh_i}{dt} = t_s(k_{on}[K_{inh} - ([Ca^{2+}]_i + K_{inh})h_i]), \tag{2.8}$$

$$J_{IP3i} = J_{max}\left[\left(\frac{[IP_3]_i}{[IP_3]_i + K_I}\right)\left(\frac{[Ca^{2+}]_i}{[Ca^{2+}]_i + K_{act}}\right)h\right]^3\left[1 - \frac{[Ca^{2+}]_i}{[Ca^{2+}]_{ER}}\right], \tag{2.9}$$

$$J_{pump} = V_{max}\frac{[Ca^{2+}]_i^2}{[Ca^{2+}]_i^2 + K_P^2}, \tag{2.10}$$

$$J_{leak} = P_L\left(1 - \frac{[Ca^{2+}]_i}{[Ca^{2+}]_{ER}}\right). \tag{2.11}$$

As radial glial cells exhibit molecular and cellular characteristics of astrocytes [35], we model ATP mediated calcium release by adapting Bennett *et al*'s model of ATP mediated calcium waves in astrocytes. Indeed the signal transduction pathway described by Weissman *et al* [93] is identical to the pathway in astrocytes, as modelled by Bennett *et al*. Our adapted version of Bennett *et al*'s model with our changes coloured blue is given by

$$\rho_i = \frac{[ATP_{Ei}]}{K_R + [ATP_{Ei}]}, \tag{2.12}$$

$$\delta = \frac{K_G[IP_3]_{min}K_{deg}}{r_h^* - [IP_3]_{min}K_{deg}}, \tag{2.13}$$

$$G_i^* = \frac{\rho_i + \delta}{K_G + \rho_i + \delta}, \tag{2.14}$$

$$\frac{d[IP_3]_i}{dt} = t_s(r_h^* G_i^* - k_{deg}[IP_3]_i), \tag{2.15}$$

$$\begin{aligned}\frac{d[ATP_I]_i}{dt} = t_s\Bigg(&\alpha([ATP_I]_{max} - [ATP_I]_i) \\ &- T(H_i, H_c, \varrho)T([IP_3]_i, [IP_3]_c, \varrho)V_{ATP}([ATP_I]_i - [ATP_E]_i)\left(\frac{[IP_3]_i - [IP_3]_{min}}{K_{rel} + [IP_3]_i}\right)\Bigg),\end{aligned} \tag{2.16}$$

$$\begin{aligned}\frac{d[ATP_E]_i}{dt} = t_s\Bigg(&D_{ATP}\frac{[ATP_E]_{i-1} - 2[ATP_E]_i + [ATP_E]_{i+1}}{\Delta x^2} \\ &+ T(H_i, H_c, \varrho)T([IP_3]_i, [IP_3]_c, \varrho)V_{ATP}([ATP_I]_i - [ATP_E]_i)\frac{[IP_3]_i - [IP_3]_{min}}{K_{rel} + [IP_3]_i} \\ &- V_{deg}\frac{[ATP_E]_i}{K_{deg} + [ATP_E]_i}\Bigg),\end{aligned} \tag{2.17}$$

$$T(H_i, H_c, \varrho) = \frac{1}{2}\left(\tanh\left(\frac{H_i - H_c}{\varrho}\right) + 1\right). \tag{2.18}$$

The first point to note is that we use $[ATP_I]_i$ rather than χ to describe the internal ATP dynamics. We then add the $\alpha([ATP_I]_{max} - [ATP_I]_i)$ term to equation (2.16) which governs the internal ATP dynamics of the cell. This term accounts for internal ATP production at rate α. In adding this term we are able to account for the production of ATP, something that Bennett *et al* who investigated single event ATP mediated calcium waves were not concerned with. An ATP refilling term is essential to study the long term dynamics of the system and without it ATP release would be very short lived indeed. We have added the $T(H_i, H_c, \varrho)$ term to equations (2.16) and (2.17) with $T(H_i, H_c, \varrho)$ defined as in equation (2.18). This term models the switch like release of ATP from open hemichannels. The H argument in this term is the concentration of one of the cell cycle variables from (2.1)-(2.5). As different proteins peak at different times during the cell cycle, we can use the point at which they do this to signal different stages in cell cycle progression. Hence, in replacing H with one of the five cell cycle variables from (2.1)-(2.5), we will be able to model ATP release at different times during the cell cycle. We can form different models by replacing

H with different cell cycle variables. H_c represents the critical concentration that H must exceed in order for ATP to be released. ϱ controls the stiffness of the switch.

In addition to including the term which accounts for ATP release via hemichannels in equation (2.16), we add a $([ATP_I]_i - [ATP_E]_i)$ term to this equation as well. This term ensures that ATP is only secreted into the extracellular space if $[ATP_I] > [ATP_E]$; otherwise there would be a countergradient and the secretion would require active pumping of ATP. This in turn ensures that the concentration of extracellular ATP never exceeds the maximum value $[ATP_I]_{max}$. Bennett *et al* use ATP sinks at all boundaries in their model to ensure that ATP is degraded and that the extracellular space does not fill up with a physically unrealistic concentration of ATP. The K_{loss} component from Bennett's model has been replaced with V_{ATP} in equation (2.16). This ensures that internal ATP stores deplete at the same rate ATP is released into extracellular space. The disparity between the different timescales of the cell cycle dynamics and ATP mediated calcium dynamics are addressed via the t_s term in equations (2.7)-(2.8) and (2.15)-(2.17). The t_s term ensures that one unit of non-dimensional time in equations (2.1)-(2.5) governing the cell cycle is equivalent to one hour of dimensional time in the rest of the system. Henceforth, in order to avoid confusion we use dimensional time units. All variables in our model take whatever dimension they had in Obeyesekere *et al*'s, Bennett *et al*'s and Li *et al*'s models. Hence, in our model, we have a mix of dimensional and dimensionless variables.

It is possible to reduce our adapted version of Bennett *et al*'s model given by equations (2.12)-(2.17) to its original form. In order to achieve this, one would have to set α to 0, which ensures internal ATP stores are not refilled. In addition to this, $T(H_i, H_c, \varrho)$ will have to be set to 1 and $[ATP_E]_i << [ATP_I]_i$, removing the dependence of ATP release upon the extracellular ATP concentration.

With our model formed, it is illuminating to briefly review how ATP release, leading to increased Cyclin D activity is mathematically described in our model. The reader is directed as an aid to Figure 1.6 in the previous chapter where this process is illustrated schematically. The $T(H_i, H_c, \varrho)$ term in equation (2.17) models the release of ATP through the opening of hemichannels. The point during the cell cycle at which this occurs is determined by the cell cycle variables, whose dynamics are governed by equations (2.1)-(2.5).

Extracellular ATP leads to an increase in the number of bound receptors (equation (2.12)), which in turn leads to an increase in G-Protein activity (equation (2.14)). This results in the release of calcium from internal stores (equation (2.22)), mediated via $[IP_3]$ production (equation (2.15)). Calcium liberated from the cell's internal store then increases Cyclin D activity (equation (2.6)).

As a further aid to understanding how, in particular we couple Obeyesekere *et al*'s, Bennett *et al*'s and Li *et al*'s models to form our model, the reader is directed to Figure 2.1.

We use a finite difference method to discretise the system, approximating the Laplacian (present in Bennett *et al*'s model) on a string of cells as $\nabla^2[ATP_E] = \frac{[ATP_E]_{i-1}-2[ATP_E]_i+[ATP_E]_{i+1}}{\Delta x^2}$ in equation (2.17), where Δx is the distance between the cells in the lattice. It is this discretisation of the spatial component of ATP that provides the coupling between our cells. In subsequent calculations, we use zero flux boundary conditions at all boundaries.

2.2.1 Choice of Parameter Values

We have kept the parameter values for Obeyesekere *et al*'s cell cycle model given by equations (2.1)-(2.5) expect for the Cyclin D synthesis rate a_d which we now define via equation (2.6). We use Li and Rinzel's parameter values given in [90] for the calcium dynamics. The parameters used in equations (2.12)-(2.18) are the same as those used by Bennett [5], with a few notable exceptions outlined below.

With regard to the rate constants governing the ATP dynamics, it is useful to briefly outline the process by which ATP is degraded. ATP is degraded into Adenosine diphosphate (ADP) by ecto-nucleotidases present on the extra-cellular surface of cells [43, 73]. It is also broken down naturally in solution when ecto-nucleotides are not present but at a far slower rate [80]. In the literature ATP degradation by ecto-nucleotidases is typically modelled using Michaelis Menten kinetics [68]

$$\frac{d[ATP_E]}{dt} = \frac{-V_{deg}[ATP_E]}{K_{deg} + [ATP_E]}. \tag{2.19}$$

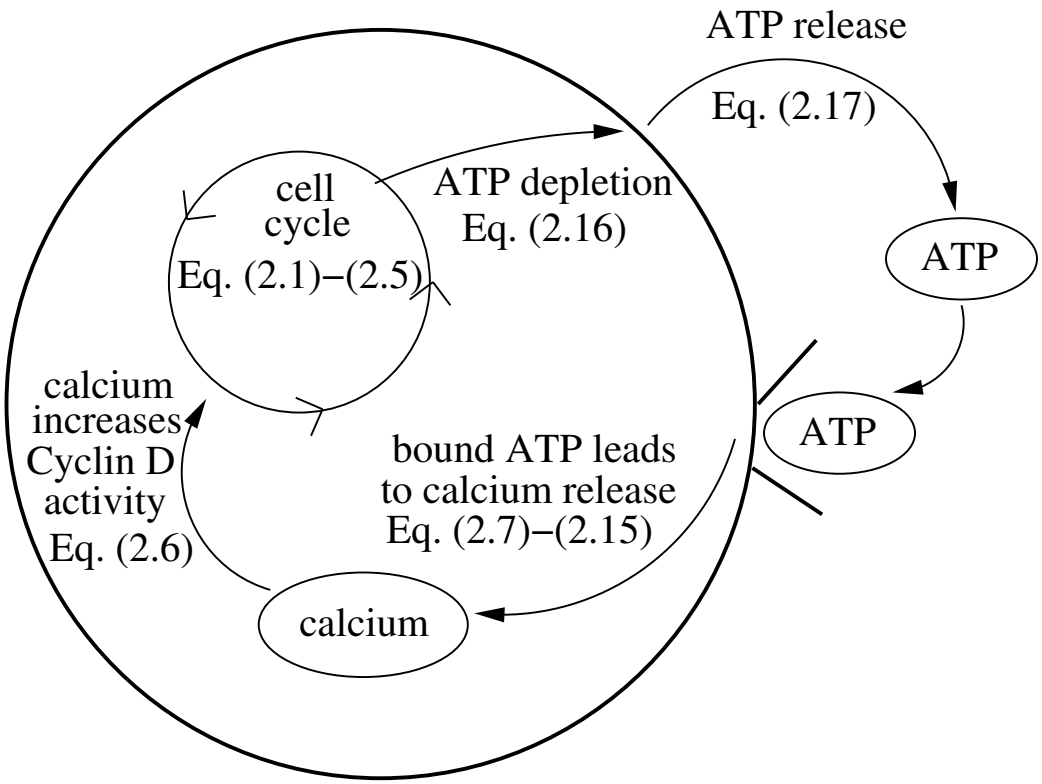

Figure 2.1: Schematic showing how we couple Obeyesekere *et al*'s, Bennett *et al*'s and Li *et al*'s models to form our model. The cell cycle variables are modelled using Obeyesekere *et al*'s model (equations (2.1)-(2.5)). At a certain point in the cell cycle, hemichannels form and ATP is released into the extracellular space (modelled by the $T(H_i, H_c, \varrho)$ term in equation (2.17)). ATP binds to extracellular receptors, leading via a G-protein cascade (modelled using Bennett *et al*'s model, given by equations (2.12)-(2.15)) to the release of calcium from internal stores (modelled using Li *et al*'s model, given by equations (2.7)-(2.11)). Free calcium affects the cell cycle by increasing Cyclin D activity (modelled by equation (2.6)).

However a consensus has not been reached with regard to the rate constants [5, 82].

Gordon *et al* investigated the degradation of extracellular ATP by ecto-nucleotidases in arterial smooth muscle cells and calculated values for K_{deg} and V_{deg}, using the least squares method to fit a curve for ATP degradation to experimentally observed data points [33]. They arrived at values of 221 μM for K_{deg} and 2.5 μMs^{-1} for V_{deg}. It is important to note however that ATP degradation depends heavily upon cell type as well as extracellular concentration. As different cell types express different ecto-nucleotidases in different proportions, their ability to degrade extra-cellular ATP will differ also. Further results arrived at by Gordon *et al*, where the time course of the degradation of ATP in a culture of smooth muscle cells is compared to the time course in a culture of endothelial cells illustrates this [32, 33]. The profile of ATP degradation as well as the time before all ATP is degraded in each case differs, leading to different predicted values for K_{deg} and V_{deg}. As cellular concentration is increased so will the concentration of ecto-nucleotidases and hence extracellular ATP will be degraded more quickly. Koike *et al* showed that the proportion of ATP degraded in three minutes by ecto-nucleotidases in a cluster of hepatocytes (a type of liver cell) bore a non-linear relationship to the cellular concentration of hepatocytes [47]. Gordon *et al*'s values for K_{deg} and V_{deg} can therefore only act as a guide when applied to ATP degradation facilitated by radial glial cells.

Joseph *et al* [43] also investigated ATP degradation by ecto-nucleotidases, and their results seem to be at odds with Gordon *et al*'s. Joseph *et al* looked at astrocytes, a cell type very similar to radial glial cells. By investigating the rate at which various ATP analogs were degraded they drew conclusions as to the roles different ecto-nucleotidases played in facilitating the degradation of ATP. Included in the results for the degradation of the ATP analogs were results for the degradation of ATP itself. These results are reproduced Figure in 2.2.

It is possible to arrive at estimates for the parameters V_{deg} and K_{deg} from the raw data displayed in Figure 2.2. After reading off the values for ATP concentration at all points in time, one can use `fminsearch` in Matlab to calculate values for V_{deg} and K_{deg} for this data, by fitting the data to the ODE defining ATP degradation defined above. Doing so yields values of 0.005925 μMs^{-1} and 5.1434 μM for V_{deg} and K_{deg} respectively. The second plot in

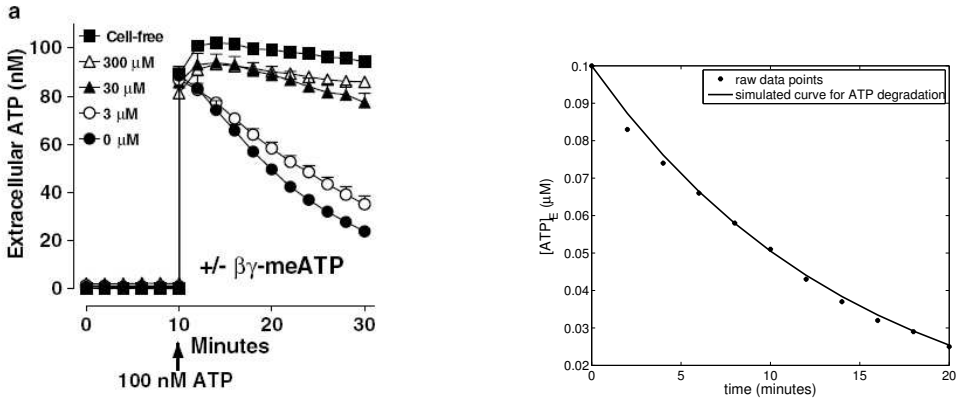

Figure 2.2: Joseph *et al*'s data concerning ATP degradation by astrocytes is shown in the left hand plot. The right hand plot consists of Joseph *et al*'s data (at 0 μM) complete with a curve of best fit that we produced (see text for details). Parameter values given by V_{deg}=0.005925 μMs^{-1} and K_{deg} =5.1434 μM. Initial conditions given by $[ATP_E](0)$ =0.0982 μM. Results obtained using `ode45` (a Runge-Kutta formula) within Matlab. Left hand graph reproduced from [43].

Figure 2.2 shows that for these parameter values our simulated model for ATP degradation fits well to the raw data produced by Joseph *et al*. These values for V_{deg} and K_{deg} are far lower than the values arrived at by Gordon *et al*, suggesting that it takes far longer for astrocytes to degrade ATP than the arterial cells Gordon *et al* looked at. It would be desirable however to have more data points particularly for higher ATP concentrations which we may model in order to ensure that the values for V_{deg} and K_{deg} arrived at are as accurate as possible. The lack of such points perhaps renders the conclusions we can draw from this data less reliable.

Other authors have investigated ATP degradation, but have taken a different approach to displaying their results. Reigada *et al* [73] for example assume that ATP degradation can be modelled by the following ODE,

$$\frac{d[ATP_E]}{dt} = -\frac{[ATP_E]}{\tau}, \tag{2.20}$$

where τ is the time constant.

They consider an initial concentration of ATP and then measure the concentration that is left at subsequent points in time. They then fit an exponential curve to this data using the least squares method to obtain a value for τ. Their plot of the time constant for ATP degradation by retinal pigment epithelium (RPE) cells against the initial ATP concentration is shown in Figure 2.3. The fact that the curve intercepts the origin does not seem realistic if our model for ATP degradation as outlined in equation (2.17) is correct, as it will lead to a K_{deg} value of zero for the reasons that we come to shortly. Reigada *et al* comment that higher initial concentrations of ATP lead to further ATP release from RPE cells, leaving the possibility that the time constant Reigada *et al* arrive at for higher initial ATP concentrations may be skewed, due to extra ATP being released as a result of the feedback mechanism. All this suggests that the curve of best fit plotted in Figure 2.3 should be a line of best fit. If we equate the ODE describing ATP degradation according to Michaelis Menten kinetics with Reigada *et al*'s ODE for ATP degradation (equation (2.20)) we get

$$\tau = \frac{K_{deg} + [ATP_E]}{V_{deg}}. \tag{2.21}$$

Differentiating this expression with respect to $[ATP_E]$ gives $\frac{d\tau}{d[ATP_E]} = \frac{1}{V_{deg}}$. By calculating the slope of the line in Figure 2.3, it will therefore be possible to obtain an approximate value for V_{deg} from Reigada *et al*'s results, with $V_{deg} = 1/\text{slope}$. Fitting a straight line of best fit to the Reigada data by hand gives a slope of approximately 0.05, giving a V_{deg} value of approximately 20 $n\text{Mmin}^{-1}$, i.e. $V_{deg} \approx 0.00033$ μMs^{-1}. If we assume the $[ATP_E]$ term from equation (2.21) to no longer be dynamic but instead just represent the initial ATP concentration, then it is possible to arrive at an approximate value for K_{deg} from Reigada *et al*'s results also. If we return to our expression $\tau = \frac{K_{deg}+[ATP_E]}{V_{deg}}$ (equation (2.21)), when $[ATP_E] = 0$, we get $\tau = \frac{K_{deg}}{V_{deg}}$. If we read off the value for τ when $[ATP_E] = 0$ from our line of best fit in Figure 2.3, we arrive at a value of τ of around 10s. Substituting the above value for V_{deg} of 0.00033, $K_{deg} = \tau \cdot V_{deg} = 600 \cdot 0.00033 \approx 0.2\mu\text{M}$. Note that if our line of best fit had passed through the origin, then $K_{deg} = \tau \cdot V_{deg} = 0 \cdot 0.00033 = 0$. These values for V_{deg} and K_{deg} do not agree at all well with Gordon *et al*'s results. Indeed a V_{deg} value of 0.00033 seems very low and physically unrealistic when applied to large ATP concentrations as it would take a time longer than the period of the cell cycle for initially large concentrations of ATP to be degraded. This suggests that fitting the data in Figure 2.3 to a straight line does not yield satisfactory results.

It therefore seems that we are unable to obtain satisfactory values for V_{deg} and K_{deg} from Reigada *et al*'s results. It is interesting to note however, that for larger concentrations of ATP, the time constant as calculated using Reigada *et al*'s exponential curve of best fit agrees reasonably well with the time constant that it is possible to calculate from Gordon *et al*'s results. Reigada *et al* curve of best fit shown in Figure 2.3 obeys $y = 60.21(1 - \exp^{-0.03x})$, and hence τ tends to 60.21 minutes as ATP tends to infinity. For larger ATP values therefore, of order μM say, $\tau \approx 60$mins. This is almost within one order of magnitude of an approximate value of τ it is possible to calculate from Gordon *et al*'s results. As stated above, assuming that ATP degrades according to Michaelis Menten kinetics, then $\tau = \frac{K_{deg}+[ATP_E]}{V_{deg}}$ (equation (2.21)). If as before we assume $[ATP_E]$ from this expression to be static, representing the initial concentration of ATP, then we can calculate a time constant from Gordon *et al*'s results. For ATP concentration of 0 $\tau = \frac{K_{deg}+[ATP_E]}{V_{deg}} = \frac{221+0}{2.5} = 89.6\text{s} \approx 1.47\text{mins}$. While for an ATP concentration of 500 μM, $\tau = \frac{221+500}{2.5} \approx 4.806$ mins.

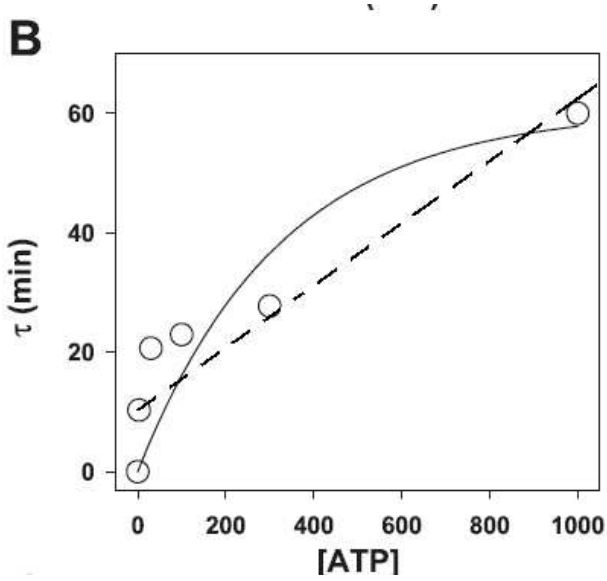

Figure 2.3: Reigada *et al*'s results showing a plot of the time constant for ATP degradation against initial ATP concentrations. ATP concentrations given in units of nM. Solid line correspond to Reigada's curve of best fit, broken line corresponds to our proposed line of best fit. Graph adapted from [73].

Koike *et al* investigated the effect different cellular densities of hepatocytes (a type of

liver cell) have on ATP degradation [47]. They consider relatively high initial ATP concentrations of 100 μM. Koike's results are shown in Figure 2.4. If one reads off the percentage of ATP remaining after 3 minutes at a certain cellular concentration from Figure 2.4, then it is possible to calculate the time constant τ for ATP degradation at this value, assuming as before $\frac{d[ATP_E]}{dt} = -\frac{1}{\tau}[ATP_E]$ (equation (2.20)). The value for τ ranges from around 2 mins for a cellular concentration of 6 dry wt/ml up to around 60 mins . These values for τ seem to agree well with Reigada *et al*'s results and seem to lie within one order of magnitude of the approximate value for τ reached from Gordon *et al*'s and Joseph *et al*'s results (see Table 2.1).

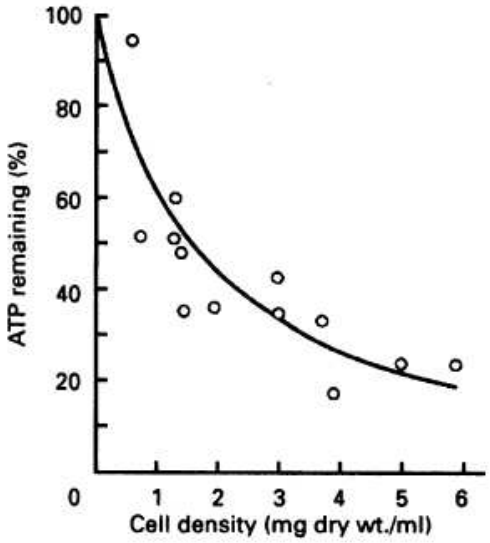

Figure 2.4: Curve of best fit to data from [47] showing the proportion of an initial concentration of 100 μM of ATP left after three minutes after being exposed to different cell densities of hepatocytes. Units of cell density are given in dry weight per ml. Reproduced from [47].

We compiled the various results we obtained from our investigations into Table 2.1. Assuming Michaelis Menten kinetics, we would expect K_{deg} to be independent of cell density, while V_{deg} would be dependent upon it. If we doubled the cellular density, one would expect V_{deg} to double, as the concentration of ecto-nucleos would double. As Gordon *et al* [32, 33] and Joseph *et al* [43] are the only authors to publish how the extracellular ATP concentration varies over several points in time coupled with the fact that there is evidence to suggest that ATP degradation exhibits Michaelis Menten kinetics, it seems reasonable to give their

results more credence over the others. Therefore, in choosing values for V_{deg} and K_{deg}, it seems reasonable that they should be heavily influenced by Gordon *et al*'s and Joseph *et al*'s results. As radial glial cells bear a closer cellular resemblance to the astrocytes that Joseph *et al* studied than to the arterial muscle cells that Gordon *et al* studied, it seems reasonable to choose values V_{deg} and K_{deg} skewed more towards Joseph *et al*'s results. We therefore choose a value for K_{deg} of 50 μM and consider values for V_{deg} of between 0.01 and $2\mu\text{Ms}^{-1}$ to be physically realistic.

Interestingly, these values differ from those used in current mathematical models that include ATP degradation. Although Bennett *et al*'s term for ATP degradation is disregarded in all simulations, with the ATP boundary conditions ensuring ATP degradation [5], Stamatakis *et al* do consider the same form of ATP degradation in their simulations [82]. They use $V_{deg} = 6\ \mu Ms^{-1}$ and $K_{deg} = 5\ \mu$M in their model. Our analysis of ATP degradation seems to suggest that these values may not be appropriate. Having such a high value for V_{deg} will lead to ATP degradation which is far faster than that physically observed by Gordon *et al* and Joseph *et al*. Indeed, if we calculate τ using the same procedure outlined above, but using the values for V_{deg} and K_{deg} provided by Stamatakis *et al* and the ATP concentrations considered in their model, we arrive at an approximate value of between 0.02 and 0.04 mins. This is far lower than the τ that has either been experimentally observed or calculated via other means from the biological literature and will lead to very fast and physically unrealistic ATP degradation. It is difficult to know how Stamatakis *et al* arrived at these values as they do not reveal their sources for the values used [82].

Table 2.1: ATP rate constants

Author	$\tau(min)$	$V_{deg}(\mu\text{Ms}^{-1})$	K_{deg} (μM)
Gordon *et al*	1.47-4.806 *	2.5	221
Joseph *et al*	≈14.468 *	0.005925	5.1434
Reigada *et al*	0-60	0.00033 *	0.2 *
Koike *et al*	2-30 *	-	-

* Values calculated from paper under certain assumptions.

With regard to the $[ATP_I]_{max}$ term in equation (2.16), representing the maximum intracellular ATP concentration, it has proved very difficult to arrive at a realistic value from data in the literature. However, Guthrie *et al* claim that a value of 5000 μM represents

the upper limit of the cytoplasmic ATP concentration in astrocytes. We therefore consider values of 500 μM for $[ATP_I]_{max}$.

The value of the ATP diffusion coefficient D_{ATP} from equation (2.17) is based upon work conducted by de Graaf *et al* [17] and Bennett *et al* [6]. Our chosen parameter values are given in Table 2.2.

2.3 Single Cell Simulations

With our chosen parameter values, we are now in a position to numerically simulate the system (2.1)-(2.18). As the literature is unclear about the precise timing of ATP release during the cell cycle [10, 34, 93], we consider two models, one where ATP release is mainly towards mid G_1 phase and another where release occurs later, towards the G_1/S phase transition.

Cyclin D levels are high during G_1 phase, before dropping off during S phase [13, 81, 96], while Cyclin E levels peak during late G_1 phase [20, 44]. Therefore, modelling ATP release as occurring during mid G_1 phase can be achieved by setting $H_i = D_i$ and $H_c = D_c$. D_c is the critical concentration of Cyclin D, above which ATP release is 'switched on'. This ensures that high Cyclin D concentrations which signal mid G_1 phase allow for the release of ATP through a cell's hemichannels. This scenario is shown in the first plot in Figure 2.5.

When modelling ATP release during the G_1/S phase transition, our cell cycle protein of interest becomes Cyclin E, represented by E in our model. Cyclin E activity peaks during the G_1/S phase transition. However, in our model its steady state value, which corresponds to the quiescent state can be higher than the maximum value of the limit cycle solutions as seen in Figure 2.5. Therefore, in modelling the quiescent G_0 state by allowing the system to sit on the stable fixed point, there is a danger ATP will be released (a physically unrealistic event) if we were to replace H_i and H_c with E_i and E_c respectively. This is because at steady state Cyclin E levels may still be greater than the critical threshold E_c (see Figure 2.5). However, when the system oscillates, R_s reaches its minimum almost exactly at the same time that Cyclin E reaches its peak. In addition, steady state values of R_s are sig-

Table 2.2: Parameter values

Parameter	Value	Source	
r_h^*	$0.6\,\mu\text{Ms}^{-1}$	Section 1.8.1	IP_3 production rate
a'_D	0.41	[66]	Maximum Cyclin D synthesis rate in absence of calcium
a_E	0.16	[66]	E2F independent Cyclin E synthesis rate
a_X	0.08	[66]	Rate of Cyclin E/Cdk2 dependnet CPI production
k	0.054	[66]	Efficiency of Growth Factor signal transduction pathway
q_D	0.6	[66]	Michaelis constant
q_E	0.6	[66]	Michaelis constant
q_X	0.8	[66]	Michaelis constant
f	0.2	[66]	Rate of free E2F dependnet CPI production
g	0.528	[66]	CPI autocatalytic reaction rate
p_s	0.6	[66]	Rate at which free unphosphorylated RB sequesters E2F
p_D	0.48	[66]	Maximum rate at which active Cyclin D/Cdk4 phosphorylates RB
p_E	0.096	[66]	Rate at which free unphosphorylated RB sequesters E2F
p_X	0.48	[66]	Maximal rate at which the CPI dephosphorylates RB
d_D	0.4	[66]	Rate at which active Cyclin E/Cdk2 degrades Cyclin D
d_E	0.2	[66]	Rate at which the CPI degrades Cyclin E
d_X	1.04	[66]	CPI degradation rate
a_f	0.9	[66]	E2F dependent Cyclin E synthesis rate
R_T	2.5	[66]	Total RB
$\ominus$	1.5	[66]	Total concentration of E2F
GF	6.3	[66]	Growth Factors
t_s	3600	Section 2.2	Time scaling parameter
V_{deg}	$0.01 - 2\,\mu\text{Ms}^{-1}$	[32, 33, 43, 47, 73]	Maximal ATP degradation rate
$[ATP_I]_{max}$	$500\,\mu\text{M}$	Section 2.2.1	Maximum internal ATP concentration

Table 2.2: Parameter values (cont.)

Parameter	Value	Source	
V_{ATP}	50 s^{-1}	Section 1.8.1	ATP production rate
$[IP_3]_{min}$	0.013 μM	[5]	Minimum IP_3 concentration
D_c	0.5	Section 2.3	Critical Cyclin D concentration which must be reached to allow for ATP release
$[IP_3]_c$	0.012 μM	[5]	Minimum IP_3 concentration which must be reached to allow for ATP release
ϱ	0.01 μM^{-1}		Stiffness of switch
γ	0.4		Calcium coupling strength
D_{ATP}	350 $\mu m^2 s^{-1}$	[5]	ATP diffusion coefficient
Δx	10 μm		Distance between cells
$p1$	0.0159835 μM	Section 2.4	Basal calcium concentration
$p2$	0.514987	Section 2.4	Hill function coefficient
$p3$	1.31319	Section 2.4	Hill function coefficient
$p4$	0.332195	Section 2.4	Hill function coefficient
$p5$	0.787902	Section 2.4	Hill function coefficient
m	24.1946	Section 2.4	Hill function coefficient
n	9.79183	Section 2.4	Hill function coefficient
α	0.083 s^{-1}		ATP refill rate
K_{deg}	50 μM	[32, 33, 43, 47, 73]	Michaelis constant
$[Ca^{2+}]_b$	0.0159835 μM	[90]	Basal calcium concentration
k_{deg}	0.0625 s^{-1}	Section 1.8.1	IP_3 degradation rate
R_{sc}	1	Section 2.3	Critical Cyclin D concentration, below which ATP is released
β	0.0244	[90]	Calcium buffering
K_I	0.03 μM	[90]	IP_3 dissociation constant
K_{act}	0.17 μM	[90]	Calcium dissociation consant
$[Ca^{2+}]_{ER}$	400 μM	[90]	ER calcium concentration
k_{on}	8.0 $\mu M^{-1} s^{-1}$	[90]	'On rate' of calcium binding
K_{inh}	0.1 μM	[90]	Dissociation constant
V_{max}	5.85 $\mu M s^{-1}$	[90]	Maximal pumping rate
K_P	0.24 μM	[90]	Dissociation consant
P_L	0.67739936 $\mu M s^{-1}$	[90]	Leak constant

nificantly higher than the minimum R_s in the oscillatory regime. Therefore the modelling of ATP release during the G_1/S transition could be achieved by ensuring ATP is released when R_s is approaching its minimum. If we replace H_i and H_c in our model with R_{sc} and R_{si} respectively, ATP release will occur when R_s falls below R_{sc} which will co-incide with Cyclin E peaking. Again, this scenario is illustrated in Figure 2.5, where it can also be seen that the steady state value of R_s is so high that there is no danger of ATP release at steady state. Replacing H_i and H_c in our model with R_{sc} and R_{si} respectively is therefore the approach we take to model ATP release during the G_1/S transition.

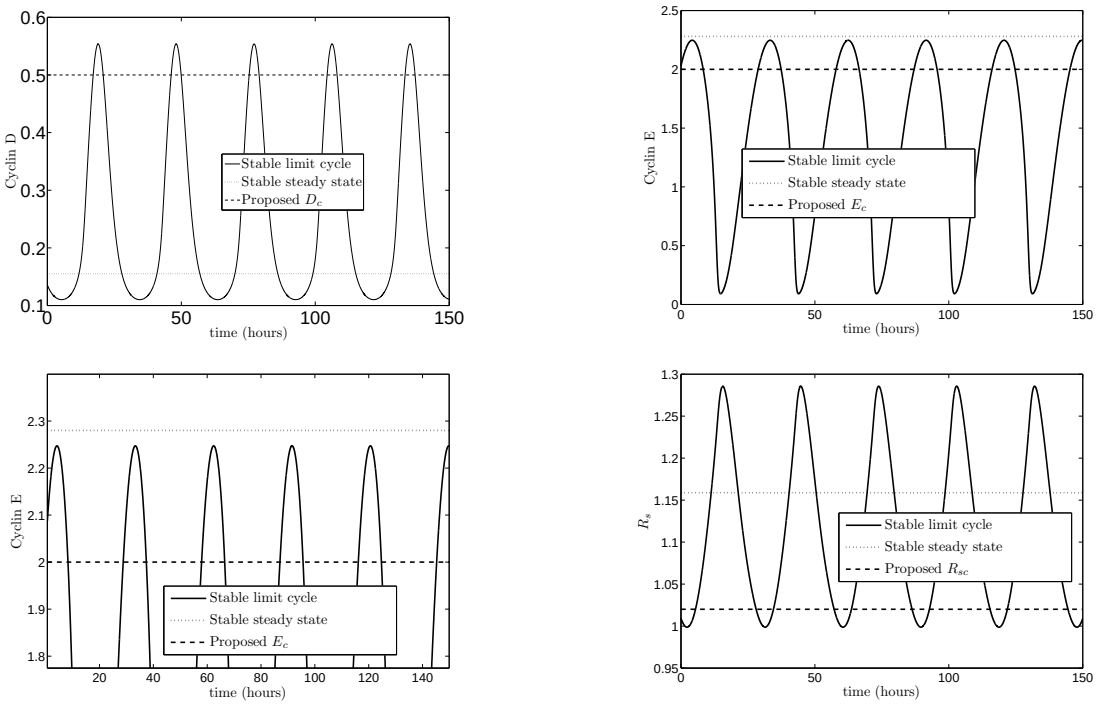

Figure 2.5: Plots of a number of cell cycle variables for Obeyesekere's cell cycle model given by equations (2.1)-(2.5). The results show how the limit cycle and steady state solutions relate to proposed critical thresholds for three different variables (D, E and R_s) with a view to accurately modelling the timing of ATP release. Parameter values as for Table 2.2.

Numerically integrating system (2.1)-(2.18) for a single cell, which is achieved by ignoring the spatial component of equation (2.17) for both the Cyclin D dependent ATP release model ($(H_i, H_c) = (D_i, D_c)$) and the R_s dependent ATP release model ($(H_i, H_c) = (R_{sc}, R_{si})$) leads to oscillations seen in Figure 2.6. It can be seen that the system (2.1)-(2.18) captures many

Table 2.3: Initial Conditions

	Cyclin D dependent ATP release		R_s dependent ATP release	
	Full model	Cell cycle model	Full model	Cell cycle model
$D(0)$	0.1564	0.1482	0.6054	0.4975
$E(0)$	1.2034	1.3467	0.2322	0.2108
$R(0)$	0.6410	0.6164	0.8940	0.8925
$R_s(0)$	1.1695	1.1645	1.2422	1.2710
$X(0)$	2.5225	2.0436	2.0436	2.3819
$[ATP_E](0)$ (μM)	0	-	0	-
$[ATP_I](0)$ (μM)	500	-	500	-
$[IP_3](0)$ (μM)	0.013	-	0.013	-
$[Ca^{2+}](0)$ (μM)	0.02	-	0.02	-
$h(0)$	0.9524	-	0.9524	-

of the qualitative features of cell cycle coupled ATP signalling in radial glial cells for both Cyclin D and R_s dependent ATP release. Simulations of our model for Cyclin D dependent release are shown in the first column of plots in the figure. From these plots, it can also be seen that ATP induced calcium spiking occurs as Cyclin D levels peak, before calcium returns to steady state when Cyclin D begins to fall below D_c. As outlined above, G_1 phase is associated with high values of Cyclin D and therefore in this model we have successfully modelled the opening of a cell's hemichannels, leading to the release of ATP during mid G_1 phase.

Similarly, it can be seen from the second column of plots in Figure 2.6, that the model with R_s dependent release leads to ATP induced calcium release during the G_1/S phase transition. As mentioned above, the G_1/S phase transition is associated with high Cyclin E levels and it at this point that ATP induced calcium spiking occurs.

Additionally, it is clear that Cyclin D production is greater with both forms of autocrine ATP-$[Ca^{2+}]$ signalling than without such autocrine signalling (c.f. Cyclin D levels in Figure 2.6). This is in keeping with Kahl's findings that Cyclin D production is increased by the release of calcium from internal stores [45, 46]. The periods of the coupled models were 28.5

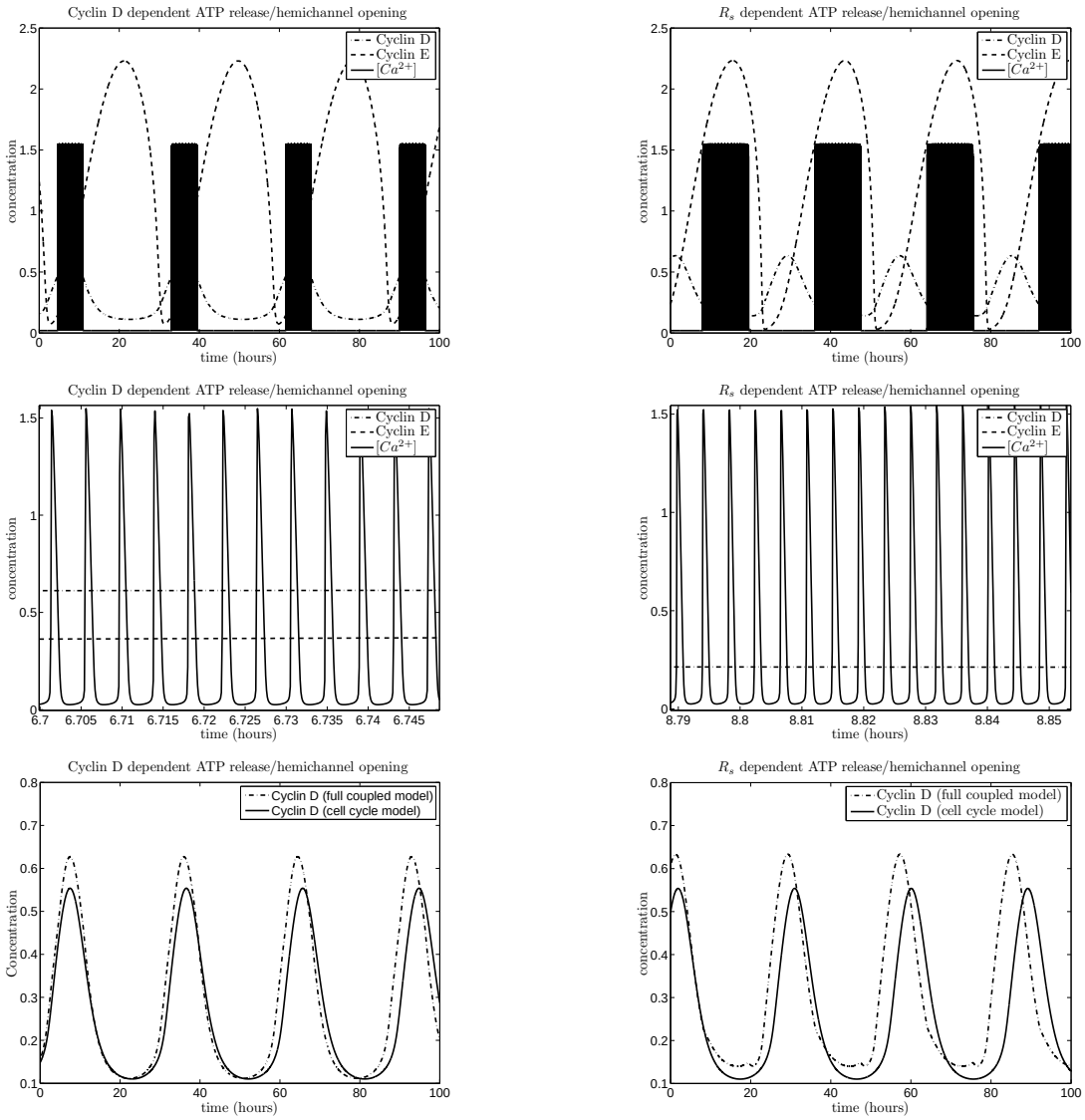

Figure 2.6: Simulations obtained by numerically integrating system (2.1)-(2.18) for a single cell. Parameter values as for Table 2.2, except for $V_{deg} = 2\mu\text{Ms}^{-1}$. The first column of plots correspond to Cyclin D dependent ATP release ($(H_i, H_c) = (D_i, D_c)$). They show ATP mediated calcium release occurring as Cyclin D peaks (mid G_1 phase), leading to a decrease in the period of the cell cycle of the original cell cycle model. The second column of plots correspond to R_s dependent ATP release ($(H_i, H_c) = (R_{sc}, R_{si})$). They show ATP mediated calcium release occurring as Cyclin E peaks (late G_1 phase), leading to a decrease in the period of the cell cycle of the original cell cycle model. Initial conditions as for Table 2.3. All results obtained using `Stiff` (an adaptive step integrator useful for stiff problems) within XPP a software tool used to solve differential equations [21].

hours in the Cyclin D dependent case and 28 hours in the R_s dependent case, compared to 29.1 hours in the original cell cycle model. The reduction in the period although small is clear upon inspecting the plots in the bottom row in Figure 2.6. If one increases the calcium coupling strength γ to 1.2, the period of oscillation for the Cyclin D dependent ATP release model falls further to 26.9 hours and that of the R_s dependent model to 26.55 hours (results not shown). These reductions are still modest however, which suggests that the modulation of the frequency of oscillation achieved through a calcium signalling mechanism can not in itself account for the large increase in neural production observed by Weissman *et al* [93], although it may still play an important role in this process, e.g. by inducing oscillations that would not otherwise occur.

One can also see from Figure 2.6 that calcium spiking lasts longer in the R_s dependent ATP release model than for the Cyclin D dependent model. It is the choice of R_{sc} and D_c that lead to the disparity in the duration of the calcium spikes. We chose values for R_{sc} and D_c to ensure that qualitatively speaking, ATP was released predominantly during the G_1/S phase transitions in the R_s dependent ATP release model and during mid G_1 phase in the Cyclin D dependent ATP release model. Although it would be possible to change the value of R_{sc} and/or D_c so that the duration of calcium spikes is the same under the parameter regime considered in Figure 2.6, as soon as the parameter regime is changed the disparity in the duration of calcium spiking will return. This is because the timing of the calcium spiking plays an important role in how and by how much the cell cycle variables are affected. Calcium spiking towards the beginning of the cell cycle may not have the same effect upon Cyclin D and as a consequence the rest of the cell cycle variables as the same transients towards the end of the cell cycle for example. Under a parameter regime whereby calcium is released for a longer period of time than is the case in Figure 2.6, Cyclin D will be affected for a longer period of time. However, in this case the change brought about by the extra calcium upon Cyclin D activity in the R_s dependent model may be qualitatively and quantitatively different to the change brought about in the Cyclin D dependent model due to the different timing of the release of the extra calcium. This is something that becomes more apparent later in the chapter. In this sense therefore our two models should only be compared qualitatively and this is the approach we take in this thesis.

2.4 Reduction of the Model

The calcium dynamics and cell cycle dynamics occur over very different timescales. In order to faithfully model the calcium dynamics, and in particular the small period of the calcium oscillations, one has to set a very small time step when numerically integrating the system (2.1)-(2.18). This will make it extremely computationally expensive to simulate systems of many cells and will present problems with regard to the production of bifurcation diagrams. Therefore we explored whether it is reasonable to model the calcium dynamics as a smooth average instead of allowing calcium to oscillate. Moreover, we do not consider performing asymptotic analysis on the systems in this thesis, instead focussing upon producing numerical results. Looking at the bifurcation diagram from Figure 1.20 it would appear that it is a simple task to calculate a smooth calcium average, as it looks as if the average calcium levels over an oscillatory cycle would be halfway between the maximum and minimum values indicated in this diagram. If this were the case, an approximation to the average would be a simple step function. However, due to the spiking nature of the calcium the average can not be calculated in this way as can be seen from Figure 2.7 which gives the true average calcium per oscillation. It can be seen that the average concentration of calcium takes on a more complicated form. In fact by inspection it appears that a curve defined by the sum of two hill functions could pass through the stable solutions shown in the figure. With this in mind we collected the data for the average calcium values along with their respective values of $[IP_3]$ with a view to numerically fitting a curve to these values. With this achieved, it will be possible to replace the values for calcium given by equation (2.7) with this new function. Not only this, but with equation (2.7) replaced, equations (2.8)-(2.11) governing amongst other things the calcium 'gating' variable h will become superfluous and can be ignored in future simulations. Our curve of best fit is defined as

$$[Ca^{2+}]_i = p1 + \frac{p2[IP_3]_i^m}{p3^m + [IP_3]_i^m} + \frac{p4[IP_3]_i^n}{p5^n + [IP_3]_i^n}. \tag{2.22}$$

Utilising `fit` within Gnuplot, which uses an implementation of the non-linear least squares Marquardt-Levenberg algorithm [57] we arrived at the values for $p1, p2, p3, p4, p5, n$ and m shown in Table 2.2. Figure 2.7 illustrates how our new function fits the average calcium data. Note that, although for higher values of $[IP_3]$ our function does not fit the data very well, this should not matter. We are only concerned with $[IP_3]$ fluctuations that sweep the system into the limit cycle solutions from the lower stable steady state and back out again. Hence, our line of best fit need only fit the data for the lower steady steady state

and stable oscillatory states.

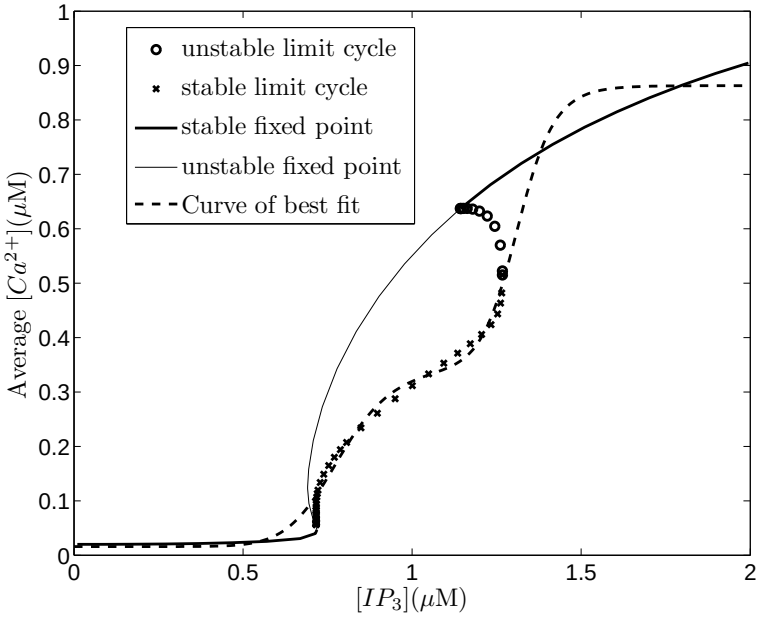

Figure 2.7: Bifurcation diagram for the Li and Rinzel model for $[IP_3]$ mediated calcium release, given by equations (2.7)-(2.11) showing which values of the parameter IP_3 give rise to calcium oscillations, as well as a plot of the curve of best fit given by equation (2.22). Bifurcation diagram calculated using AUTO (a package for numerical continuation) [21] within XPP. Parameter values given in Table 2.2 except for $[IP_3]$, which is as indicated.

In order to satisfy ourselves that our function approximating the calcium dynamics leads to results qualitatively and quantitatively very similar to results for the full model, we ran a number of simulations for each scenario, for each model. Some of the results of these simulations are shown in Figure 2.8. From this it is clear that the results of the reduced system are almost identical to those of the full system. We therefore adopt the reduced system in all further work. In all subsequent simulations and calculations we do not change the calcium parameters and there is therefore no need for us to recalculate our curve of best fit at any point.

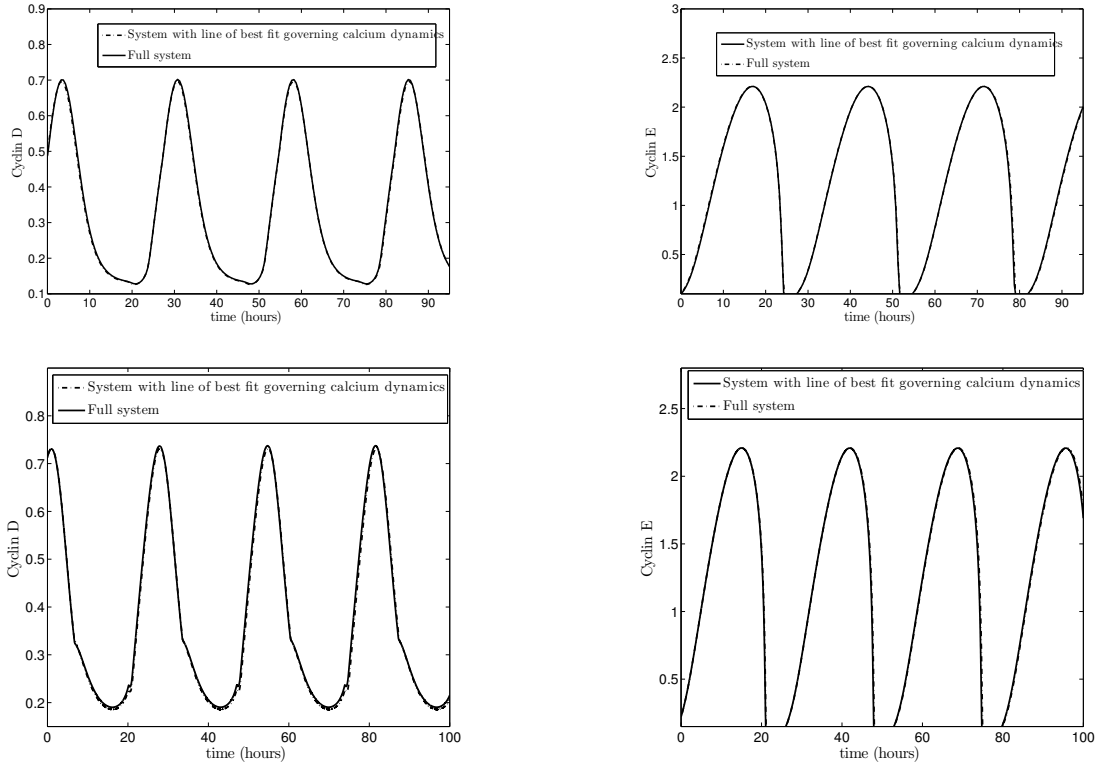

Figure 2.8: Simulations obtained by numerically integrating system (2.1)-(2.18) and system (2.1)-(2.6), (2.12)-(2.18), (2.22). The results show that the match between the full model and reduced model is excellent. First row of plots correspond to the system with Cyclin D dependent release, modelled by replacing H_i and H_c in the system with D_i and D_c respectively. Initial conditions for these simulations were $D(0) = 0.4646$, $E(0) = 0.0857$, $R(0) = 0.9047$, $R_s(0) = 1.2763$, $X(0) = 8.6954$, $[IP_3](0) = 0.013\ \mu$M, $[ATP_I](0) = 499.9998\ \mu$M, $[ATP_E](0) = 0.00013\ \mu$M, $[Ca^{2+}](0) = 0.02\ \mu$M, $H(0) = 1$. The second row of plots correspond to R_s dependent ATP release, modelled by replacing H_i and H_c with R_{sc} and R_s. Initial conditions for these simulations were $D(0) = 0.7128$, $E(0) = 0.2218$, $R(0) = 0.8919$, $R_s(0) = 1.2088$, $X(0) = 2.3361$, $[IP_3](0) = 0.013\ \mu$M, $[ATP_I](0) = 500\ \mu$M, $[ATP_E](0) = 0\ \mu$M, $[Ca^{2+}](0) = 0.02\ \mu$M, $H(0) = 0.9524$. Results were calculated using the `Stiff` within XPP. Parameter values as per Table 2.2, except for $V_{deg} = 2\ \mu\text{Ms}^{-1}$ and $\gamma = 1$

2.5 Analysis of the System for a Single Cell

2.5.1 Bifurcation Analysis

In calculating the bifurcation diagram for a single cell for the system it was necessary to assume a quasi-steady state approximation for the $[IP_3]$ dynamics governed by equation (2.15). This is because AUTO, the software package we use for continuation, has difficulty resolving the saddle node bifurcation point of limit cycles (marked FP1^D in Figure 2.10(a) and FP1^{Rs} in Figure 2.10(b)) unless the total number of ODEs is reduced. As the timescale governing the $[IP_3]$ dynamics is very short compared to that of the cell cycle dynamics, there should be little quantitative difference in the results. Direct simulations of the system, under different parameter regimes with and without the quasi-steady state approximation for $[IP_3]$, suggest that it has no qualitative effect on the system. The results of one such simulation are shown in Figure 2.9.

Bifurcation diagrams for both the Cyclin D dependent ATP release and R_s dependent ATP release model with quasi-steady state approximation for equation (2.15) are shown in Figure 2.10. Both models yield qualitatively similar bifurcation digrams. If we take the Cyclin D dependent case first (Figure 2.10(a)), we see that stable small amplitude oscillations are created via a Hopf bifurcation point at $a_d' \approx 0.409957$. The stability of this branch of limit cycle solutions is lost via a saddle node bifurcation (FP3^D) and regained at FP2^D, where $a_d' \approx 0.3956$. Up until this point the bifurcation diagram for the system is identical to that of Obeyesekere *et al*'s original cell cycle model discussed in the previous chapter. However, when this branch of solutions begins to approach $D_c = 0.5$, Cyclin D production increases as a result of ATP mediated calcium release and the stability of the solution is again lost via a saddle node bifurcation, before being recovered at FP1^D, where $a_d' \approx 0.3852$.

The bifurcation diagram for R_s dependent ATP release (Figure 2.10(b)) is similar in form. However, the effect of ATP mediated calcium release is seen earlier than for the Cyclin D dependent case. This effect is characterised by the dog leg (marked DL) in the branch of limit cycle solutions at $a_d' \approx 0.3965$. In this model, under this parameter regime, increased Cyclin D production, facilitated by ATP mediated calcium release, occurs before the saddle node bifurcation point (FP1^{Rs}) that we saw in the Cyclin D dependent case and this is why we do not see a bifurcation point equivalent to FP2^D in the R_s dependent model.

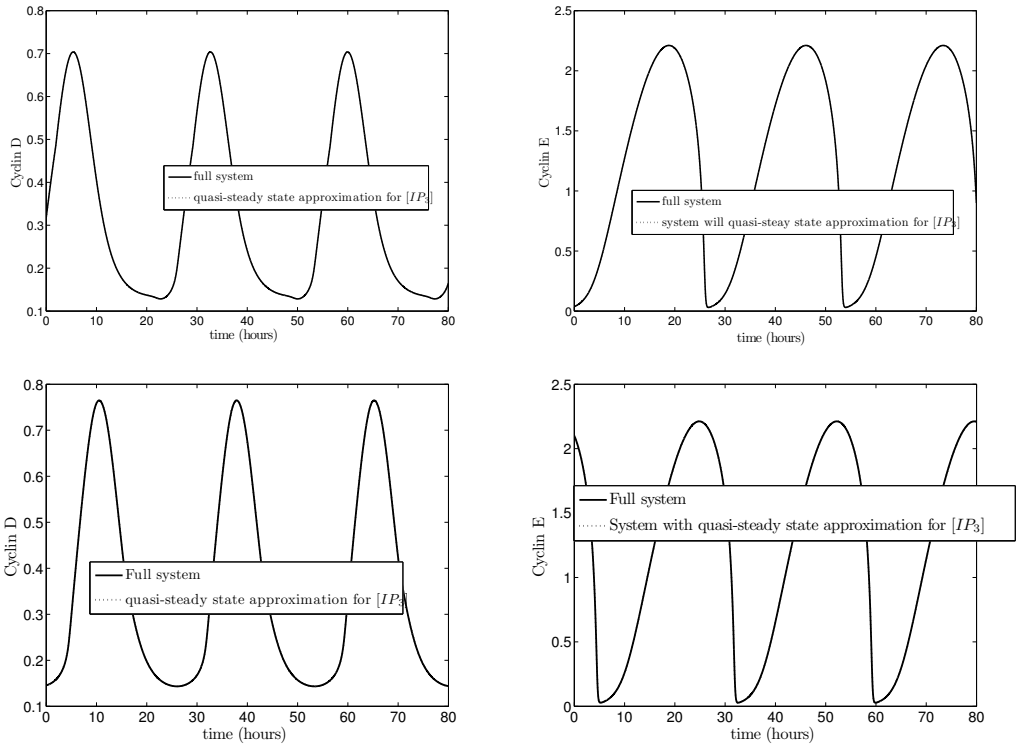

Figure 2.9: Simulations of system (2.1)-(2.6), (2.12)-(2.18), (2.22) with and without quasi-steady state approximation for equation (2.15). The first row of plots correspond to Cyclin D dependent release, the bottom row to R_s dependent release. Parameter values given in Table 2.2 in the Cyclin D dependent case and as for Table 2.2 except for $V_{deg} = 0.02\,\mu\text{Ms}^{-1}$ in the R_s dependent case. Initial conditions for Cyclin D dependent case were $D(0) = 0.3168$, $E(0) = 0.0325$, $R(0) = 0.8365$, $R_s(0) = 1.2369$, $X(0) = 28.2354$, $[IP_3](0) = 0.5137\ \mu M$, $[ATP_I](0) = 499.9999\ \mu$M, $[ATP_E](0) = 23.6701\ \mu$M. Initial conditions for R_s dependent case were $D(0) = 0.1454$, $E(0) = 2.1012$, $R(0) = 0.3818$, $R_s(0) = 0.9838$, $X(0) = 0.7823$, $[IP_3](0) = 0.9458\,\mu$M, $[ATP_I](0) = 499.7765\,\mu$M, $[ATP_E](0) = 499.7809\,\mu$M. Results obtained using `ode23s` (an explicit Runge-kutta (2,3) formula useful for solving stiff systems) in Matlab.

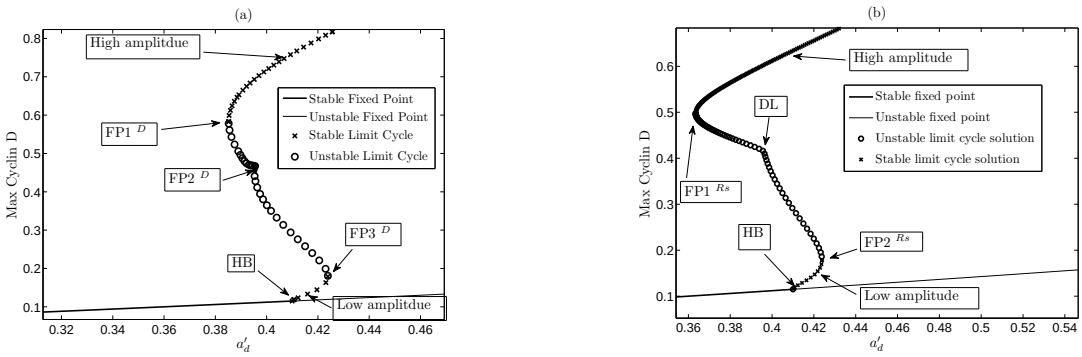

Figure 2.10: Bifurcation diagrams of system (2.1)-(2.6), (2.12)-(2.18), (2.22) with quasi-steady state approximation for equation (2.15). The bifurcation diagram shows how the maximum Cyclin D concentration depends upon the Cyclin D synthesis rate a_d'. Plot (a) corresponds to Cyclin D dependent ATP release model ($(H_i, H_c) = (D_i, D_c)$) and plot (b) to the R_s dependent ATP release model ($(H_i, H_c) = (R_{sc}, R_{si})$). Diagrams calculated using AUTO within XPP. Parameter values by Table 2.2, except $\gamma = 1, V_{deg} = 2\ \mu\text{Ms}^{-1}$ and a_d' which is as shown. FP1^D, FP2^D, FP3^D, FP1^{Rs} and FP2^{Rs} correspond to fold or saddle node bifurcation points, while HB corresponds to a Hopf bifurcation point.

It can also be seen from this figure that there exists an area of multistability in the Cyclin D dependent model and an area of bistability in the R_s dependent model. By referring to Figure 2.10(a), it can be seen that the area of mulitstability is bounded to the right hand side by FP3^D and to the left by FP1^D in the Cyclin D dependent case. In the R_s dependent case, FP1^{Rs} and FP2^{Rs} form the bounds of the area of bistability. It is hypothesised in the literature that a cycling radial glial cell may have the ability to induce a quiescent cell into the G_1 phase of the cell cycle [93]. These areas of multistability and bistability could be relevant to this process. Let us consider a multicellular model and a parameter regime such that all cells lie within the area of multistability or bistability. Quiescent cells would have initial conditions such that they sit on the stable fixed point. A driving cell whose initial conditions are such that it is oscillating on the upper limit cycle could recruit quiescent cells to which it is coupled on to the upper limit cycle branch. Such recruitment would depend, amongst other factors, upon the existence and stability of phase locked solutions in the chosen model and this forms the basis for the work in Sections 2.6 and 2.7. Alternatively, one could model quiescent cells with a parameter regime so that at rest they sit on

a stable steady sate that lies outside the area of multistability or bistability. In referring to Figure 2.10, one can see that this could be achieved by having a value for a'_d for the quiescent cell below FP1^D in the Cyclin D dependent model and below FP1^{Rs} in the R_s dependent model. A pacemaker cell which has parameter values and initial conditions such that it is oscillating could then release ATP, leading to a release of calcium from the internal stores of the quiescent cells, thus potentially sweeping the quiescent cells into the area of multistability or bistability and onto the upper branch of limit cycle solutions. When extracellular ATP falls to zero, the quiescent cells will sweep back out the area of multistability or bistability and return to the stable steady state which lies outside this area. Again this possibility would depend upon the existence and stability of phase locked solutions under different parameter regimes (see Sections 2.6 and 2.7). Whichever approach is taken it will be instructive to analyse the dependence of the fold points, which form the bounds of the area of multistability, upon parameter values. Two parameter bifurcation diagrams where we do just this are shown in Figure 2.11. In this figure we use γ, which represents the calcium coupling strength as one of the control parameters.

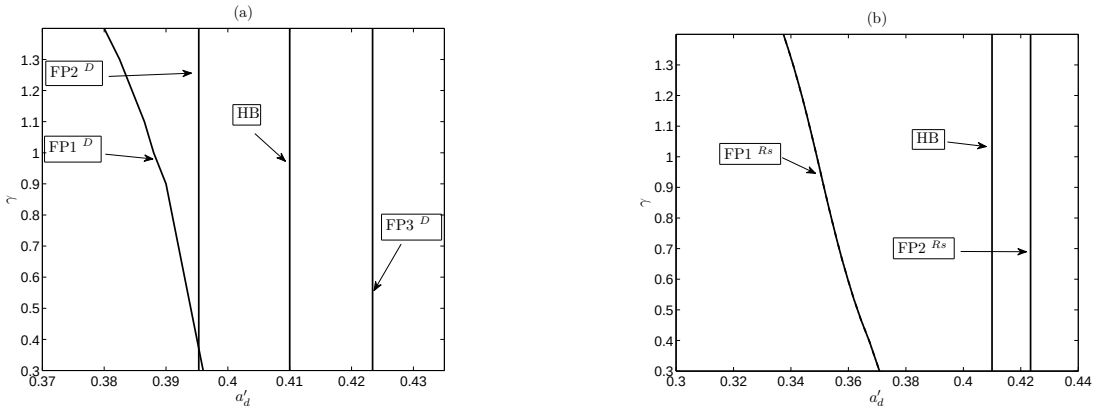

Figure 2.11: Bifurcation diagrams of system (2.1)-(2.6), (2.12)-(2.18), (2.22) with quasi-steady state approximation for equation (2.15). The bifurcation diagram shows how the fold points and Hopf bifurcation points from Figure 2.10 depend upon the calcium coupling strength γ and in turn how this affects the areas of multistability and bistability in our models. Plot (a) corresponds to the Cyclin D dependent ATP release model ($(H_i, H_c) = (D_i, D_c)$) and (b) to the R_s dependent ATP release model ($(H_i, H_c) = (R_{sc}, R_{si})$). Diagrams calculated using AUTO within XPP. Parameter values by Table 2.2, except $V_{deg} = 2\,\mu\text{Ms}^{-1}$, a'_d and γ as as shown.

Figure 2.11 illustrates how the boundaries of the areas of multistability and bistability depend upon γ. For both models the area increases as the calcium coupling strength γ increases. Interestingly, in the Cyclin D dependent case, for values of $\gamma < 0.3705$, $FP2^D$ and not $FP1^D$ forms the left hand boundary of the area of multistability. Under the parameter regime considered in the figure, $FP3^D$ and $FP2^{Rs}$ remain unaffected by a change in γ. This is because the effect of ATP release is only seen above this point. This is also true of the Hopf bifurcation point HB.

2.6 Weakly Coupled Non-Linear Oscillator Theory

In this section we introduce the theory of weakly coupled non-linear oscillators, which we shall use to investigate the existence and stability of phase locked solutions of systems of two coupled cells.

Before we introduce the theory itself, we first of all introduce a number of concepts. Several mathematical approaches concerning coupled oscillators have been outlined in the literature [41, 61]. However, a consensus has not been reached as to the definitions of phase, phase locking, synchronisation, etc. We therefore introduce these concepts here and the definitions that we will use for them henceforth.

2.6.1 Phase

Let us consider a dynamical system,

$$\frac{dX}{dt} = F(X), \tag{2.23}$$

which has an asymptotically stable solution

$$X_0(t) = X_0(t+T), \tag{2.24}$$

with period T (and hence frequency $\Omega = \frac{1}{T}$).

Let $X(t)$ be another T periodic solution to equation (2.23), starting from $X(0)$. For each point on the limit cycle $X(t)$, there is a unique $s \in [0, T]$, such that $X_0(s) = X(t)$.

Now the natural phase $\theta(t)$ is a solution to

$$\frac{d\theta}{dt} = \Omega, \quad \text{with } \theta(t+T) = \theta(t) \tag{2.25}$$
$$\text{and } \theta(0) = s \text{ where}$$
$$X_0(s) = X(0).$$

As we traverse $X_0(t)$, perhaps at a discontinuous speed, the natural phase θ changes at a constant speed (see Figure 2.12).

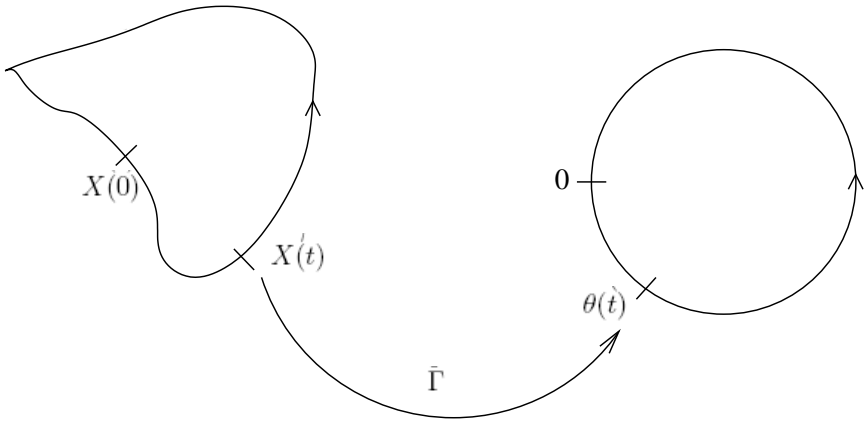

Figure 2.12: Schematic illustrating the parameterisation Γ that we adopt to calculate the phase $\theta(t)$ of an oscillator

2.6.2 Phase Locking, Synchronisation and the Theory of Weakly Coupled Oscillators

Before embarking upon our definitions of phase locking and synchronisation, Let us consider two coupled identical oscillators of the form given by equation (2.23), to give

$$\frac{dX_1}{dt} = F(X_1) + \epsilon G(X_2, X_1), \tag{2.26}$$

$$\frac{dX_2}{dt} = F(X_2) + \epsilon G(X_1, X_2). \tag{2.27}$$

In this system, G is a function that provides the isotropic coupling between the two oscillators and ϵ is the coupling coefficient accounting for the coupling strength. If we let the phase of the first oscillator be θ_1 and that of the second be θ_2, with θ defined by equation (2.25), then the two oscillators are said to be *phase locked* when the phase difference, $\Phi =$

$\theta_2 - \theta_1$ is equal to a constant. If $\Phi = 0$, then the two oscillators are said to be *synchronised*. If $\Phi = \frac{T}{2}$ then the oscillators are said to be *anti-phase* phase locked. For any other constant value of Φ this phase locking is said to be *out of phase* or *asynchronous*.

The theory of weakly coupled oscillators tells us that if $\epsilon \ll 1$, which ensures that the coupling between the oscillators is weak then system (2.26)-(2.27) can be reduced to the phase model (see [41] for proof)

$$\frac{d\theta_1}{dt} = \Omega + \epsilon L(\theta_2 - \theta_1), \tag{2.28}$$

$$\frac{d\theta_2}{dt} = \Omega + \epsilon L(\theta_1 - \theta_2), \tag{2.29}$$

where the T periodic function $L(\Phi)$, known as the phase interaction function, is defined by

$$L(\Phi) = \frac{1}{T}\int_0^T X^*(t)G[X_0(t+\Phi), X_0(t)]dt. \tag{2.30}$$

$X_0(t)$ in this expression is the asymptotically stable solution (defined in equation (2.24)) of dynamical system (2.23). $X^*(t)$ is a T periodic function called the adjoint or response function. It is the phase resetting curve of the oscillator in the limit of vanishingly small perturbations. If $X^*(t) > 0$ at any point, perturbing the system at this point will advance the period and if $X^*(t) < 0$, it will be retard the phase. The response function satisfies the linear differential equation and normalisation given by

$$\frac{dX^*}{dt} = -[D_X F(X_0(t))]^T X^*(t), \quad X^*(t)X_0' = 1. \tag{2.31}$$

where $D_X F$ is the derivative of matrix F with respect to X, A^T is the transpose of the matrix A and X' denotes the derivative of X with respect to t.

The interaction function $L(\Phi)$, defined in equation (2.30), is calculated by averaging the effect of the coupling, given by $G[X_0(t+\Phi), X_0(t)]$, with the response function $X^*(t)$ over the period of oscillation. Note also, that the interaction function depends only on the dynamics of a single oscillator.

The important concept with regard to the phase locking of two oscillators is the phase difference between the two oscillators which is defined by

$$\Phi = \theta_2 - \theta_1. \tag{2.32}$$

From equations (2.28), (2.29) and (2.32), it is clear that

$$\Phi' = \epsilon(L(-\Phi) - L(\Phi)). \tag{2.33}$$

Phase locked solutions exist when Φ is constant. Note the synchronous solution $\Phi = 0$ will always exist, due to the isotropic nature of the spatial coupling in the system. As $L(\Phi)$ is T periodic, the anti-phase phase locked state $\Phi = \frac{T}{2}$ will also always be a solution. In order to find other solutions it will be necessary to calculate $M(\Phi) = L(-\Phi) - L(\Phi)$.

It is next important to investigate the stability of the solutions. Let us consider a small perturbation $\tilde{\Phi}$ to a phase locked solution Φ^*, so that $\Phi = \Phi^* + \tilde{\Phi}$. Substitution into equation (2.33) gives

$$\begin{aligned}\tilde{\Phi}' =& \epsilon(M(\Phi^* + \tilde{\Phi})) \\ \approx& \epsilon(M(\Phi^*) + M'(\Phi^*)\tilde{\Phi}) \\ =& \epsilon(M'(\Phi^*)\tilde{\Phi}).\end{aligned} \tag{2.34}$$

Hence, solutions will be stable if $M'(\Phi^*)$ is negative and unstable if $M'(\Phi^*)$ is positive.

2.7 Analysis of a System of Two Coupled Cells

We are now in a position to consider a system of two coupled identical radial glial cells and investigate through weakly coupled oscillator theory and bifurcation analysis the existence and stability of phase locked solutions.

2.7.1 Cyclin D Dependent ATP Release

Let us consider a system of two cells given by (2.1)-(2.6), (2.12)-(2.18), (2.22) for Cyclin D dependent ATP release ($(H_i, H_c) = (D_i, D_c)$). We let the phase of oscillation of each cell be θ_1 and θ_2, with θ as defined above. XPP implements a method devised by Graham Bowtell to calculate the response curve $X(t)^*$ [21] and from this we can calculate $M(\Phi)$.

As noted above, the coupling between cells in the system is via the transport of of external ATP governed by equation (2.17). In our 2 cell system therefore, the coupling function from equation (2.26), $G(X_2, X_1)$ will be equivalent to $[ATP_E]_2 - [ATP_E]_1$ and the coupling function from equation (2.27), $G(X_1, X_2)$ will be equivalent to $[ATP_E]_1 - [ATP_E]_2$. As our single cell system is 8 dimensional and spatial coupling is facilitated through external ATP only, all components of the coupling function $G[X_0(t+\Phi), X_0(t)]$ from equation (2.30) will be zero except for the external ATP component. This means that with our model, only the external ATP component of the response function $X(t)^*$ will be a factor when calculating $L(\Phi)$ and from it $M(\Phi)$. A plot of the external ATP component of the response function is shown in the Figure 2.13.

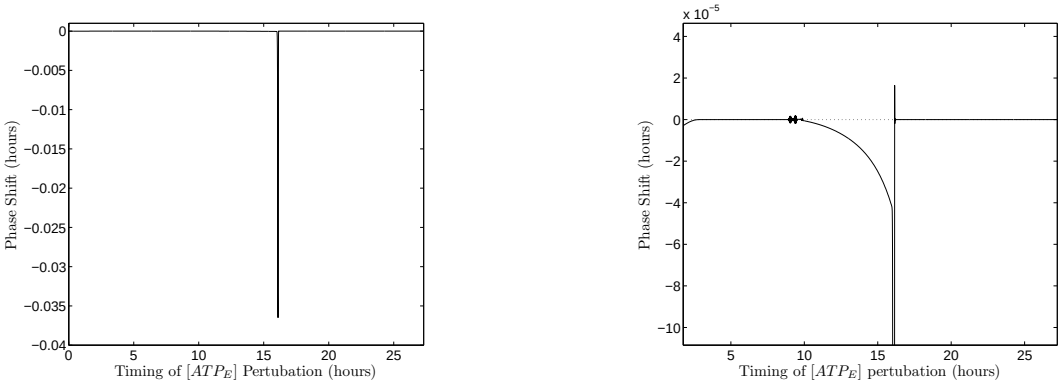

Figure 2.13: Plots of the external ATP component of the response function $X(t)^*$ for the system given by (2.1)-(2.6), (2.12)-(2.18), (2.22) for Cyclin D dependent ATP release ($(H_i, H_c) = (D_i, D_c)$). The left hand panel indicates how the phase would be shifted if ATP is perturbed throughout its period of oscillation. Right hand panel is a zoomed in profile of the left hand panel. The response function was calculated using XPP. Parameter values given in Table 2.2, except for $V_{deg} = 0.01\ \mu\text{Ms}^{-1}$.

From Figure 2.13, it can be seen that the external ATP component of the response function is initially negative, indicating that if external ATP is perturbed at this point, the phase of the system will be retarded. However, it quickly becomes positive at $t \approx 1$, indicating that the phase would be advanced if ATP is perturbed at this point in the cycle. It then becomes negative again, falling sharply around $t \approx 16$. However, although it is difficult to see from the figure, it becomes positive again. Having calculated $X(t)^*$ for the system, we are now in a position to calculate $M(\Phi)$. The results of these calculations are

shown in Figure 2.14.

As discussed above, phase locked solutions correspond to $M(\Phi) = 0$. From Figure 2.14, it can be seen that $M(\Phi) = 0$ four times. As $M(\Phi)$ is a periodic function of period T, existence of one equilibrium implies the existence of a whole family of solutions that differ by nT ($n \in \mathbb{Z}$). As $M(\Phi)$ crosses the horizontal axis 4 times within the period of one oscillation, we shall consider the system to have four equilibria and we will not consider the family of solutions with the correspondingly equivalent phase differences. The equilibria we are concerned with occur at $\Phi = 0$, 6.57, 13.655 and 20.73. The slope of $M(\Phi)$ indicates the stability of these solutions, a negative slope being stable and a positive slope indicating an unstable solution. Therefore, the synchronous solution $\Phi = 0$ and the anti-phase phase locked solution $\Phi = 13.65$ (13.65 being half 27.3, the period of oscillation) are stable. The other two solutions are unstable, indicated by the positive slope of $M(\Phi)$ at these points. The theory of weakly coupled oscillators therefore suggests that whether two coupled oscillators settle down to the synchronous or anti-phase phase locked solution will depend upon the initial conditions of the two different cells. Bifurcation analysis confirms that for two coupled oscillators, under this parameter regime, two stable limit cycle solutions exist, supporting the predictions of the weakly coupled oscillator theory. The results from this analysis are shown in Figure 2.15.

From Figure 2.15, it can be seen that there exist two stable limit cycle solutions. It may seem that the analysis using weakly coupled oscillator theory is superfluous, as it can not tell us anything that our bifurcation analysis can not. However, the theory of weakly coupled oscillators can be extended to larger systems of several cells in one and two spatial dimensions and this will not be the case for numerical bifurcation analysis where limitations are imposed upon the number of ODEs that AUTO can handle. In the two cell case, bifurcation analysis acts as a useful tool to confirm the results from the application of the theory of weakly coupled oscillators.

Results from simulating the system, which can be seen in Figures 2.16 and 2.17, confirm the findings of our analysis. Figure 2.16 shows that an initial phase difference of 4.5 hours leads to synchronous phase locked solutions, while Figure 2.17 shows that an initial phase difference of 8.5 hours leads to solutions that are anti-phase phase locked, as predicted by

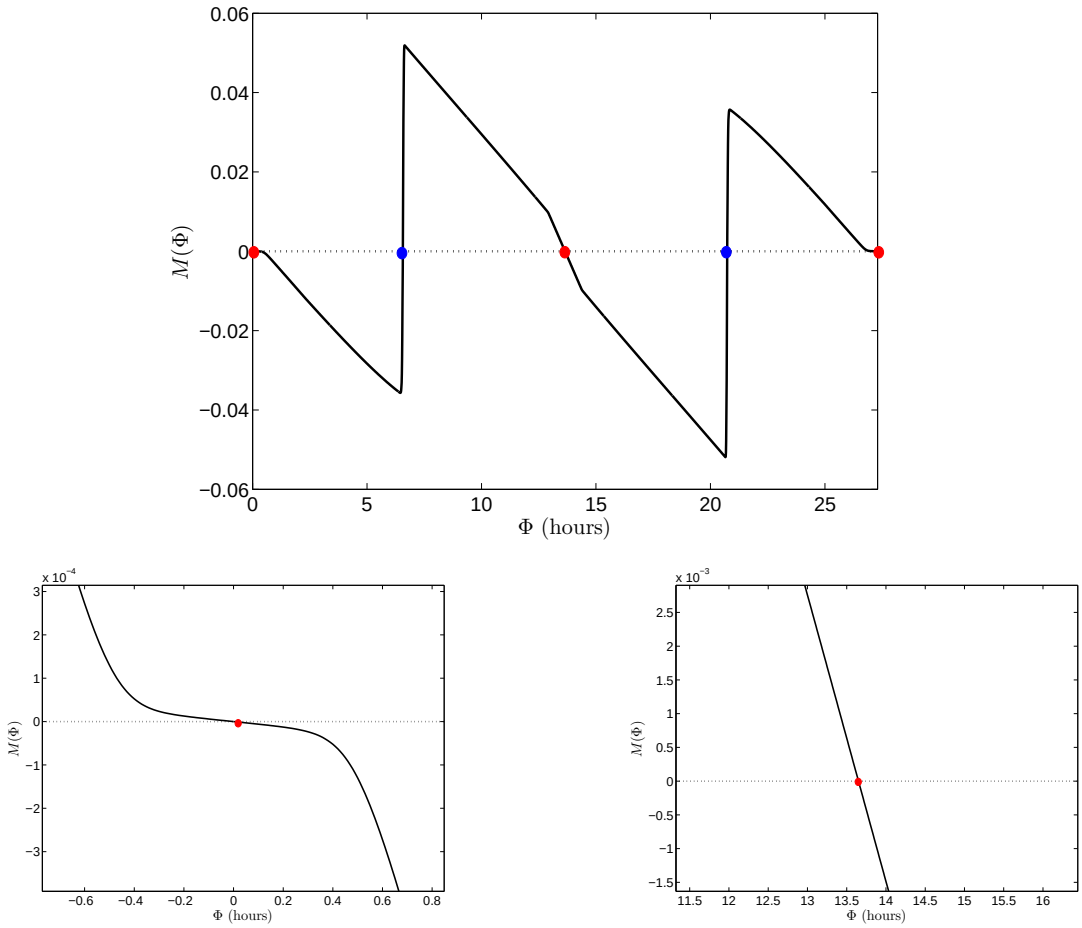

Figure 2.14: Plot of $M(\Phi)$ for the system (2.1)-(2.6), (2.12)-(2.18), (2.22) for Cyclin D dependent ATP release ($(H_i, H_c) = (D_i, D_c)$). Intersections with the x axis are indicated by coloured dots. Red dots relate to stable phase locked solutions and blue to unstable phase locked solutions as predicted by the theory of weakly coupled oscillators. Under this parameter regime, the theory predicts that the synchronous solution and anti-phase phase locked solutions are stable. $M(\Phi)$ was calculated using XPP. Parameter values given in Table 2.2, except for $V_{deg} = 0.01\ \mu\text{Ms}^{-1}$.

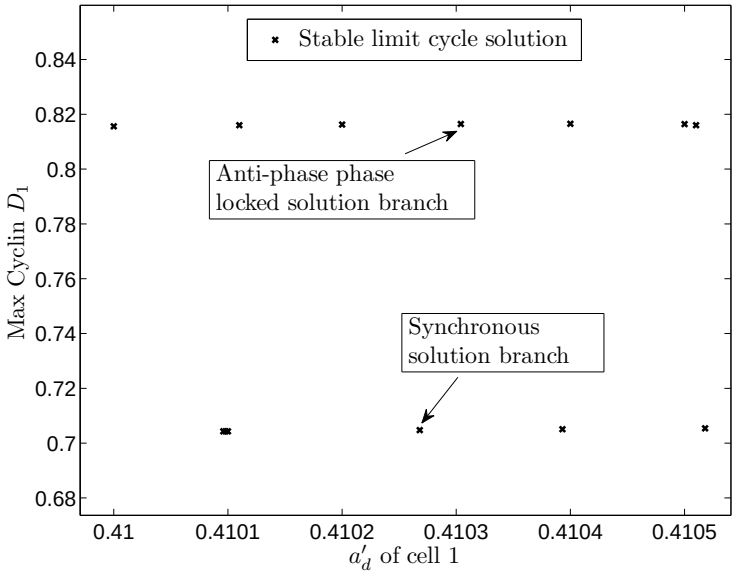

Figure 2.15: Bifurcation diagram of system (2.1)-(2.6), (2.12)-(2.18), (2.22) for two cells for Cyclin D dependent ATP release ($(H_i, H_c) = (D_i, D_c)$). Parameter values as for Table 2.2, except for $V_{deg} = 0.01\,\mu\text{Ms}^{-1}$ and a'_d of cell 1, which is as shown and a'_d of cell 2 which is 0.41. Diagram produced using AUTO within XPP. The diagram confirms the existence of a stable synchronous solution and stable anti-phase phase locked solution.

the analysis. Interestingly, in this case the coupling leads to a small reduction in the period of the cell cycle of both cells. This can be seen from Figure 2.17 by comparing the dynamics of two coupled cells to those of a single cell under the same parameter regime. The coupling reduces the period of oscillation from 27.3 to 26.9 hours, which is brought about by an increase in extracellular ATP and consequently a greater increase in the Cyclin D synthesis rate than would be the case if the cells were uncoupled. This increase in ATP can be seen by comparing the extracellular ATP dynamics for the coupled case against the extracellular ATP dynamics of an uncoupled cell in Figure 2.17. There is no such increase in the frequency of the coupled oscillators in the synchronous case, since synchronous oscillations are identical to those without coupling.

As mentioned above, the theory of weakly coupled oscillators tells us that, if $\epsilon \ll 1$ then the system can be reduced to a phase model. The condition $\epsilon \ll 1$ ensures that amplitude effects are negligible. In reality, the predictions from this reduction are valid, at least qualitatively, for larger vales of the coupling strength ϵ, where the condition $\epsilon \ll 1$ is not strictly satisfied (see [39, 53] for a discussion), although there is no *a priori* method to assess whether this is true for any given system. In the anti-phase phase locked solution shown in Figure 2.17, the coupling is so strong that it has brought amplitude effects into the oscillations. In fact these amplitude effects are responsible for the reduction in the period of the cell cycle. From Section 2.6, it is clear that our definition of phase, which is used in the theory of weakly coupled oscillators, is dependent upon the limit cycle of a single uncoupled cell. However, as the coupling has introduced amplitude effects into the system in Figure 2.17, this definition is not valid. When this is the case we use a definition of phase first proposed by Golomb and Rinzel [31] (discussed in more detail in Section 3.4 of chapter 3) and take the difference in the times the two cells' Cyclin D concentrations peak to give us the phase difference. This definition is consistent with the definition of phase used in the theory of weakly coupled oscillators when amplitude effects are not introduced, as for all synchronous solutions for example. Even though, strictly speaking, the theory is not valid in Figure 2.17 because of the amplitude effects introduced by the strong coupling, it was still able to correctly predict the existence and stability of the anti-phase phase locked solutions and in such cases it can act as a useful predictive tool.

Different parameter regimes lead to different profiles for $M(\Phi)$ and in some cases to a loss of stability of the synchronous solution. Although our analysis suggests that the syn-

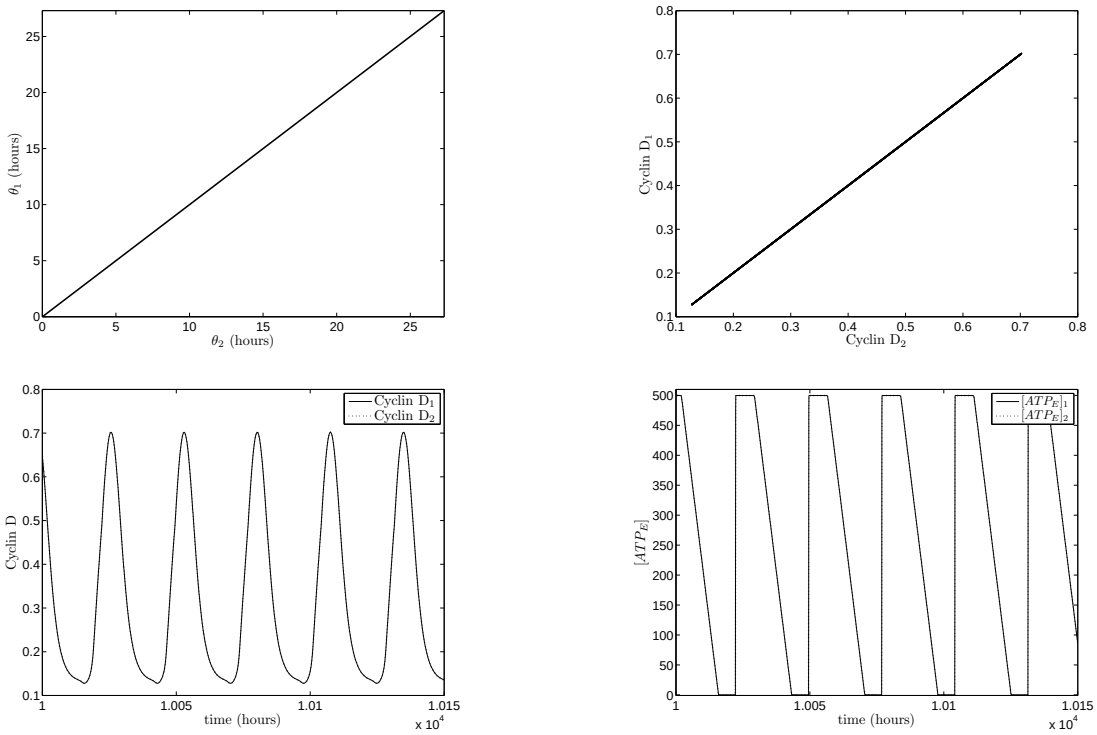

Figure 2.16: Simulation of system (2.1)-(2.6), (2.12)-(2.18), (2.22) for the Cyclin D dependent ATP release model ($(H_i, H_c) = (D_i, D_c)$) for one and two cells. The results were calculated using `Stiff` within XPP and show that for a small initial phase difference the solution trajectory tends towards a stable synchronous solution. In the simulations of the two cell system, the initial phase difference between the two cells was 4.5 hours (based on the phase of a single uncoupled cell). Initial conditions: $D_1(0) = 0.6010899$, $D_2(0) = 0.6047926$, $E_1(0) = 0.1775467$, $E_2(0) = 0.8364856$, $R_1(0) = 0.9056494$, $R_2(0) = 0.5939475$, $R_{s1}(0) = 1.253212$, $R_{s2}(0) = 1.110384$, $X_1(0) = 3.161909$, $X_2(0) = 0.1884256$, $[IP_3]_1(0) = 0.945814$ μM, $[IP_3]_2(0) = 0.945814$ μM, $[ATP_E]_1(0) = 499.733$ μM, $[ATP_E]_2(0) = 499.733$ μM, $[ATP_I]_1(0) = 499.8795$ μM, $[ATP_I]_2(0) = 499.8795$ μM. Transients not shown. Parameter values given in Table 2.2, except for $V_{deg} = 0.01$ μMs^{-1}.

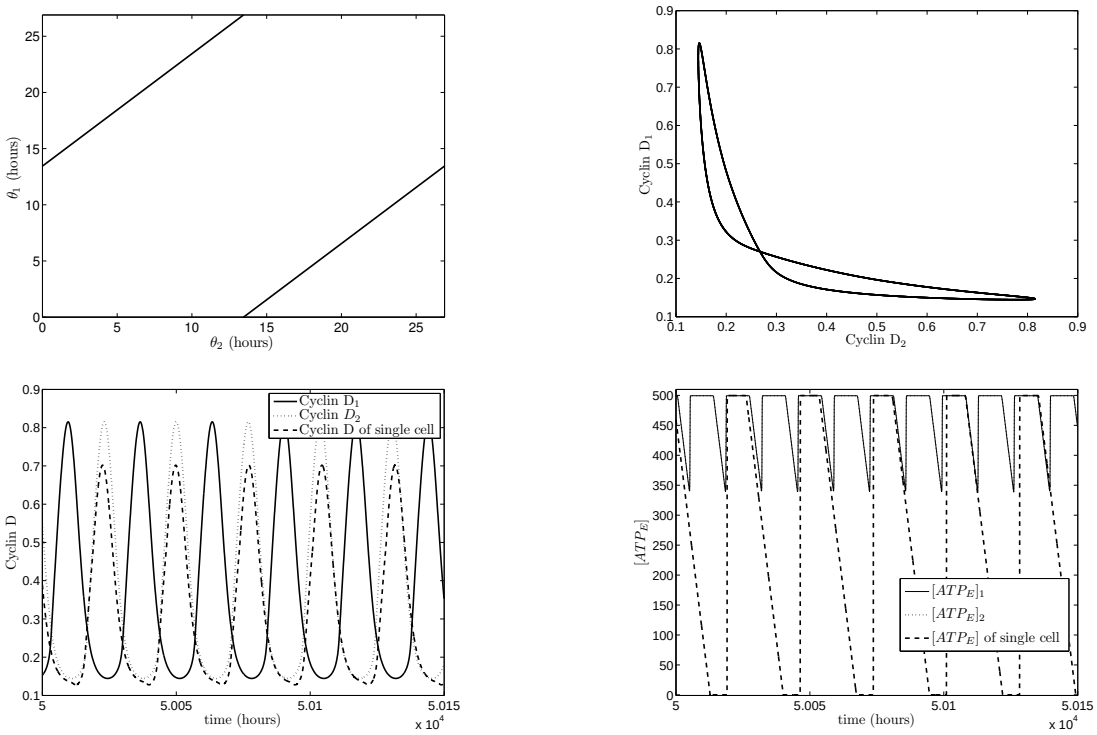

Figure 2.17: Simulation of system (2.1)-(2.6), (2.12)-(2.18), (2.22) for the Cyclin D dependent ATP release model ($(H_i, H_c) = (D_i, D_c)$) for one and two cells. The results which were calculated using `Stiff` within XPP show that if the initial phase difference between two cells is large then the system settles down to a stable anti-phase phase locked solution. In the simulations of the two cell system, the initial phase difference between the two cells was 8.5 hours (based on the phase of a single uncoupled cell). Initial conditions: $D_1(0) = 0.6010899$, $D_2(0) = 0.2920837$, $E_1(0) = 0.1775467$, $E_2(0) = 1.550719$, $R_1(0) = 0.9056494$, $R_2(0) = 0.315571$, $R_{s1}(0) = 1.253212$, $R_{s2}(0) = 0.9876701$, $X_1(0) = 3.161909$, $X_2(0) = 0.2330289$, $[IP_3]_1(0) = 0.945814$ μM, $[IP_3]_2(0) = 0.9367997$ μM, $[ATP_E]_1(0) = 499.733$ μM, $[ATP_E]_2(0) = 407.1908$ μM, $[ATP_I]_1(0) = 499.8795$ μM, $[ATP_I]_2(0) = 500$ μM. Parameter values given in Table 2.2, except for $V_{deg} = 0.01$ μMs^{-1}. Transients not shown.

chronous state is stable for low values of the calcium coupling strength γ, high values of γ, coupled with high values for the external ATP degradation rate V_{deg}, render this state unstable according to our analysis. The plot of $M(\Phi)$ for such a parameter regime be can seen in Figure 2.18. There now exist 6 steady states at $\Phi = 0$, 0.35451, 7.8583, 13.41, 18.9617 and 26.4655. Interestingly, however the synchronous state is now unstable, as indicated by the positive slope at $\Phi = 0$. As before the anti-phase phase locked state remains stable. Our bifurcation analysis, the results of which are shown in Figure 2.19, confirm that for large values of γ and V_{deg} the synchronous state becomes unstable.

Figure 2.19 reveals that the lower branch of limit cycle solutions (this is the branch of synchronous solutions) is lost via a bifurcation point at $\gamma \approx 1.065856$, while a higher branch of limit cycle solutions (the anti-phase phase locked state) persists. Unfortunately, our attempts at continuing the solution from this bifurcation point using AUTO were unsuccessful. It was unclear to us as to precisely why AUTO failed in this regard. However, if we directly simulate the system from the unstable limit cycle solutions for a value of $\gamma = 1.2$ near the bifurcation point with slightly perturbed initial conditions, the system evolves to the branch of stable anti-phase phase locked solutions (Figure 2.20). This coupled with the fact that the theory of weakly coupled oscillators predicted the existence of a stable asynchronous solution for large values of V_{deg} and γ, suggests that the bifurcation point shown in the figure is likely to be a supercritical pitchfork bifurcation point of limit cycles (the limit cycle analogue of the local pitchfork bifurcation). We were unable to find the stable asynchronous state predicted by the analysis. This does not necessarily mean that it does not exist however, as it may exist on a branch of solutions independent of those shown in Figure 2.19. Finding this state through direct numerical simulation would be akin to finding a needle in a haystack however. Simulations of the system for two cells under the parameter regime of Figure 2.19 are shown in Figure 2.20 below.

It can be seen from Figure 2.20 that the system settles down to an anti-phase phase locked state when it is initialised from a perturbed synchronous state, indicating that the synchronous phase locked solution is unstable, as predicted by the analysis. As before the coupling in the anti-phase state reduces the period of oscillation. In this case from 27.02 to 24.85 hours. Again this is ultimately due to the greater concentration of extracellular ATP in the anti-phase state, as can be seen by comparing the ATP profile of the coupled case to the uncoupled case in this figure.

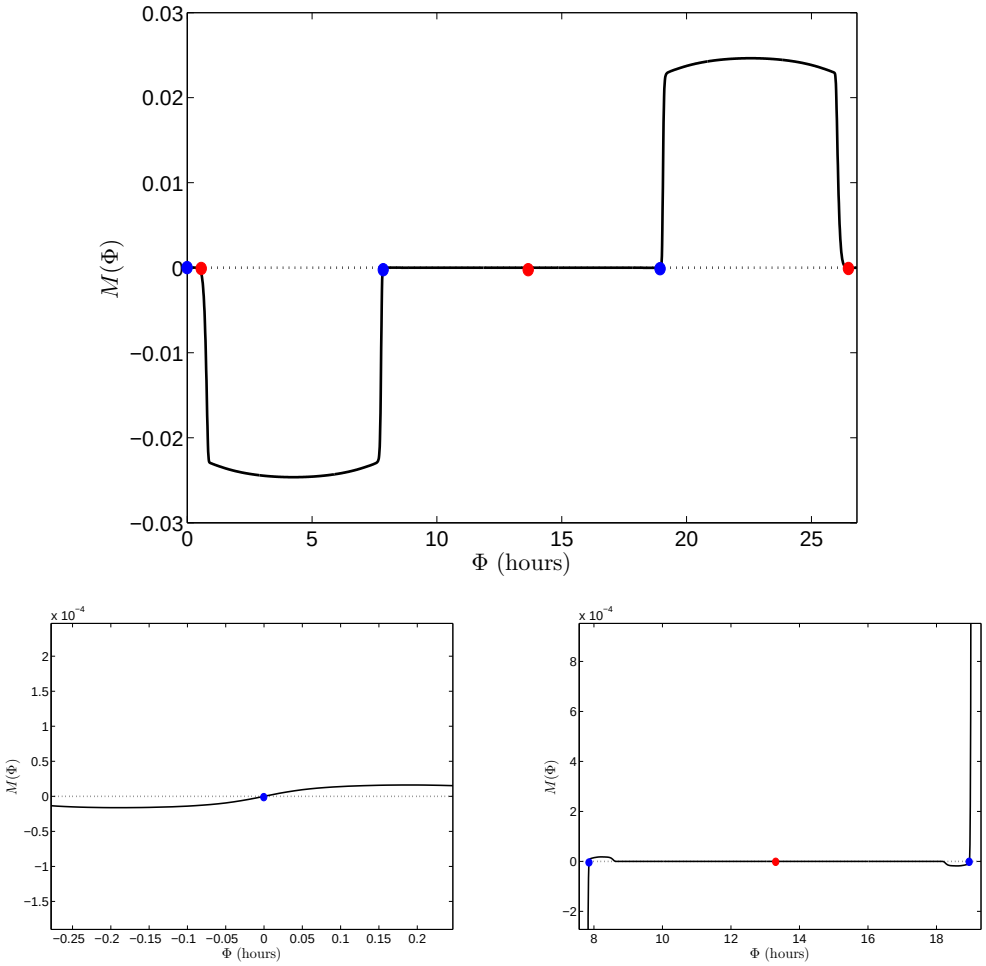

Figure 2.18: Plot of $M(\Phi)$ for the system (2.1)-(2.6), (2.12)-(2.18), (2.22). In this case, the theory of weakly coupled oscillators predicts that the synchronous solution is unstable. This is in contrast to Figure 2.14, where the theory predicted that the synchronous solution was stable. The theory also predicts that the anti-phase phase locked solution and asynchronous solution are stable. $M(\Phi)$ was calculated using XPP. Parameter values given in Table 2.2 except for $V_{deg} = 2\,\mu\text{Ms}^{-1}$ and $\gamma = 1.2$.

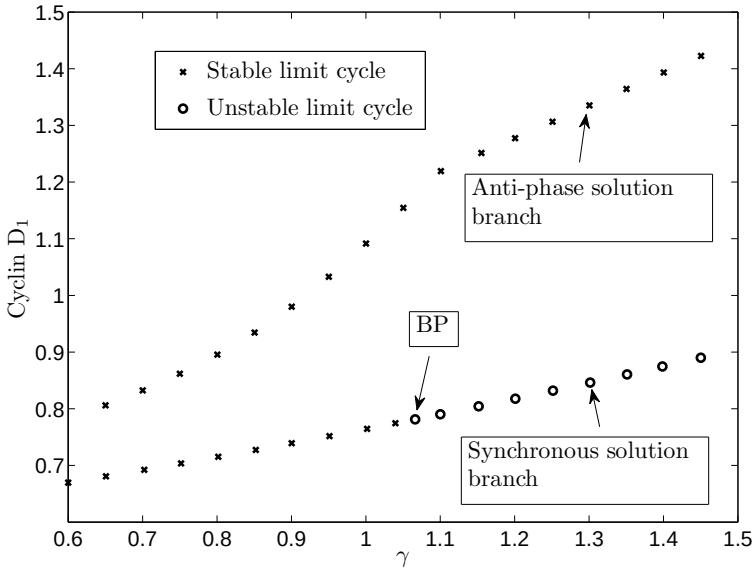

Figure 2.19: Bifurcation diagram of system (2.1)-(2.6), (2.12)-(2.18), (2.22) for two cells. The diagram reveals that the synchronous solution branch loses stability at a bifurcation point for larger values of γ while the anti-phase phase locked branch remains stable, as predicted by the theory of weakly coupled oscillators. Parameter values as for Table 2.2, except for $V_{deg} = 2\ \mu\text{Ms}^{-1}$ and γ which is as shown. Key: BP corresponds to bifurcation point. Diagram produced using AUTO within XPP.

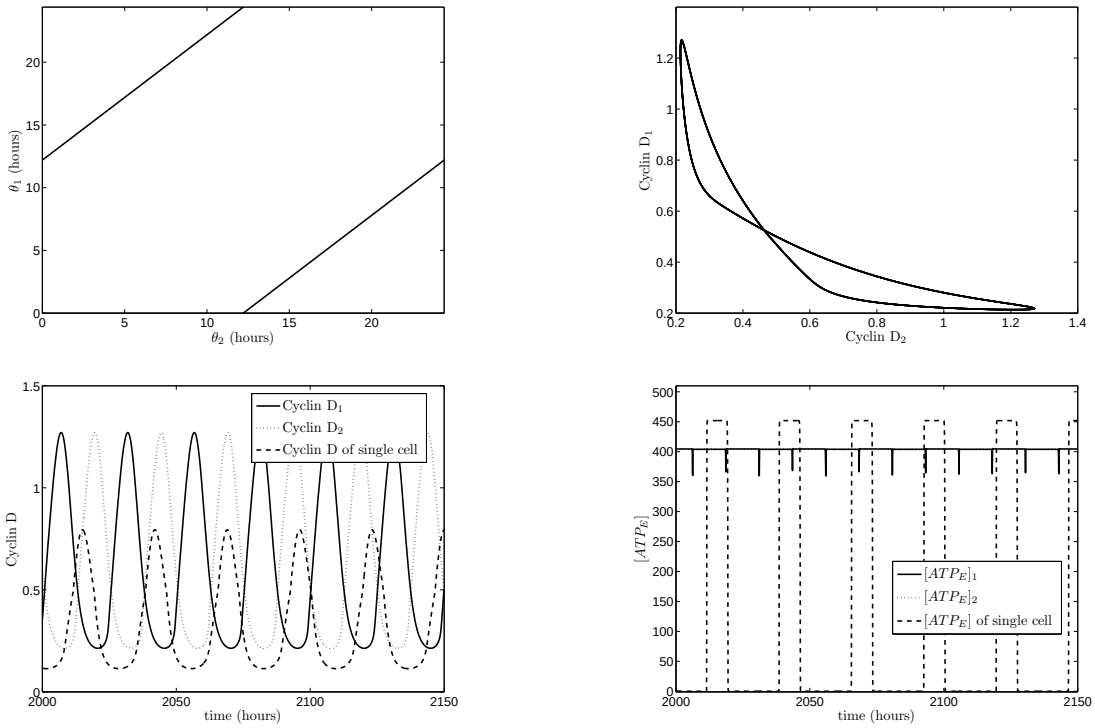

Figure 2.20: Simulation of system (2.1)-(2.6), (2.12)-(2.18), (2.22) for one and two cells. The simulations confirm that the synchronous state is unstable under this parameter regime and the system evolves to the stable anti-phase phase locked solution. Calculated using `Stiff` within XPP. Initial conditions were such that the system was slightly perturbed from the synchronous state ($\approx \pm 0.001$) and are given by: $D_1(0) = 1.010007$, $D_2(0) = 1.011007$, $E_1(0) = 0.7302775$, $E_2(0) = 0.7292775$, $R_1(0) = 0.6201518$, $R_2(0) = 0.6211518$, $R_{s1}(0) = 1.049325$, $R_{s2}(0) = 1.038325$, $X_1(0) = 0.2490771$, $X_2(0) = 0.2480771$, $[IP_3]_1(0) = 0.9436596\ \mu$M, $[IP_3]_2(0) = 0.9446596\ \mu$M, $[ATP_E]_1(0) = 474.2088\ \mu$M, $[ATP_E]_2(0) = 474.2078\ \mu$M, $[ATP_I]_1(0) = 474.702\ \mu$M, $[ATP_I]_2(0) = 474.7031\ \mu$M. Parameter values given in Table 2.2 except for $V_{deg} = 2\,\mu\text{Ms}^{-1}$ and $\gamma = 1.2$. Transients not shown.

2.7.2 R_s Dependent ATP Release

We next investigated the existence and stability of phase locked solutions for the R_s dependent ATP release case. Like the Cyclin D dependent case, there exist multiple phase locked solutions. Indeed, as in the Cyclin D case, the stability of the synchronous solutions can be lost under certain parameter regimes. A plot of $M(\Phi)$ under a parameter regime that leads to stable synchronous solutions is shown in Figure 2.21

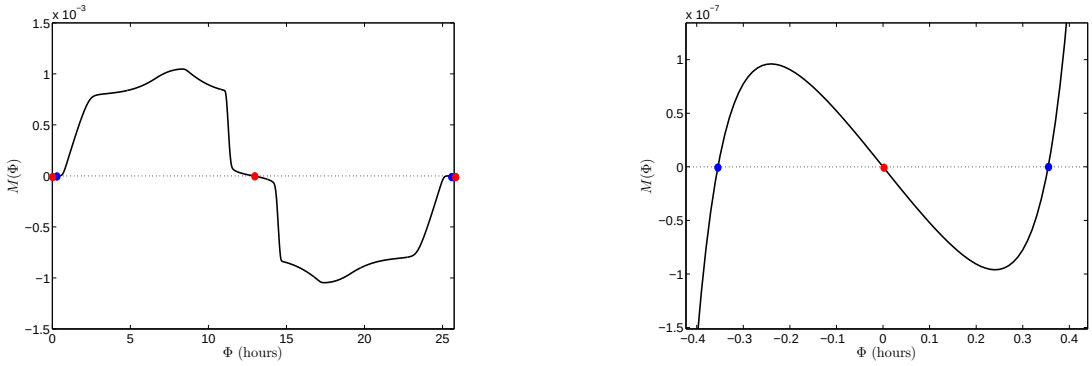

Figure 2.21: Plot of $M(\Phi)$ for the system (2.1)-(2.6), (2.12)-(2.18), (2.22) for a single cell, with $(H_i, H_c) = (R_{sc}, R_{si})$. Intersections with the x axis are indicated by coloured dots. Red dots relate to stable phase locked solutions and blue to unstable phase locked solutions as predicted by the theory of weakly coupled oscillators. Under this parameter regime, the theory of weakly coupled oscillators predicts that the stable and anti-phase phase locked solutions are stable. $M(\Phi)$ was calculated using XPP. Parameter values given in Table 2.2 except for $V_{deg} = 0.1\ \mu\text{Ms}^{-1}$ and $\gamma = 1.4$.

From Figure 2.21, it can be seen that the weakly coupled oscillator theory predicts 4 phase locked solutions at $\Phi = 0, 0.3545, 12.87$ and 25.386. The synchronous solution and anti-phase phase locked solution (corresponding to $\Phi = 12.87$) are stable, while the two asynchronous solutions are unstable. As mentioned above, the synchronous solution is rendered unstable under certain parameter regimes. The plot of $M(\Phi)$ under one such regime is shown in Figure 2.22.

From Figure 2.22 our analysis predicts four phase locked solutions at $\Phi = 0, 5.8379, 12.62$ and 19.4201. The two asynchronous solutions, corresponding to $\Phi = 5.8379$ and 19.4201 are stable with all other solutions including the synchronous solution being unstable. In

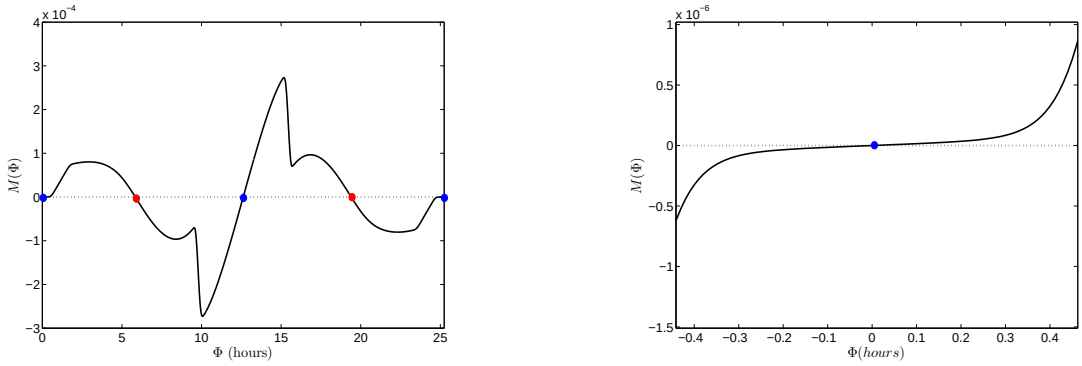

Figure 2.22: Plot of $M(\Phi)$ for the system (2.1)-(2.6), (2.12)-(2.18), (2.22) and (2.22) for a single cell, with $(H_i, H_c) = (R_{sc}, R_{si})$. The theory of weakly coupled oscillators predicts that the synchronous solution is unstable in this case. $M(\Phi)$ was calculated using XPP. Parameter values given in Table 2.2 except for $V_{deg} = 0.04\,\mu\text{Ms}^{-1}$ and $\gamma = 1.4$.

fact the two asynchronous solutions are the same solution, since 19.4201=T-5.8379, where T=25.24 hours, the period of oscillation. This is always the case since

$$\begin{aligned} M(\Phi) =& L(-\Phi) - L(\Phi) \\ =& L(T-\Phi) - L(\Phi - T) \\ =& L(T-\Phi) - L(-T+\Phi) \\ =& -\left(L(-T+\Phi) - L(T-\Phi)\right) \\ =& -M(T-\Phi); \end{aligned}$$

and it follows that

$$M'(\Phi) = -M'(T-\Phi)\cdot -1 = M'(T-\Phi),$$

so that if a solution is stable at $\Phi = \Phi^*$, it will be stable at $\Phi = T - \Phi^*$.

As before, we conducted bifurcation analysis on the system to confirm the predictions of the weakly coupled oscillator theory. The results of this analysis are shown in Figure 2.23.

In Figure 2.23 we use V_{deg} as the control parameter, while for the Cyclin D dependent ATP release model, we used γ. We change the control parameter here in order to demonstrate that the R_s dependent ATP release model can exhibit the same interesting behaviour we saw when studying the Cyclin D dependent model in the previous section. From Figure

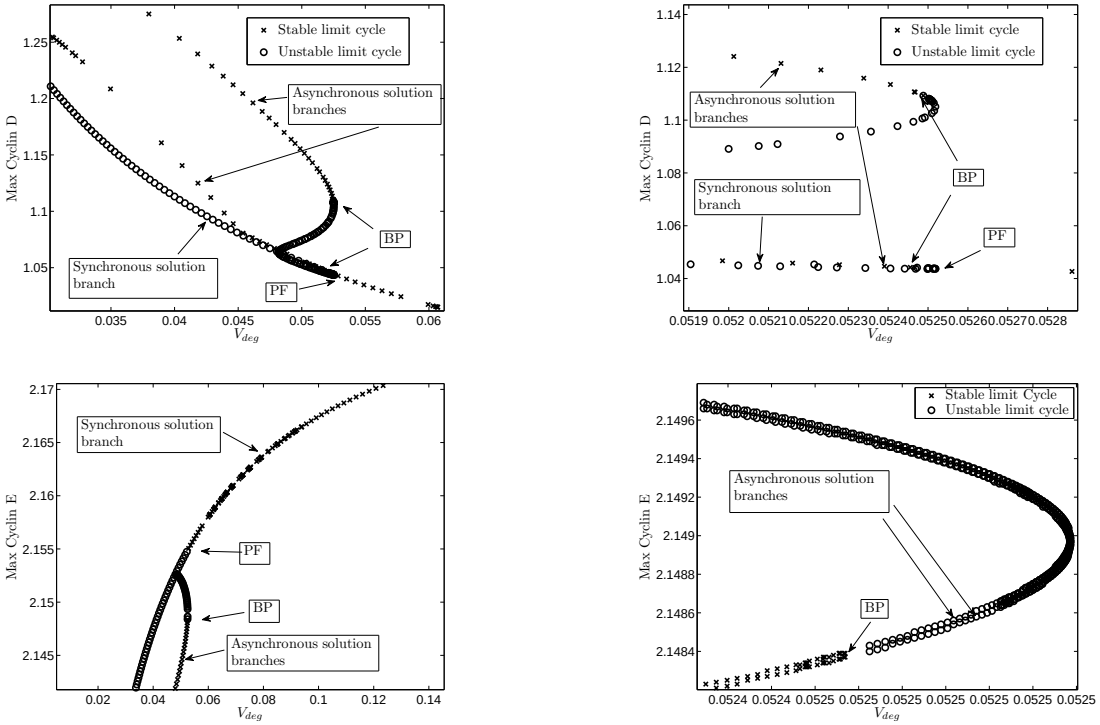

Figure 2.23: Bifurcation diagram of system (2.1)-(2.6), (2.12)-(2.18), (2.22) for two cells with $(H_i, H_c) = (R_{sc}, R_{si})$. The right hand plots correspond to zoomed in sections of the left hand plots. The diagram shows that for a sufficiently small value for V_{deg} the stability of the synchronous branch of solutions is lost, illustrating that as for the Cyclin D dependent model, the R_s dependent model can exhibit asynchronous behaviour. Parameter values as for Table 2.2, except for $\gamma = 1.4$ and V_{deg} which is as shown. BP corresponds to bifurcation point, PF to a pitchfork bifurcation. Diagram produced using AUTO within XPP.

2.23 it can be seen that as V_{deg} is reduced the stability of the limit cycle solution which corresponds to the branch of synchronous solutions is lost at $V_{deg} \approx 0.0525$ via a pitchfork bifurcation of limit cycles. The two branches that emanate from the pitchfork bifurcation point correspond to the two possible stable solutions that each cell will evolve to when the cells are phase locked in an asynchronous manner. These asynchronous solutions are initially unstable but become stable at a bifurcation point at $V_{deg} \approx 0.0525$. For $V_{deg} < 0.0525$, which cell ends up on which solution branch will depend upon the initial conditions of the system.

Simulating the system from a perturbed synchronous state for two cells under the two different parameter regimes considered above shows how the stability of the synchronous state is lost, as predicted by our analysis. The results of these simulations are shown in Figures 2.24 and 2.25. Figure 2.24 shows that for certain parameters the system evolves to the synchronous state when initialised from the perturbed synchronous state, as predicted by the analysis. The period of the two cells in this case is the same as in the single cell case, i.e. 25.74 hours, as one would expect, as in the synchronous case the cells behave as if uncoupled.

The qualitative conclusions of our analysis are further confirmed by simulations of the system. Figure 2.25 shows an example where a small perturbation of the synchronous state evolves to an asynchronous state with a phase difference of 3.49 hours, which differs from the 5.8379 predicted by the analysis, providing further confirmation that for stronger coupling, the theory of weakly coupled oscillators holds only qualitatively. There is a slight reduction in the period of oscillation in the asynchronous case. The spatial coupling brings about a reduction period of oscillation from 25.24 hours to 24.92 hours over and above the reduction brought about by the internal calcium coupling of the cell. Interestingly, in the stable asynchronous case the two cells do not evolve to identical oscillatory solutions, although the period of oscillation of both are the same (e.g. in Figure 2.25 the maximum Cyclin D concentration of cell 1 is higher than that of cell 2). In Figure 2.25, the initial conditions of the system were such that cell 1 evolved onto the upper branch of limit cycle solutions seen in the top left hand plot in Figure 2.23, while cell 2 evolved to the lower branch of limit cycle solutions seen in the same figure. The fact that these two solutions are not identical is not a surprising result, since perturbing the cell cycle at different phases will result in the cycle being retarded or accelerated at different rates. Indeed the fact that the plot of the Cyclin D component of the response function shown in figure in 2.13 is not

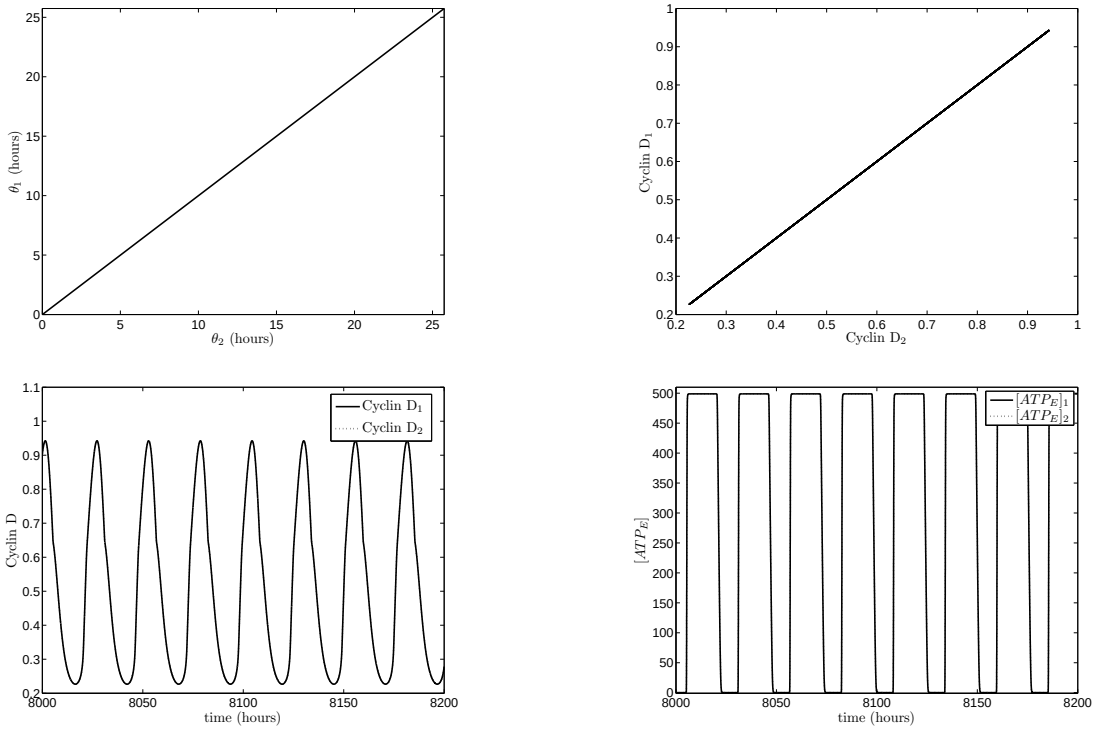

Figure 2.24: Simulation of system (2.1)-(2.6), (2.12)-(2.18), (2.22) for one and two cells with $(H_i, H_c) = (R_{sc}, R_{si})$. Calculated using `Stiff` within XPP. The results show that the system initialised from a state that is slightly perturbed from the synchronous state evolves to the stable synchronous solution. Initial conditions given by are given by: $D_1(0) = 0.9379$, $D_2(0) = 0.9389$, $E_1(0) = 0.2122$, $E_2(0) = 0.2132$, $R_1(0) = 0.8804$, $R_2(0) = 0.8814$, $R_{s1}(0) = 1.1453$, $R_{s2}(0) = 1.1463$, $X_1(0) = 1.1453$, $X_2(0) = 1.1463$, $[IP_3]_1(0) = 0.013\ \mu M$, $[IP_3]_2(0) = 0.013\ \mu$M, $[ATP_E]_1(0) = 0\ \mu$M, $[ATP_E]_2(0) = 0\ \mu$M, $[ATP_I]_1(0) = 500\ \mu$M, $[ATP_I]_2(0) = 500\ \mu$M. Parameter values given in Table 2.2 except for $V_{deg} = 0.1\ \mu\text{Ms}^{-1}$ and $\gamma = 1.4$. Transients not shown.

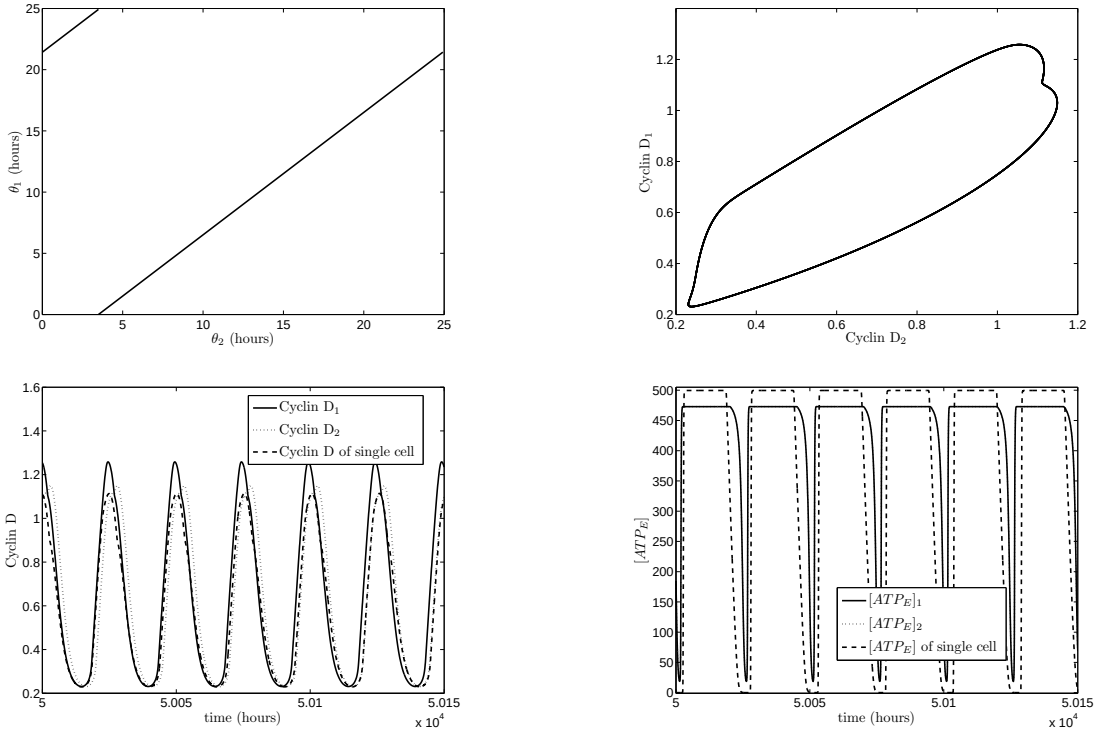

Figure 2.25: Simulation of system (2.1)-(2.6), (2.12)-(2.18), (2.22) for one and two cells with $(H_i, H_c) = (R_{sc}, R_{si})$. Calculated using `Stiff` within XPP. The simulations show that the system, which is initialised from a state very close to the synchronous solution diverges from this solution and tends towards a stable asynchronous solution. Initial conditions given by: $D_1(0) = 1.1113$, $D_2(0) = 1.1114$, $E_1(0) = 0.2518$, $E_2(0) = 0.2519$, $R_1(0) = 0.8581$, $R_2(0) = 0.8582$, $R_{s1}(0) = 1.1027$, $R_{s2}(0) = 1.1028$, $X_1(0) = 2.2066$, $X_2(0) = 2.2067$, $[IP_3]_1(0) = 0.0170\,\mu$M, $[IP_3]_2(0) = 0.0171\,\mu$M, $[ATP_E]_1(0) = 45.75\,\mu$M, $[ATP_E]_2(0) = 45.76\,\mu$M, $[ATP_I]_1(0) = 500\ \mu$M, $[ATP_I]_2(0) = 500.001\ \mu$M. Parameter values given in Table 2.2 except for $V_{deg} = 0.04\,\mu\text{Ms}^{-1}$ and $\gamma = 1.4$. Transients not shown.

a straight line illustrates this fact well.

This final observation provides us with the reason why the theory of weakly coupled oscillators failed to correctly predict the phase difference for the stable asynchronous solution, even though it successfully predicted the existence and stability of this solution. The condition on the coupling strength $\epsilon \ll 1$ ensures that amplitude effects caused by the coupling can be neglected when reducing the system to a phase model [25, 39]. Indeed, if one refers to equation (2.30), one can see that the interaction function is calculated by averaging the effect of the coupling and response function over the period of oscillation of a single uncoupled oscillator. It is clear from Figure 2.25 that the coupling in this case leads to amplitude effects in both oscillators. It is important to note that the theory of weakly coupled oscillators is more robust at predicting the stability of the synchronous solution for stronger coupling. This is because by definition the period and indeed limit cycles of two oscillators cycling in a synchronous manner will remain invariant when the system is uncoupled, i.e. no matter what the strength, the coupling will not bring about amplitude effects in the oscillators in the synchronous state. For this reason, the theory of weakly coupled oscillators will be far better at successfully predicting the stability and existence of synchronous solutions than it is at all other phase locked solutions. Nevertheless, the fact that we have encountered this quantitative limitation of the theory for the system should act as a cautionary tale when considering asynchronous phase locked solutions of systems of several cells. These issues are discussed in [39, 53].

2.8 Conclusions and Further work

In this chapter we have introduced a model for the coupling of calcium to the cell cycle dynamics of a radial glial cell which captures many of the qualitative characteristics displayed by radial glial cells, such as ATP induced calcium signalling facilitated via the opening of a cell's hemichannels during a point in the cell cycle. Bifurcation analysis of a single cell model reveals an area of multistability for our Cyclin D dependent ATP release model and an area of bistability in our R_s dependent ATP release model.

Using a phase averaging technique, bifurcation analysis and direct simulation we have shown how the existence and stability of phase locked solutions for two cells depends not

only upon different parameter regimes but also upon the timing of the release of ATP during the cell cycle. We have shown that, although stable synchronous solutions exist for both of our models, their stability is lost under certain parameter regimes. This may seem like a counter intuitive result, especially if one is familiar with the story of the physicist Christian Huygens discovering that two clocks connected by a supporting beam synchronise as a result of the passing of vibrations from one clock to the other along the beam. However, it is perhaps illuminating to note that there are a number of examples in the literature of coupling between oscillators, which takes the same or similar form to the coupling in our system, leading to unusual behaviour. Ermentrout and Kopell showed that under certain circumstances excitatory coupling between oscillators can lead to oscillator death [24]. There is also an example of diffusive coupling between oscillators leading the system to display chaotic behaviour [71]. The fact that two oscillators in the system do not always synchronise is not therefore surprising. These results suggest that, for two cells at least ATP mediated coupling can lead to the phase locking of cells in a synchronous manner, as hypothesised by Weissman *et al* [93]. However, our results also suggest that the stability of this synchronous state will be highly dependent upon the strength of the calcium coupling as well as the rate of extra-cellular ATP degradation. This will need to investigated further by considering systems of several cells under different parameter regimes.

According to Weissman *et al* [93] the introduction of an ATP receptor agonist over a period of an hour brought about a decrease in the proportion of proliferating radial glial cells to 54.7 % of control. This could be due to a decrease in the speed with which cells cycle or a decrease in the number of cells cycling. ATP induced calcium signals in our simulations, where both cells are initially oscillating, can not account for this decrease. However bifurcation analysis of single cell systems revealed an area of multistability in the Cyclin D dependent ATP release model and an area of bistability in the R_s dependent ATP release model. These areas could reflect the recruitment of quiescent cells by driving cells via ATP mediated calcium waves, which could in turn account for the normal proportion of proliferating cells seen in the literature. This is something we explore in chapters 4 and 5.

Chapter 3

Existence and Stability of Phase Locked Solutions in Several Coupled Cells

3.1 Introduction

In this chapter we build upon work in the previous chapter concerning the phase locked behaviour of 2 cells by investigating the existence and stability of phase locked solutions for several cells in 1 and 2 spatial dimensions. We begin by outlining how the theory of weakly coupled oscillators can be applied to systems of more than two coupled cells. We then use the theory to make predictions about the existence and stability of phase locked solutions for several cells in one and two spatial dimensions for both our models under certain parameter regimes. We then discuss 'synchrony' measures with a view to applying a suitable measure to simulations of large systems of cells in order to characterise the degree to which the cells within these systems are synchronised. Through direct numerical simulation of both models under different parameter regimes we attempt to confirm the findings of our analysis and also investigate the degree to which the cells in each model synchronise under these different parameter regimes.

Let us first remind ourselves of the system of ODEs governing the coupling between the calcium dynamics and cell cycle dynamics of a cluster of radial glial cells

$$\frac{dD_i}{dt} = a_{di}\left(\frac{kGF}{1+kGF}\right) - d_D E_i D_i, \tag{3.1}$$

$$\frac{dE_i}{dt} = a_E(1 + a_f(\ominus - R_{si})) - d_E X_i E_i, \tag{3.2}$$

$$\frac{dR_i}{dt} = \frac{p_X(R_T - R_{si} - R_i)X_i}{q_X + (R_T - R_{si} - R_i) + X_i} - p_s(\ominus - R_{si})R_i, \tag{3.3}$$

$$\frac{dR_{si}}{dt} = p_s(\ominus - R_{si})R_i - \frac{p_D R_{si} D_i}{q_D + R_{si} + d} - \frac{p_E R_{si} E_i}{q_E + R_{si} + E_i}, \tag{3.4}$$

$$\frac{dX_i}{dt} = a_X E_i + f(\ominus - R_{si}) + gX_i^2 E_i - d_X X_i, \tag{3.5}$$

$$a_{di} = a'_d + \gamma([Ca^{2+}]_i - [Ca^{2+}]_b), \tag{3.6}$$

$$[Ca^{2+}]_i = p1 + \frac{p2[IP_3]_i^m}{p3^m + [IP_3]_i^m} + \frac{p4[IP_3]_i^n}{p5^n + [IP_3]_i^n}, \tag{3.7}$$

$$\rho_i = \frac{[ATP_E]_i}{K_R + [ATP_E]_i}, \tag{3.8}$$

$$\delta = \frac{K_G[IP_3]_{min}K_{deg}}{r_h^* - [IP_3]_{min}K_{deg}}, \tag{3.9}$$

$$G_i^* = \frac{\rho_i + \delta}{K_G + \rho_i + \delta}, \tag{3.10}$$

$$\frac{d[IP_3]_i}{dt} = t_s(r_h^* G_i^* - k_{deg}[IP_3]_i), \tag{3.11}$$

$$\begin{aligned}\frac{d[ATP_I]_i}{dt} = t_s\Bigg(&\alpha([ATP_I]_{max} - [ATP_I]_i) \\ &- T(H_i, H_c, \varrho)T([IP_3]_i, [IP_3]_c, \varrho)V_{ATP}([ATP_I]_i - [ATP_E]_i)\left(\frac{[IP_3]_i - [IP_3]_{min}}{K_{rel} + [IP_3]_i}\right)\Bigg),\end{aligned} \tag{3.12}$$

$$\begin{aligned}\frac{d[ATP_E]_i}{dt} = t_s\Bigg(&D_{ATP}L_D \\ &+ T(H_i, H_c, \varrho)T([IP_3]_i, [IP_3]_c, \varrho)V_{ATP}([ATP_I]_i - [ATP_E]_i)\frac{[IP_3]_i - [IP_3]_{min}}{K_{rel} + [IP_3]_i} \\ &- V_{deg}\frac{[ATP_E]_i}{K_{deg} + [ATP_E]_i}\Bigg),\end{aligned} \tag{3.13}$$

$$T(H_i, H_c, \varrho) = \frac{1}{2}\left(\tanh\left(\frac{H_i - H_c}{\varrho}\right) + 1\right). \tag{3.14}$$

We index variables by i in the one dimensional case and i, j in two spatial dimensions. L_D in equation (3.13) provides the spatial component of the system and in one spatial

dimension

$$L_D = \frac{[ATP_E]_{i-1} - 2[ATP_E]_i + [ATP_E]_{i+1}}{\Delta x^2}. \tag{3.15}$$

In two spatial dimensions

$$L_D = \frac{[ATP_E]_{i,j-1} + [ATP_E]_{i-1,j} - 4[ATP_E]_{i,j} + [ATP_E]_{i+1,j} + [ATP_E]_{i,j+1}}{\Delta x^2}. \tag{3.16}$$

As before, we adopt zero-flux boundary conditions, such that in one spatial dimension

$$[ATP_E]_{i-1} = [ATP_E]_{i+1} \text{ at } i = 1, l, \tag{3.17}$$

and in two spatial dimensions

$$[ATP_E]_{i-1,j} = [ATP_E]_{i+1,j} \text{ at } i = 1, m,$$
$$[ATP_E]_{i,j-1} = [ATP_E]_{i,j+1} \text{ at } j = 1, n,$$

where l is the total number of cells in the 1D case, m is the width of the 2D array (in number of cells) and n the height.

3.2 Weak Coupling Theory Applied to Regular Arrays of Oscillators

As mentioned in the previous chapter, computational limitations make it difficult to extend our bifurcation analysis to systems of several cells, yet we can extend our weakly coupled oscillator theory analysis to systems of several cells relatively easily. Let us firstly remind ourselves briefly of the weakly coupled oscillator theory that we introduced in the previous chapter. The theory states that it is possible to reduce a higher dimensional system of coupled oscillators to a system of phase equations. As in the previous chapter we introduce an oscillator, given by the dynamical system

$$\frac{dX}{dt} = F(X), \tag{3.18}$$

which has an asymptotically stable solution $X_0(t) = X_0(t + T)$, with period T and frequency ω. Let us now consider n identical oscillators indexed by i, coupled firstly in a one dimensional linear chain and secondly in a two dimensional square grid with zero flux boundary conditions for each. We let function $G(X_i, X_j)$ provide the coupling between oscillators i and j and ϵ is the coupling strength. If we assume all coupling to be isotropic then our coupled system becomes:

One spatial dimension

$$\frac{dX_i}{dt} = F(X_i) + \epsilon G(X_{i-1}, X_i) + \epsilon G(X_{i+1}, X_i), \tag{3.19}$$

with zero-flux boundary conditions of $G(X_{i-1}, X_i) = G(X_{i+1}, X_i)$ for $i = 1, l$ where l is the the length of the lattice.

Two spatial dimensions

$$\frac{dX_i}{dt} = F(X_1) + \epsilon G(X_{i-1,j}, X_{i,j}) + \epsilon G(X_{i+1,j}, X_{i,j}) + \epsilon G(X_{i,j-1}, X_{i,j}) + \epsilon G(X_{i,j+1}, X_{i,j}), \tag{3.20}$$

with zero flux boundary conditions of $G(X_{i-1,j}, X_{i,j}) = G(X_{i+1,j}, X_{i,j})$ for $i = 1, m$, $G(X_{i,j-1}, X_{i,j}) = G(X_{i,j+1}, X_{i,j})$ for $j = 1, n$ where m is the width of the array and n the height.

These scenarios are illustrated schematically in Figure 3.1.

Proceeding as in the previous chapter, providing $\epsilon \ll 1$, systems (3.19) and (3.20) can be reduced to the canonical models given by

One spatial dimension

$$\theta_i' = \omega + \epsilon(L(\theta_{i-1} - \theta_i) + L(\theta_{i+1} - \theta_i)), \tag{3.21}$$

with zero-flux boundary conditions of $L(\theta_{i-1} - \theta_i) = L(\theta_{i+1} - \theta_i)$ for $i = 1, l$. θ_i is the phase of oscillator i defined as in the previous chapter.

Two spatial dimensions

$$\theta_{i,j}' = \omega + \epsilon(L(\theta_{i-1,j} - \theta_{i,j}) + L(\theta_{i+1,j} - \theta_{i,j}) + L(\theta_{i,j-1} - \theta_{i,j}) + L(\theta_{i,j+1} - \theta_{i,j})), \tag{3.22}$$

with zero-flux boundary conditions of $L(\theta_{i-1,j} - \theta_{i,j}) = L(\theta_{i+1,j} - \theta_{i,j})$ for $i = 1, m$, $L(\theta_{i,j-1} - \theta_{i,j}) = L(\theta_{i,j+1} - \theta_{i,j})$ for $j = 1, n$. $\theta_{i,j}$ is the phase of oscillator i, j defined as in

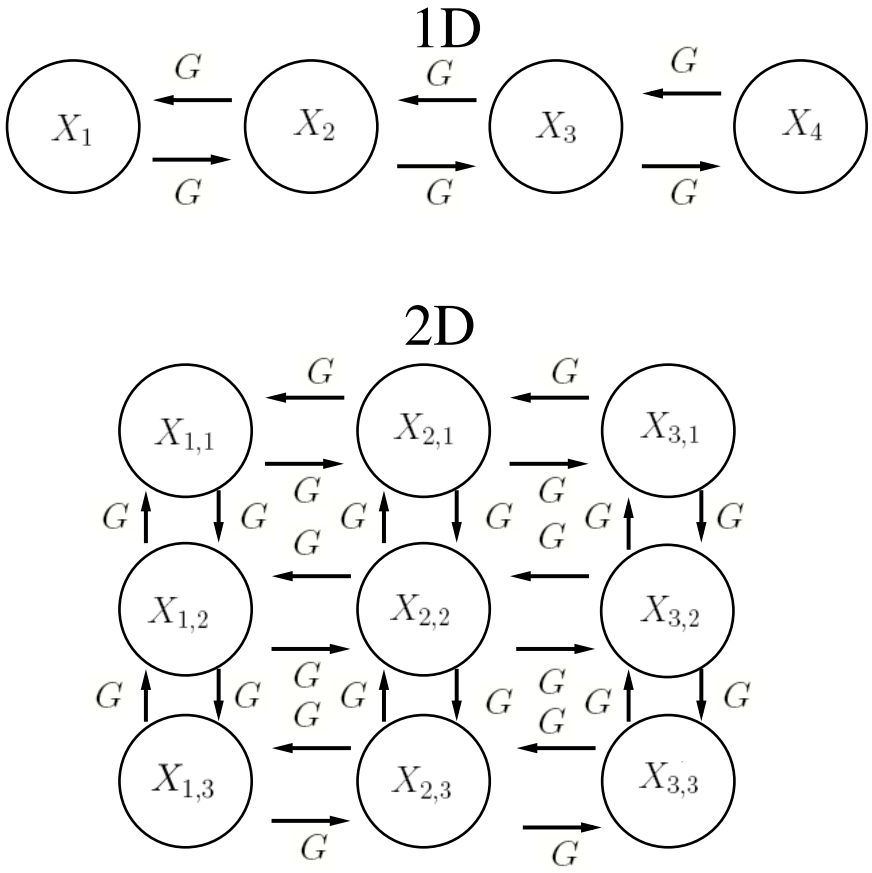

Figure 3.1: Schematic, illustrating the coupling in a 1D linear chain of $n = 4$ oscillators and a 2D square grid of $n = 9$ oscillators.

the previous chapter and we define $L(\Phi)$ as in equation (2.30).

Phase locked solutions correspond to $\theta_i' = \Omega$ for all i in 1D and $\theta_{i,j}' = \Omega$ for all i, j in 2D, where Ω is a constant and can be thought of as a common frequency for all cells, called the 'ensemble frequency'. By analysing the form of L therefore, it will be possible to identify phase locked solutions for linear chains and grids of coupled oscillators. Ascertaining the stability of these solutions however is a more difficult task.

As in the previous chapter, the condition $\epsilon \ll 1$ is not necessarily satisfied with the system, yet as discussed previously the theory of weakly coupled oscillators can still provide qualitative predictions on the existence and stability of phase locked solutions.

Ermentrout and Kopell have devoted much research into ascertaining the stability of phase locked solutions in linear chains of nearest neighbour coupled oscillators [23, 25, 48, 49, 50]. Their earliest work relied upon an odd L function (i.e. $L(\Phi) = -L(-\Phi)$) [23], while their later work relied upon L satisfying the condition $L(0) \neq 0$ [25, 48, 49, 50]. With isotropic couping $L(0) = 0$ always and the L function will often contain both even and odd parts. These approaches will not therefore work with both of our systems. However, Ermentrout proved that if a phased locked solution satisfies two sufficient conditions then this solution is asymptotically stable [22]. There is no proof that the converse is true.

We shall provide an outline of the theorem and proof here. The reader who wishes to study the proof in more detail is directed to [22]. Suppose we have a phase locked solution of system (3.21) of $\theta_j^0(t)$ and a phase locked solution of system (3.22) of $\theta_{j,l}^0(t)$. Then in 1D if for coupled oscillators j and k

$$a_{jk} = L_\theta(\theta_k^0 - \theta_j^0) > 0 \tag{3.23}$$

and in 2D if for coupled oscillators j, l and j, m

$$a_{jljm} = L_\theta(\theta_{j,m}^0 - \theta_{j,l}^0) > 0, \tag{3.24}$$

where L_θ is the derivative of L with respect to θ and if the network is 'connected' (i.e. each oscillator is influenced even indirectly, by every other oscillator) then the solutions

$\theta_j^0(t)$ and $\theta_{j,l}^0(t)$ are asymptotically stable.

The proof relies upon the use of a continuation argument from a phase locked solution $\theta_j^0(t)$ in 1D and $\theta_{j,l}^0(t)$ in 2D and is based upon the implicit function theorem. The same conditions that allow the continuation of a branch of solutions via the implicit function theorem also prove asymptotic stability.

Indirect influence is defined as follows: oscillator k indirectly influences oscillator j if there exists a finite sequence $i_1, ..., i_n$ such that $a_{i_1 k} a_{i_2 i_1} \cdots a_{j i_n} \neq 0$. The diffusion term ensures that this will be the case for both of our systems.

3.3 The Application of Weakly Coupled Oscillator Theory in 1 and 2 Spatial Dimensions

3.3.1 Cyclin D Dependent ATP Release

We first focus upon our Cyclin D dependent ATP release model where ATP release during mid G_1 phase is ensured by replacing H_i and H_c in equation (3.14) with D_i and D_c respectively. In the previous chapter we showed that for two cells there existed parameter regimes that lead to a stable synchronous solution as well as regimes that lead to an unstable synchronous solution. When calculating $L(\theta_{i-1} - \theta_i), L(\theta_{i+1} - \theta_i)$ in 1D and $L(\theta_{i,j-1} - \theta_{i,j}), L(\theta_{i,j+1} - \theta_{i,j})$ in 2D, it is important to note that as the coupling between neighbouring cells is identical in the system, in 1D $L(\theta_{i-1} - \theta_i)$ will be identical for all i and in 2D $L(\theta_{i,j-1} - \theta_{i,j})$ will be identical for all i, j's. This is because the calculation for L depends only upon the nature of the coupling and the response function of a single cell (see equation (2.30)). Likewise $L(\theta_{i+1} - \theta_i)$ will be of identical form for all i and $L(\theta_{i,j+1} - \theta_{i,j})$ for all i, j's. For simplicity we therefore let the phase difference between oscillators $\Phi = \theta_{i-1} - \theta_i$ for all i in the 1D case and $\Phi = \theta_{i-1,j} - \theta_{i,j}$ and $\theta_{i,j-1} - \theta_{i,j}$, for all i, j's in the 2D case. We begin our analysis by calculating $L(\Phi)$ and $L(-\Phi)$ for the system under the parameter regime that gave rise to a stable synchronous solution for two cells. The results of these calculations are shown in Figure 3.2.

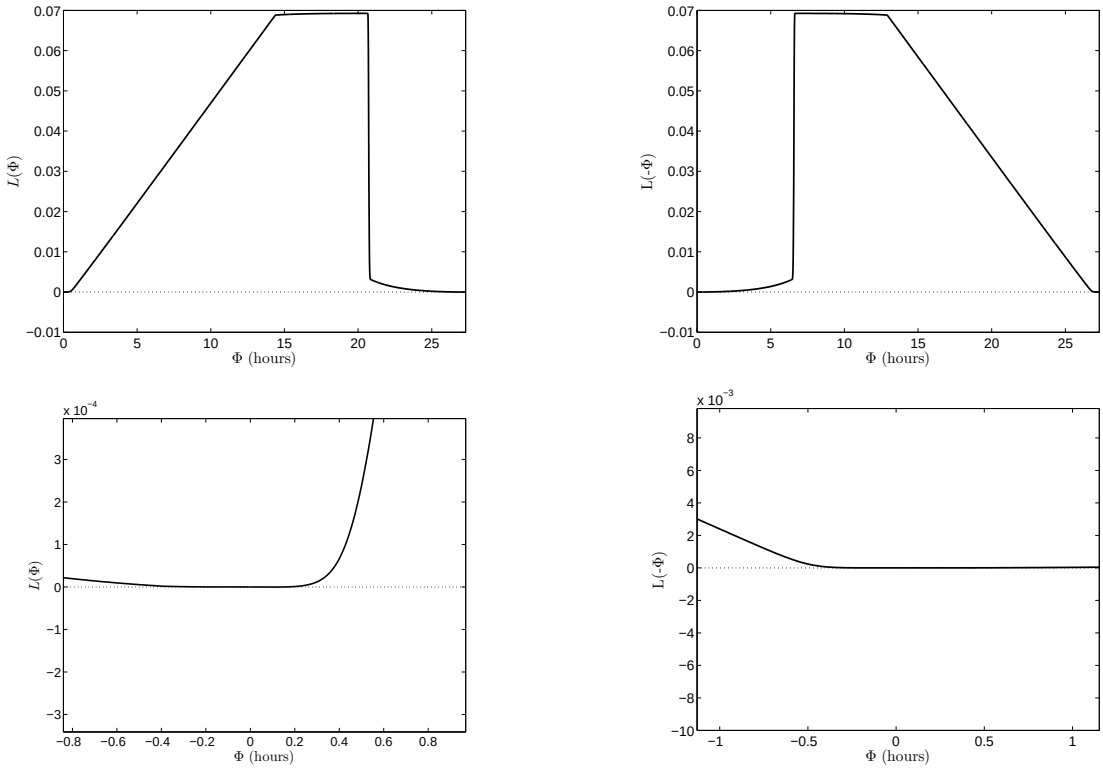

Figure 3.2: Plots of $L(\Phi)$ (first column) and $L(-\Phi)$ (second column), with $L(\Phi)$ defined as in equation (2.30) for system (3.1)-(3.14) with Cyclin D dependent ATP release ($(H_i, H_c) = (D_i, D_c)$). The bottom row plots show the region around $\Phi = 0$. The positive slope at $L(0)$ in the first column of plots ($L_\Phi(0) > 0$) and negative slope in the second column ($L_{-\Phi}(0) > 0$) indicate that the analysis predicts that the synchronous solution is stable. Parameter values as in Table 2.2, except for $V_{deg} = 0.01\mu\text{Ms}^{-1}$. All plots calculated using XPP.

It is clear from Figure 3.2 that $L(0) = 0$ and this corresponds to the synchronous solution. This is because if we substitute $\Phi = 0$ into system (3.21), we get $\theta_i' = \omega + \epsilon(L(\Phi) + L(-\Phi)) = \omega + \epsilon(L(0) + L(0)) = \omega = \Omega$ for all i's. Similarly from system (3.22), we get $\theta_{i,j}' = \omega = \Omega$ for all i, j's. It is more difficult to ascertain the stability of this solution which depends upon the slope of the curve at $L(0)$ from Figure 3.2. One can make out that from the plot of $L(\Phi)$, the slope is positive at $\Phi = 0$ and for the plot of $L(-\Phi)$, the slope is negative at $\Phi = 0$. Therefore, for the synchronous solution $\Phi = 0$, $L_\Phi(0) > 0$ and $L_{-\Phi}(0) > 0$ meaning that $a_{jk} > 0$ in 1D (equation (3.23)) and $a_{jljm} > 0$ in 2D (equation 3.24). Therefore, as $a_{jk}, a_{jljm} > 0$ and the system is 'connected', the theory of weakly coupled oscillators predicts that the synchronous solution is stable under this parameter regime.

In principle it would be possible to use our numerical calculation for $L(\Phi)$ to determine the existence of non-synchronous phase locked solutions. However, as was noted in the previous chapter in some cases the strong coupling in the system led to amplitude effects in the limit cycle solutions which can lead to the theory of weakly coupled oscillators failing to correctly predict the phase difference of asynchronous phase locked solutions. This problem is further complicated when considering systems of several cells as the phase difference between all of the respective cells needs to be considered, not just the phase difference between two. Therefore, the theory of weakly coupled oscillators will become even less useful in predicting the existence and stability of asynchronous phase locked solutions for systems of several cells than it is for a system for two. For these reasons in this chapter, we do not use the theory to predict the existence and stability of phase locked solutions other than the synchronous solution.

We now turn our attention to the second parameter regime that we considered in the previous chapter, that lead to unstable synchronous solutions in a system of two cells. Plots of our numerical calculations of $L(\Phi)$ and $L(-\Phi)$ for this system are shown in Figure 3.3. It can be seen that in this case, at $\Phi = 0$, $L_\Phi(0) < 0$ and $L_{-\Phi}(0) < 0$ and consequently we can not comment upon the stability of this solution as it does not satisfy the sufficient condition which ensures stability. However, we show via direct numerical simulation in Sections 3.5.1 and 3.6.1 that the synchronous solution is also unstable in 1 and 2 spatial dimensions with these parameter values.

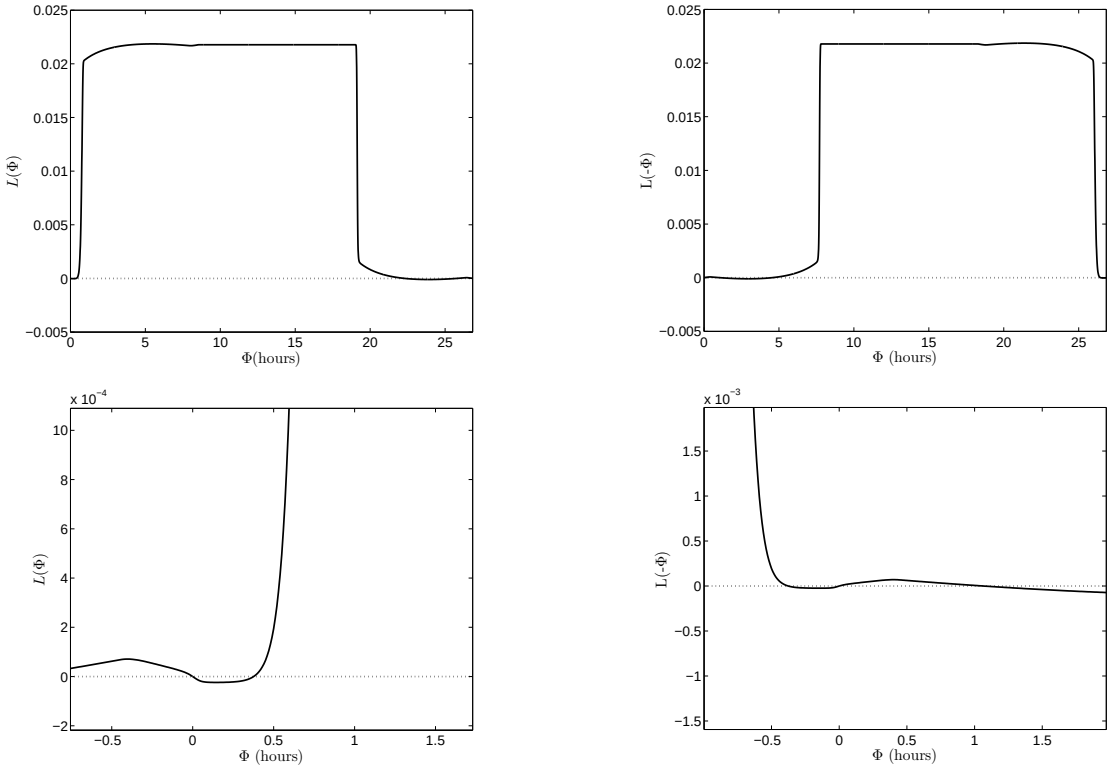

Figure 3.3: Plots of $L(\Phi)$ (first column) and $L(-\Phi)$ (second column) for system (3.1)-(3.14) with Cyclin D dependent ATP release ($(H_i, H_c) = (D_i, D_c)$). The negative slope at $\Phi = 0$ in the first column of plots ($L_\Phi(0) < 0$) and positive slope in the second column ($L_{-\Phi}(0) < 0$) mean that the stability of the synchronous solutions is not guaranteed. However, the results of simulations discussed in Section 3.5.1 and 3.6.1 indicate it is unstable. Parameter values as in Table 2.2, except for $V_{deg} = 2\,\mu\text{Ms}^{-1}$ and $\gamma = 1.2$. All plots calculated using XPP.

3.3.2 R_s Dependent ATP Release

We now consider the release of ATP as occurring during the G_1/S phase transition. We begin by calculating $L(\Phi)$ and $L(-\Phi)$ under the parameter regime that lead to stable synchronous behaviour for two cells in Section 2.7.2. The results of these calculations are shown in Figure 3.4.

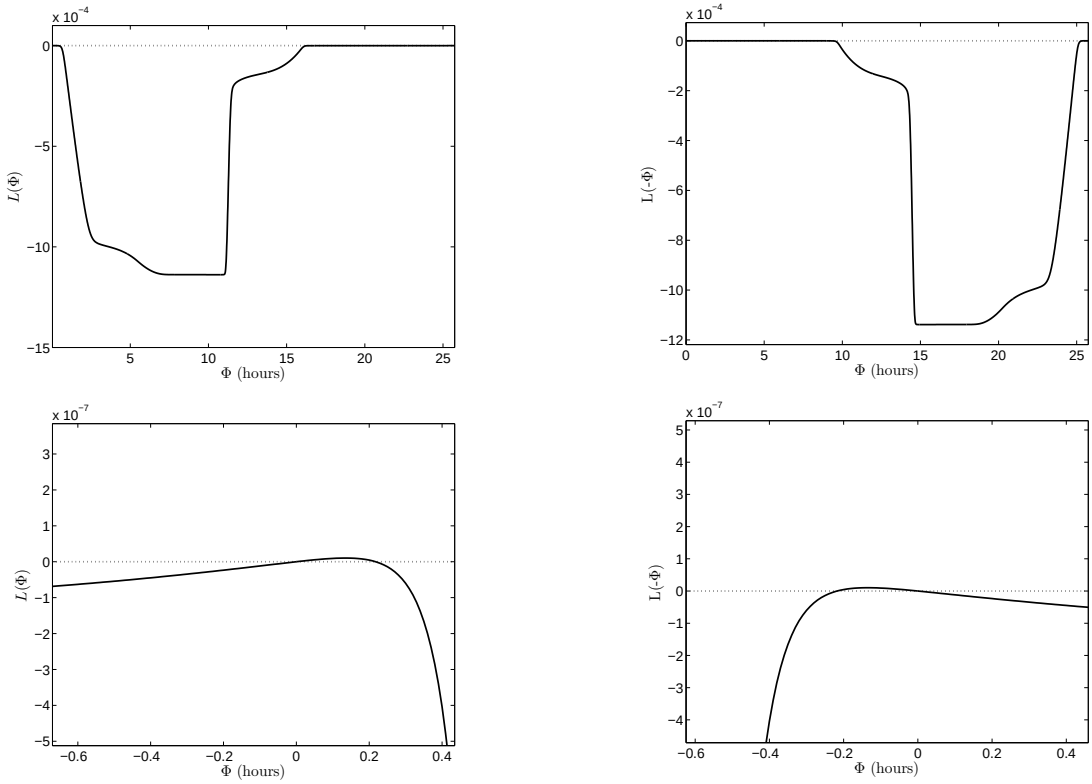

Figure 3.4: Plots of $L(\Phi)$ and $L(-\Phi)$ for system (3.1)-(3.14) with R_s dependent ATP release ($(H_i, H_c) = (R_{sc}, R_{si})$). The bottom row plots show the region around $\Phi = 0$. The positive slope at $L(0)$ in the first column of plots ($L_\Phi(0) > 0$) and negative slope in the second column ($L_{-\Phi}(0) > 0$) indicate that the analysis predicts that the synchronous solution is stable. Parameter values given in Table 2.2 except for $V_{deg} = 0.1\,\mu\text{Ms}^{-1}$ and $\gamma = 1.4$. All plots calculated using XPP. To note, even though the magnitudes of $L(\Phi)$ and $L(-\Phi)$ are small in this case, we do not believe that this will result in a degenerative system.

Figure 3.4 reveals that $L_\Phi(0) > 0$ and $L_{-\Phi}(0) > 0$ and our analysis predicts that the synchronous solution is stable. Plots of $L(\Phi)$ and $L(-\Phi)$ under the parameter regime that lead

to an unstable synchronous solution for two cells are shown in Figure 3.5. In this case, as $L_\Phi(0) < 0$ and $L_{-\Phi}(0) < 0$ at $\Phi = 0$ we can not comment upon the stability of this solution. However in Sections 3.5.2 and 3.6.2 we show that it is unstable in 1 and 2 spatial dimensions.

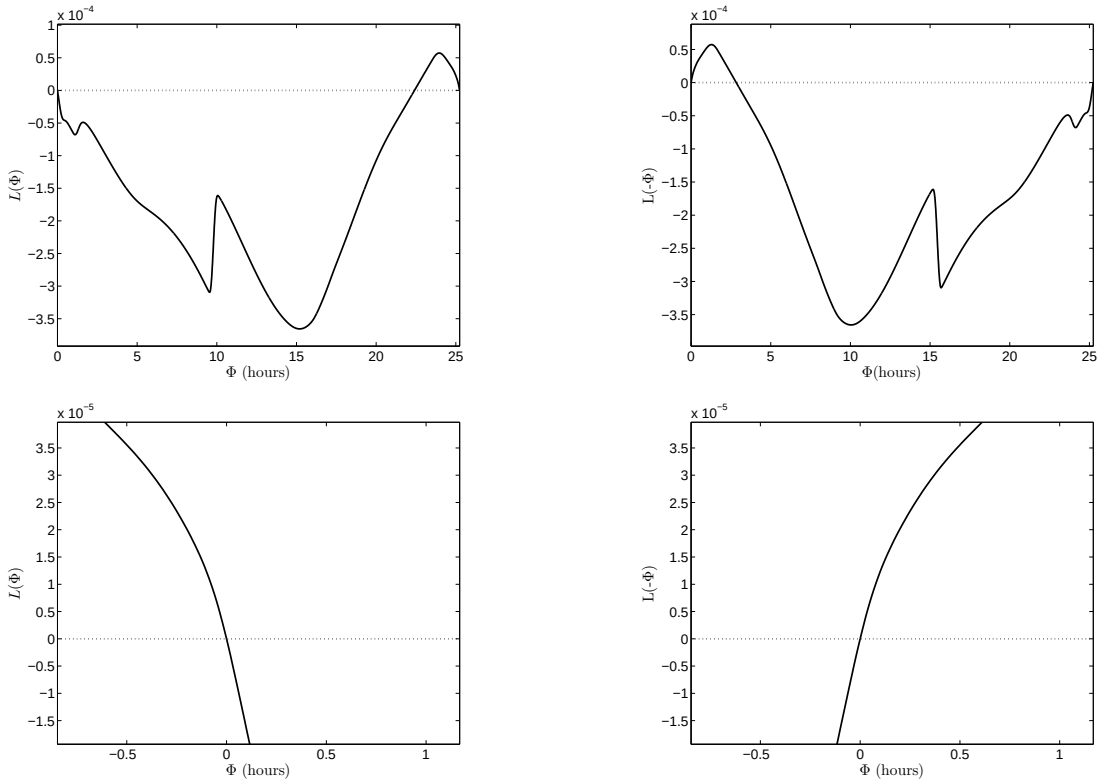

Figure 3.5: Plots of $L(\Phi)$ and $L(-\Phi)$ for system (3.1)-(3.14) with R_s D dependent ATP release ($(H_i, H_c) = (R_{sc}, R_{si})$). The negative slope at $L(0)$ in the first column of plots ($L_\Phi(0) < 0$) and positive slope in the second column ($L_{-\Phi}(0) < 0$) mean that stability of the synchronous solutions is not guaranteed. Parameter values given in Table 2.2 except for $V_{deg} = 0.04\,\mu\text{Ms}^{-1}$ and $\gamma = 1.4$. All plots calculated using XPP.

3.4 Synchrony Measures

It is important to introduce a quantitative measure of the degree to which several cells cycle in a synchronous manner. Any such measure should be consistent with the definition of phase we introduced in the previous chapter when we studied two cell systems, but also flexible enough to provide us with a realistic synchrony measure when the coupling leads to

amplitude effects or other more complex behaviour and our current definition of phase is no longer applicable. Several measures of synchrony have been proposed for coupled oscillators, most of which were developed to measure synchronous behaviour in clusters of spiking neurons, although they can be adapted to networks of any oscillators [51, 52, 83, 92]. We consider two of these measures here.

Wang-Buzsáki Measure

Wang *et al* propose a coherence measure or synchrony measure of a network of neurons which is based upon dividing time into small segments and investigating whether or not the neurons which make up a network 'spike' within these segments [92]. In order to outline the Wang-Buzsáki Measure let us first consider a long time interval which we segment into a number of regular time bins τ. Let us then consider two neurons l and m and introduce the functions $S_l(j)$ and $S_m(j)$, $j = 1, 2 \ldots\ldots K$, where K is the total number of time bins. Now let $S_l(j) = 1$ if oscillator l spikes within time bin j and 0 otherwise and likewise for S_m. The coherence measure for a pair of neurons is then given by

$$k_{lm}(\tau) = \frac{\sum_{j=0}^{K} S_l(j) S_m(j)}{\sqrt{\sum_{j=1}^{K} S_l(j) \sum_{j=1}^{K} S_m(j)}}. \tag{3.25}$$

The numerator in equation (3.25) gives the total number of bins that both neurons spike in. While the denominator is the square root of the product between the total number bins with spikes for neuron l and the total number of bins with spikes for neuron m.

It is then possible to average over many pairs of neurons in a large network to obtain the coherence measure of the population $k(\tau)$ which is the arithmetic mean of $k_{lm}(\tau)$ for all combinations of pairs of neurons l, m. This method could be adapted to provide a coherence measure of a population of radial glial cells by instead of considering the 'spiking' time of a neuron, considering the time at which one of the cell cycle variables such as Cyclin D peaks.

There are two obvious weaknesses with adopting Wang *et al*'s coherence measure. Firstly one will obtain different results depending upon the size of the time bins τ that one chooses, with no obvious way in which to select the size of τ in a non-arbitrary manner (although perhaps this problem could be resolved by introducing a very high bin size resolution). Secondly, the measure proposed by Wang *et al* is of a 'binary' nature in the sense that two oscillators l and m will have a value for $k_{lm}(\tau)$ of 1 if they are synchronised, or 0 otherwise. The measure can not differentiate from two cells that are oscillating in a near synchronous manner and two cells that are oscillating in an anti-phase phase locked manner as both would be given a value for $k_{lm}(\tau)$ of 0. Qualitatively speaking these two behaviours are very different and it would be desirable for a synchrony measure to reflect this fact.

Pinsky-Rinzel Measure

Pinsky and Rinzel proposed a measure which captures many of the intuitive concepts associated with phase [11, 69]. As for the Wang-Buzsáki measure, Pinsky and Rinzel considered populations of spiking neurons when developing their synchrony measure. When calculating the phase of the neurons in their system, they considered the firing times of these neurons, with the delay (if any) of firing times between one neuron and the next being used as basis to form a vector of phases associated with each neuron. It is possible in our system to consider the times at which the cell cycle variables such as Cyclin D 'peak' to form such a vector of phases

$$\underline{\Phi^i}(t) = [\Phi^i_1(t), \Phi^i_2(t), \Phi^i_3(t), ..., \Phi^i_k(t), ..., \Phi^i_n(t)], \tag{3.26}$$

where $\underline{\Phi^i}(t)$ is the vector of phases associated with oscillator i, n the total number of oscillators and $\Phi^i_k(t)$, the phase of oscillator k in relation to oscillator i normalised to 1, which is calculated as follows

$$\Phi^i_k(t) = \frac{T(k,m) - t_{i,m}}{t_{i,m+1} - t_{i,m}}, \;\; t_{i,m} \leq T(k,m) < t_{i,m+1} \text{ and } 1 \leq k \leq n. \tag{3.27}$$

Here $t_{i,m}$ is the m^{th} Cyclin D peak time of radial glial cell i and $T(k,m)$ is the peak Cyclin D time of cell k in the interval $[t_{i,m}, t_{i,m+1})$.

Essentially, if we take a cell i and attribute a phase value of 0 to when its Cyclin D variable peaks, then we can form a vector of phases associated with it as defined in equations

(3.26) and (3.27). The phase values for the cells other than cell i are determined by the first time after the Cyclin D in cell i peaks that the Cyclin D in these cells peak. These times are then normalised so that they lie in the interval $[0, 1)$. This definition of phase was first proposed by Golomb and Rinzel [31] and it is consistent with the definition of phase used in chapter 2 when identical oscillators are considered and where the coupling does not lead to amplitude effects.

The Pinsky-Rinzel synchrony measure associated with oscillator i is then defined by

$$r_i^2 = \frac{1}{n^2} \sum_{j,l=1}^{n} \cos 2\pi(\Phi_j^i - \Phi_l^i). \tag{3.28}$$

When $r_i^2 = 1$, all of the cells are oscillating in a synchronous manner (see Figure 3.6). A value of 0 indicates maximal asynchrony analogous to the anti-phase phase locked state for two cells commonly referred to as the *splay* state, where the cells are uniformly distributed throughout phase space (see Figure 3.6). Consequently, the closer the value of r_i^2 is to 1, the more synchronous the behaviour can be considered, the closer to 0, the more asynchronous the behaviour. Finally, to obtain an overall synchrony measure S_{PR} we average r_i^2 over all oscillators, i.

It is clear that this measure can differentiate between two cells that are oscillating in a near synchronous manner and two cells that are phase locked in an anti-phase manner. A system where almost all cells are cycling in a synchronous manner will have $S_{PR} \approx 1$, while a system whereby all cells are in the splay state will have $S_{PR} = 0$, reflecting the greater asynchrony in this case. Pinsky and Rinzel's definition of phase is also consistent with the definition of phase used in the previous chapter and used with regard to the theory of weakly coupled oscillators. For these reasons we adopt Pinsky and Rinzel's synchrony measure when considering systems of several cells.

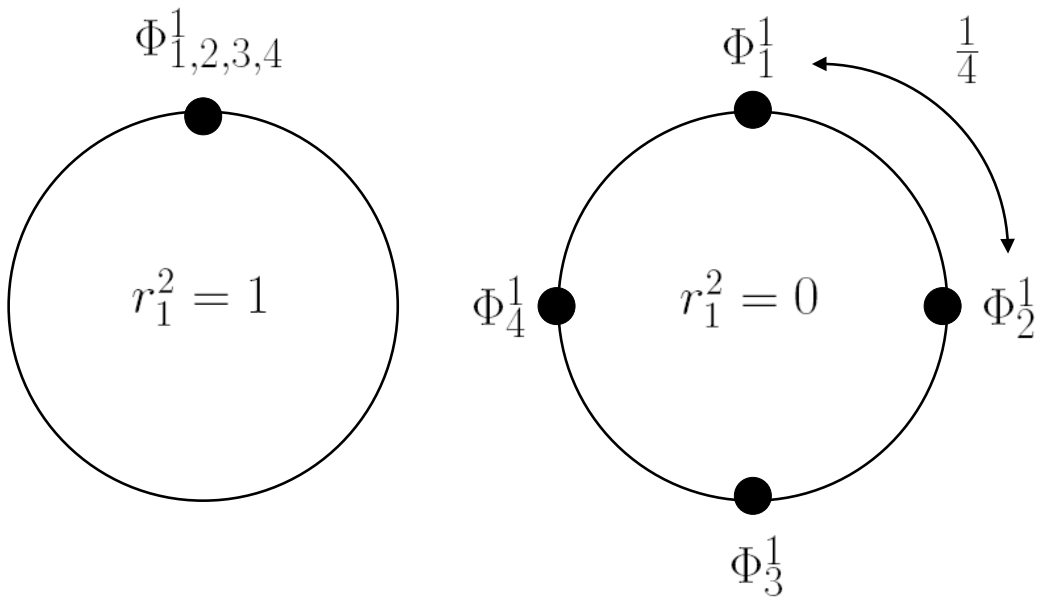

Figure 3.6: Schematic where the relative phases associated with oscillator 1 (defined by equations (3.27)and (3.28)) in a four cell system is represented on the unit circle. The diagram illustrates the phase differences between the cells that lead to values for r^2_1 of 1 (the synchronous state) and 0 (the splay state).

3.5 One Dimensional Simulations

Choice of initial conditions and stability analysis

The initial conditions are such that all cells sit on the branch of stable limit cycle solutions (Figure 2.10). When calculating the initial phase difference between cells, we use the limit cycle solution of a single uncoupled cell. We then specify a maximum initial phase difference PD_{max} between cells, before using Matlab's uniformly distributed pseudo-random number generator `rand` on the open interval (0,PD_{max}) to set the initial phase differences between cells. To ascertain the stability of a solution, we simulated the system for a long period of time (60 000 hours of simulated time) and recorded the solution over the last 150 hours of simulated time, to produce a solution 'snapshot'. Next, we perturbed all variables ($\pm$ 0.001) and numerically integrated the system again for a further 10 000 hours of simulated time. We then compared the results of this second simulation with our 'snapshot', in order to investigate if the system had returned to the 'snapshot' solution, which we took to indicate that the solution was stable.

3.5.1 Cyclin D Dependent ATP Release

We first consider the model where ATP release is modelled as occurring during the middle of G_1 phase of the cell cycle (equations (3.1)-(3.14), with $(H_i, H_c) = (D_i, D_c)$).

Fixed calcium coupling strength γ

We consider the parameter regime that lead to stable synchronous solutions for two cells (chapter 2, Section 2.7.1) and has been predicted to lead to stable synchronous solutions in systems of many cells (Section 3.3.1). Numerical integration of our model for a line of 30 cells with zero flux boundary conditions given by equation (3.17) and an initial phase difference between each cell of no more than 1 hour ($PD_{max} = 1$), leads to results illustrated in Figure 3.7. The results reveal that if the initial phase difference is small, the cells settle down to a synchronous phase locked state under this particular parameter regime with a synchrony measure S_{PR} of 1, as predicted by the theory of weakly coupled oscillators.

Next we investigated how the system behaves when the initial phase difference between the cells is larger. These results are illustrated in Figure 3.8. In the two cell case, a large enough initial phase difference between the cells resulted in the cells locking in an anti-phase manner. The results from Figure 3.8 suggest that if the initial phase difference between each cell is sufficiently large in a system of several cells, then the cells lock in an asynchronous manner with a synchrony measure S_{PR} of 0.007154346, indicating that the system is very close to the splay state. In this case, due to the larger concentration of ATP in the extracellular space, the period of the cell cycle is reduced from 27.3 to 26.8 hours.

Next we investigated the behaviour of a system under the parameter regime that yielded an unstable synchronous phase locked state for two cells. Our analysis in Section 3.5.1 proved inconclusive with regard to ascertaining the stability of this solution in systems of several cells. Simulations for several cells can be seen in Figure 3.9 which suggest that the synchronous solution remains unstable under this parameter regime for several cells too. The cells settle down to an asynchronous phase locked state of synchrony measure S_{PR} = 0.02148381. Again as in the previous asynchronous case, the period of the cell cycle is reduced from 26.235 to 24.8, due to the increased concentration of extra-cellular ATP.

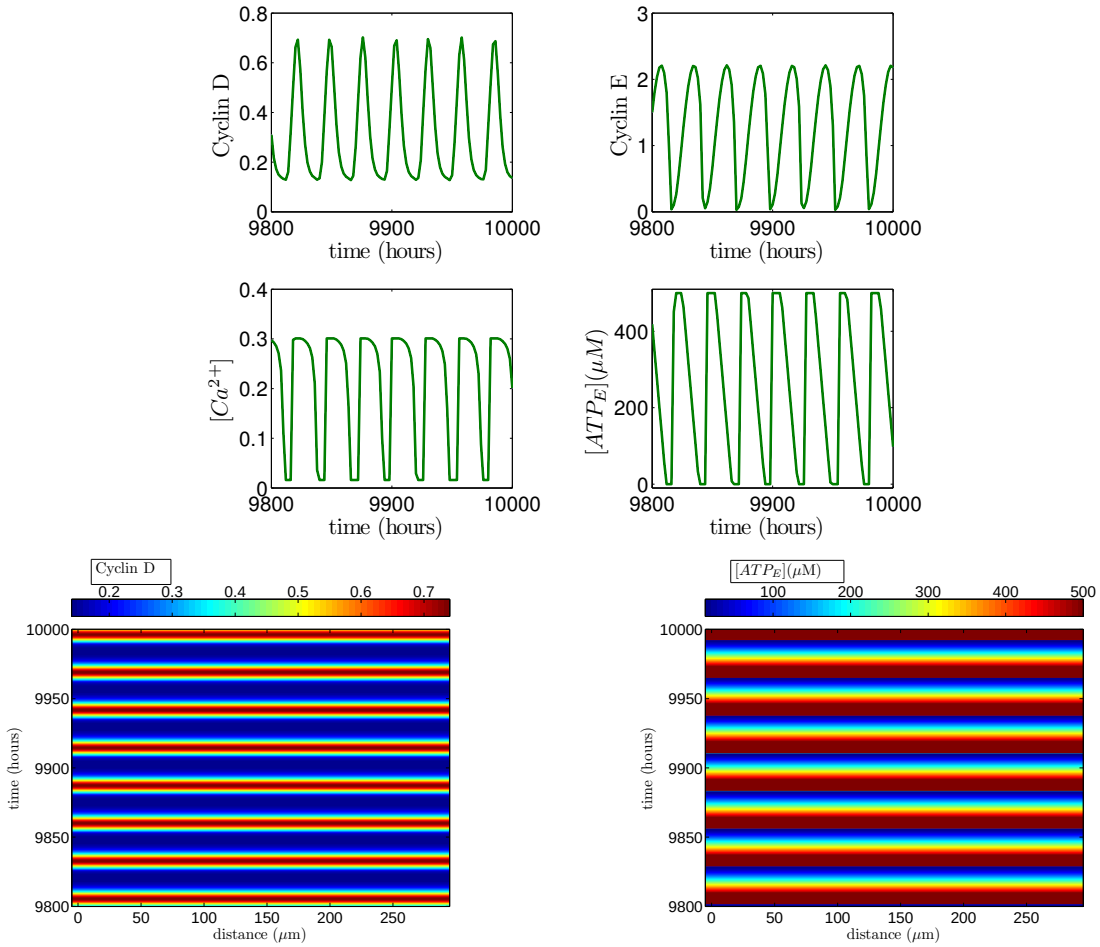

Figure 3.7: Simulations of system (3.1)-(3.14) for 30 cells, with Cyclin D dependent ATP release ($(H_i, H_c) = (D_i, D_c)$). The top four plots show the evolution of Cyclin D, Cyclin E, external ATP and calcium against time. The bottom two plots are colour plots, showing the concentrations of Cyclin D and external ATP across the spatial domain. The results show that for a small initial phase difference the system tends towards the synchronous solution, indicating that this solution is stable. Parameter values given in Table 2.2, except for $V_{deg} = 0.01\mu\text{Ms}^{-1}$. Each cell was started at a different position on the cell cycle but at an initial phase difference (PD_{max}) from any other cell of no more than 1 hour. Solutions obtained using `ode23s` within Matlab. Transients not shown.

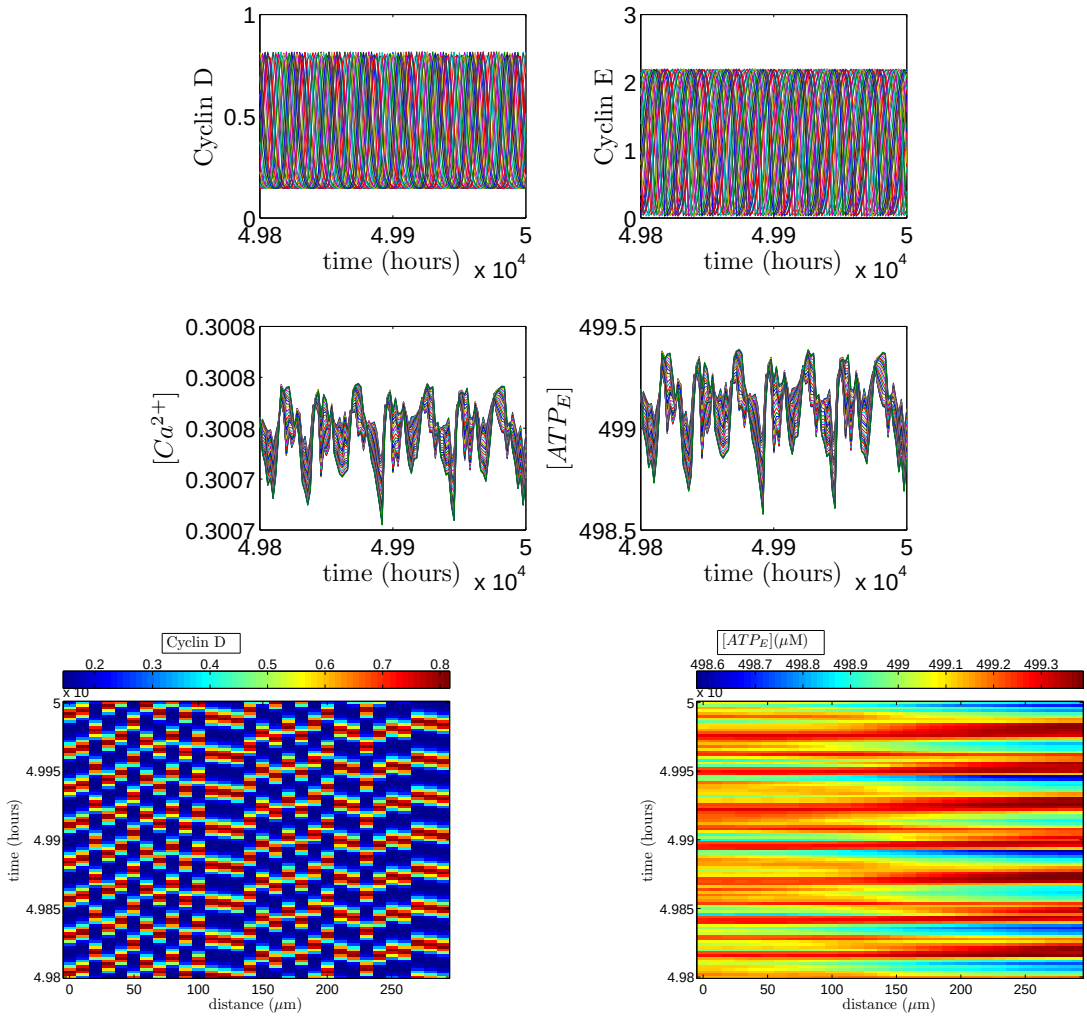

Figure 3.8: Simulations of system (3.1)-(3.14) for 30 cells, with Cyclin D dependent ATP release ($(H_i, H_c) = (D_i, D_c)$). The simulations reveal that for a larger initial phase difference the system evolves to an asynchronous solution, indicating that the 30 cell system is bistable under this parameter regime. Parameter values as in Table 2.2, except for $V_{deg} = 0.01\mu\text{Ms}^{-1}$. $PD_{max} = 27$ hours. Transients not shown.

Following on from the work on two cells, we investigated which values of V_{deg} render the synchronous state unstable for a system of 10 cells. This we achieved by running simulations for different values of V_{deg} with two different sets of initial conditions: one set such that the cells were initially close to the synchronous state, achieved by setting $PD_{max} = 1$ and the other where we allowed for larger initial phase differences by setting $PD_{max} = 27$. The results are plotted in Figure 3.10 which indicates that the synchronous state becomes unstable for a system of 10 cells at $V_{deg} \approx 0.06\,\mu\text{Ms}^{-1}$. However, even when this occurs, the bistability of the system with regard to the phase locked behaviour seems to persist as different initial conditions lead to different values of the synchrony measure S_{PR}. Once the synchronous state becomes unstable the asynchronous phase locked state that results becomes increasingly asynchronous as V_{deg} is increased. The phase locked state that results from a large initial phase difference seems almost invariant under changes to the rate of external ATP degradation. The value for the synchrony measure for this state is very close to that for the splay state (i.e. close to zero).

Fixed ATP degradation rate V_{deg}

In Section 2.7.1 of chapter 2 we showed that in the Cyclin D dependent ATP release model, when $V_{deg} = 2$, the synchronous solution was only stable for $\gamma < 1.065856$. Here we investigate if this behaviour persists in this model in systems of several cells. Numerical integrating of our Cyclin D dependent ATP release model for 30 cells with zero flux boundary conditions with $V_{deg} = 2$ and $\gamma = 0.4$, leads to results illustrated in Figures 3.11 and 3.12.

It can be seen from Figure 3.11 that the synchronous state is stable for a system of several cells under this particular parameter regime. Figure 3.12 reveals that the system exhibits bistability with regard to phase locked solutions. The trajectory of the solution in this case tends towards a stable asynchronous state of synchrony measure 0.0356548, close to the splay state. In this case, the spatial coupling leads to a reduction in the period of the cell cycle from 28.6 to 27 hours.

In the two cell case, we showed that if the calcium coupling strength γ was sufficiently large when $V_{deg} = 2$ then the stability of the phase locked state was lost. We investigated

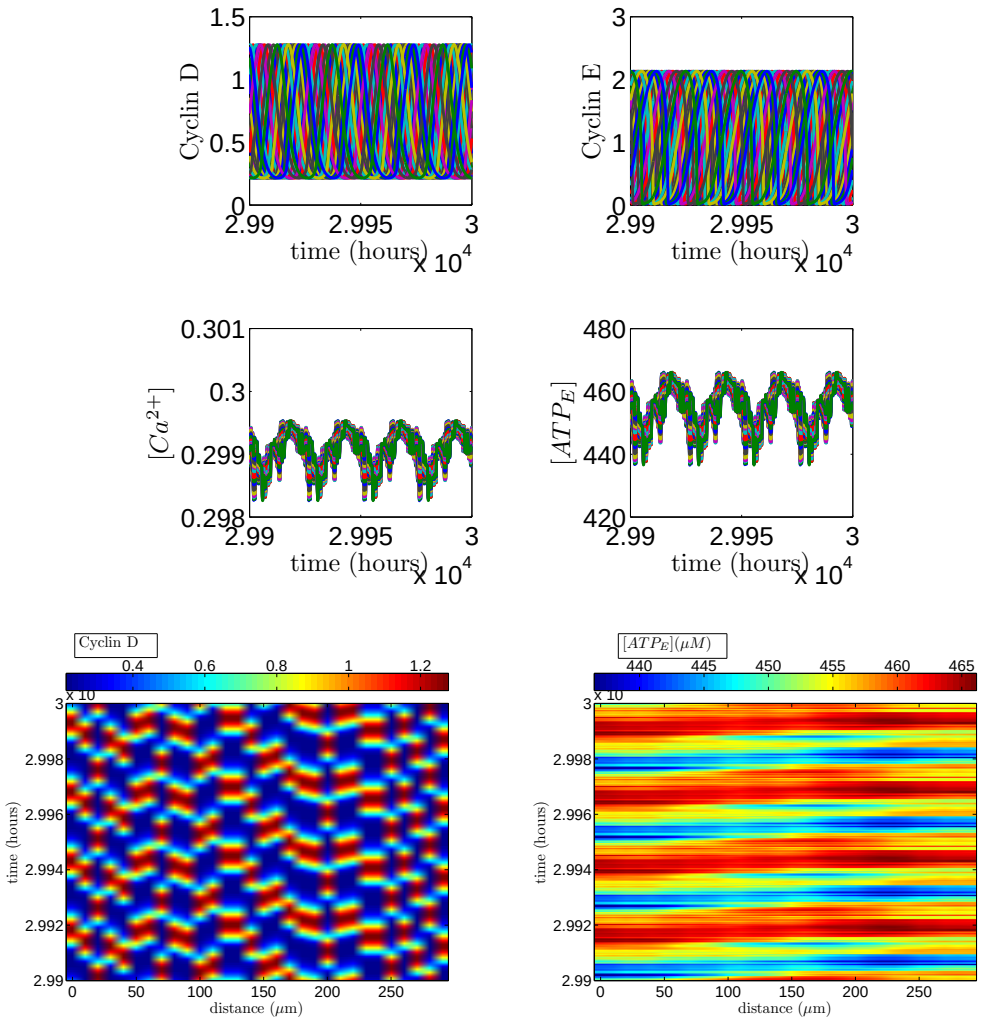

Figure 3.9: Simulations of system (3.1)-(3.14) for 30 cells, with Cyclin D dependent ATP release ($(H_i, H_c) = (D_i, D_c)$). The results show that with a small initial phase difference the system evolves to an asynchronous solution indicating that the synchronous solution is unstable. Parameter values given in Table 2.2 except for $V_{deg} = 2\,\mu\text{Ms}^{-1}$ and $\gamma = 1.2$. $PD_{max} = 1$ hour. Transients not shown.

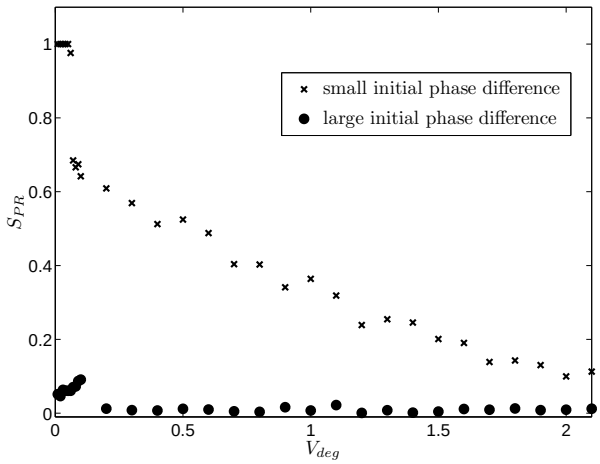

Figure 3.10: Plot showing how the synchrony measure depends upon V_{deg} for system (3.1)-(3.14) of 10 cells with Cyclin D dependent ATP release ($(H_i, H_c) = (D_i, D_c)$). The results indicate that two phase locked solutions exist and at $V_{deg} \approx 0.06$ the stability of the synchronous solution is lost. The system was simulated twice for each value of V_{deg} considered, once with $PD_{max} = 1$ (small initial phase difference) and once with $PD_{max} = 27$ (large initial phase difference). The synchrony measure S_{PR} was taken once the system had settled down to a stable oscillatory solution. Parameter values as in Table 2.2, except for V_{deg} as given and $\gamma = 1.2$.

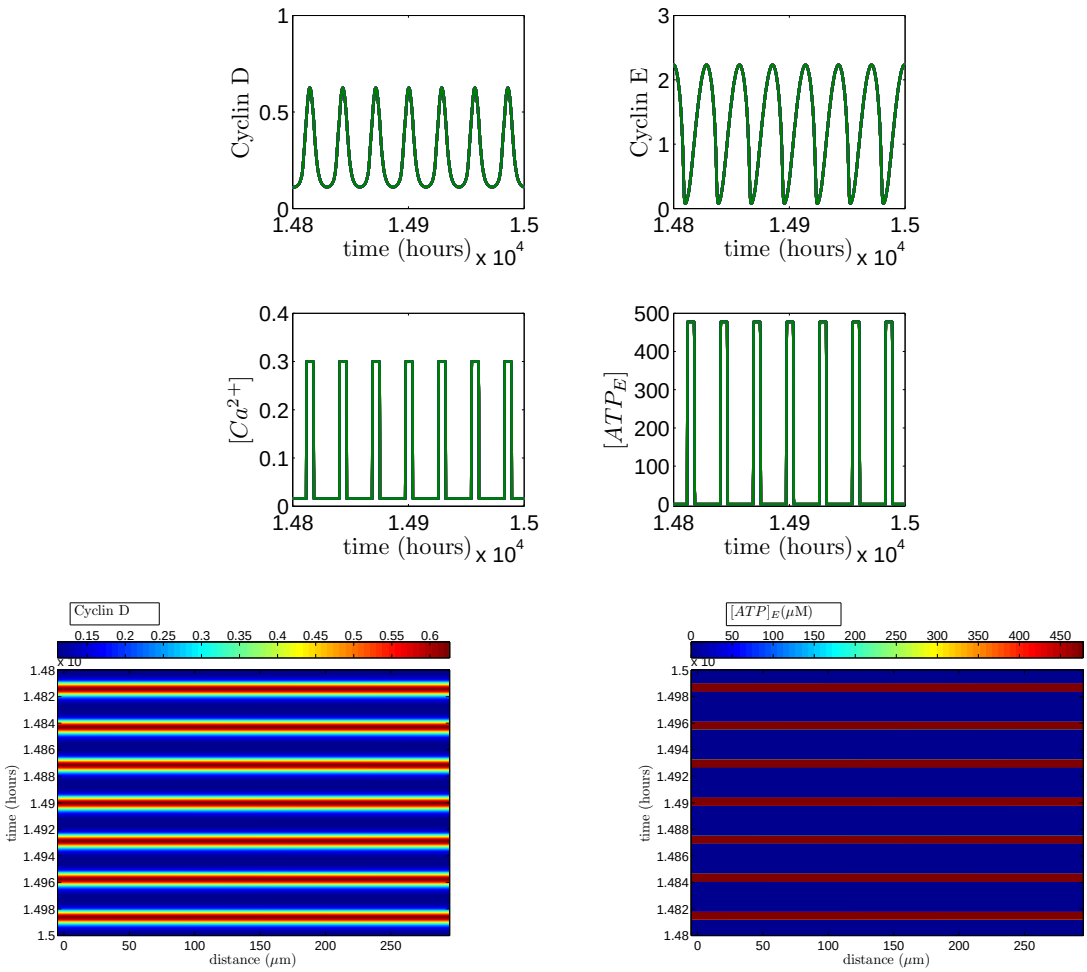

Figure 3.11: Simulations of system (3.1)-(3.14) for 30 cells, with Cyclin D dependent ATP release ($(H_i, H_c) = (D_i, D_c)$). The simulations show that for an initially small initial phase difference, the system evolves to the synchronous solution, indicating that this solution is stable. Parameter values as in Table 2.2, except for $V_{deg} = 2\,\mu\text{Ms}^{-1}$. $PD_{max} = 1$. Transients not shown.

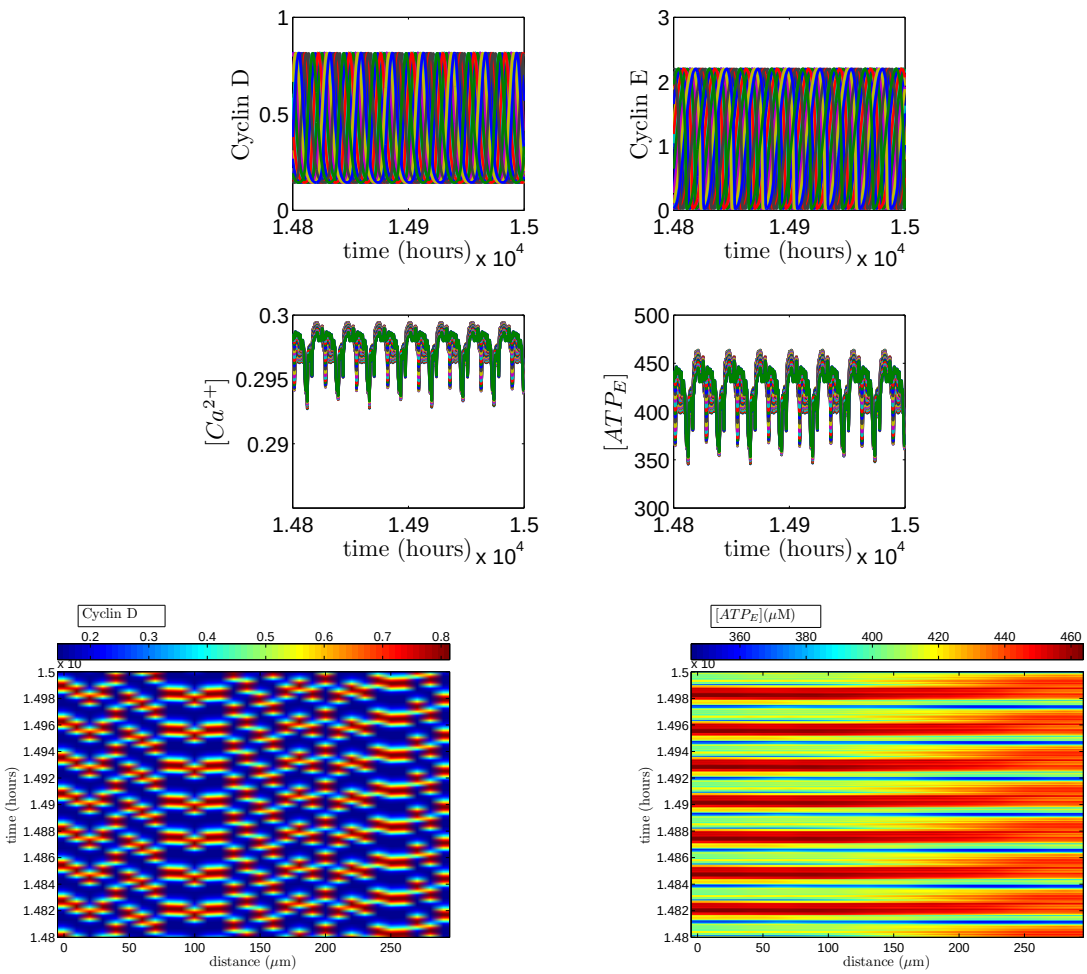

Figure 3.12: Simulations of system (3.1)-(3.14) for 30 cells, with Cyclin D dependent ATP release ($(H_i, H_c) = (D_i, D_c)$). For a larger initial phase difference, the system evolves to an asynchronous solution, indicating that not only is this solution stable but it co-exists with the synchronous solution shown in Figure 3.11. Parameter values as in Table 2.2, except for $V_{deg} = 2\ \mu\text{Ms}^{-1}$. $PD_{max} = 27$. Transients not shown.

if this was the case for several cells by simulating a system of 10 cells several times but each time with different value for γ and calculated the corresponding synchrony measure S_{PR}. The results can be seen in Figure 3.13. which suggest that the synchronous state becomes unstable at $\gamma \approx 0.65$ for 10 cells in a 1-D lattice. The stability of this branch of solutions is then lost completely at $\gamma \approx 0.95$, with all trajectories tending towards the stable asynchronous state. In the two cell system that we considered in the previous chapter, under this parameter regime, we showed that the synchronous solution branch became unstable at $\gamma \approx 1.065856$, with all trajectories we studied after this point tending to the anti-phase phase locked state. Qualitatively speaking therefore, our results for 10 cells are similar to those of the two cell system, as in both cases the the stability of the synchronous branch is lost as γ is increased and in both cases for larger values of γ we were only able to find one phase locked solution as opposed to two for smaller values of γ.

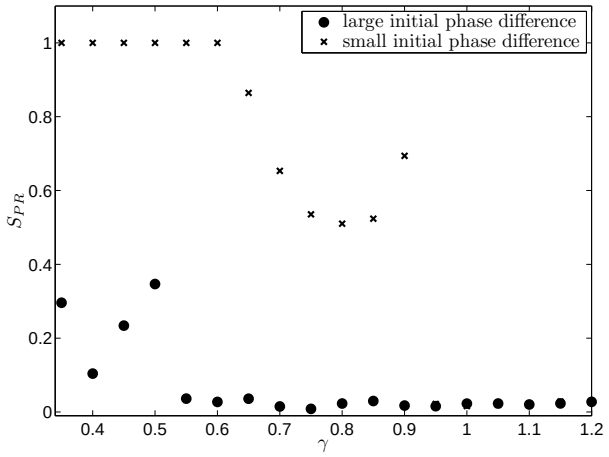

Figure 3.13: Plot showing how the synchrony measure S_{PR} defined in equation (3.28) depends upon γ for system (3.1)-(3.14) for 10 cells with Cyclin D dependent ATP release ($(H_i, H_c) = (D_i, D_c)$). The results indicate that for low values of γ the system exhibits bistability with regard to phase locked solutions. However at $\gamma \approx 0.65$, the stability of the synchronous solution is lost at $\gamma \approx 0.95$ the system appears to undergo another bifurcation, leaving one stable oscillatory solution. The system was simulated twice for each value of V_{deg}, once with $PD_{max} = 1$ (small initial phase difference) and once with $PD_{max} = 27$ (large initial phase difference). The synchrony measure S_{PR} was taken once the system had settled down to a stable oscillatory solution. Parameter values as in Table 2.2, except for γ as given and $V_{deg} = 2\,\mu\text{Ms}^{-1}$.

3.5.2 R_s Dependent ATP Release

Fixed calcium coupling strength γ

We begin our investigations for the R_s dependent ATP release model by attempting to confirm the results of the analysis conducted in Section 3.3.2 of this chapter. Our analysis predicted that for $\gamma = 1.4$ and $V_{deg} = 0.1\ \mu\text{Ms}^{-1}$ the synchronous solution for a system of several cells in one and two spatial dimensions is stable. In the previous chapter we showed that this was the case for two cells under this parameter regime. Simulating the system under this parameter regime leads to the results shown in Figure 3.14.

Figure 3.14 suggests that the synchronous solution is in fact unstable, with the system evolving to a near synchronous solution with a synchrony measure S_{PR} of 0.9926183. Other realisations from different sets of initial conditions will lead to different near synchronous solutions, where the cell cycling asynchronously differs, although the value of S_{PR} in such cases will be the same. We first encountered this phenomenon in Section 2.7.2 in chapter 2 where we showed in Figure 2.25 that two stable asynchronous solutions existed. In this case the trajectories of the two cells differed, with the initial conditions of the system determining which cell would evolve to which asynchronous solution. In order to show that something similar is happening here, and to confirm that, contrary to the predictions of the analysis, the synchronous solution is unstable, we simulated the system again, from a set of initial conditions very close to the synchronous state. The results of this simulation are shown in Figure 3.15.

The reason why the analysis fails becomes clear when one inspects the Cyclin D profile of the 'rogue' cell and notices that it differs to that of the other cells. This means that the coupling has introduced amplitude effects into the system. As in the Cyclin D dependent model we investigated whether other phase locked solutions exist by considering a larger initial phase difference between the cells. Figure 3.16 shows that, in addition to the near synchronous state, there also exists a stable asynchronous phase locked state, of synchrony measure 0.08822138. There is a slight increase in the period of the cell cycle from 25.74 to 26 hours for this case.

We next turned our attention to the parameter set that led to unstable phase locked so-

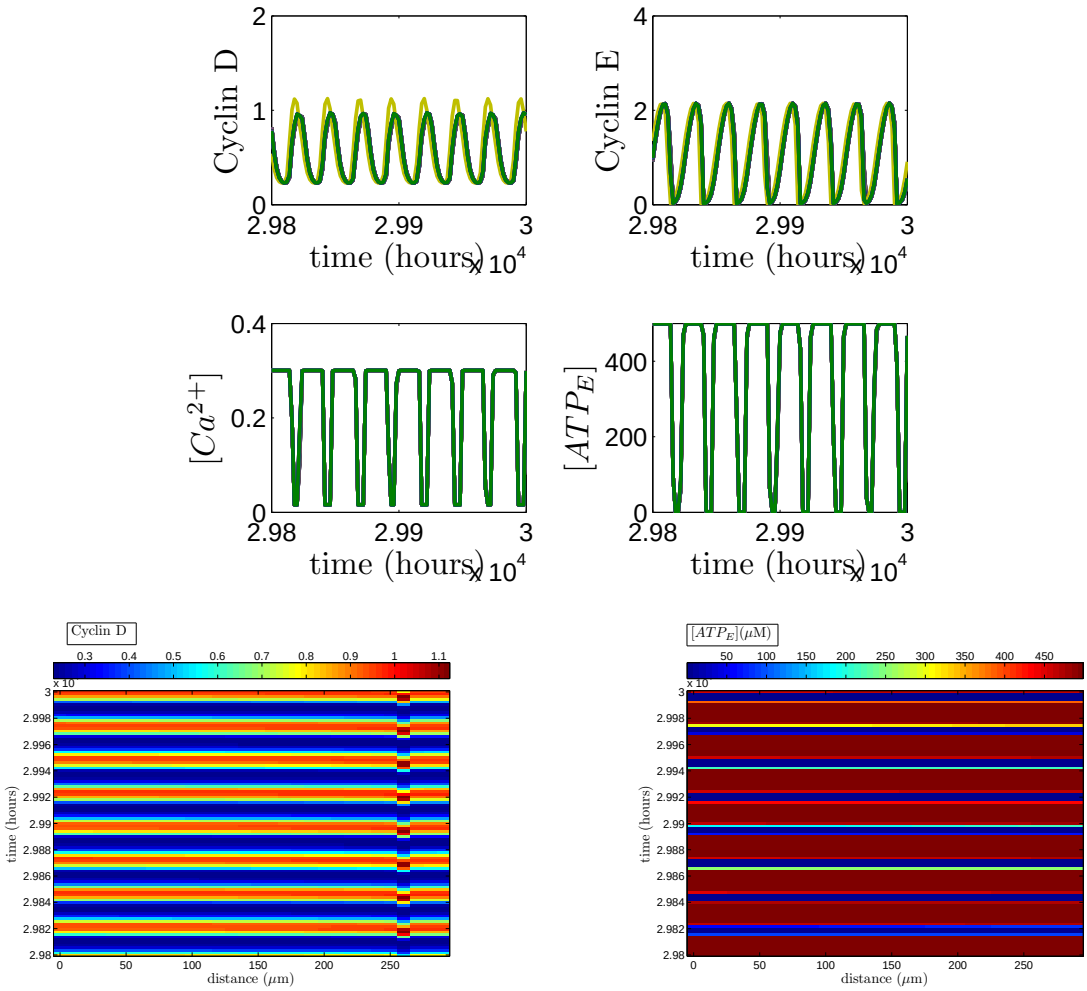

Figure 3.14: Simulations of system (3.1)-(3.14) for 30 cells with R_s dependent ATP release ($(H_i, H_c) = (R_{sc}, R_{si})$). As for the the results in the previous subsection, the top four plots show the evolution of Cyclin D, Cyclin E, external ATP and calcium against time. The bottom two plots are colour plots, showing the concentrations of Cyclin D and external ATP across the spatial domain. The results suggest that the synchronous solution is unstable, with the system evolving to a stable near synchronous solution. Parameter values given in Table 2.2 except for $\gamma = 1.4$ and $V_{deg} = 0.1\ \mu\text{Ms}^{-1}$. Each cell was started at a different position on the cell cycle but at an initial phase difference (PD_{max}) from any other cell of no more than 1 hour. System solved using `ode23s` within Matlab. Transients not shown.

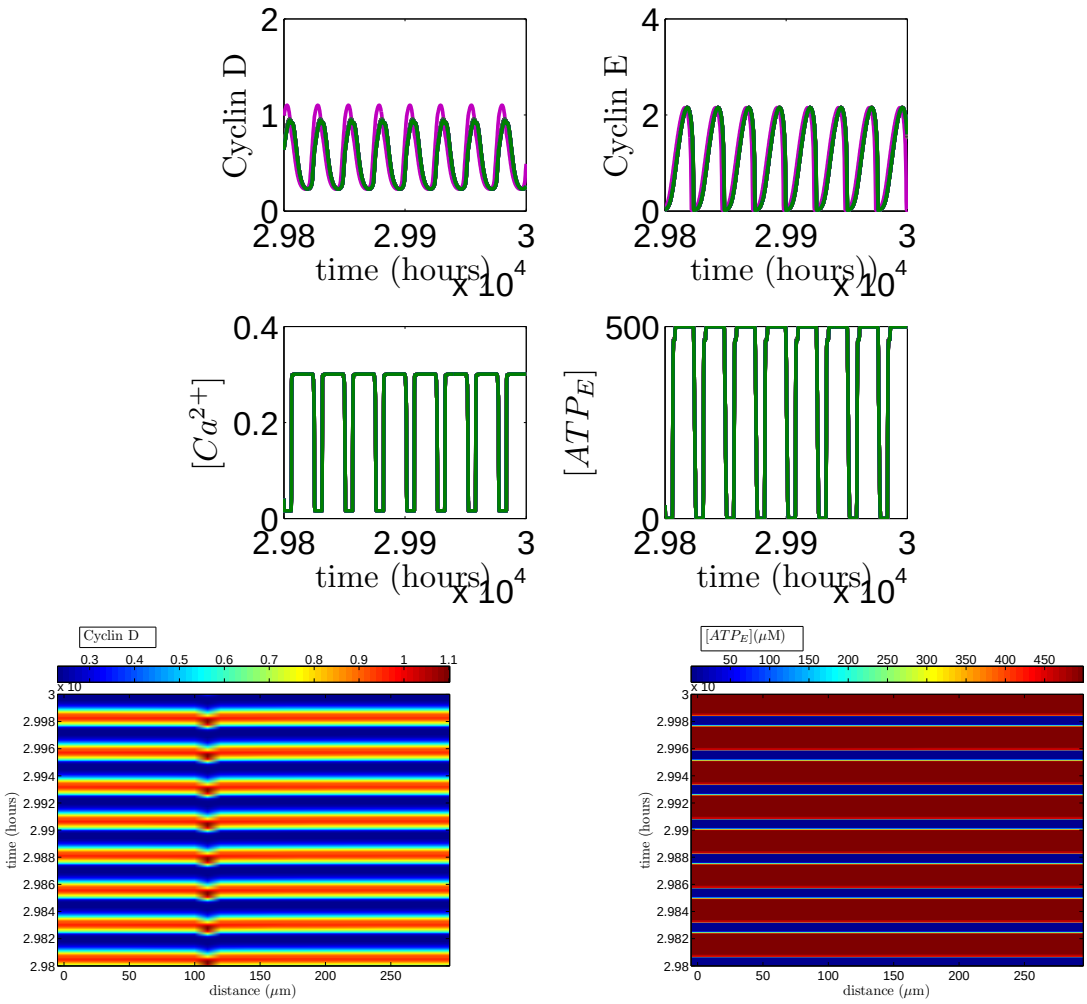

Figure 3.15: Simulations of system (3.1)-(3.14) for 30 cells with R_s dependent ATP release ($(H_i, H_c) = (R_{sc}, R_{si})$). The results augment the results in Figure 3.14. In this instance the near synchronous solution differs to that shown in Figure 3.14 due to the different initial conditions, although the value of the synchrony measure S_{PR} in both cases is identical. Parameter values as in Figure 3.14. The system was initialised from a perturbed synchronous state where the perturbation was smaller than that in Figure 3.14. Transients not shown.

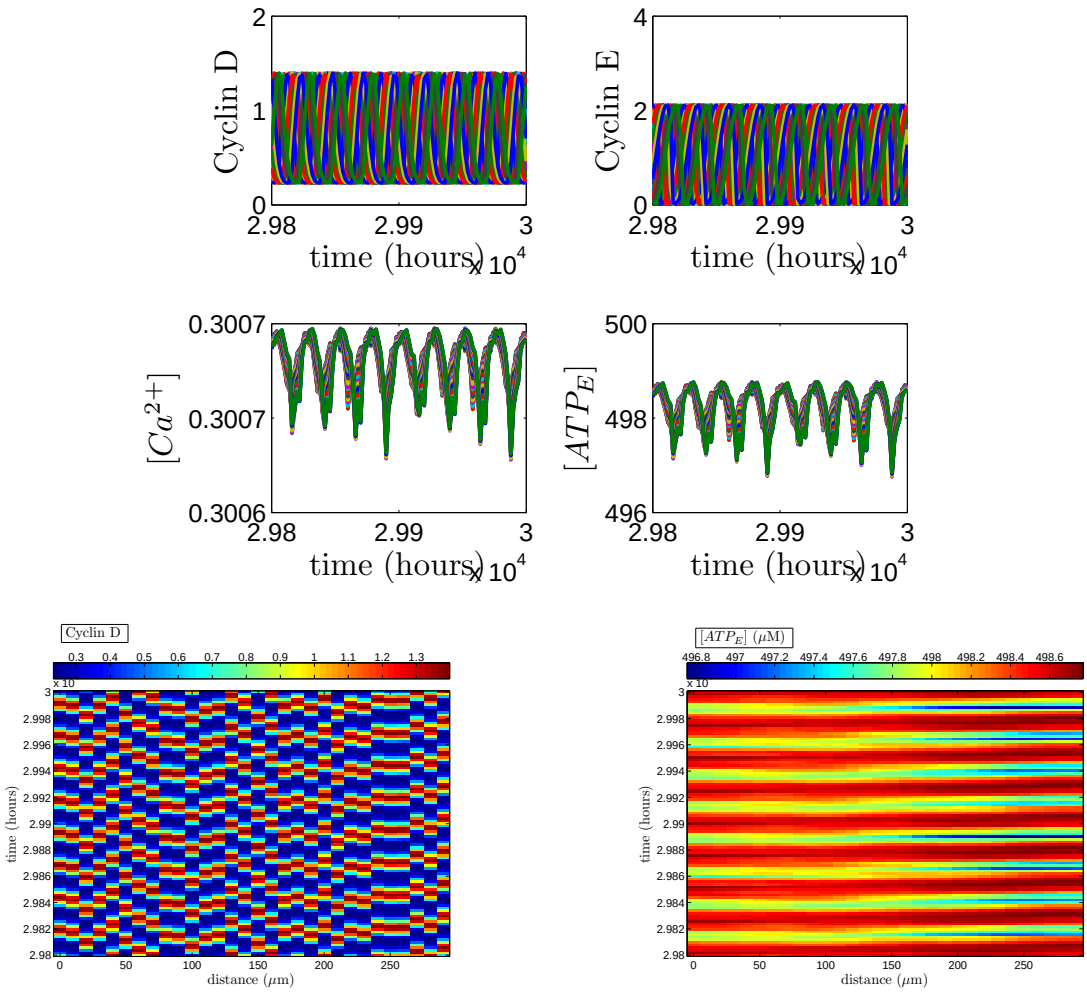

Figure 3.16: Simulations of system (3.1)-(3.14) for 30 cells with R_s dependent ATP release ($(H_i, H_c) = (R_{sc}, R_{si})$). The results show for the same parameter set as in Figure 3.14, a larger initial phase difference leads to the system evolving to a highly asynchronous solution. Parameter values as in Figure 3.14. $PD_{max} = 27$. Transients not shown.

lutions for two cells. Our analysis was inconclusive with regard to ascertaining the stability of the synchronous solution in large numbers of cells. The results of simulating the system under this parameter regime are shown in Figure 3.17. As in the two cell case (Figure 2.25), Figure 3.17 indicates that, for several cells, the synchronous state is unstable and the system settles down to an asynchronous (but near synchronous) phase locked state. The value of the synchrony measure S_{PR} in this case is 0.9743544. In this case the coupling brings about a reduction in the period of the cell cycle of 0.64 hours. In order to confirm that the synchronous solution was unstable, we simulated the system from a initial state slightly perturbed from the synchronous state (results not shown). In this instance the system evolved to a near synchronous solution. Our numerical simulations also revealed that as is the case for the results shown in Figure 3.14, there are many near synchronous solutions, each with the same value for S_{PR}, with the initial conditions determining which cell cycled out of phase with all other cells (results not shown).

As for the Cyclin D dependent model, we investigated via direct simulation how the ATP degradation rate V_{deg} affects the existence and stability of phase locked solutions for the R_s dependent ATP release model. The results of such simulations are displayed in Figure 3.18.

Although it appears that the synchronous state is unstable for all values of V_{deg} investigated, there exists a near synchronous solution in the R_s dependent model for all parameter values considered. The same can not be said of the Cyclin D dependent model, the results of which are shown in Figure 3.10, as in the case when the stability of the synchronous solution is lost at $V_{deg} \approx 0.06$ the two phase locked solutions that persist were highly asynchronous.

Fixed ATP degradation rate V_{deg}

Up until this point we have considered parameter regimes with relatively low values for the ATP degradation rate V_{deg} for the R_s dependent ATP release model. Our results for the Cyclin D dependent model showed that the system displayed different qualitative behaviour under parameter sets which included high values of V_{deg}. In this section we investigate whether such parameter regimes significantly change the dynamics of the system in the R_s dependent ATP release model.

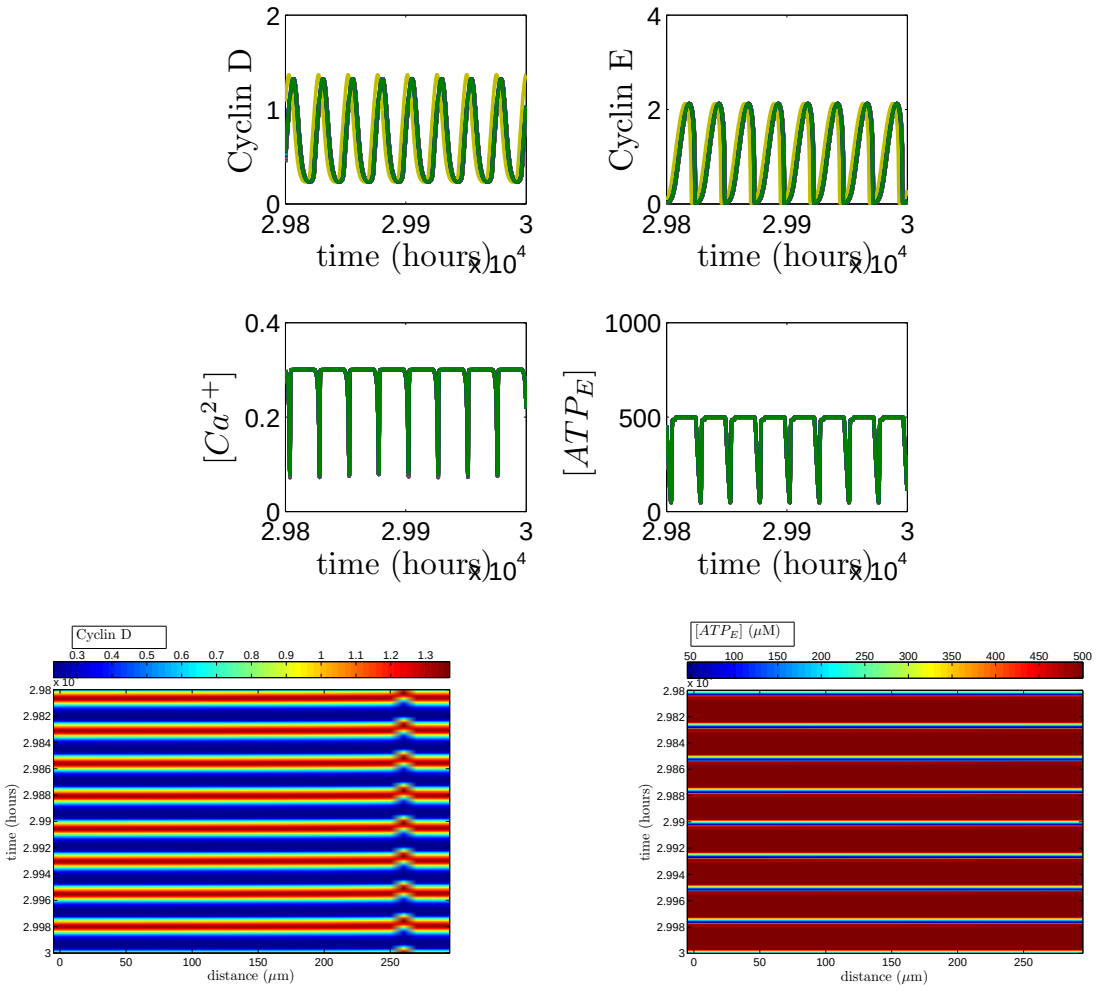

Figure 3.17: Simulations of system (3.1)-(3.14) for 30 cells with R_s dependent ATP release ($(H_i, H_c) = (R_{sc}, R_{si})$). The simulations indicate that the synchronous solution is unstable, although there exists a stable near synchronous solution, as was the case for the two cell system for this parameter set (Figure 2.23). Parameter values given in Table 2.2 except for $\gamma = 1.4$ and $V_{deg} = 0.04$. $PD_{max} = 27$. Transients not shown.

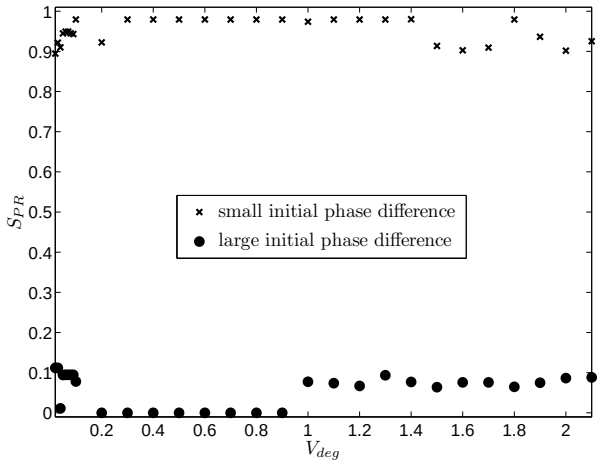

Figure 3.18: Plot showing how the synchrony measure S_{PR} depends upon V_{deg} for system (3.1)-(3.14) of 10 cells with R_s dependent ATP release ($(H_i, H_c) = (R_{sc}, R_{si})$). The results indicate that that stable near synchronous and stable asynchronous solutions co-exist. The system was simulated twice for each value of V_{deg} considered, once with $PD_{max} = 1$ (small initial phase difference) and once with $PD_{max} = 27$ (large initial phase difference). The synchrony measure S_{PR} was taken once the system had settled down to a stable oscillatory solution. Parameter values as in Table 2.2, except for V_{deg} as given and $\gamma = 1.2$. Solutions obtained using `ode23s` within Matlab

As for the Cyclin D dependent release model under a similar parameter regime, for a small initial phase difference between the cells the trajectory of the system settles down to a stable synchronous state (Figure 3.19) and there also exists a stable asynchronous phase locked state (Figure 3.20). In the latter case the spatial coupling brings about a reduction in the period of the cell cycle from 28.13 to 26.925 hours. The synchrony measure of this particular solution is 0.1680679.

As before, via direct numerical integration we investigated the dependence of the existence and stability of the phase locked solutions on the value for the calcium coupling strength γ for a system of 10 cells. The results shown in Figure 3.21 show that the stability of the synchronous solution for the R_s dependent ATP release is far more tolerant of changes in γ than in the Cyclin D dependent case, although it it is eventually rendered unstable for a sufficiently large value of $\gamma \approx 1.2$. However, even after this point the solutions are near synchronous. At $\gamma = 1.3$, for example, the synchrony measure is 0.9994. It is also apparent from Figure 3.21 that there exists a branch of asynchronous solutions under this parameter regime, which persists as γ is increased. In summary, there always exist a stable synchronous or near synchronous solution for the R_s dependent model under parameter sets where V_{deg} is relatively high. The results displayed in Figure 3.13 reveal that this is not the case for the Cyclin D dependent model however.

3.6 Two Dimensional Simulations

In this section we simulate our two models on square grids. As two dimensional simulations are computationally expensive (the simulations in Figure 3.23 took nearly 24 hours on a single AMD Opteron 64-bit processor in a Sun X4100 machine for example) we consider only a small number of specific cases in order to investigate whether the results of our analysis hold for several cells in two spatial dimensions and to investigate whether the behaviour discovered in the previous section persists in two spatial dimensions.

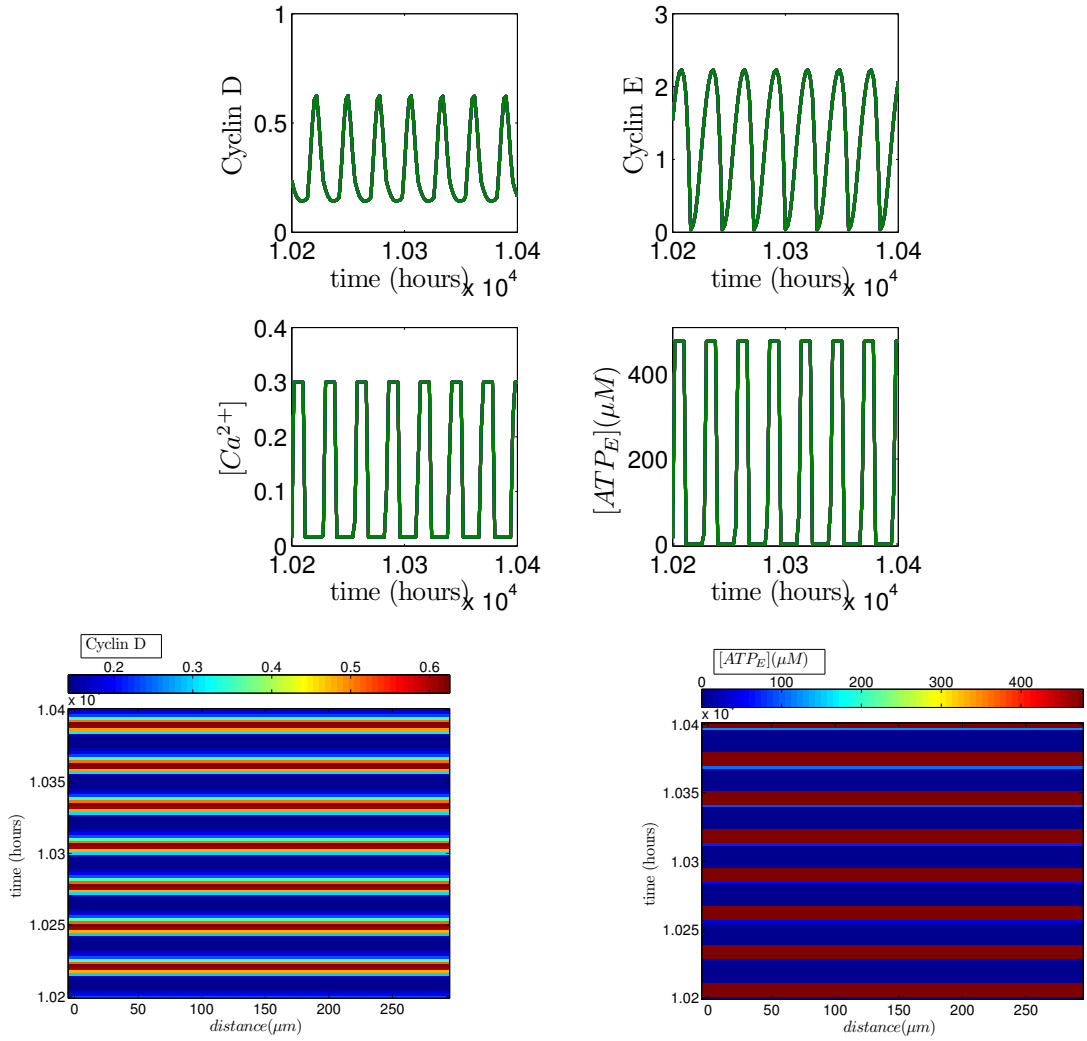

Figure 3.19: Simulations of system (3.1)-(3.14) for 30 cells with R_s dependent ATP release ($(H_i, H_c) = (R_{sc}, R_{si})$). The results show that with a small initial phase difference the system evolves to a stable synchronous solution for this parameter set. Parameter values given in Table 2.2 except for $V_{deg} = 2\,\mu\text{Ms}^{-1}$. $PD_{max} = 1$. Transients not shown.

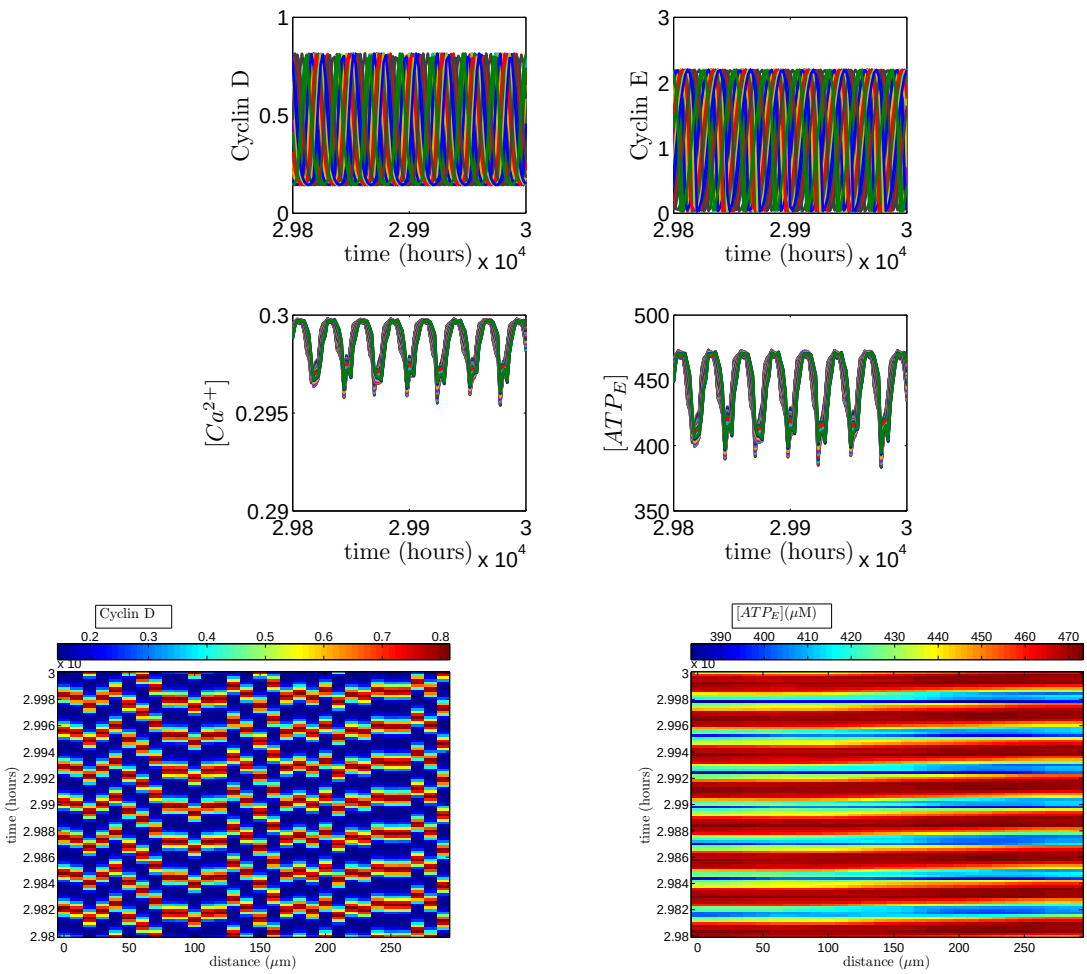

Figure 3.20: Simulations of system (3.1)-(3.14) for 30 cells with R_s dependent ATP release ($(H_i, H_c) = (R_{sc}, R_{si})$). The results indicate that in addition to the stable synchronous solution shown in Figure 3.19, a stable asynchronous solution also exists under the same parameter regime. Parameter values given in Table 2.2, except for $V_{deg} = 0.01\mu\text{Ms}^{-1}$. $PD_{max} = 27$ hours. Transients not shown.

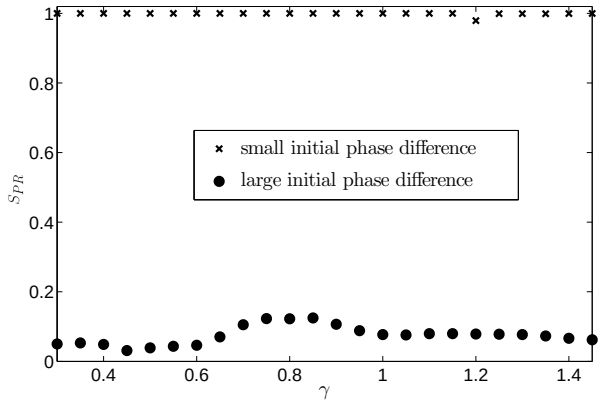

Figure 3.21: Plot showing how the synchrony measure S_{PR} (defined in Section 3.4) depends upon γ for system (3.1)-(3.14) of 10 cells with R_s dependent ATP release ($(H_i, H_c) = (R_{sc}, R_{si})$). The results indicate that that the stability of synchronous solutions is lost at $\gamma \approx 1.2$, however beyond this stable near synchronous solutions were discovered. Stable highly asynchronous solutions also exist for all parameter sets considered. The system was simulated twice for each value of γ considered, once with $PD_{max} = 1$ (small initial phase difference) and once with $PD_{max} = 27$ (large initial phase difference). The synchrony measure S_{PR} was taken once the system had settled down to a stable oscillatory solution. Parameter values as in Table 2.2, except for $V_{deg} = 2\ \mu\text{Ms}^{-1}$ and γ as shown. Solutions obtained using `ode23s` within Matlab.

3.6.1 Cyclin D Dependent ATP Release

We first consider the Cyclin D dependent model and attempt to confirm the results of our analysis. In Section 3.3.1 the theory of weakly coupled oscillators predicted that for $\gamma = 0.4$ and $V_{deg} = 0.01\,\mu\text{Ms}^{-1}$ the synchronous solution would be stable for systems of several cells in two spatial dimensions. Figure 3.22 reveals that this is indeed the case, showing that, for a small initial phase difference, the system settles down to a synchronous solution. As in the one dimensional case, we investigated whether another phase locked solution existed by simulating the system again but with a larger initial phase difference. Figure 3.23 shows that, as in the one dimensional case, the system exhibits bistability with regard to stable phase locked solutions in two spatial dimensions. In this particular case the system settled down to an asynchronous state of synchrony measure 0.02622549. As for all previous asynchronous solutions that we have encountered, the increased release of ATP brings about a reduction in the period of the cell cycle; in this case from 27.3 to 24.8 hours.

3.6.2 R_s Dependent ATP Release

We next turned our attention to the R_s dependent model. As before we attempted to confirm the predictions of our analysis for the two dimensional case. The theory of weakly coupled oscillators predicted that under a parameter regime which included $\gamma = 1.4$ and $V_{deg} = 0.1\,\mu\text{Ms}^{-1}$, a stable synchronous solution existed. We initiated the system with a small initial phase difference in an attempt to confirm this. The results shown in Figure 3.24 reveal that the system settles down to a near synchronous solution of synchrony measure 0.997439, indeed only one cell out of 100 is cycling out of phase. This is similar to the one dimensional case under this parameter regime, where we saw that one cell was cycling out of phase, with all others synchronised. Our analysis therefore has failed to predict the stability of the synchronous solution in the two dimensional case as well, although the solution shown in Figure 3.24 is very close to the synchronous solution. If the perturbation is very small (smaller than that in Figure 3.24), the synchronous solution is still lost, with S_{PR} of the resulting solution taking the same value as in Figure 3.24. In this case the initial conditions determine which cell ends up cycling out of phase from all other cells. This is the same phenomenon we encountered for the one dimensional case (discussed in Section 3.5.2). We next investigated whether a stable strongly asynchronous solution exists, as we saw was the case in one spatial dimension.

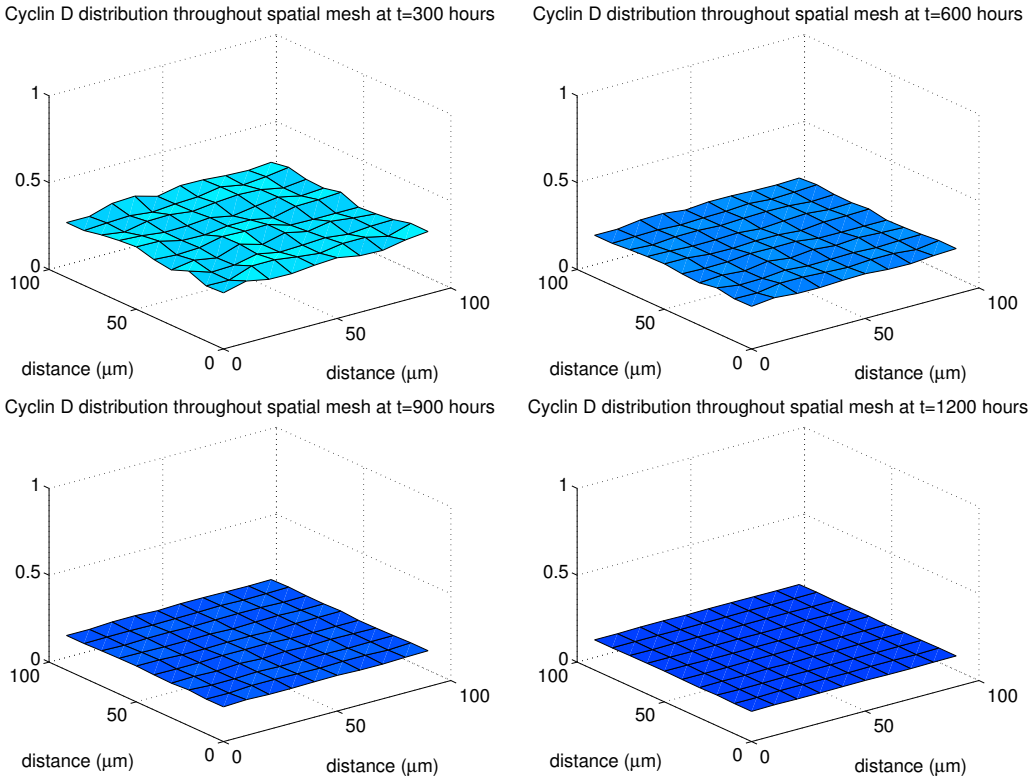

Figure 3.22: Simulations of system (3.1)-(3.14) for 100 cells for the Cyclin D dependent ATP release model ($(H_i, H_c) = (D_i, D_c)$). The plots show the concentrations of Cyclin D across the spatial domain at various times during the period of integration. To note, different colours represent different concentrations of Cyclin D. The results show that for a small initial phase difference between cells the solution trajectory of the system tends towards the synchronous solution, indicating that this solution is stable. $PD_{max} = 1$. System solved using `ode23s` within Matlab. Parameter values as in Table 2.2, except for $V_{deg} = 0.01\mu\text{Ms}^{-1}$.

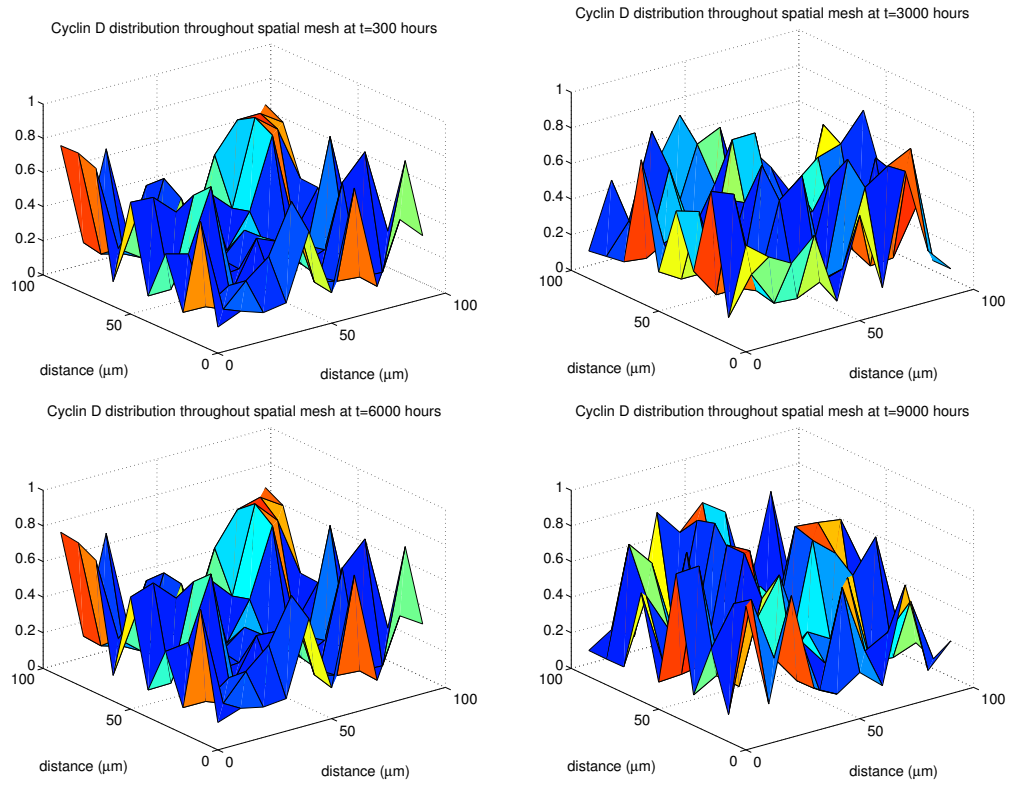

Figure 3.23: Simulations of system (3.1)-(3.14) for 100 cells for the Cyclin D dependent ATP release model ($(H_i, H_c) = (D_i, D_c)$). The results show that under the same parameter regime as in Figure 3.22, there exists a stable asynchronous solution, as was the case in one spatial dimension. $PD_{max} = 27$. Parameter values as in Figure 3.22.

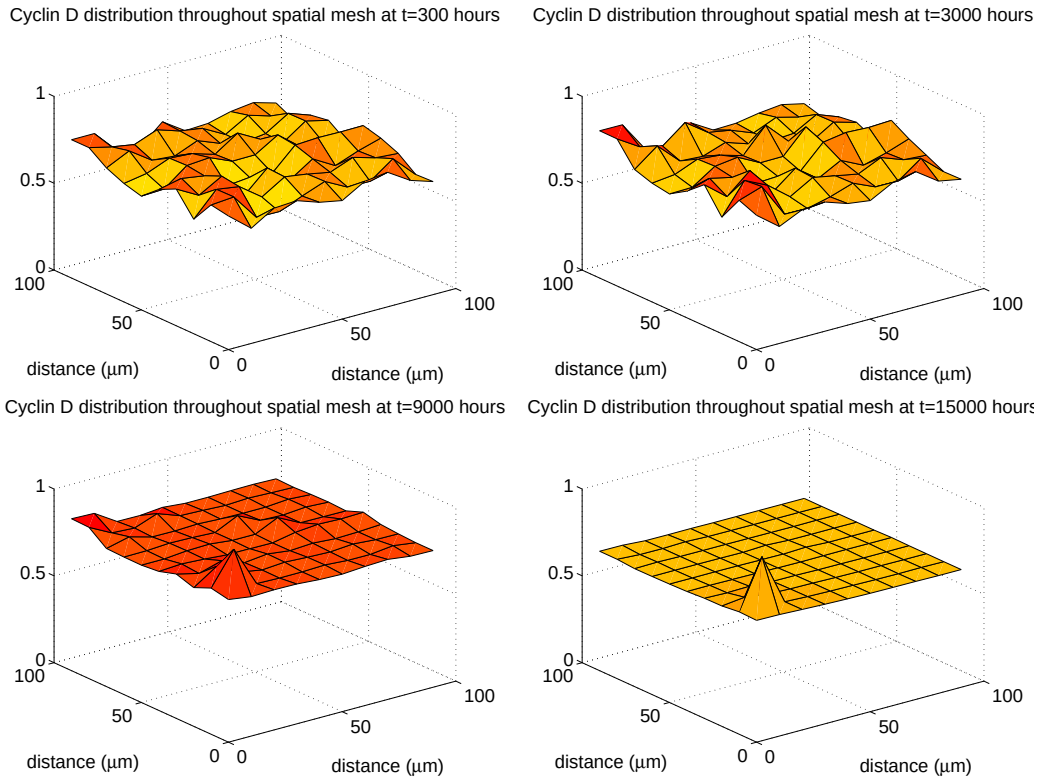

Figure 3.24: Simulations of system (3.1)-(3.14) for 100 cells for the R_s dependent ATP release model ($T(H_i, H_c, \varrho) = T(R_{sc}, R_{si}, \varrho)$). The simulations show that for an initially small phase difference between cells, the system evolves to a near synchronous solution, suggesting the synchronous solution is unstable, contrary to the predictions of the analysis. $PD_{max} = 1$. Parameter values as in Table 2.2 except for $\gamma = 1.4$ and $V_{deg} = 0.1\ \mu\text{Ms}^{-1}$.

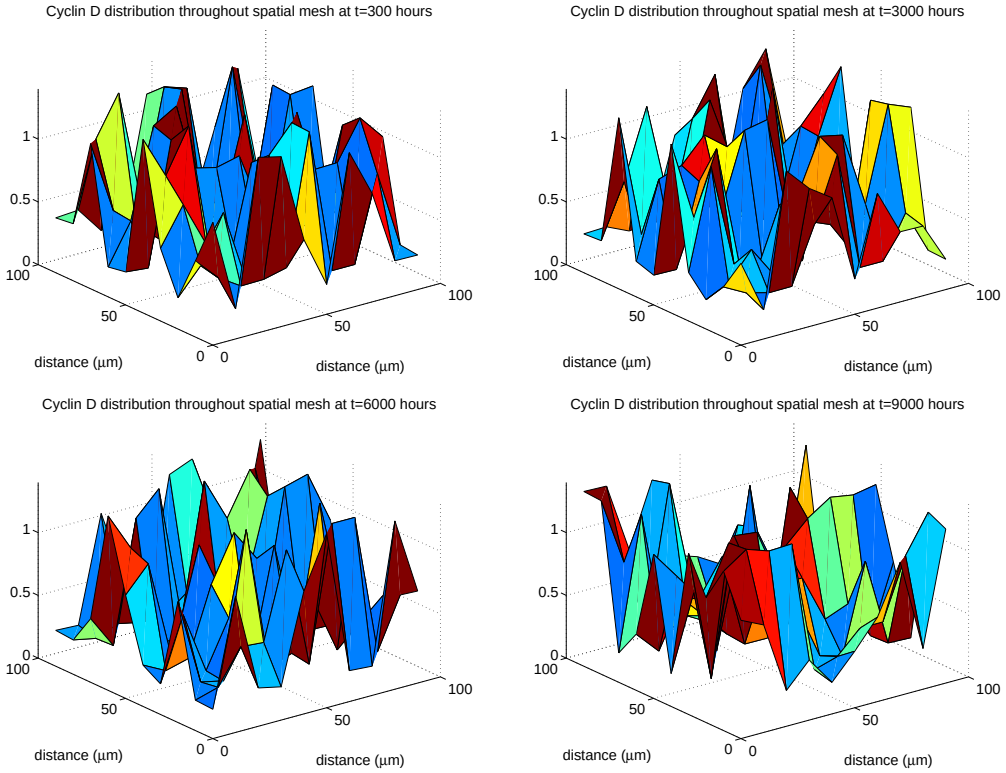

Figure 3.25: Simulations of system (3.1)-(3.14) for 100 cells for the R_s dependent ATP release model ($T(H_i, H_c, \varrho) = T(R_{sc}, R_{si}, \varrho)$). The simulations show that for the same parameter set as in Figure 3.24, there exists a stable highly asynchronous solution. $PD_{max} = 27$. Parameter values as in Figure 3.24.

Figure 3.25 shows that as in the one dimensional case, a highly asynchronous stable solution exists, of synchrony measure $S_{PR} = 0.0093874$ (cf. $S_{PR} = 0.08822138$ for 30 cells in 1D (Figure 3.16)).

3.7 Conclusions and Further work

The results of this chapter suggest that release of ATP towards the middle of G_1 phase (Cyclin D dependent release) and release towards the end of G_1 phase (R_s dependent ATP release) can both lead to the synchronous phase locked solutions which have been hypothesised in the biological literature. Generally speaking, the behaviour of the system observed for two cells seems to persist when several cells in one and two spatial dimensions are considered. Indeed, bistability of phase locked solutions for both models was discovered under most, but not all, parameter regimes.

Our results in this chapter, which are summarised in Table 3.1, suggest that ATP release during the G_1/S phase transition (the R_s dependent ATP release model) is more likely to lead to synchronous or near synchronous behaviour than the case where ATP is released predominantly during mid G_1 phase (the Cyclin D dependent model). Indeed, for all parameter regimes considered there exists a stable synchronous or near synchronous solution for the R_s dependent ATP release model. This is not the case however in the Cyclin D dependent ATP model, where a stable synchronous solution only exists under a minority of the parameter regimes that we considered (12 out of the 48 considered in Figures 3.10 and 3.13). Under all other parameter regimes, a stable asynchronous solution or solutions existed.

As covered in chapter 1, it has been postulated that synchronised radial glial cells may be responsible for the co-ordination of uniform cortical layers [93]. The results in this chapter suggest that ATP release as occurring during the G_1/S transition is likely to lead to radial glial cells cycling in a synchronous or near synchronous manner and hence may allow for the formation of uniform cortical layers during embryonic neurogenesis. The results from the Cyclin D dependent ATP release model suggest that ATP release during mid G_1 phase is more likely to lead to cells cycling asynchronously. Clusters of cells cycling in this

manner may interfere with the co-ordination of cortical layer formation. This suggests that the timing of ATP release by radial glial cells plays an important role during embryonic neurogenesis, with a malfunction in this timing potentially leading to irregular cortical formation which may be the cause of some neurological development disorders. It has been hypothesised that irregularities in cortical formation during embryonic development may lead to infantile epilepsies, mental retardation, dyslexia and in certain conditions, even Huntington's and Alzheimer's disease [4, 70] for example. In order to confirm this however it would be desirable to run more simulations to extend the parameter regimes considered and also investigate more deeply the relationship between the number of cells and the degree to which the system is synchronised.

Additionally, it may be interesting to incorporate cell death and daughter cell production into our model. The introduction of daughter cells into the cellular population (resulting from the completion of the cell cycle) and the removal of cells from the population (due to apoptosis), during the period of integration may have an effect upon the existence and stability of phase locked solutions. However, for reasons of time, we do not consider such effects in our models, in this thesis.

Although the coupling in our model can act to promote synchrony and hence can account for well co-ordinated cortical layer formation, it can not account for the degree to which ATP release enhances overall cell proliferation in a system where all cells are initially cycling. In the previous chapter we postulated that the areas of bistability and multistability present in the bifurcation diagram of the single cell system (see Figure 2.10) may play a key role in the mechanism that is responsible for increased radial glia proliferation. We postulated that a 'driver' cell, may via the release of extracellular ATP induce a quiescent cell in G_0 phase onto the cell cycle, which may account for increased cell proliferation. In the next chapter we investigate whether this is possible.

Table 3.1: Summary of results

	mid G_1 ATP release	G_1/S ATP release
	Cyclin D dependent ATP release model	R_s dependent ATP release model
low γ, high V_{deg}	Stable synchronous and asynchronous solutions. Figures 3.11,3.12 and 3.13.	Stable synchronous and asynchronous solutions. Figures 3.19, 3.20 and 3.21.
high γ, high V_{deg}	Unstable synchronous solution stable asynchronous solution. Figures 3.9, 3.10 and 3.13.	Unstable synchronous. Stable near synchronous and asynchronous. Figures 3.18 and 3.21.
low γ, low V_{deg}	Stable synchronous and asynchronous solutions. Figures 3.7, 3.8, 3.22 and 3.23.	
high γ, low V_{deg}	Unstable synchronous. Two stable asynchronous solutions. Figure 3.10.	Unstable synchronous. Stable near synchronous and asynchronous. Figures 3.14, 3.15, 3.16, 3.17, 3.18, 3.24 and 3.25.

Chapter 4

Cell Cycle Recruitment of Quiescent Cells

4.1 Introduction

Although the results of the previous chapters proved promising in accounting for synchronous behaviour in radial glial cells, they also suggested that calcium coupling alone could not account for the increase in the rate of radial glia proliferation, where all cells are initially cycling. In this chapter, we investigate whether the increase in proliferation can be accounted for by the ability of radial glial cells to recruit quiescent cells in G_0 phase into G_1 phase and onto the cell cycle.

We begin our investigation by re-introducing the bifurcation diagrams of a single cell system for both models and comment upon how the area of multistability in both models may provide a mechanism for the recruitment of a quiescent cell onto the cell cycle by a driving cell. We then, through bifurcation analysis and direct numerical simulations consider systems of two cells for both models in order to explore the range of behaviour exhibited for the two cell system.

With this complete, we then investigate via direct numerical simulation not only the ability of a driving cell to recruit a quiescent cell onto the cell cycle, but also the duration for which (if at all) the two cells remain entrained in a synchronous manner for both models under several different parameter regimes. We then devote the remainder of the chapter to extending the results of two cells to systems of several cells. Due to lack of time, we do not consider the continuum analogue of our models in this chapter; instead we focus upon obtaining numerical results from our discrete models.

4.2 Bifurcation Analysis

4.2.1 Cyclin D Dependent ATP Release

We begin our analysis by re-introducing in Figure 4.1 the bifurcation diagrams we first saw in chapter 2 for the Cyclin D dependent ATP release model, where ATP is modelled as predominantly occurring during mid G_1 phase of the cell cycle. In order to do this, we replace (H_i, H_c) in equation (3.14) with (D_i, D_c) in all calculations. From Figure 4.1 it is clear that there exists an area of multistability which is bounded on one side by either the point marked $FP1^D$ or $FP2^D$ depending on the parameter regime chosen. A cell is considered quiescent when it sits on the stable fixed point branch at the bottom of the figure, or on the stable branch of low amplitude limit cycle solutions which bifurcates from this branch at the Hopf bifurcation point [66]. Consequently, a quiescent cell will either lie within the area of multistability or, when a'_{d1} (the Cyclin D synthesis rate in absence of calcium) is sufficiently small ($a'_{d1} < \min(FP1^D, FP2^D)$), outside the area of multistability. In the former case one would intuitively expect that a pacemaker cell could induce the quiescent cell onto the branch of stable high amplitude limit cycle solutions above, where it would remain. In the latter case one would expect that a pacemaker cell could, via the release of extracellular ATP, sweep a quiescent cell into and out of the area of multistability. In this particular case we anticipate that the sweeping of the quiescent cell into and out of the area of multistability would be sufficient to induce oscillations in this cell.

In order to study whether our intuition is correct, we calculated the bifurcation diagram for two cells, shown in Figure 4.2. In calculating this diagram we fixed the value of a'_{d1} (the value of the Cyclin D synthesis rate in cell 1) and varied a'_{d2} (the value of the Cyclin D synthesis rate in cell 2).

Figure 4.2 reveals that for small values of $a'_{d2} < 0.3795$ (TB), there exists a stable branch of limit cycle solutions. However, the amplitude of the oscillations of the entrained cell is so small that it can not be considered as being on the cell cycle. Increasing a'_{d2} eventually leads to a torus bifurcation point (marked TB on the diagram) beyond which the solution trajectory of our 2 cell system sits on a n-dimensional torus. In addition to the torus so-

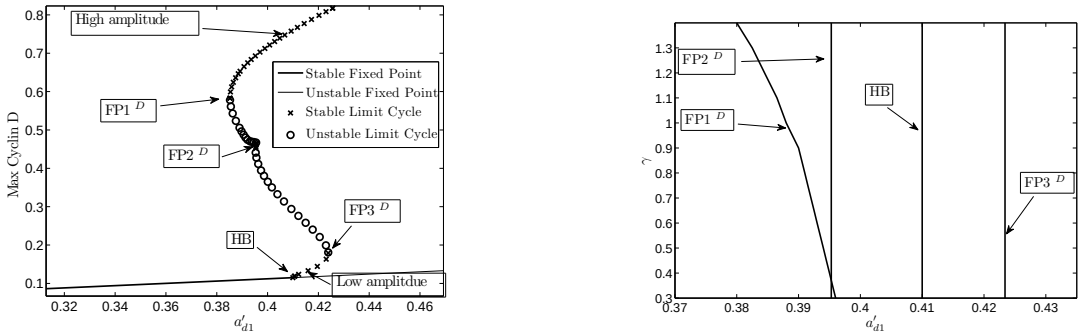

Figure 4.1: Bifurcation diagrams for a single cell of system (3.1)-(3.14) for the Cyclin D dependent ATP release model ($(H_i, H_c) = (D_i, D_c)$). As we have previously done when calculating single cell bifurcation diagrams, we replace equation (3.11) with its steady state approximation. HB corresponds to a Hopf bifurcation point. The first bifurcation diagram reveals an area of multistability which is bounded on one side by one of two fold points ($FP1^D$ and $FP2^D$), depending on the value of γ and on the other side by the fold point marked $FP3^D$. In this area there exists either a branch containing stable limit cycle solutions or a branch containing stable limit cycle solutions and a branch of stable fixed point solutions. The second diagram shows how these fold points ($FP1^D$, $FP2^D$ and $FP3^D$) depend upon γ and a'_{d1}. Parameter values as for Table 4.2, except for $V_{deg} = 2\,\mu\text{Ms}^{-1}$, $\gamma = 1$ or as shown and a'_{d1} as shown. AUTO within XPP was used to produce both diagrams.

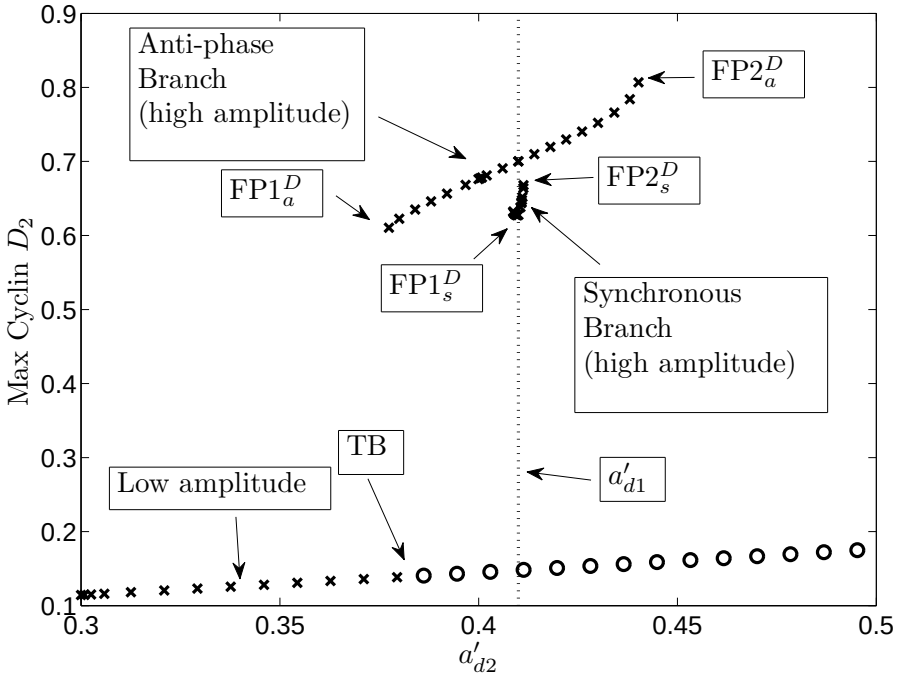

Figure 4.2: Bifurcation diagram of two cell Cyclin D dependent ATP release system ($(H_i, H_c) = (D_i, D_c)$). TB corresponds to a torus bifurcation point, FP1$_s^D$, FP1$_a^D$, FP2$_s^D$, FP2$_a^D$ correspond to saddle node bifurcation or fold points of the limit cycle solutions. The diagram reveals the existence of torus solutions and two branches of high amplitude limit cycle solutions in the two cell system. The parameter values are as in Table 4.2, except for $V_{deg} = 2\ \mu\text{Ms}^{-1}$ and a_{d2} as shown.

lution there also exist two more stable high amplitude limit cycle solutions. Although we have named the lower branch the synchronous solution branch and the upper branch the anti-phase phase locked solution branch, this is slightly misleading. This is because it is only for $a'_{d1} = a'_{d2} = 0.41$ that these branches correspond to the synchronous and anti-phase phase locked solutions. For $a'_{d1} \neq a'_{d2}$, both solutions are in fact asynchronous. Naming the two branches the synchronous branch and anti-phase branch provides a convenient way to distinguish between the two branches. When $a'_{d1} \neq a'_{d2} \neq 0.41$, the 'synchronous' branch is in fact near synchronous and the 'anti-phase' branch is highly asynchronous. Both of these branches correspond to phase locked solutions and it appears that for sufficiently disparate values for the two cells' intrinsic frequencies, which are partly governed by a'_{d2}, their stability is lost via saddle node bifurcations of limit cycle solutions (marked $\mathrm{FP1}_s^D$, $\mathrm{FP1}_a^D$, $\mathrm{FP2}_s^D$ and $\mathrm{FP2}_a^D$). We were unable to continue beyond $\mathrm{FP1}_s^D$, $\mathrm{FP1}_a^D$, $\mathrm{FP2}_s^D$ and $\mathrm{FP2}_a^D$ to detect the unstable limit cycle solutions. However, we took the last stable solution detected, changed the value of the control parameter slightly and then numerically integrated the system. In all cases, the system evolved to a solution which was qualitatively different to the limit cycle solution of the original parameter value. This suggests that $\mathrm{FP1}_s^D$, $\mathrm{FP1}_a^D$, $\mathrm{FP2}_s^D$ and $\mathrm{FP2}_a^D$ correspond to saddle node bifurcation points. Furthermore, XPP does not have the capacity to continue torus solutions and consequently we were unable to detect where the branch of torus solutions goes nor ascertain where the stability of the branch of torus solutions is lost. Our numerical simulations revealed that the stable phase locked solutions and stable torus solutions co-exist, at least for some values of a'_{d2}.

In order to demonstrate the different behaviours that are indicated in Figure 4.2, we simulated the system for two different parameter regimes, one where torus solutions existed and one where they did not. Figure 4.3 shows that, for sufficiently small values of a'_{d2} ($a'_{d2} = 0.35$ in the first row of plots), there exists a low amplitude stable limit cycle solution and it can be seen in this case that the two cells cycle in an almost synchronous manner. However, the amplitude of oscillation of the entrained cell is so small that it can not be considered to be cycling. For $a'_{d2} = 0.4$ (the second row of plots), the system exhibits torus solutions, although it is interesting to note by referring to Figure 4.1, that there also exist phase locked solutions under this parameter regime. With the particular initial conditions of Figure 4.3 the trajectory of the solutions tends to the torus solutions rather than the phase locked solutions. It is possible, by integrating the system from other sets of initial conditions, for the system to display limit cycle solutions. Interestingly, the torus solu-

tion appears to oscillate between a near synchronous solution and a near anti-phase phase locked solution. We next, through the calculation of a two parameter bifurcation diagram, explored how the stability of the high amplitude phase locked solutions depended upon both a'_{d2} and γ, which represents the strength of the calcium coupling. Our results are displayed in Figure 4.4.

Figure 4.4 indicates that there exists a large area in parameter space where the system exhibits stable phase locked solutions with both cells on the cell cycle. Interestingly, it is clear from the plots of FP1^D,FP2^D and FP3^D in Figure 4.4 that this area lies far outside the area of multistability seen in Figure 4.1. Although this area is large, direct numerical simulation suggests that it co-exists with the branch of stable torus solutions for at least some of the parameter values considered in the figure and therefore it can not be guaranteed that a system would always exhibit limit cycle solutions, even if they existed.

These results suggest that our two cell Cyclin D dependent ATP release model is capable of sustaining oscillations in both cells, where both cells can be considered as being on the cell cycle. This appears to be the case under several different parameter regimes, with these oscillations resulting from limit cycle or torus solutions. This is a promising result with regard to investigating a driving cell's ability to recruit a quiescent cell onto the cell cycle.

4.2.2 R_s Dependent ATP Release

We next turned our attention to the model for ATP release during the G_1/S phase transition, using $(H_i, H_c) = (R_{sc}, R_{si})$ in equation (3.14). The single cell bifurcation diagram for this model, that we first encountered in chapter 2 is reproduced in Figure 4.5. It is clear from this figure that, similar to the Cyclin D dependent case, there exists an area of bistability which is bounded on one side by the point marked FP1^{Rs} and on the other by a point marked FP2^{Rs}. As before, a cell is considered to be quiescent when it sits on the stable fixed branch at the bottom of the figure, or the stable branch of low amplitude limit cycle solutions that bifurcates off this branch at the Hopf bifurcation point. As for the Cyclin D dependent model, we calculated the bifurcation diagram for a two cell system, using a'_{d2}, the Cyclin D synthesis rate in cell 2 in the absence of calcium as the bifurcation parameter. This diagram can be seen in Figure 4.6.

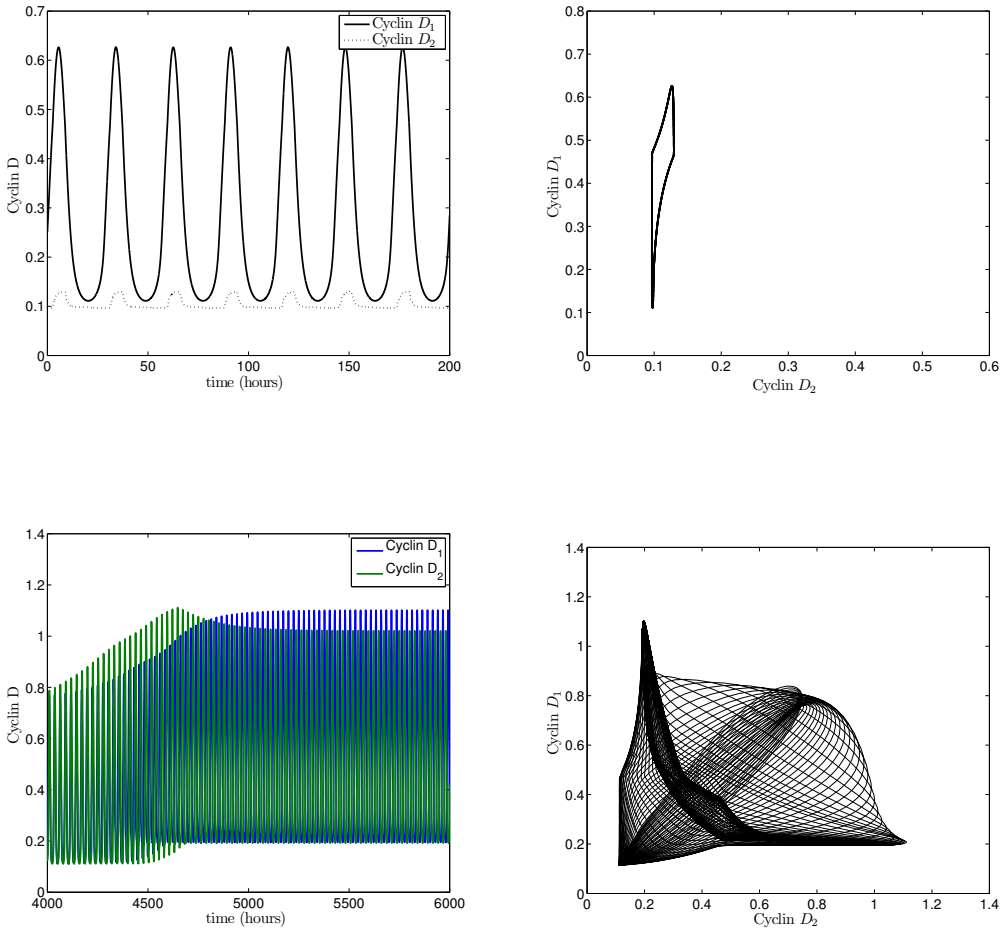

Figure 4.3: Simulations for 2 cells of system (3.1)-(3.14) for Cyclin D dependent ATP release ($(H_i, H_c) = (D_i, D_c)$) . The parameter values are as in Table 4.2, except for $V_{deg} = 2\ \mu\text{Ms}^{-1}$, and $a'_{d2} = 0.35$ in the first row of plots and $a'_{d2} = 0.4$ in the second row of plots. Initial conditions were such that cell 1 (the driving cell) sat on the branch of stable limit cycle solutions and cell 2 (the quiescent cell) sat on the branch stable fixed point solutions shown in Figure 4.1. The plots confirm the existence of the low amplitude limit cycle solutions and torus solutions indicated by the bifurcation diagrams in Figure 4.2. Results were obtained using `ode23` within Matlab.

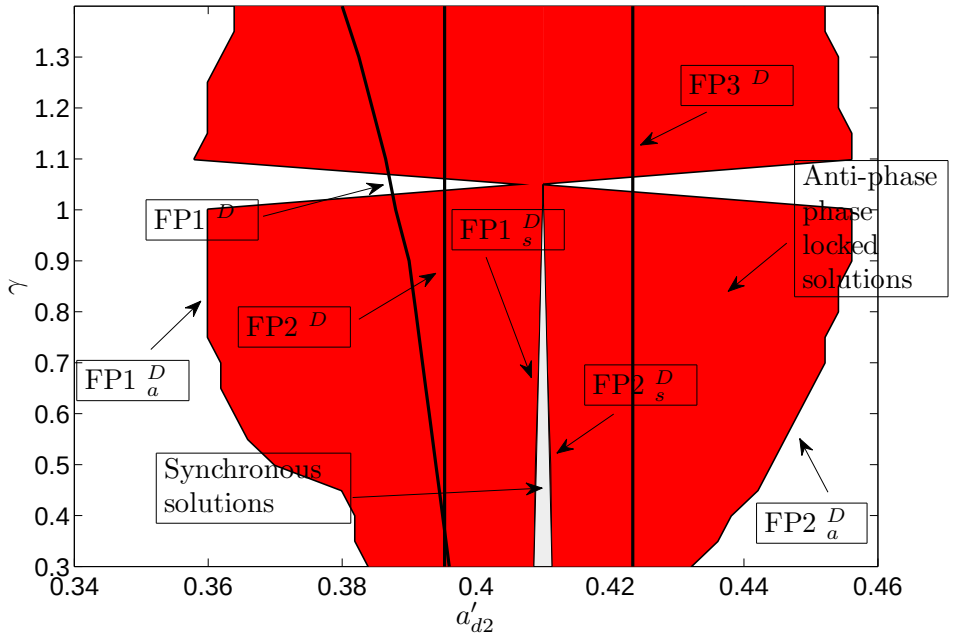

Figure 4.4: Two parameter bifurcation diagram for the existence of stable phase locked solutions of system (3.1)-(3.14) for Cyclin D dependent ATP release ($(H_i, H_c) = (D_i, D_c)$). FP1^D, FP2^D and FP3^D correspond to the fold points from Figure 4.1, while FP1_s^D, FP1_a^D, FP2_s^D and FP2_a^D correspond to the fold points from Figure 4.2. The area where anti-phase phase locked solutions exist is coloured red, while the area where synchronous solutions exist is coloured light grey. Note that all synchronous solutions co-exist with anti-phase phase locked solutions and the stability of synchronous solutions is lost at $\gamma \approx 1.05$ (discussed in chapter 2). The figure shows that phase locked solutions for two cells (bounded by FP1_a^D and FP2_a^D) exist under parameter regimes that lie outside the area of multistability of the single cell system (bounded by FP1^D, FP2^D and FP3^D). The parameter values are as in Table 4.2, except for $V_{deg} = 2\ \mu\text{Ms}^{-1}$, γ and a_{d2} as shown. AUTO was used to calculate the bifurcation diagram except for FP1_a^D and FP2_a^D, which were calculated via direct numerical simulation using `ode23` within Matlab using a prediction-correction scheme. Under this scheme, we numerically integrated the system under a certain parameter regime and then used the method outlined in Section 3.5 to ascertain the stability of the resultant solution. We then changed the value of the control parameter and repeated the process until the resulting solution did not exhibit limit cycle behaviour.

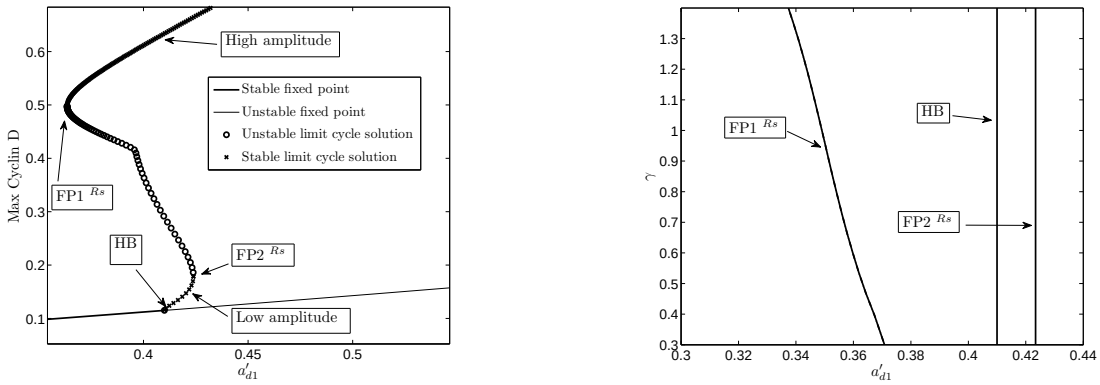

Figure 4.5: Bifurcation diagrams for a single cell of system (3.1)-(3.14) for the R_s dependent ATP release model ($(H_i, H_c) = (R_{sc}, R_{si})$). As before, in order to produce the single cell bifurcation diagram, the steady state approximation is assumed for equation (3.11). HB corresponds to a Hopf bifurcation point, FP1^{Rs} and FP2^{Rs} to fold or saddle node bifurcation points. The diagrams reveal an area of bistability where both stable limit cycle and stable fixed point solutions co-exist. Parameter values as for Table 4.2, except for $V_{deg} = 2\,\mu\text{Ms}^{-1}$, a'_{d1} as shown in all plots and γ as shown in the second plot. AUTO within XPP was used to produce both diagrams.

The parameter space in Figure 4.6 is similar to the one we encountered for the Cyclin D dependent model in Figure 4.2. There exists a branch of limit cycle solutions for $a'_{d2} < 0.366313$, where the amplitude of oscillations of the second cell are very small. Interestingly, at $a'_{d2} \approx 0.366313$ (TB) the stability of these solutions is lost at a supercritical torus bifurcation point. At $a'_{d2} \approx 0.4026$ (FP1$_s^{Rs}$), a branch of large amplitude limit cycle solutions is created via a saddle node bifurcation, before being destroyed by a saddle node bifurcation at $a'_{d2} \approx 0.415$ (FP2$_s^{Rs}$). This is the branch of solutions that connects to the synchronous solution we first encountered in chapter 2. We were unable to continue the branch of torus solutions, but as was the case for the Cyclin D dependent model, numerical simulations indicate that torus solutions and higher amplitude phase locked solutions co-exist for some parameter regimes at least. Simulations of a 2 cell system which confirm the behaviour discovered by our analysis can be seen in Figure 4.7.

The first row of simulations in Figure 4.7 show that for a'_{d2} sufficiently small (here $a'_{d2} = 0.35$), stable limit cycle solutions exist for both cells, although the amplitude of the oscillations of the second, initially quiescent cell are very small. In this case, the cells do

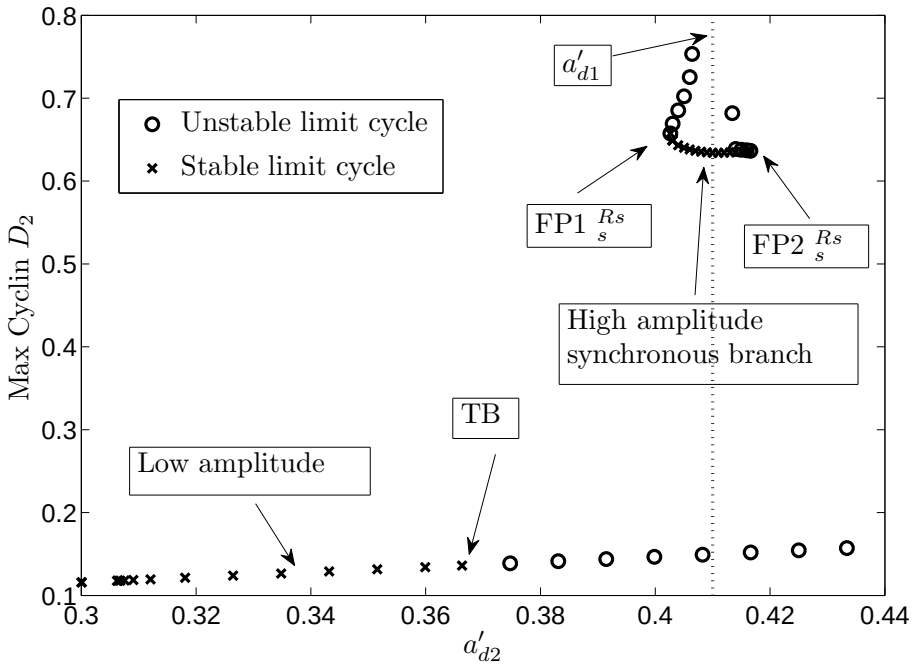

Figure 4.6: Bifurcation diagram of system (3.1)-(3.14) for 2 cells for the R_s dependent ATP release model ($(H_i, H_c) = (R_{sc}, R_{si})$). TB corresponds to a torus bifurcation point, FP1_s^{Rs} and FP2_s^{Rs} correspond to saddle node bifurcation or fold points of the limit cycle solutions. The diagram reveals the existence of torus solutions and a branch of limit cycle solutions. The parameter values are as in Table 4.2, except for $V_{deg} = 2\,\mu\text{Ms}^{-1}$ and a'_{d2} as shown. AUTO within XPP was used to produce the bifurcation diagram.

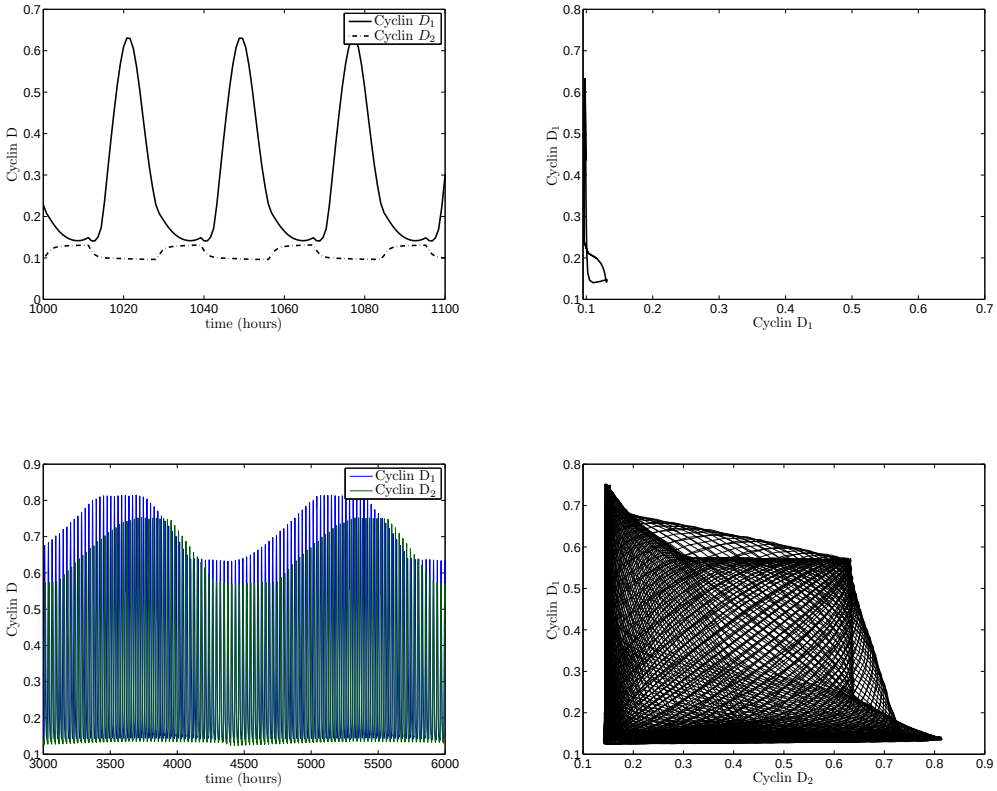

Figure 4.7: Simulations for 2 cells of the system (3.1)-(3.14) for the R_s dependent ATP release model ($(H_i, H_c) = (R_{sc}, R_{si})$). The parameter values are as in Table 4.2, except for $V_{deg} = 2\,\mu\text{Ms}^{-1}$, with $a'_{d2} = 0.35$ in the first row of plots and $a'_{d2} = 0.38$ in the second row of plots. Initial conditions were such that cell 1, the driving cell, sat on the branch of stable limit cycle solutions and cell 2, the initially quiescent cell sat on the branch of stable fixed point solutions in Figure 4.5. The results illustrate how our two cell system can sustain low amplitude limit cycle as well as torus solutions, confirming the behaviour discovered by our bifurcation analysis.

not cycle synchronously as is clear when one compares the peaks of the Cyclin D levels of the two cells against each other in the top right hand plot of the figure. When a'_{d2} is sufficiently large (here $a'_{d2} = 0.38$) the system moves past the torus bifurcation point shown in Figure 4.6 and the stability of the stable low amplitude limit cycle solution is lost. Here the solution trajectory of the system sits on a higher dimensional analogue of a torus as can clearly be seen in the second row of plots in Figure 4.7. The maximum Cyclin D concentration of the formerly quiescent cell is far larger under the parameter regime that leads to torus solutions than it is under the regime that lead to the lower branch of stable limit cycle solutions, even though the difference in the value for a'_{d2} between these regimes is relatively modest. This becomes clear when one inspects the second column of plots in Figure 4.7

Under the parameter regime considered above, the low amplitude stable limit cycle solutions become unstable at $a'_{d2} \approx 0.366313$, which is very close to the left boundary of the area of bistability for a single cell ($a'_{d1} = 0.3673167$, marked FP ^{Rs} in Figure 4.5).

Figure 4.8 shows a two parameter bifurcation diagram, including the bistability boundary and the region where low amplitude limit cycles are stable. It is clear that the point at which the stable limit cycle solutions become unstable does not necessarily correspond to the point at which the quiescent cell enters the area of bistability. There exist stable torus solutions for the system, where the parameter regime for the quiescent cell is such that it lies outside the area of bistability shown in Figure 4.5. Indeed as γ is increased, the torus bifurcation point moves further away from the boundary of the area of bistability and hence further away from the area of bistability itself. This result is confirmed by simulating the system for two cells but with a high value for γ and with a value a'_{d2} such that the quiescent cell lies outside the area of bistability. The results of these simulations can be seen in the Figure 4.9.

In Figure 4.9, a'_{d2} takes a value of 0.33 which means that cell 2 lies outside the area of bistability for a single cell (Figure 4.5). However it can be seen that as predicted by our bifurcation analysis, the branch of low amplitude limit cycle solutions is unstable and the solution trajectory of the system sits on a n-dimensional torus.

Interestingly, by comparing Figures 4.8 and 4.4, the system with Cyclin D dependent

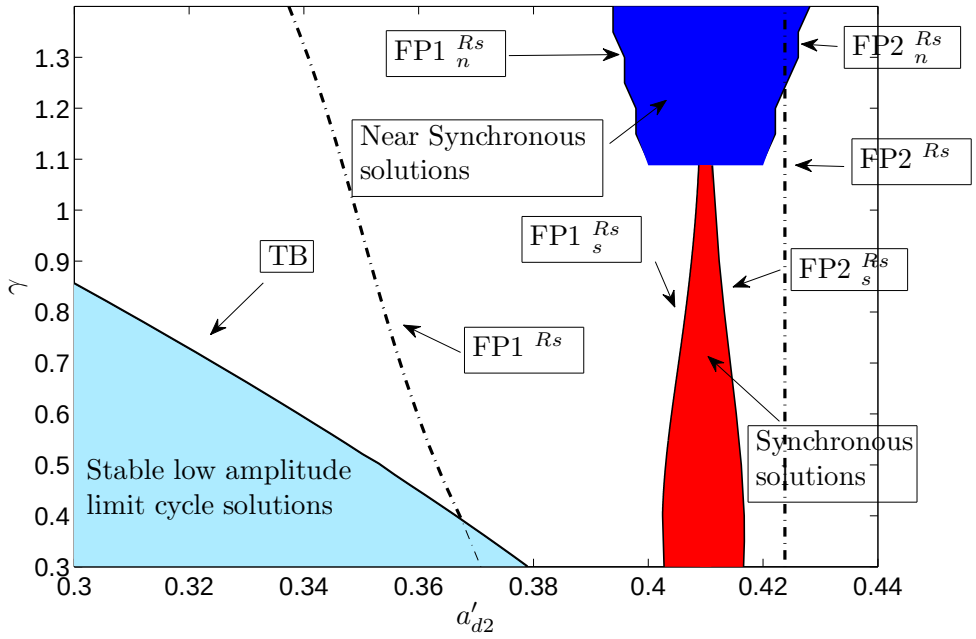

Figure 4.8: Two parameter bifurcation diagram of system (3.1)-(3.14) for two cells for the R_s dependent ATP release model ($(H_i, H_c) = (R_{sc}, R_{si})$). TB corresponds to a torus bifurcation point, FP1^{Rs}_{s} and FP2^{Rs}_{s} correspond to the fold points from Figure 4.6. At $\gamma \approx 1.088$ the stability of the synchronous solution is lost via a pitch fork bifurcation, leading to the creation of a stable near synchronous solution (discussed in chapter 2). FP1^{Rs}_{n} and FP2^{Rs}_{n} correspond to the points at which this solution is lost via saddle node bifurcation points. The diagram also contains a plot showing how the fold points (FP1^{Rs} and FP2^{Rs}) from Figure 4.5 which form the bounds of the area of bistability in the single cell system relate to γ and a'_d. The parameter values are as in Table 4.2, except for $V_{deg} = 2\,\mu\text{Ms}^{-1}$ and a_{d2} as shown. The diagram was calculated using AUTO within XPP, except for the calculating the area of near synchronous solutions. This was calculated via direct numerical integration using the same method as outlined in Figure 4.4.

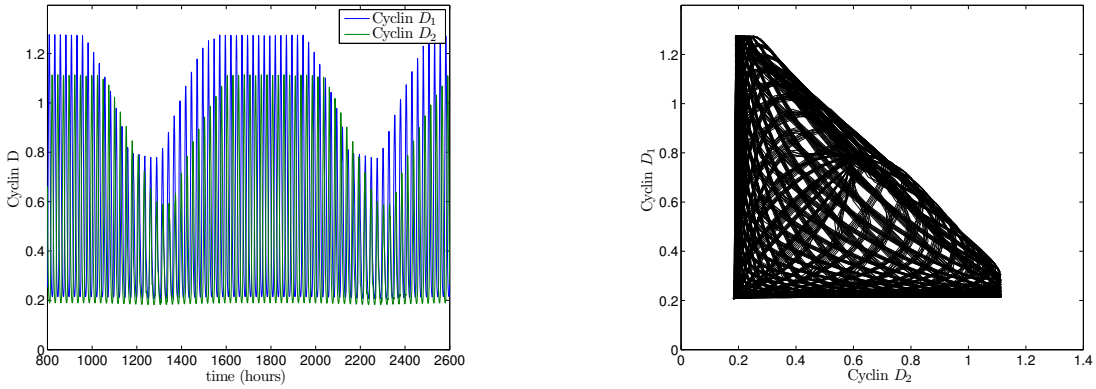

Figure 4.9: Simulations for 2 cells of system (3.1)-(3.14) for the R_s dependent ATP release model ($(H_i, H_c) = (R_{sc}, R_{si})$). Parameter values as for Table 4.2 except for $\gamma = 1.2$, $V_{deg} = 2\ \mu\text{Ms}^{-1}$ and $a'_{d2} = 0.33$. Initial conditions were such that cell 1, the driving cell sat on the branch of stable limit cycle solutions, while the cell 2, the initially quiescent cell sat on the branch of stable fixed point solutions in Figure 4.5. The results were obtained using `ode23` within Matlab and they show that even under a parameter regime where the initially quiescent cell lies outside the area of bistability of the single cell system, our two cell system is capable of sustaining high amplitude oscillations in both cells.

ATP release exhibits phase-locked solutions for a far wider range of values of γ and a'_{d2}. This suggests that it could be far more adept at recruiting a quiescent cell on the cell cycle and then for the two cell to phase lock, as it would theoretically be able to recruit quiescent cells in a phase locked manner that could not be recruited by the R_s dependent ATP release model.

4.3 Duration of Near Synchronous Entrainment

From our analysis, it appears that we can not always expect a quiescent cell to become induced onto the cell cycle. Even if this is the case the existence of torus solutions means that we can not always expect two cells to phase lock in a synchronous manner or otherwise. However, there remains the possibility that although we will not see synchronous behaviour in the long term, the shorter term transient behaviour of the system before it settles down to a stable solution may exhibit near synchronous behaviour. As the period in which neurogenesis takes place is relatively short, there remains the possibility that the two cells will be in near synchrony for a sufficiently long period of time, even if a synchronous or near synchronous solution is unstable or non existent. Neurogenesis in the rat embryo lasts 6 days while it has been estimated that in the human embryo it is far longer, of the order of 10 weeks [2, 12, 16]. It has been calculated that a proliferating cell cycles a total of 11 times during the period of neurogenesis in mice [12]. This number is likely to be far larger during embryonic neurogenesis in humans. We therefore decided to investigate the ability of a driving cell to induce a quiescent cell onto the cell cycle in a near synchronous manner.

4.3.1 Cyclin D Dependent ATP Release

We first consider the Cyclin D dependent ATP release model. In this section we study systems of two cells with the driving cell's initial conditions such that it sits on the branch of stable limit cycle solutions seen in Figure 4.1. We then consider a quiescent cell for different values of its Cyclin D synthesis rate in the absence of calcium (a'_{d2}) under different parameter regimes. The initial conditions of the quiescent cell are such that it sits on the branch of stable fixed point solutions or the branch of low amplitude limit cycle solutions

that bifurcate from it. Both of these states can be seen in the lower part of the bifurcation diagram in Figure 4.1. Note that the bifurcation diagram in Figure 4.1 was produced for one cell. When considering a two cell system it may seem misleading to refer to it. However, if we start the system for two cells from a point where ATP has not yet been released (before the Cyclin D concentration reaches the critical threshold D_c), our two cell system will be effectively uncoupled and for this short period of time the bifurcation diagram for a single cell will be valid for both of the cells individually.

We regard an initially quiescent cell to have embarked upon the cell cycle when its Cyclin D levels reach a threshold. The value for this we chose to be 0.4. At Cyclin D concentrations below this the cell is still considered to be quiescent. By the same argument, this is why a cell on the branch of stable limit cycle solutions with very small amplitudes seen in the bottom part of Figure 4.1 is considered to be quiescent. These definitions are consistent with those used in the formulation of this particular mathematical model for the cell cycle [66].

As we discovered in the previous section, for some parameter values our two cell system exhibits stable torus solutions. On these solutions the intrinsic frequencies of the two cells are so disparate that they do not phase lock. Therefore we can not, as we previously have in chapters 2 and 3, measure the phase difference between the cells when the system has settled down to a phase locked state. The synchrony measure used in the previous chapter requires a stable solution of some kind (not necessarily a phase locked solution) before the synchrony measure can be calculated [69]. However, it may take some time for transients to vanish and for our system to evolve to a stable solution. This time may be far longer than the period of neurogenesis. The synchrony measure used in the previous chapter will therefore miss the transient behaviour of our system which could prove to be very important. It is therefore inappropriate to use this synchrony measure here. Instead we will use the times at which the two cells' Cyclin D concentrations pass through 0.4 and consider the differences in these times. Two cells are considered to be entrained in a near synchronous manner when this time is less than 5 hours. 5 hours may seem somewhat arbitrary, yet it gives us an idea of the degree to which cells are entrained to cycle together.

We begin by examining the ability of a driving cell to recruit a quiescent cell onto the

cell cycle in a near synchronous manner by ranging through different values of γ and a'_{d2}. In order to achieve this we numerically integrated the system for a total of 1400 hours under every parameter regime considered from a set of initial conditions whereby cell 1, the driving cell was initially on the branch of limit cycle solutions and cell 2, the initially dormant cell, was initially on the branch of stable fixed point solutions or branch of low amplitude limit cycle solutions. We then detected the time at which the Cyclin D levels of cell 2 first passed through 0.4, indicating that it had begun to oscillate. This gave us the 'time of entrainment' of the initially quiescent cell. We then calculated the time difference between the first instance cell 2's Cyclin D levels passed through 0.4 and the temporally closest instance in which the Cyclin D levels of cell 1 pass through 0.4. If this difference was greater than 5 hours, then the 'duration of near synchronous entrainment' under this parameter regime is zero. If, however, this difference was less than 5 hours then we considered the next instance that both of the cell's Cyclin D levels pass through 0.4 from below and calculated the difference in time between these events and then the instance after this and so on, until (if at all) the time difference between each cell's Cyclin D levels passing through 0.4 exceeded 5 hours. At this point we took the period of time for which the time differences between each cell's Cyclin D levels passing through 0.4 were less than 5 hours to give us the 'duration of near synchronous entrainment'. Once near synchronicity is lost, or if it is not initially present, we do not study whether it is regained later in the simulation.

Figure 4.10 shows that, generally speaking, the Cyclin D model seems very poor at recruiting a quiescent cell onto the cell cycle in a near synchronous manner, for the parameter values considered here at least. Indeed, it is only for values of a'_{d2} of between 0.41 and 0.42 that the system displays near synchronous behaviour and this behaviour only persists for a very short time. The large white area in the bottom left part of the first plot in Figure 4.10 indicates that the driving cell failed to recruit the quiescent cell onto the cell cycle at all within the period of integration for these parameter values. In order to illustrate the Cyclin D dependent model's general inability to recruit a cell onto the cell cycle in a synchronous manner we consider a couple of specific examples.

It is clear from Figure 4.11 that when the quiescent cell is recruited onto the cell cycle, its Cyclin D concentration passes through 0.4 long after (9.965 hours) the driving cell's concentration passes through 0.4 and therefore can not be considered entrained in a synchronous manner. In Figure 4.12 an example where the initially quiescent cell is recruited

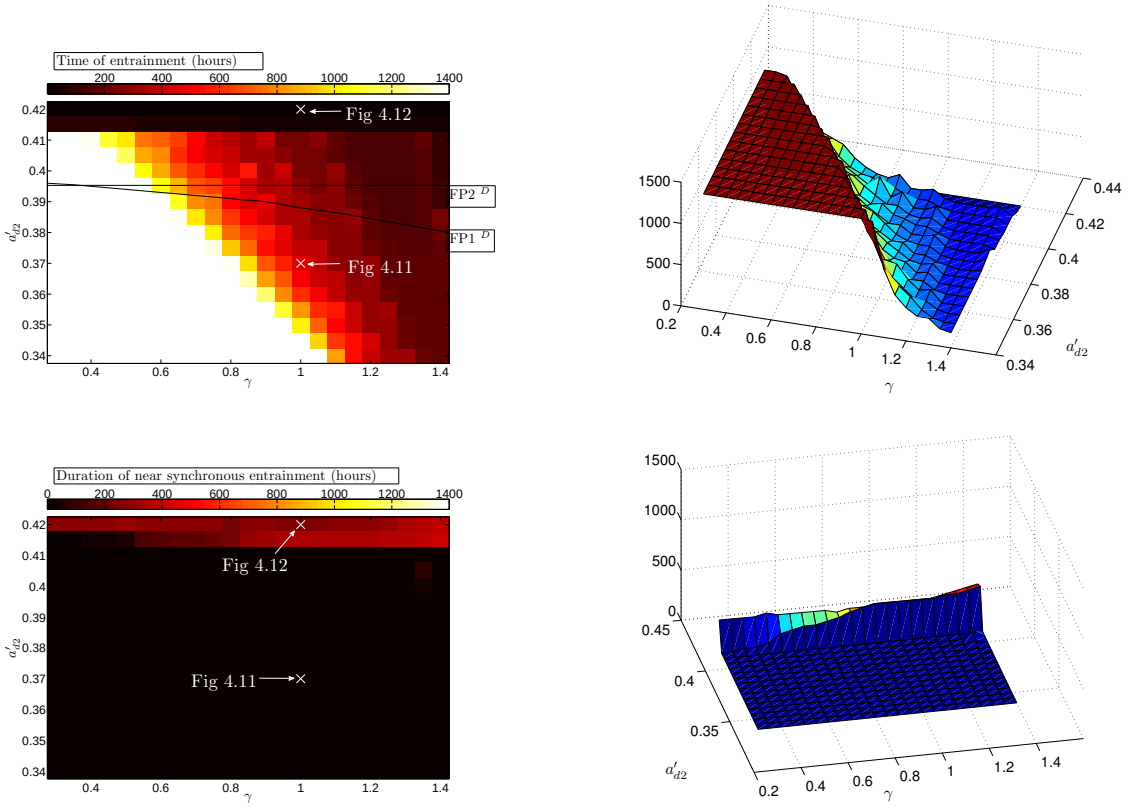

Figure 4.10: Time to and duration of near synchronous entrainment of an initially quiescent cell by a cycling cell for the Cyclin D dependent ATP release model ($(H_i, H_c) = (D_i, D_c)$). The first row of plots indicates the time at which the initially quiescent cell embarks on the cell cycle (when its Cyclin D value reaches 0.4) for a range of values for a'_{d2} and γ. The data is displayed in a colour plot in the first column and in a surface plot in the second column. The second row of plots indicate the period of time for which the cells cycle in a near synchronous manner. The results show that the quiescent cell can be driven to cycle, but there is little evidence of prolonged near synchronous behaviour. Lines FP1^D hand FP2^D in the top left and plot correspond to the boundary of the area of multistability for a single cell (c.f. Figure 4.1). The driving cell's initial conditions were such that it sat on the branch of stable limit cycle solutions seen in the top of Figure 4.1. The entrained cell's initial conditions were such that it sat on the branch of fixed point solutions and small amplitude stable limit cycle solutions below this. Parameter values as for Table 4.2, except for γ and a'_{d2} as given and $V_{deg} = 2\ \mu\text{Ms}^{-1}$. Solutions obtained using `ode23s` within Matlab.

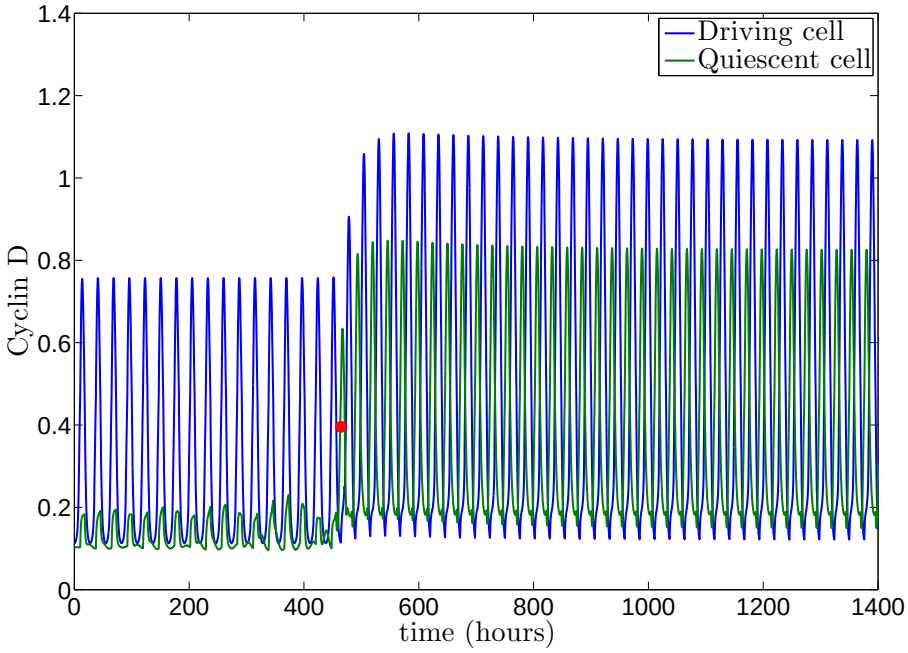

Figure 4.11: An example of cell cycle entrainment in which the initially quiescent cell is entrained in a far from synchronous manner. The quiescent cell is entrained at $t \approx 463$ hours (marked by a red dot). Results obtained by numerically integrating system (3.1) - (3.14) for two cells for the Cyclin D dependent ATP release model ($(H_i, H_c) = (D_i, D_c)$) for a period of 1400 hours. The driving cell's initial conditions were such that it sat on the branch of stable limit cycle solutions seen in the top of Figure 4.1. The entrained cell's initial conditions were such that it sat on the branch of fixed point solutions below this. Parameter values as for Table 4.2, except for $\gamma = 1$, $a'_{d2} = 0.37$ and $V_{deg} = 2\,\mu\text{Ms}^{-1}$. Solutions obtained using `ode23s` within Matlab.

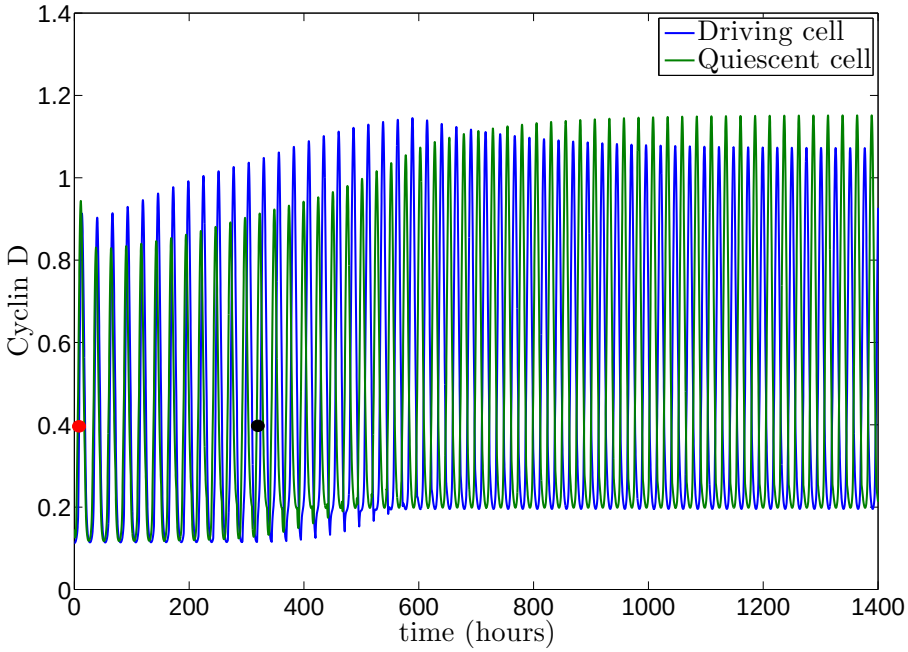

Figure 4.12: An example of cell cycle entrainment where the initially dormant cell is entrained in a synchronous manner for a short period of time. The red dot corresponds to the point at which the quiescent cell is entrained and the black dot to the point at which near synchronous behaviour is lost. Results obtained by numerically integrating system (3.1) - (3.14) for two cells for the Cyclin D dependent ATP release model ($(H_i, H_c) = (D_i, D_c)$) for a period of 1400 hours. The driving cell's initial conditions were such that it sat on the branch of stable limit cycle solutions seen in the top of Figure 4.1. The entrained cell's initial conditions were such that it sat on the branch of fixed point solutions below this. Parameter values as for Table 4.2, except for $\gamma = 1$, $a'_{d2} = 0.42$ and $V_{deg} = 2\,\mu\text{Ms}^{-1}$.

very quickly onto the cell cycle is shown. Furthermore, in this example cell 2 is entrained in a near synchronous manner, although for a short period of time ($\approx$ 250 hours). These results therefore can be considered as broadly representative of the results displayed in Figure 4.10. The parameter values used in Figures 4.11 and Figure 4.12 are marked with white crosses in Figure 4.10.

We next investigated the Cyclin D model's ability to recruit a quiescent cell onto the cell cycle but this time we used V_{deg} as the control parameter. The results of this investigation are shown in Figure 4.13.

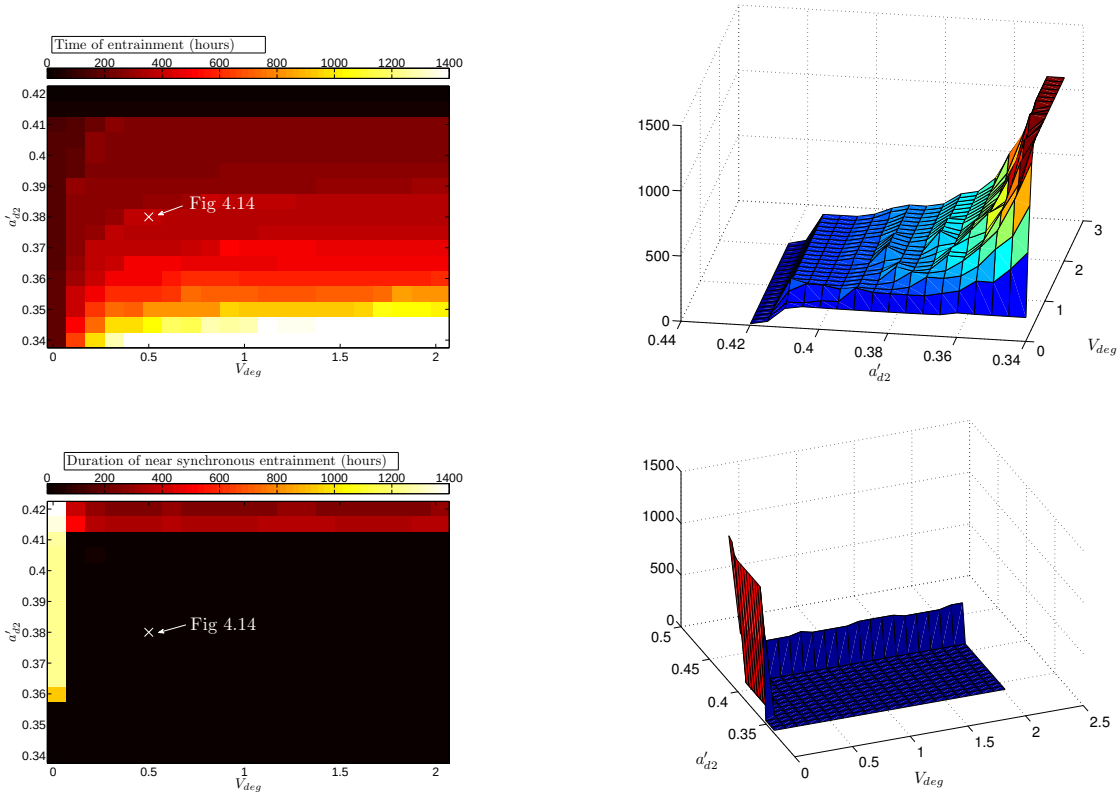

Figure 4.13: Time to and duration of near synchronous entrainment of an initially quiescent cell by a cycling cell for the Cyclin D dependent ATP release model ($(H_i, H_c) = (D_i, D_c)$). The results are similar to those displayed in Figure 4.10 and show that although quiescent cells can be entrained by a driving cell, this is not achieved in a near synchronous manner. Parameter values as for Table 4.2, except for V_{deg} and a'_{d2} as given and $\gamma = 1$.

As was the case when γ was the control parameter, Figure 4.13 suggests that the Cyclin D dependent model is very poor at recruiting a quiescent cell onto the cell cycle in a near synchronous manner except for low values of V_{deg}. This echoes the results in the previous chapter, where we showed that for low values of V_{deg}, the Cyclin D model exhibited stable synchronous solutions, the stability of which was lost as V_{deg} was increased. Nevertheless, the results of Figures 4.10 and 4.13 strongly suggest that although the increase in radial glia proliferation can be accounted for by a driving cell's ability to recruit a quiescent cell onto the cell cycle when ATP is modelled as predominantly occurring during mid G_1 phase, the model is unable to account for the synchronisation of the cell cycles of clusters of radial glial cells. As before, in order to illustrate the results shown in Figure 4.13 we consider in Figure 4.14 one specific example.

In Figure 4.14, although the driving cell is able to recruit the initially quiescent cell onto the cell cycle, the two cells are not cycling in a near synchronous manner. This is indicative of the general behaviour of the Cyclin D dependent model for all parameter regimes that we have so far considered.

Finally, we investigated whether the parameter governing the rate of extracellular ATP diffusion D_{ATP} influenced our results. Figure 4.15 suggests that the ability of a driving cell to induce a quiescent cell onto the cell cycle in a synchronous manner is unaffected by the rate of extracellular diffusion, under the parameter regime considered here at least, and for values of D_{ATP} of between 10 and 350 $\mu m^2 s^{-1}$.

4.3.2 R_s Dependent ATP Release

We next turned our attention to the R_s dependent ATP release model. The definition we use for when an initially quiescent cell can be considered to be cycling and consequently the definition for synchrony we use here are slightly different than those used for the Cyclin D dependent model for reasons we shall explain below.

As noted when studying the Cyclin D dependent model our bifurcation diagram for a single cell is only valid for two cells for a short period of time when the cells are uncoupled, which corresponds to ATP not being present in the extra-cellular space. With regard to the

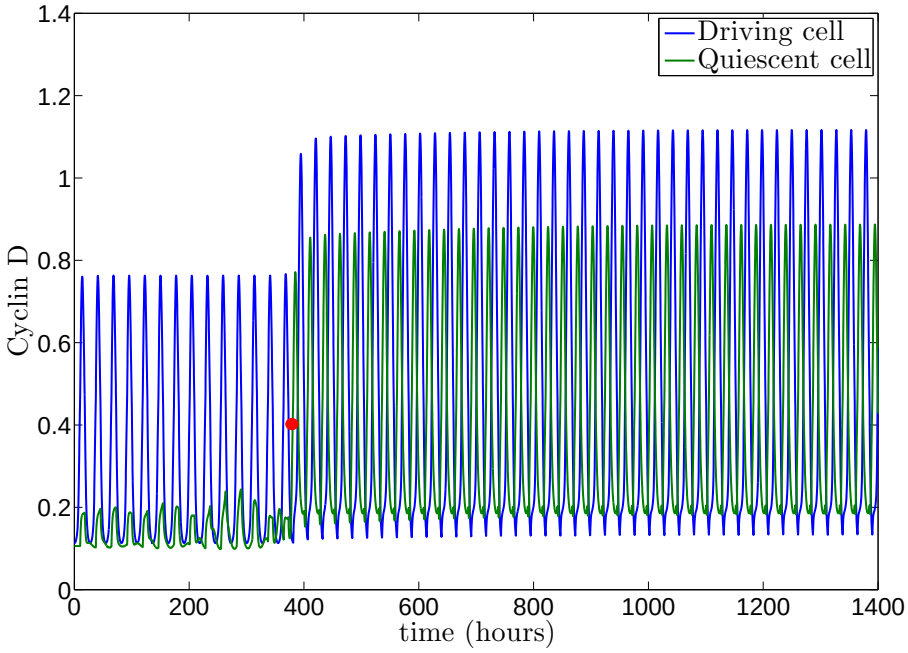

Figure 4.14: Example of an initially quiescent cell becoming entrained by a driving cell but not in a near synchronous fashion. The red dot indicates the point at which the initially quiescent cell is entrained. Results obtained by numerically integrating system (3.1) - (3.14) for two cells for the Cyclin D dependent ATP release model ($(H_i, H_c) = (D_i, D_c)$) for a period of 1400 hours. The driving cell's initial conditions were such that it sat on the branch of stable limit cycle solutions seen in the top of Figure 4.1. The entrained cell's initial conditions were such that it sat on the branch of fixed point solutions below this. Parameter values as for Table 4.2, except for $\gamma = 1$, $a'_{d2} = 0.38$ and $V_{deg} = 0.5\ \mu\text{Ms}^{-1}$.

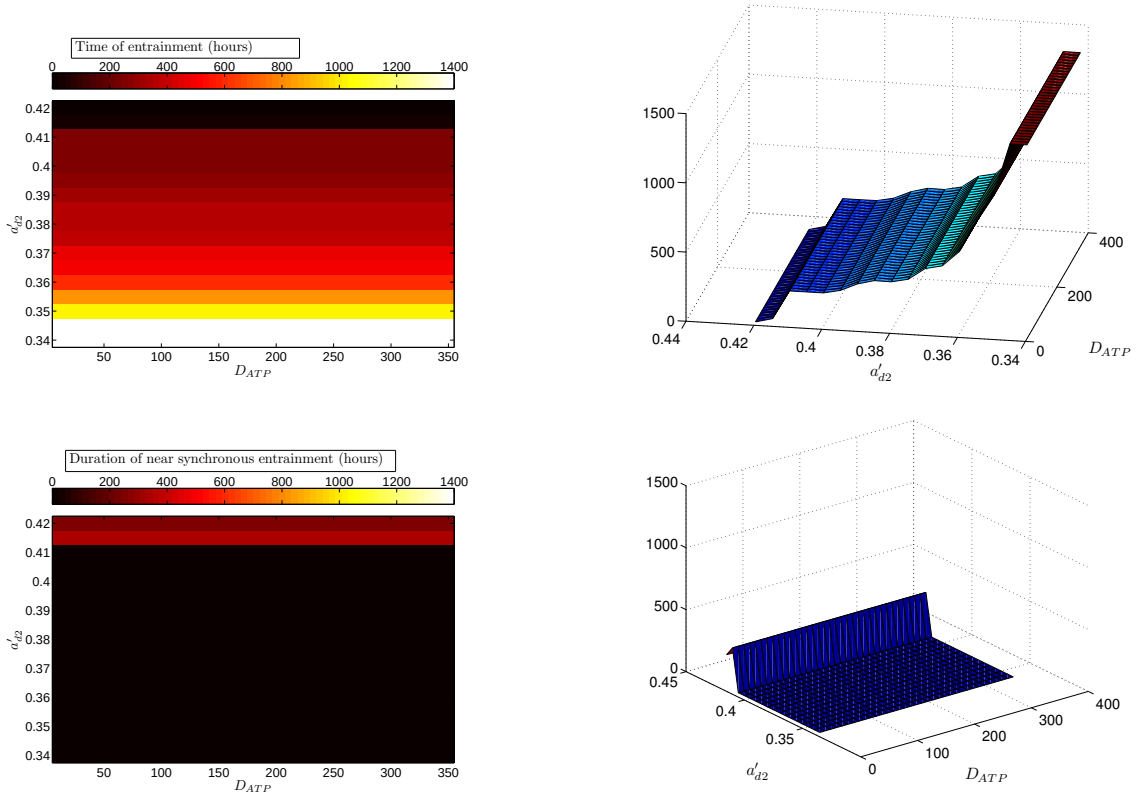

Figure 4.15: For the Cyclin D dependent ATP release model ($(H_i, H_c) = (D_i, D_c)$), near synchronous entrainment, although poor for a wide range of values of D_{ATP}, appears to be independent of changes in D_{ATP}. Parameter values as for Table 4.2, except for D_{ATP} and a'_{d2} as given, $\gamma = 1$ and $V_{deg} = 2\,\mu\text{Ms}^{-1}$.

Cyclin D case, the simulations were started when the driving cell's Cyclin D concentration was at its minimum, as this corresponded to ATP not being released. However, as the timing of ATP release is different for the R_s dependent model, low Cyclin D concentrations correspond to ATP being released in the R_s dependent model. Therefore we start the simulations from a point where the Cyclin D concentration for the driving cell is at a peak, as this corresponds to a time when ATP is not released in the R_s dependent model. In this case when a simulation is started, a driving cell's Cyclin D concentration will pass through 0.4 from above initially, rather than from below as for the Cyclin D dependent model. We therefore use the point at which a cell's Cyclin D concentration passes through 0.4 from above as our reference point to measure the 'phase difference' between the two cells in the system in this section. Consequently, the entrained cell will not be regarded as being on the cell cycle until its Cyclin D concentration passes through 0.4 from above. As before two cells are considered to be entrained in a near synchronous manner if the difference between the times that each passes through 0.4 is less than 5 hours. With these new definitions, we investigated the time it takes for the initially quiescent cell to embark on the cell cycle and for how long, if at all, it remains entrained in a near synchronous manner to the driving cell.

As for the Cyclin D dependent ATP release model, we begin our investigations by simulating the system for different values of the quiescent cell's basic Cyclin D synthesis rate a'_{d2} and calcium coupling strength γ. The top row of plots in Figure 4.16 indicate that the R_s dependent model enjoys similar success to its Cyclin D dependent counterpart (cf. Figure 4.10) in recruiting the initially quiescent cell onto the cell cycle. This is evidenced by the large dark area in the top left hand plot of the figure. Dark areas in this and similar plots correspond to the success of a driving cell in entraining a quiescent cell quickly. It is clear from the bottom row of plots that the R_s dependent model enjoys far more success in maintaining near synchrony for a significant period, at least under the parameter regimes considered in Figure 4.16. Indeed, large parts of the bottom left plot in Figure 4.16 are lightly coloured (light colours correspond to long periods of synchronous entrainment in this and similar plots), indicating that the two cells remained entrained in a near synchronous manner for large periods of the total time of integration. In Figure 4.17 we take an isolated example in order to illustrate the general story shown in Figure 4.16. Once the initially quiescent cell first embarks upon the cell cycle, it begins to cycle in a near synchronous fashion with the driving cell. However, it is also clear that the two trajectories diverge towards the end of the period of integration, indicating that near synchrony, although maintained for

a long period of time, does not last for ever. If we compare Figure 4.17 to Figures 4.11 and 4.12, which show the results for the Cyclin D dependent ATP release model, it is clear that near synchrony is maintained for a far longer period of time in the example of the R_s dependent ATP release model (Figure 4.17).

As for the Cyclin D dependent ATP release model, we also consider a different control parameter V_{deg} (see Figure 4.18). As was the case when γ was the control parameter, the top row of plots in Figure 4.18, which show the time of recruitment onto the cell cycle, are not too dissimilar to their Cyclin D dependent counterpart (cf. Figure 4.13). In both cases the initially quiescent cell is recruited quickly onto the cell cycle, with the exception of the lower values for $a_{d2'}$ in the Cyclin D dependent case. Again, however it is clear that, by comparing the bottom row of plots in Figures 4.18 and 4.13, the R_s dependent model is far more successful at maintaining near synchrony, although its dependence on V_{deg} is weak. A specific example of this behaviour is illustrated in Figure 4.19, in which the initially dormant cell embarks on the cell cycle and rapidly begins to cycle synchronously with the driving cell. This behaviour appears to be indicative of the behaviour that we have observed for the R_s dependent model under the majority of parameter regimes so far considered. In this particular example, the two cell trajectories begin to drift apart towards the end of the period of integration and at $t \approx 1097$ hours the delay between Cyclin D peaks is greater than 5 hours and near synchrony, according to this chapter's definition is lost.

As for the Cyclin D dependent model, we investigated whether the rate of extracellular ATP diffusion has an effect on the behaviour discovered for the R_s dependent model. Figure 4.20 shows that, as was the case for the Cyclin D dependent model, the ability of a driving cell to induce a quiescent cell onto the cell cycle in a near synchronous manner is not strongly affected by the rate of extracellular diffusion. It therefore seems unlikely that the ATP diffusion rate D_{ATP} has a significant effect on the general behaviour of the system in this section, for values of D_{ATP} above 10 $\mu\text{m}^2\text{s}^{-1}$ at least.

Although we would expect the results from this Section to be quantitatively different if we changed the criteria for near synchrony, we would expect the qualitative results to remain the same. This is what our numerical investigations into the matter suggested (results not shown).

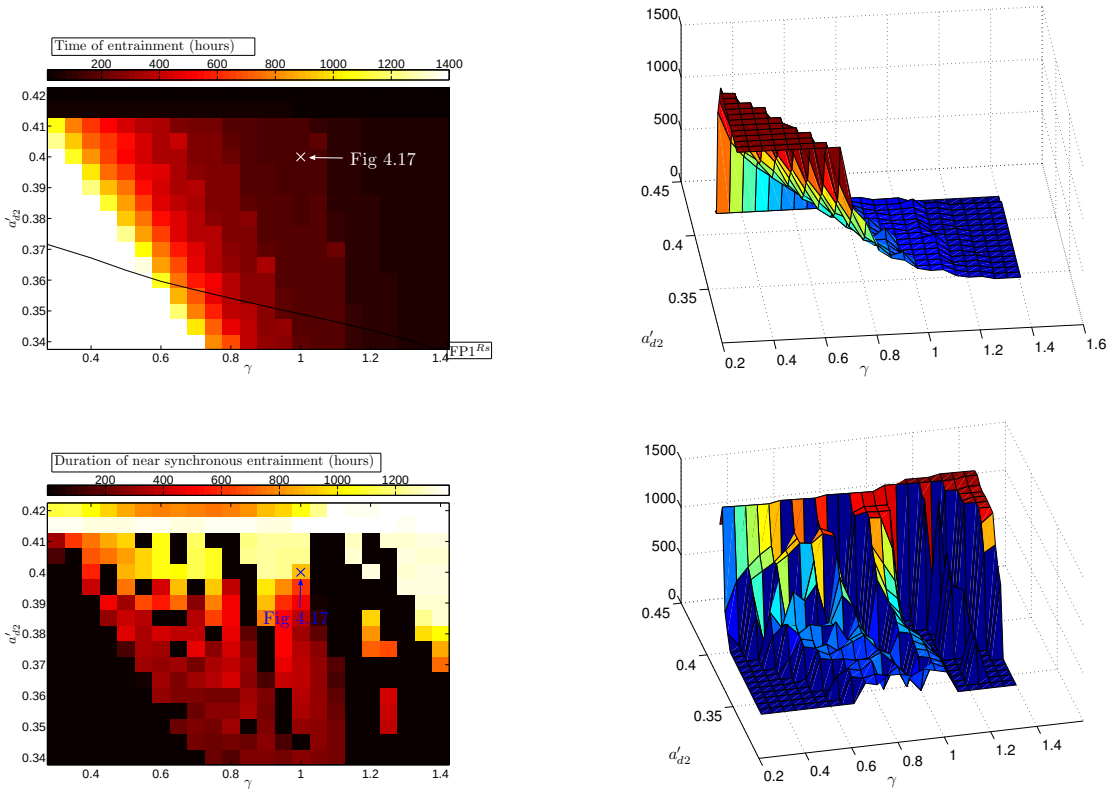

Figure 4.16: Time to and duration of near synchronous entrainment of an initially quiescent cell by a cycling cell for the R_s dependent ATP release model ($(H_i, H_c) = (R_{sc}, R_{si})$, system (3.1) - (3.14)). These results indicate that this model enjoys a great deal of success in maintaining near synchronous entrainment under the parameter values considered here. The first row of plots indicates the time at which the initially quiescent cell embarks on the cell cycle (when its Cyclin D value falls below 0.4) for a range of values for a'_{d2} and γ. The second row of plots indicate the period of time for which the cells cycle in a near synchronous manner. The line marked FP1^{Rs} corresponds to the boundary of the area of bistability in the single cell bifurcation diagram (Figure 4.5). The driving cell's initial conditions were such that it sat on the branch of stable limit cycle solutions seen in the top of Figure 4.5. The entrained cell's initial conditions were such that it sat on the branch of fixed point solutions and small amplitude stable limit cycle solutions below this. Parameter values as for Table 4.2, except for γ and a'_{d2} as given and $V_{deg} = 2\ \mu\text{Ms}^{-1}$.

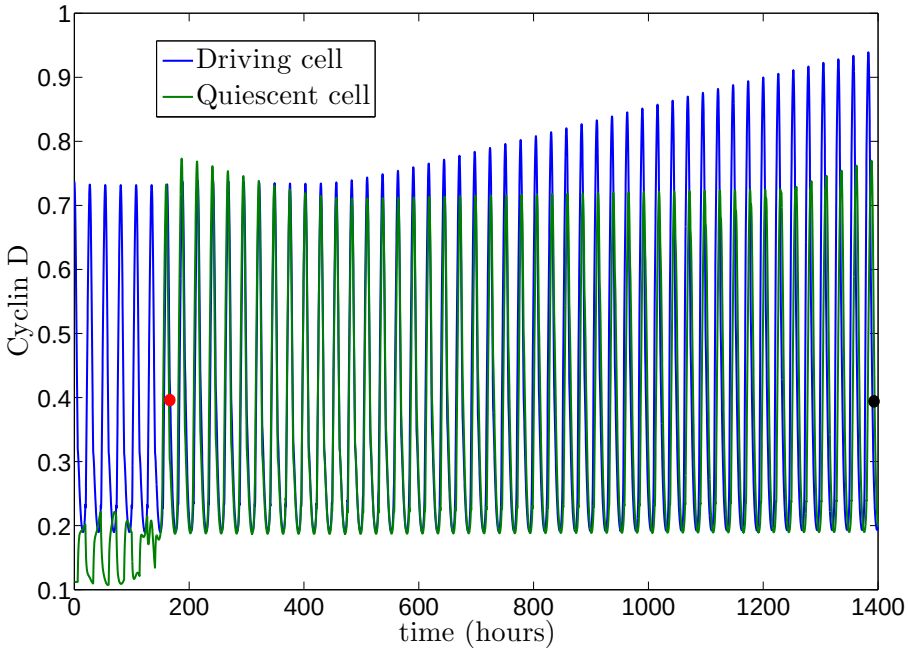

Figure 4.17: An example of rapid cell cycle entrainment of a quiescent cell where near synchronous behaviour is maintained for a long period of time for the R_s dependent ATP release model ($(H_i, H_c) = (R_{sc}, R_{si})$, system (3.1) - (3.14)). The red dot indicates the point at which the quiescent cell is entrained and the black dot the point at which near synchrony is lost. The driving cell's initial conditions were such that it sat on the branch of stable limit cycle solutions seen in the top of Figure 4.5. The entrained cell's initial conditions were such that it sat on the branch of fixed point solutions below this. Parameter values as for Table 4.2, except for $\gamma = 1$, $a'_{d2} = 0.4$ and $V_{deg} = 2\,\mu\text{Ms}^{-1}$. Solutions obtained using `ode23s` within Matlab.

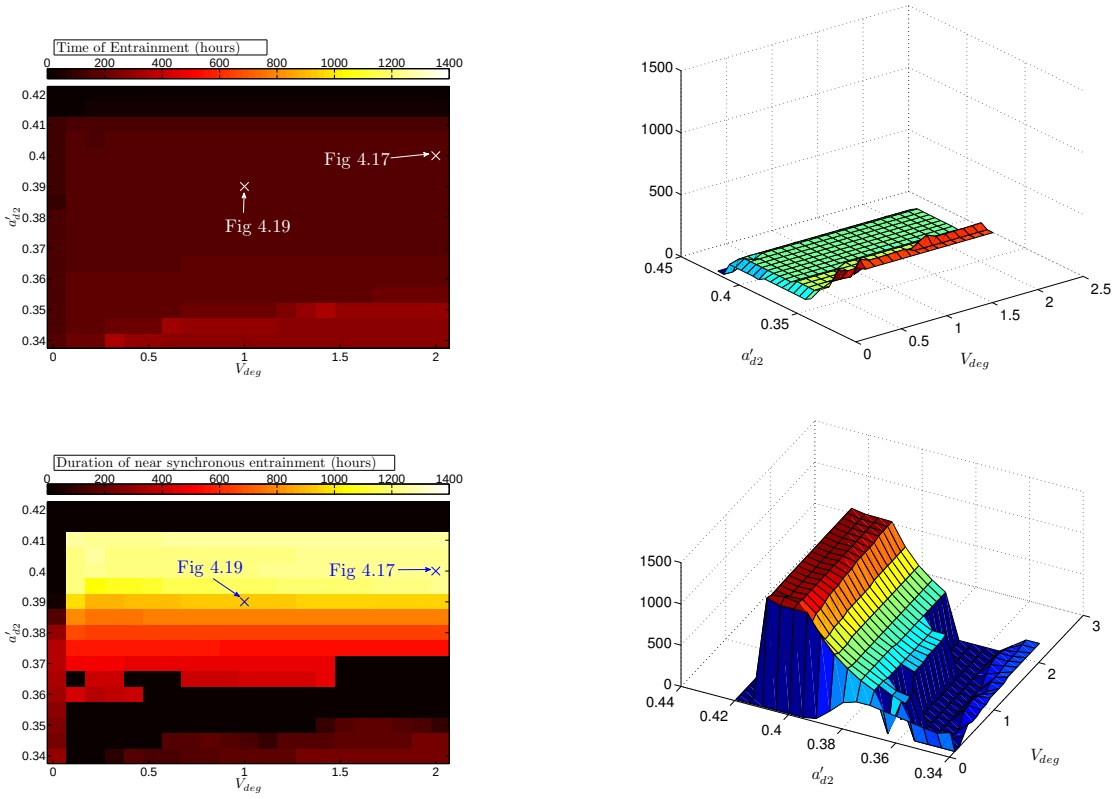

Figure 4.18: Time to and duration of near synchronous entrainment for the R_s dependent ATP release model ($(H_i, H_c) = (R_{sc}, R_{si})$, system (3.1) - (3.14)). The results provide more evidence that the R_s dependent ATP release model is more successful at maintaining near synchronous entrainment than the Cyclin D dependent ATP release model. They also suggest that dependence of near synchronous entrainment on V_{deg} is weak. Parameter values as for Table 4.2, except for V_{deg} and a'_{d2} as given and $\gamma = 1$.

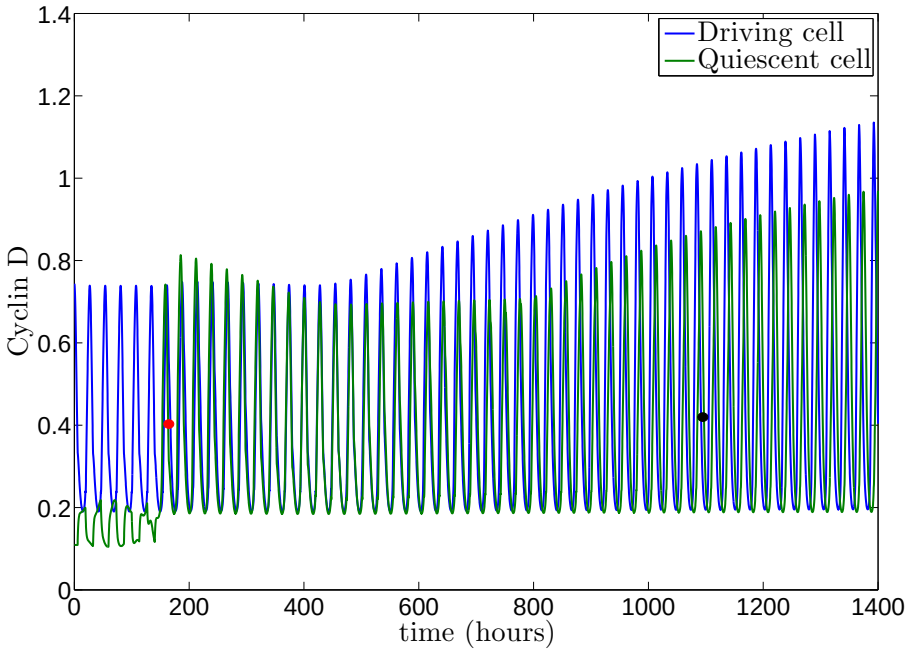

Figure 4.19: Another example of rapid cell cycle entrainment where near synchrony is maintained for a long period of time via R_s dependent ATP release ($(H_i, H_c) = (R_{sc}, R_{si})$, system (3.1) - (3.14)). The red dot indicates the point at which the quiescent cell is entrained and the black dot the point at which near synchrony is lost. The driving cell's initial conditions were such that it sat on the branch of stable limit cycle solutions seen in the top of Figure 4.5. The entrained cell's initial conditions were such that it sat on the branch of fixed point solutions below this. Parameter values as for Figure 4.17 except for $V_{deg} = 1\ \mu\text{Ms}^{-1}$ and $a'_{d2} = 0.39$.

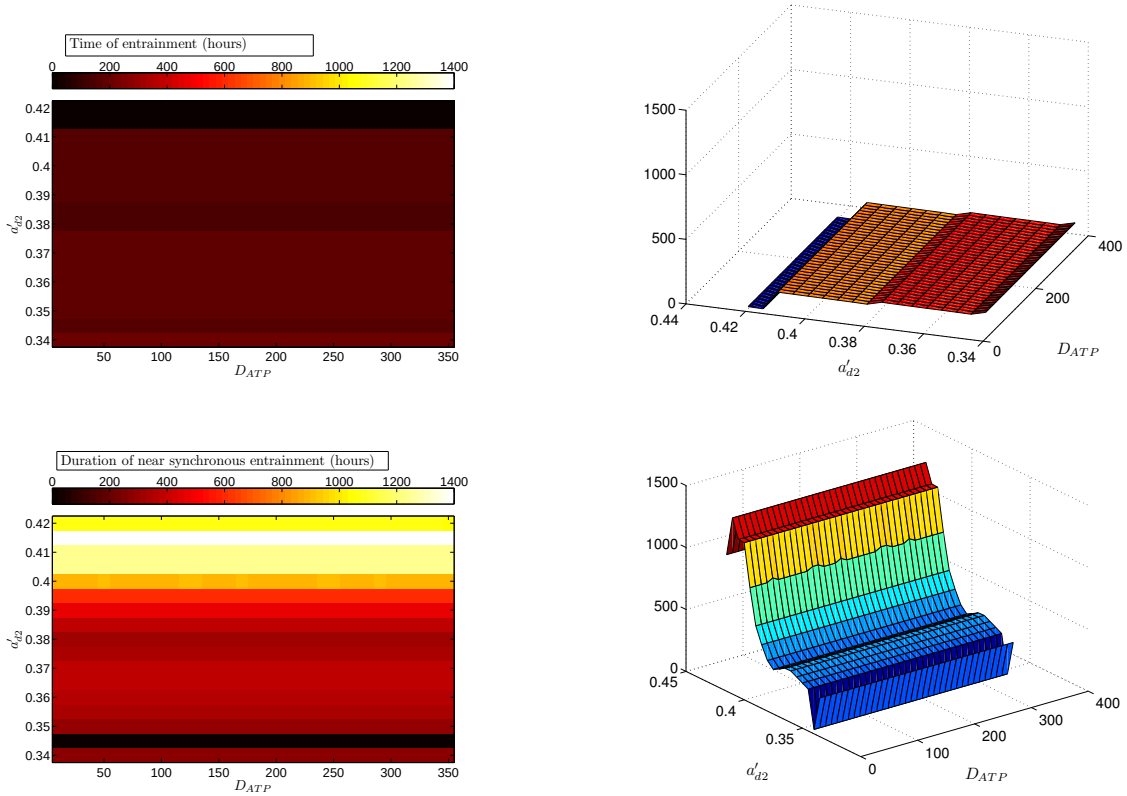

Figure 4.20: Results indicating that time to and duration of entrainment of a quiescent cell remain largely unaffected by a change in rate of extracellular ATP diffusion in the R_s dependent ATP release model ($(H_i, H_c) = (R_{sc}, R_{si})$, system (3.1) - (3.14)). Parameter values as for Table 4.2, except for D_{ATP} and a'_{d2} as given, $\gamma = 1$ and $V_{deg} = 2\,\mu\text{Ms}^{-1}$.

4.4 Pacemaker Recruitment in Systems of Several Cells

The results in the previous section appear promising in accounting for the increase in radial glia proliferation that is brought about by the calcium coupling. Weissman *et al*'s results suggest that ATP mediated calcium waves are responsible for maintaining higher numbers of cells in S-phase (as indicated by BrdU incorporation). The blocking of ATP release for an hour on day 16 of development in the rat resulted in a decrease in the density of proliferating radial glial cells to 54.7 % of control [93]. This could be accounted for in our model by initiating the system from a state where around half the cells are quiescent and the other half cycling. If ATP release in the system was turned off (achieved by setting the rate of extracellular ATP release V_{ATP} to 0, analogous to the *in vitro* blocking of ATP release), then all of the driving cells will continue to oscillate, while the quiescent cells will remain dormant. If however, ATP release is switched on in this system, the quiescent cells could be recruited onto the cell cycle, resulting in an approximate doubling in the density of proliferating cells.

In order to investigate whether this is indeed the case, we will need to consider systems of several cells in one spatial dimension under several different parameter regimes for both the driving and quiescent cells. This would be a very computationally expensive task and time constraints imposed upon the production of this thesis mean that this is not practical. Consequently in this section we, as a 'proof of concept', consider only one example for each model.

4.4.1 Cyclin D Dependent ATP Release

We first of all consider a system of 10 cells for the Cyclin D dependent model, where even numbered cells are initially quiescent, with a value for a'_d of 0.38, and all other cells are initially cycling, with a value for a'_d of 0.41. Simulating this system with the coupling turned on and off leads to the results illustrated in Figures 4.21 and 4.22.

In Figure 4.21, where ATP release is turned on the cumulative total of cell cycle os-

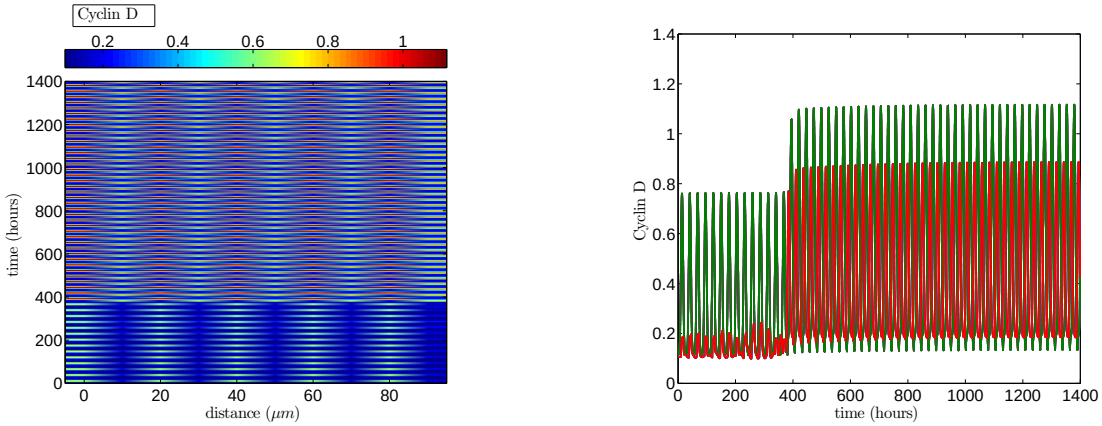

Figure 4.21: An example of ATP mediated calcium signalling bringing about an increase in the density of proliferating cells in a 10 cell system for the Cyclin D dependent ATP release model ($(H_i, H_c) = (D_i, D_c)$, system (3.1) - (3.14)). The driving cells' initial conditions were such that they sat on the branch of stable limit cycle solutions seen in the top of Figure 4.1. The entrained cells' initial conditions were such that they sat on the branch of fixed point solutions and small amplitude stable limit cycle solutions below this. In the right hand plot, the green curve is the trajectory of all of the cells which are initially cycling whereas the red curve is the trajectory of the initially quiescent cells. To note, the trajectories of all of the driving cells are identical and likewise the trajectories of all of the initially quiescent cells are identical. Parameter values as for Table 4.2, except for $a'_{di} = 0.38$ (for even i), $a'_{di} = 0.41$ (for odd i), $\gamma = 1$ and $V_{deg} = 0.5\,\mu\text{Ms}^{-1}$.

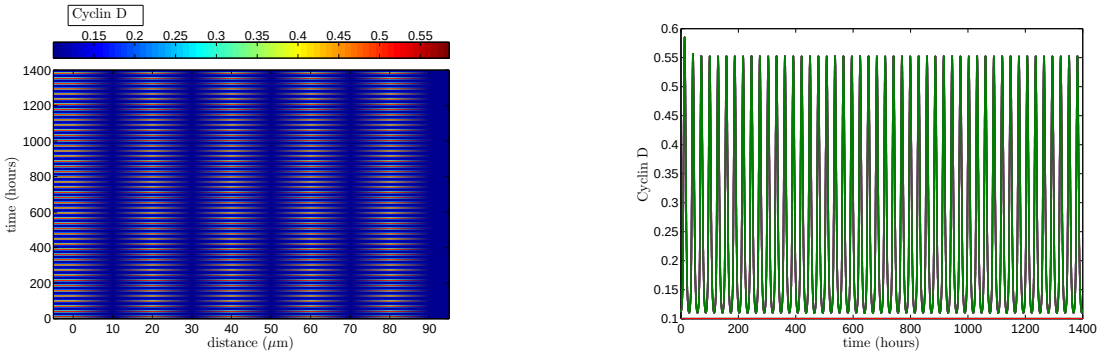

Figure 4.22: An example showing how the blocking of ATP release can lead to a significant decrease in the number of proliferating cells. The driving cells' initial conditions were such that they sat on the branch of stable limit cycle solutions seen in the top of Figure 4.1. The entrained cells' initial conditions were such that they sat on the branch of fixed point solutions and small amplitude stable limit cycle solutions below this. As for Figure 4.21, in the right hand plot, the green curve is the trajectory of all of the cells which are initially cycling whereas the red curve is the trajectory of the initially quiescent cells. Parameter values as for Table 4.2, except for $a'_{di} = 0.38$ (for even i), $a'_{di} = 0.41$ (for odd i) $\gamma = 1, V_{ATP} = 0\,\mathrm{s}^{-1}$ and $V_{deg} = 0.5\,\mu\mathrm{Ms}^{-1}$.

cillations over the period of integration is 465, while it is 240 in Figure 4.22, where the system was simulated without ATP release. Therefore, in this example the absence of ATP mediated calcium signalling brings about a decrease in the density of proliferating cells to 51.6% of the control, which is very close to the 54.7 % that has been observed experimentally. Strictly speaking, we are not quite comparing like with like. Weissman *et al* measured the proportion of radial glial cells in S-phase during one hour under different experimental conditions (i.e. with and without ATP receptor blocking) in a large population of cells. However, we have measured the total number of cells in a small population over a large period of time under different conditions (i.e. with and without ATP receptor blocking). Weissman *et al* would expect their results to be representative for the whole developing neocortex across the time of neurogenesis and likewise we would expect our results to be representative for the whole developing neocortex across the time of neurogenesis. It is in this sense that our quantitative findings can be directly compared to Weissman *et al*'s. The result from our simulations strongly suggests that the ability of a driving cell to recruit a quiescent cell onto the the cell cycle via an ATP mediated calcium signal could be the mechanism responsible for the increase in radial glia proliferation.

Interestingly, the time v Cyclin D plot in Figure 4.21 takes an identical form to the time v Cyclin D plot in Figure 4.14, where only two cells are considered but under an identical parameter regime. Indeed in both cases the initially quiescent cell(s) are recruited onto the cell cycle at exactly the same point, at $t \approx 380$ hours and the formerly quiescent and driving cells Cyclin D trajectories take exactly the same form. In both cases the formerly quiescent cells are not entrained in a near synchronous manner, which adds further weight to the argument that ATP release during mid G_1 phase is unlikely to lead to the synchronisation of the cell cycles of clusters of radial glial cells. It is perhaps not surprising that the 10 cell system studied in Figure 4.21 should mimic the results of the two cell system exactly, when one considers that in both cases the signal received by the quiescent cells will be identical.

It is then interesting to test whether the two cell system results can be extended to larger systems where the cells within the spatial domain are not distributed on an alternate quiescent cell/driving cell basis. The driving cell/quiescent cell distribution in Figure 4.23 was determined using Matlab's pseudo-random uniform distribution number generator *rand* with the condition that the ratio of quiescent cells to driving cells must be 1:1. It is clear that the 50 cells in the distribution do not alternate between driving cells and quiescent cells. Despite this, by comparing the Cyclin D profiles of the driving and initially quiescent cells in Figure 4.23 to Figures 4.21 and 4.14 it is clear that they are all identical. Furthermore, in the 50 cell system, the absence of ATP coupling brings about a decrease in the density of proliferating cells to 51.6% of control (1,200 oscillations (results not shown), compared to 2,325 (Figure 4.23)); the same proportion as for the 10 cell system (Figure 4.21). This suggests that the results from the two cell system can indeed be extended to larger systems where the distribution of quiescent cell to driving cell has been randomised. By inspecting the profile of external ATP across the spatial domain (results not shown), it can be seen that $[ATP_E]$ is very similar throughout the domain due to the high ATP diffusion coefficient D_{ATP}. We believe that this is the reason why the two cell results appear to scale up to larger systems even when the distribution of quiescent driving cells is randomised.

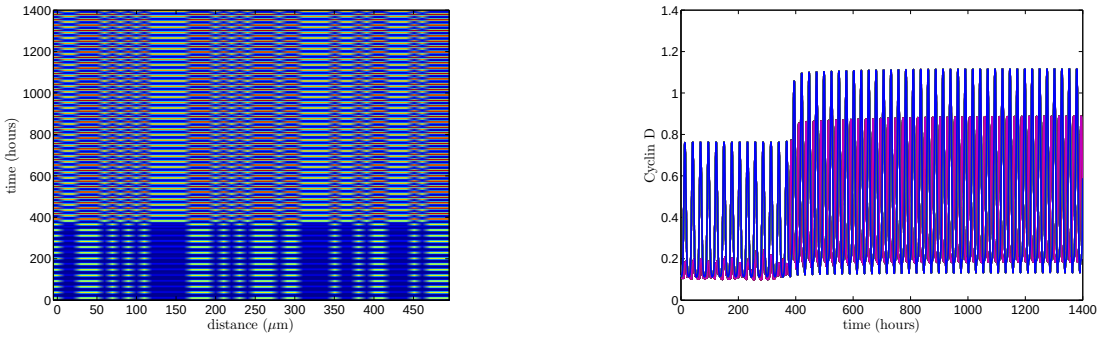

Figure 4.23: An example showing that even with a randomised distribution of driving cells and quiescent cells, the Cyclin D profiles of the driving cells and initially quiescent cells remain the same in a 50 cell system for the Cyclin D dependent ATP release model ($(H_i, H_c) = (D_i, D_c)$, system (3.1) - (3.14)). The driving cells' initial conditions were such that they sat on the branch of stable limit cycle solutions seen in the top of Figure 4.1. The entrained cells' initial conditions were such that they sat on the branch of fixed point solutions and small amplitude stable limit cycle solutions below this. In the right hand plot, the blue curve is the trajectory of all of the cells which are initially cycling and the pink curve, the trajectories of the initially quiescent cells. Parameter values as for Table 4.2, except for $a'_{di} = 0.38$ (for quiescent cells), $a'_{di} = 0.41$ (for driving cells) $\gamma = 1$, and $V_{deg} = 0.5\,\mu\text{Ms}^{-1}$.

4.4.2 R_s Dependent ATP Release

Following on from our work for the Cyclin D dependent model, we considered a system of 10 cells for the R_s dependent model and simulated it with the coupling switched on and off. As before, the initial conditions were such that odd numbered cells were initially oscillating with a value for a'_d of 0.41, while all other cells were initially quiescent with a value for a'_d of 0.39. The results of our simulations are displayed in Figures 4.24 and 4.25.

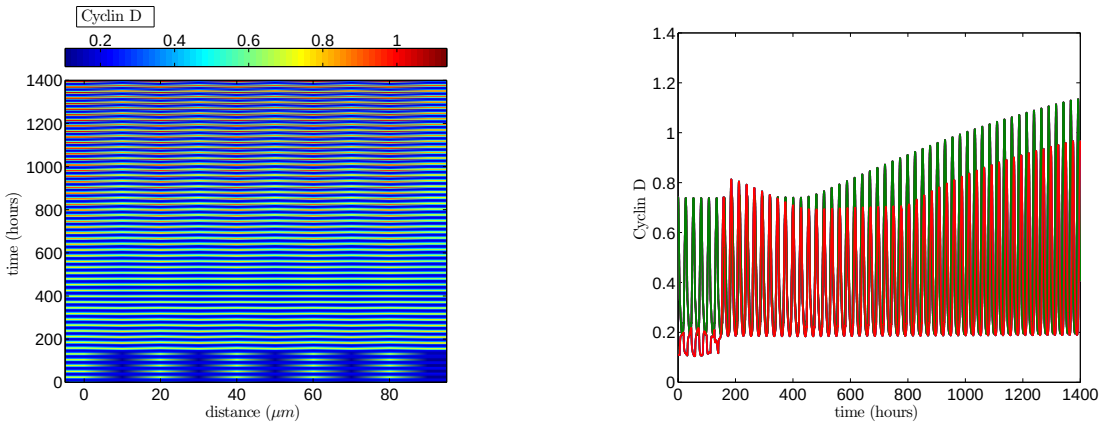

Figure 4.24: An example of a 10 cell system where ATP mediated calcium signals bring about a large increase in the proportion of proliferating cells in the R_s dependent ATP release model ($(H_i, H_c) = (R_{sc}, R_{si})$, system (3.1) - (3.14)). The driving cells' initial conditions were such that they sat on the branch of stable limit cycle solutions seen in the top of Figure 4.5. The entrained cells' initial conditions were such that they sat on the branch of fixed point solutions and small amplitude stable limit cycle solutions below this. Parameter values as for Table 4.2, except for $a'_{di} = 0.39$ (for even i), $a'_{di} = 0.41$ (for odd i), $\gamma = 1$ and $V_{deg} = 1\ \mu\text{Ms}^{-1}$.

In Figure 4.24 the cumulative total of cell cycle oscillations was 495, while it was 240 in Figure 4.25 where ATP release was blocked. Therefore, over the period of integration blocking ATP coupling brings about a decrease in the density of proliferating cells to 48.5% of control, very close to the 54.7 % that has been observed experimentally. This provides further evidence to suggest that the increase in the density of proliferating cells is mainly down to the ability of radial glial cells to recruit otherwise quiescent cells onto the cell cycle.

If we compare Figures 4.24 and 4.19, we can see that, as was the case for the Cyclin D

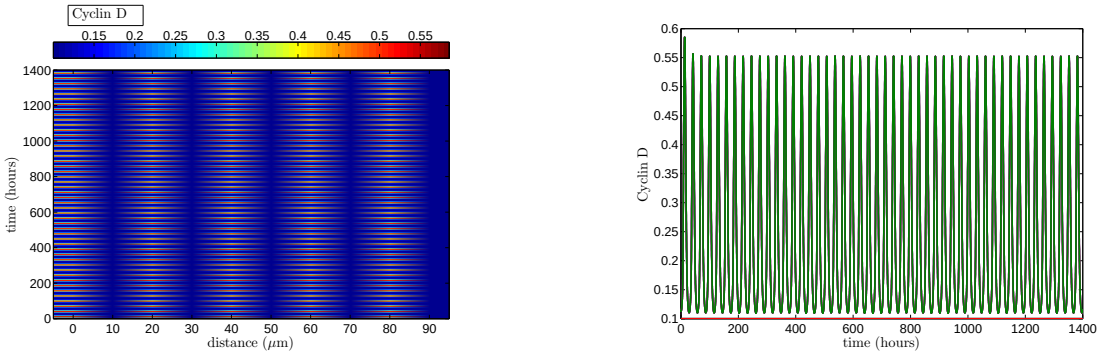

Figure 4.25: An example of how switching off ATP release leads to a decrease in the proportion of proliferating cells in the R_s dependent ATP release model ($(H_i, H_c) = (R_{sc}, R_{si})$, system (3.1) - (3.14)). The driving cells' initial conditions were such that they sat on the branch of stable limit cycle solutions seen in the top of Figure 4.5. The entrained cells' initial conditions were such that they sat on the branch of fixed point solutions and small amplitude stable limit cycle solutions below this. Parameter values as for Table 4.2, except for $a'_{di} = 0.39$ (for even i), $a'_{di} = 0.41$ (for odd i), $V_{ATP} = 0\text{s}^{-1}, \gamma = 1$ and $V_{deg} = 1\ \mu\text{Ms}^{-1}$.

dependent model, under the same parameter regime the 10 cell system exactly mimics the 2 cell system for the R_s dependent model. Furthermore in Figure 4.26 we initialised the system for a randomised distribution of driving cells and quiescent cells. Despite this the Cyclin D profiles of the driving cells and quiescent cells remained identical to the two cell case and 10 cell case under the same parameter regime. In all cases, the entrained cell(s) are recruited at $t \approx 164$ and near synchronous entrainment is lost at $t \approx 1097$ hours. If systems of several cells mimic the results of the two cell systems under every parameter regime, as we suspect and as these results suggest, then the R_s dependent's model superior ability to recruit quiescent cells onto the cell cycle in a synchronous manner reinforces the argument that the release of ATP as predominantly occurring during the G_1/S phase transition is the likely mechanism by which clusters of radial glial cells' cell cycles synchronise.

4.5 Conclusions and Further Work

The results from this chapter suggest that a possible mechanism for the increase in radial glia proliferation due to ATP mediated calcium signalling is the ability of a driving cell to

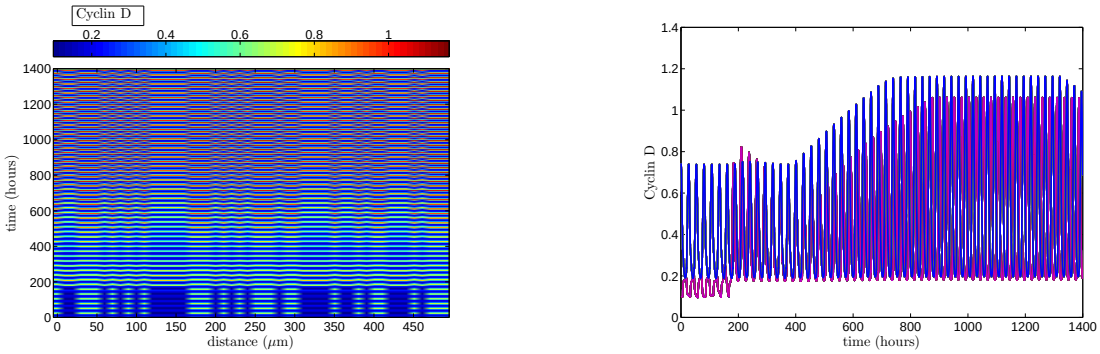

Figure 4.26: An example of a 50 cell system for the R_s dependent ATP release model ($(H_i, H_c) = (R_{sc}, R_{si})$, system (3.1) - (3.14)) showing that despite a randomised distribution of driving cells to quiescent cells, ATP mediated calcium signalling brings about an increase in the proportion of proliferating cells. The driving cells' initial conditions were such that they sat on the branch of stable limit cycle solutions seen in the top of Figure 4.5. The entrained cells' initial conditions were such that they sat on the branch of fixed point solutions and small amplitude stable limit cycle solutions below this. Parameter values as for Table 4.2, except for $a'_{di} = 0.39$ (for even i), $a'_{di} = 0.41$ (for odd i), $\gamma = 1$ and $V_{deg} = 1\,\mu\text{Ms}^{-1}$. Solutions obtained using `ode23s` within Matlab.

induce a quiescent cell onto the cell cycle. A driving cell achieves this by releasing ATP, which in turn leads to the release of calcium in the quiescent cell, resulting in an increase in Cyclin D activity in that cell, which lifts the cell from quiescence. Our results also reinforce the notion that, in order for clusters of radial glial cells to synchronise, the timing of ATP release from a cell is crucial. In particular, results in this chapter support those of chapter 3 in suggesting that ATP release occurring during late G_1 phase (the R_s dependent model) is more likely to lead to synchronous behaviour than in the case where it is released during mid G_1 phase (the Cyclin D dependent model). These results are summarised in Table 4.1. As our results suggest that the timing of ATP release plays a crucial role in neural developmental, it leaves the possibility that some neural development disorders which may stem from errors during neurogenesis such as infantile epilepsies, mental retardation, dyslexia, Huntington's and Alzheimer's disease [4, 70] may be down to a malfunction in the timing of the release of ATP into the extracellular space, although we are not aware of any evidence in the literature which supports this hypothesis.

As mentioned above, neurogenesis in the rat embryo lasts 6 days while it has been estimated that in the human embryo it is far longer, of the order of 10 weeks [2, 12, 16]. In mice, a proliferating cell cycles a total of 11 times during the period of neurogenesis [12]. However, this number is likely to be far larger during embryonic neurogenesis in humans. In the systems we have studied, stable oscillatory solutions do not always exist or the system will take a long time until it settles down to a stable oscillatory solution (far longer than the period of neurogenesis). Therefore, the 'torus' solutions or transients before the system settles down to a stable oscillatory solution become more important with regard to accounting for the synchronous behaviour of cells than the stability of the solutions themselves. Our results for two cells, which we believe can be extended to systems of several cells, suggest that cells remain entrained in a near synchronous manner for a far longer period of time when ATP is modelled as being predominantly released during the G_1/S phase transition. As we are dealing with a complex system, it is difficult to determine exactly why this is the case. However, it appears that the superior ability of the R_s dependent model to promote synchronous behaviour, which we saw in the previous chapter, is intrinsic to the R_s dependent model and helps to explain the results in this chapter. In this model, when γ was the control parameter (Figure 4.16) the cells remained entrained in a near synchronous manner for a maximum of 1385.389 hours $\approx$ 58 days, with a mean period (averaged over a range of γ and a'_{d2}) of synchronous behaviour of 415.54 hours $\approx$ 17 days. When V_{deg} was

the control parameter (Figure 4.18), the maximum period of synchronous behaviour was 1260.636 hours $\approx$ 53 days and the mean (averaged over a range of V_{deg} and a'_{d2}) was 497.927 hours $\approx$ 21 days. These results suggest that synchronous behaviour can be maintained for a long enough period of time under most parameter regimes to account for the synchrony of radial glial cells during neurogenesis in the rat. However, as neurogenesis in humans occurs over a far longer timescale, only under certain parameter regimes will the cells in simulations of our R_s dependent model yield synchronous behaviour for a sufficiently long period of time. This suggests that either neurogenesis in humans is highly parameter sensitive, with anomalies in the rate constants potentially leading to malfunctions in neurogenesis, or that perhaps there is secondary mechanism involved in the process. Perhaps newly created cells or other signalling pathways play a 'synchrony checking' role, helping to regulate synchronous behaviour by acting in concert with the ATP signalling mechanism to prevent the system from drifting from a synchronous state.

Although the results of this chapter are promising, we still have no way of accounting for the beginning of neurogenesis as all systems considered thus far have some or all cells initially cycling. Our results also rely upon clusters of radial glial cells consisting of two sets of identical cells with identical initial protein concentrations for each set. In order to arrive at the results in this chapter, the distribution of parameter values was finely tuned with each cell modelled by one of two sets of parameters. As most cells exhibit some physical differences, this is an unlikely scenario. These are some of the issues we intend to address in the next chapter.

Table 4.1: Summary of results

	mid G_1 ATP release	G_1/S ATP release
	Cyclin D dependent ATP release model	R_s dependent ATP release model
Entrainment	Generally yes Figures 4.10-4.15, 4.21-4.23	Generally yes Figures 4.16-4.20, 4.24-4.26
Near synchronous entrainment	Generally no Figures 4.10-4.15, 4.21-4.23	Generally yes Figures 4.16-4.20, 4.24-4.26

Table 4.2: Parameter values

Parameter	Value	Parameter	Value
r_h^*	0.6 μMs^{-1}	a'_{d1}	0.41
a_E	0.16	a_X	0.08
k	0.054	q_D	0.6
q_E	0.6	q_X	0.8
f	0.2	g	0.528
p_s	0.6	p_D	0.48
p_E	0.096	p_X	0.48
d_D	0.4	d_E	0.2
d_X	1.04	a_f	0.9
R_T	2.5	$\ominus$	1.5
GF	6.3	t_s	3600
V_{deg}	0.01 μMs^{-1}	$[ATP_I]_{max}$	500 μM
V_{ATP}	50 s^{-1}	$[IP_3]_{min}$	0.013 μM
D_c	0.5	$[IP_3]_c$	0.012 μM
ϱ	0.01 μM^{-1}	γ	0.4
D_{ATP}	350 μm^{2}s^{-1}	Δx	10 μm
$p1$	0.0159835 μM	$p2$	0.514987
$p3$	1.31319	$p4$	0.332195
$p5$	0.787902	m	24.1946
n	9.79183	α	0.083 s^{-1}
K_{deg}	50 μM	$[Ca^{2+}]_b$	0.0159835 μM
k_{deg}	0.0625 s^{-1}	R_{sc}	1

Chapter 5

A Role for Noise?

5.1 Introduction

In this chapter we consider the model for coupled calcium and cell cycle dynamics with an additive noise term. Molecular fluctuations are intrinsic to biological reactions, but they are often 'averaged out' by the relatively large scale of biological systems. However, this is not always the case, especially when biological mechanisms rely upon molecular thresholds to be met, such as in ion channel gating [26]. In these cases, noise can radically change the dynamics of the system. For example, White *et al* considered a stochastic neural model, where the behaviour of ion channels was randomised, reflecting the fluctuations in molecules involved with ion channel gating [94]. Their results suggest that noise may act to regulate the dynamics in the entorhinal cortex (part of the temporal lobe). Schneidman *et al* studied a stochastic Hodgkin-Huxley model of spiking neurons which incorporated random ion channel behaviour [78]. Their results led them to the counter-intuitive conclusion that noise increases the reliability and precision of spike timing.

As a preliminary investigation into the potential role noise may play in our system, we investigated modelling the calcium concentration stochastically (achieved by adding a noise term to the right hand side of equation (3.7), which expresses calcium as a function of IP_3). However, we discovered that the larger scale cell cycle dynamics 'average out' the calcium fluctuations, whose effect on the dynamics of the system was negligible (results not shown). The model (3.1) - (3.14) studied in the previous chapters incorporates a threshold switch to model the opening of hemichannels and the release of ATP. Preliminary investigations revealed that fluctuations in the threshold had a significant effect on the dynamics of our

system. This is therefore an example where fluctuations in the number of molecules may not be 'averaged out', but may in fact have significant influence over the system behaviour.

There are several examples in the literature of stochasticity leading to unusual and sometimes counter-intuitive behaviour. For example, noise can amplify the effect of periodic forcing of an oscillator, a process known as stochastic resonance (see [29, 38] for a discussion); advance saddle node bifurcation points [42] and advance Hopf bifurcation points [37]. In the previous chapter we investigated the ability of a driving cell to recruit a quiescent cell onto the cell cycle, which depended upon the existence of an area of multistability in the system. There is the possibility that, upon the introduction of noise into our system, we may see a similar change in behaviour to that observed in the examples above. Noise could shift bifurcation points in the system and in doing so increase or decrease the area of multistability in the system. This in turn could help enhance, or indeed hinder, a driving cell's ability to recruit a quiescent cell, which could have ramifications for our models' abilities to account for ATP induced calcium signals increasing the proportion of proliferating radial glia. Furthermore, we mentioned in the previous chapter that we have no way of accounting for the initialisation of neurogenesis, i.e. we have not modelled the process of going from several inert cells at steady state to several oscillating cells. Noise may be able to account for this too. Fluctuations at steady state may facilitate the spontaneous release of ATP from open hemichannels which in turn could drive a cell into the oscillatory regime signalling the start of neurogenesis.

We begin our investigation into the role of noise by firstly presenting our stochastic model and then conducting a numerical exploration of the dynamics of one and two cells. These results are then compared with the results of our deterministic model to ascertain the degree to which noise changes the dynamics of our system and the nature of this change. With this achieved, we as a 'proof of concept', consider larger stochastic systems in one spatial dimension in order to see if noise has the potential to increase neural production.

5.2 The Stochastic Model

In our model we add noise to the threshold governing the release of ATP (D_c in the Cyclin D dependent ATP release model, R_{sc} in the R_s dependent ATP release model), thus

modelling the opening of a cell's hemichannels, which governs the release of ATP, stochastically. We choose to add noise to our model in this manner, as in this case its effects are not 'averaged out' by the dynamics of the deterministic system. This will not always be the case. For example, when we added noise to the right hand side of equation 3.1, we discovered that its effect upon the system was 'averaged out' by the governing dynamics of the deterministic system (results not shown). Our model is as before, but with $H_i = D_i$ and $H_c = D_c + \xi(t, \mu, \sigma^2)$ from equation (3.14) in the Cyclin D dependent ATP release model, and $H_i = R_{sc} + \xi(t, \mu, \sigma^2)$ and $H_c = R_{si}$ in the R_s dependent model. Here $\xi(t, \mu, \sigma^2)$ is Gaussian white noise of zero mean value $\mu = 0$ and variance σ^2.

5.3 Numerical Techniques and Considerations

5.3.1 Method of Integration

In simulating system (3.1)-(3.14), we elected to take a similar approach to [15]. In [15] Coombes *et al* use a fixed step numerical solver in order that the randomness can be prescribed at regular intervals. With this in mind, we chose to use the forward Euler method of integration to numerically solve the system because, although slow, it is a fixed step method and is relatively straightforward to program.

In using the Euler method however, there is a danger that we may violate the Courant-Friedrichs-Lewy (CFL) condition which ensures the stability of the solution when the Euler method is used to solve PDEs discretised via the method of lines. If we were to violate this condition, then the Euler method may not converge. In our system, the CFL condition is satisfied if $\Delta t < \frac{\Delta x^2}{2t_s D_{ATP}}$ (where Δt is the time step for our method of integration). If we were to use the parameter values for D_{ATP} (350 $\mu m^2 s^{-1}$) and Δx (10 μm) that we have used previously then our time step would have to be of the order of 10^{-5} hrs for the CFL condition to be satisfied. With such a small time step it would take an exceptionally long period of time to numerically solve our system for all but the shortest periods of time. This problem would be exacerbated when considering a stochastic system as it would be necessary to simulate our system several times in order to obtain its 'average' behaviour. Consequently, as a matter of necessity we sought to reduce D_{ATP}, or equivalently (where the CFL condition is concerned), increase Δx. In Section 4.3 of the previous chapter we

showed that for a large area of parameter space the dynamics of our system were unaffected by a reduction in D_{ATP} to values as low as $10\mu m^2 s^{-1}$. We therefore decided to reduce D_{ATP} to 10 $\mu m^2 s^{-1}$, which meant that we required a Δt of order 10^{-3} hrs in order to satisfy the CFL condition. Such a reduction in the diffusion co-efficient is not as much at odds with the biological reality as one may initially think. Indeed studies suggest that molecules in the brain may diffuse up to five times more slowly than they do in free solution due to factors such as the presence of macromolecular obstacles in extra-cellular space and the viscous drag of cell walls [62, 76]. As a value of D_{ATP} of 350 $\mu m^2 s^{-1}$ was calculated by studying ATP diffusion in free solution and it appears that a reduction in the value of D_{ATP} does not significantly affect the dynamics of our system, in subsequent simulations we use a value of D_{ATP} of 10 $\mu m^2 s^{-1}$. This allows us to use a time step Δt of 0.001 hours. Numerical exploration revealed that reducing Δt did not qualitatively change the dynamics of the system. However it did significantly increase the real time needed to solve the system which is why we decided not to reduce it. Increasing Δt resulted in the violation of the CFL condition and the failure of the Euler method to converge to the solution. We used Matlab's pseudo-random number generator drawn from the normal distribution `randn` to sample $\xi(t, \mu, \sigma^2)$.

5.3.2 Bifurcation Analysis

In analysing stochastic systems we can not use tools such as AUTO (software for numerical continuation of deterministic systems, which is incompatible for use with stochastic systems). A different approach is needed and we use a similar technique to Hutt [42] to produce stochastic equivalents of bifurcation diagrams which we will refer to henceforce as 'stochastic bifurcation diagrams'. Hutt considers a system of two non-linear ODEs which displays hysteresis and then adds noise to the system. In order to study the behaviour of the stochastic model, an ensemble of initial conditions is considered and the system numerically solved for each set of initial conditions for different values of the control parameter. The solutions for each value of the control parameter are then plotted and compared with the bifurcation diagram of the deterministic system in order to ascertain whether additive noise affects the stability of the system in any way. Hutt discovered that noise acted to shift the bifurcation point of the deterministic system. Furthermore, by conducting analysis on the stochastic model, Hutt was able to calculate the degree to which this was the case. The red

line in Figure 5.1 is derived from Hutt's analysis. The black line corresponds to the original deterministic system. The more complex nature of our model means that it is not feasible for us to apply Hutt's analytical technique. Furthermore, we are not aware of an analytical technique which can be used universally, on all systems to determine *a priori* how noise will effect bifurcation points. However, we can still use Hutt's numerical technique.

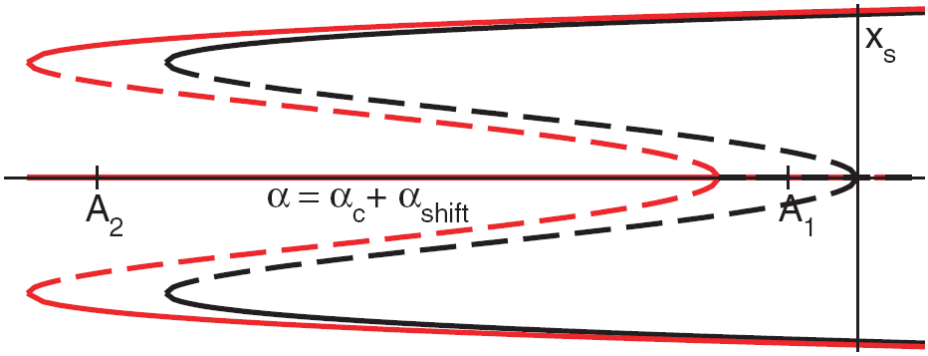

Figure 5.1: Diagram illustrating the effect an additive noise term has on a deterministic system studied by Hutt. The black line corresponds to the bifurcation diagram of the deterministic system and the red to the behaviour of the system which incorporates an additive noise term. Dashed lines correspond to unstable solutions and solid lines to stable solutions. The results indicate that the noise acts to shift the saddle node bifurcation points of the deterministic system to the left (relative to the control parameter). Reproduced from [42] with permission from EPL.

As our system is of a larger dimension, if we considered an ensemble of initial conditions where every variable's initial condition was varied, our initial condition ensemble could become very large indeed. When we also take into account that we will need to simulate our stochastic system several times for each value of the control parameter, it becomes clear that the process of producing stochastic bifurcation diagrams will be very computationally expensive. For this reason, we decided to only vary the initial conditions of Cyclin D in our ensemble, with all other initial conditions taking their steady state values. Our numerical investigations revealed that by varying $D_i(0)$ between 0 and 2 and keeping all other initial conditions at the stable steady state, our deterministic system displayed all of the behaviour it was capable of. Solution trajectories tended towards the steady state solution for small values of $D_i(0)$ and for larger values of $D_i(0)$ tended towards limit cycle or torus solutions, where both solution types existed. Therefore, in our ensemble we set a lower limit of

$D_i(0) = 0$ and an upper limit of 2, utilising Matlab's uniformly distributed pseudorandom number generator function `rand` to generate an initial condition for $D_i(0)$ between these values. Not varying the initial conditions of all other variables allowed us to keep down the size of the ensemble, allowing us to solve our stochastic system a sufficient number of times to obtain a meaningful 'average' without the process being too computationally expensive. In producing our stochastic bifurcation diagrams, we numerically integrated our system from each set of initial conditions for a total of 600 hrs. In order to ensure system transients did not affect our results, we disregarded the first 300 hrs of the solution, only taking into account the final 300 hrs when producing bifurcation diagrams. We calculate the average Cyclin D concentration over the last 300 hours and by this measure we are able to distinguish between 'steady state' and 'oscillatory' behaviour.

5.4 Single Cell Bifurcation Analysis

In this section we use the numerical technique outlined in Section 5.3.2 in order to produce bifurcation diagrams of our stochastic system for a single cell.

5.4.1 Cyclin D Dependent ATP Release

We begin our analysis by considering the model where ATP release is modelled as predominantly occurring during mid G_1 phase (equations (3.1)-(3.14), where $(H_i, H_c) = (D_i, D_c + \xi(t, \mu, \sigma^2))$). Bifurcation diagrams of our stochastic system for two different values of the variance σ^2, together with the bifurcation diagram for the deterministic system, are shown in Figure 5.2. The first column of plots in the figure shows the average Cyclin D across the ensemble. While the second column of plots show the frequency of average Cyclin D in certain bins, so that the spread of ensemble behaviour becomes apparent. The minimum value of the control parameter a'_{d1} at which oscillatory type solutions were detected for the stochastic system is marked SFP^D (stochastic fold point). We detected oscillatory type solutions by confirming that the state variables were oscillating in a limit cycle type fashion during the last 300 hours of the period of integration. As before, the saddle node bifurcation point corresponding to the value of a'_{d1} where limit cycle solutions in the deterministic system arise is marked as FP1^D.

From the figure it appears that the stochasticity in our system has the effect of moving

the bifurcation point that leads to oscillatory behaviour to the left, relative to the deterministic case. Not only this, but for a value of $\sigma^2 = 0.0005$, SFP^D corresponds to a value of a'_{d1} of 0.386, while for $\sigma^2 = 0.01$, SFP^D occurs at $a'_{d1} = 0.368$, indicating that increasing the variance shifts SFP^D further away from FP1^D, which occurs at $a'_{d1} = 0.386$. It would seem therefore that the noise introduced into our system is filtered in a non-linear manner, leading to a change in the point at which oscillations arise. Furthermore, by studying the first column of plots in Figure 5.2 one can see that the noise increases the average concentration of Cyclin D in the oscillatory type solutions. An increase in the variance σ^2 of the noise brings about a further increase in the average Cyclin D concentration. The noise also appears to shift FP3^D to the left, although not to the same degree to which FP1^D is moved. The second column of plots are colour plots which indicate the number of realisations that had the indicated average Cyclin D at each value of a'_{d1}. In this particular plot the realisations fall into one of two distinct groupings; an upper grouping which correspond to oscillatory type solutions and a lower group which correspond to stable steady state type solutions.

These results are augmented by the diagrams seen in Figure 5.3. The left hand plot is a two parameter stochastic bifurcation diagram, where σ^2 and a'_{d1} are the control parameters and it shows that as the variance of the noise is increased, SFP^D moves further and further away from FP1^D. Additionally, as is evidenced in the right hand plot, increasing the variance of the noise has the effect of increasing the average Cyclin D concentration of oscillatory type solutions.

In shifting the left hand boundary of the area of mulitstability (FP1^D) to the left more significantly than the right hand boundary (FP3^D), the noise increases the area of multistability of our system. With a larger area of multistability, quiescent cells that sit on the branch of stable steady state solutions shown in Figure 5.2, that lie outside the area of multistability of the deterministic system, may not lie outside the area of multistability of the stochastic system. Consequently a stochastic system may allow for the possibility of the recruitment of initially quiescent cells that are beyond the reach of the deterministic system and/or accelerate the speed at which formerly quiescent cells are recruited onto the cell cycle. This process could in turn lead to an increase in overall proliferation. Further work on systems of several cells would need to be carried out to confirm this hypothesis however. We investigate if this is the case in Section 5.6.

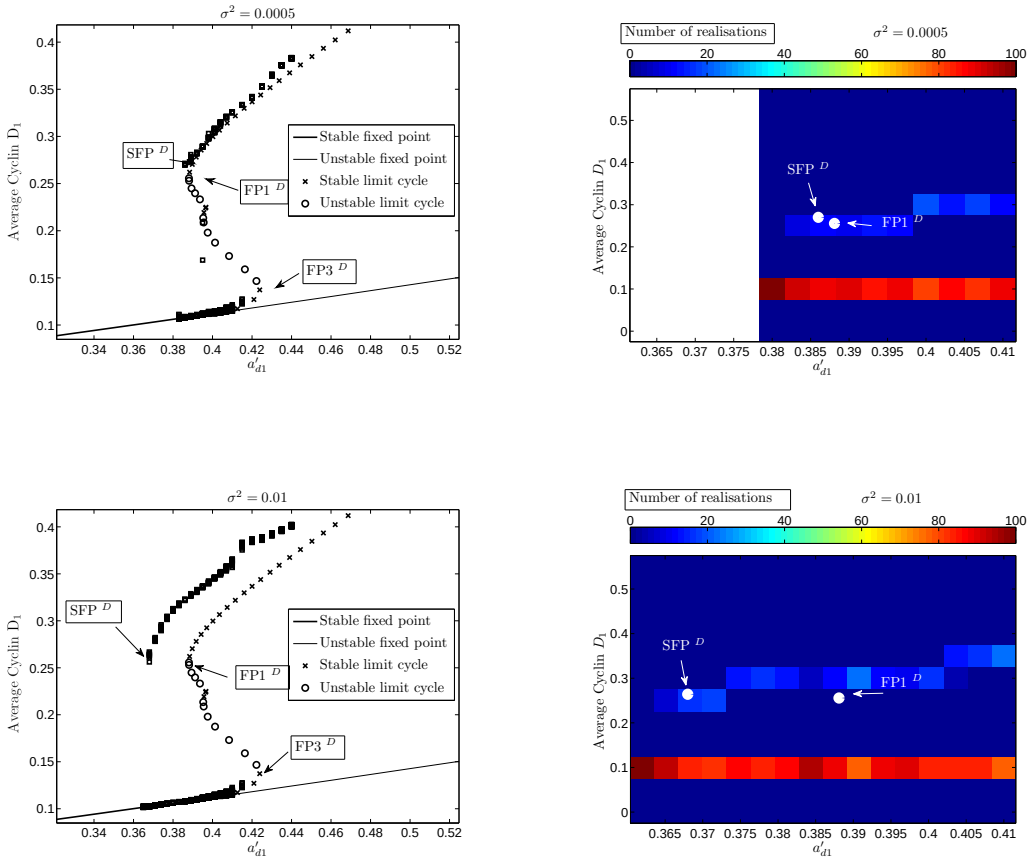

Figure 5.2: Bifurcation diagrams of system (3.1)-(3.14) for $\sigma^2 = 0$ (the deterministic system) and for two different values of the variance σ^2 (the stochastic system) for the Cyclin D dependent ATP release model ($(H_i, H_c) = (D_i, D_c + \xi(t, \mu, \sigma^2))$). The diagrams illustrate the effect the noise has on shifting the point at which oscillatory behaviour arises, as well as its effect upon the concentration of Cyclin D. SFP^D corresponds to the point at which oscillatory behaviour arises in the stochastic system, while FP1^D corresponds to the point at which oscillatory behaviour arises in the deterministic system, and FP3^D to the saddle node bifurcation point we first encountered in Figure 2.10. The average Cyclin D concentration over the last 300 hours of the period of integration for each stochastic realisation is plotted with a square in the first column of plots. X's, O's and straight lines correspond to the deterministic system. The second column of plots are colour plots with average Cyclin D within each of a set of bins (ranging from -0.025 - 0.575 at intervals of 0.05) for each value of a'_{d1} (ranging from 0.36-0.41 at intervals of 0.0003). The deterministic bifurcation diagram was produced using AUTO, and the stochastic bifurcation diagrams were produced as outlined in Section 5.3.2 with an ensemble of 100 initial conditions for each value of a'_{d1} considered. Parameter values as in Table 5.1 unless otherwise indicated.

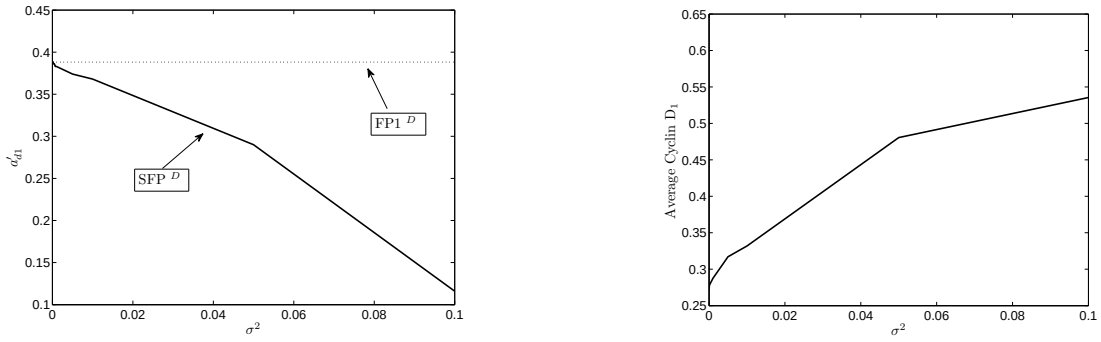

Figure 5.3: Bifurcation diagrams for the stochastic system given by equations (3.1)-(3.14) for the Cyclin D dependent ATP release model ($(H_i, H_c) = (D_i, D_c + \xi(t, \mu, \sigma^2))$). The left plot (a two parameter bifurcation diagram) shows that increasing the variance of the noise σ^2 moves the point at which oscillatory type behaviour arises (SFP^D) further away from FP1^D, the point at which oscillatory solutions arise in the deterministic system. The right plot reveals the extent to which the average concentration of Cyclin D is increased as σ^2 is increased. In the plot of the average Cyclin D concentration, the average of all oscillatory type solutions for the stochastic system at $a'_{d1} = 0.392$ was taken. Parameter values as in Table 5.1 unless otherwise indicated.

5.4.2 R_s Dependent ATP Release

Our results for the Cyclin D dependent model are parallelled here, where we consider the R_s dependent ATP release model (given by system (3.1)-(3.14), with $(H_i, H_c) = (R_{sc} + \xi(t, \mu, \sigma^2), R_{si})$). By referring to Figure 5.4, where stochastic bifurcation diagrams for the R_s dependent model are shown, it is clear that noise has the effect of moving the point at which oscillations arise away from FP1^{Rs}. The right hand boundary of the area of bistability (FP2^{Rs}) is shifted to the left but far less severely than the left hand boundary (FP1^{Rs}). Therefore noise acts increase the area of bistability in the R_s dependent ATP release system in a similar way to which it acts in the Cyclin D dependent ATP release model. As for the Cyclin D dependent model, increasing the variance of the noise leads to an increase in the average Cyclin D concentration of the solutions displaying oscillatory type behaviour, as is illustrated in Figure 5.5 (right hand plot). It therefore appears that for the R_s dependent model, additive noise acts to increase the area of bistability. This in turn raises the possibility that noise may enhance a driving cell's ability to recruit quiescent cells in the R_s dependent model as well as the Cyclin D dependent model.

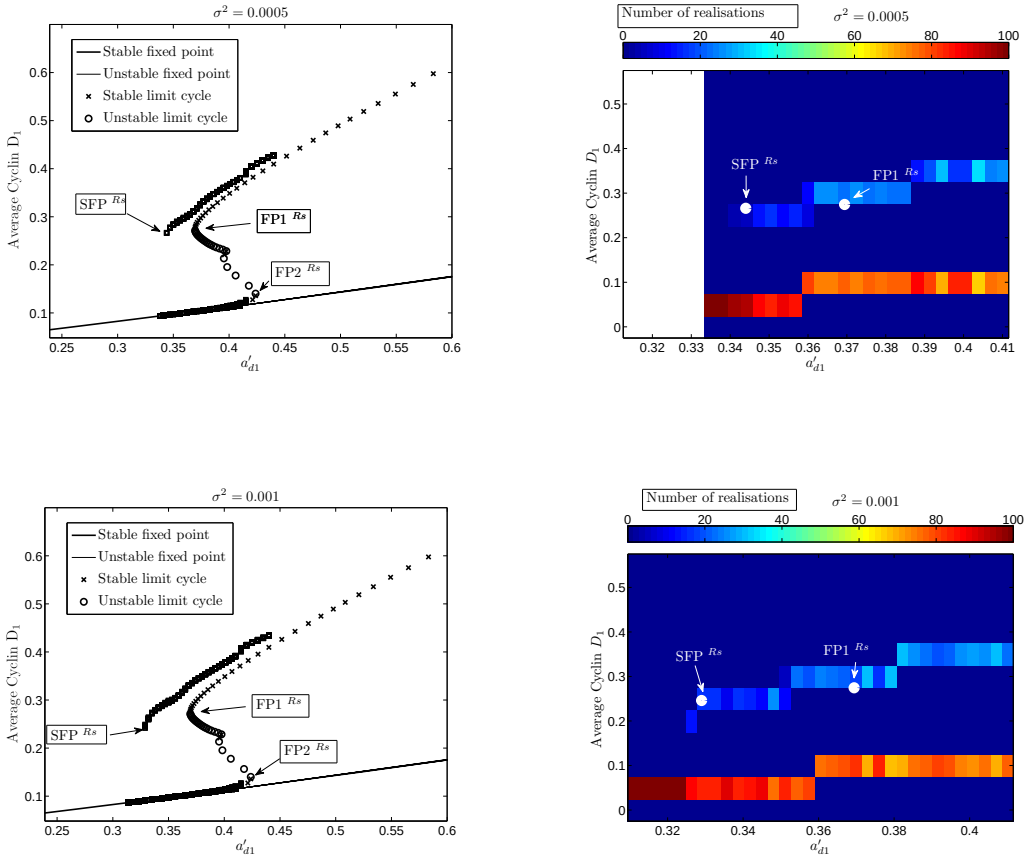

Figure 5.4: Bifurcation diagrams of system (3.1)-(3.14) for $\sigma^2 = 0$ (the deterministic system) and for two different values of the variance σ^2 (the stochastic system) for the R_s dependent ATP release model ($(H_i, H_c) = (R_{sc}+\xi(t, \mu, \sigma^2), R_{si})$). The bifurcation diagrams illustrate that the noise moves the point at which oscillatory type behaviour arises and increases the average concentration of Cyclin D. SFP^{Rs} corresponds to the point at which oscillatory behaviour arises in the stochastic system, while FP1^{Rs} corresponds to the point at which oscillatory behaviour arises in the deterministic system. The deterministic bifurcation diagram was produced using AUTO, and the stochastic bifurcation diagrams were produced as outlined in Section 5.3.2 with an ensemble of 100 initial conditions for each value of a'_{d1} considered. Parameter values as in Table 5.1 unless otherwise indicated.

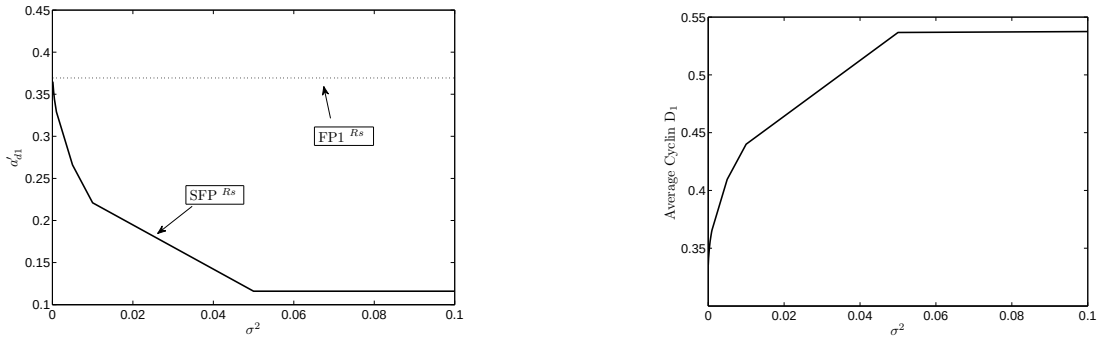

Figure 5.5: Bifurcation diagrams for the stochastic system given by equations (3.1)-(3.14) for the R_s dependent ATP release model ($(H_i, H_c) = (R_{sc} + \xi(t, \mu, \sigma^2), R_{si})$). The left plot (a two parameter bifurcation diagram) shows that increasing the variance of the noise σ^2 moves the point at which oscillatory type behaviour arises (SFP^{Rs}) further away from FP1^{Rs}, the point at which oscillatory solutions arise in the deterministic system. The right plot reveals the extent to which the average concentration of Cyclin D increases as σ^2 is increased (the average of all oscillatory type solutions for the stochastic system at $a'_{d1} = 0.392$ was taken). Parameter values as in Table 5.1 unless otherwise indicated.

Next, we investigate the hypothesis that the stochastic system has an enhanced ability to recruit quiescent cells onto the cell cycle, by considering systems of two cells for both models.

5.5 Two Cell Bifurcation Analysis

In previous chapters we have considered scenarios where all or a large number of simulated cells are identical. This is unlikely to be the case in reality, where cells often oscillate with different frequencies. With this in mind we consider two cell systems for three different values of a'_{d1} (0.35, 0.38 and 0.41), but where a'_{d2} is varied over a large range for each value of a'_{d1} considered. As the Cyclin D synthesis rate a_d influences the existence and the period of the limit cycle solutions of simulated cells, studying systems where a_d is varied in both cells will give us a better feel of the dynamics of systems of non-identical cells, oscillating at different frequencies.

In previous chapters, in producing bifurcation diagrams for our two cell deterministic

system, we discovered that, under some parameter regimes, torus and limit cycle solutions co-exist. Although we were able to detect the point at which these torus solutions were created, we were unable to continue the solution branch itself using AUTO. Our numerical results indicate that torus like solutions appear to exist for our two cell stochastic system also, which helps to explain the 'scatter gun' effect of the bifurcation diagrams of the two cell stochastic systems that we shall come to.

5.5.1 Cyclin D Dependent ATP Release

Stochastic bifurcation diagrams together with their deterministic counterparts, where a'_{d2} is the control parameter for a two cell system where $\sigma^2 = 0.0005$, are shown in Figure 5.6. This figure shows that the stochastic solutions (marked with squares) exhibit a 'scatter gun' effect throughout parameter space. This effect results from both torus like and limit cycle type solutions co-existing. This makes it very difficult to ascertain the point at which limit cycle type solutions arise, which in turn makes it very difficult to ascertain how noise affects the point at which limit cycle type solutions arise (marked FP1_a^D in Figure 5.6). However, it remains an easier task to ascertain at which point oscillatory type solutions arise (we include torus type solutions within this) and this point is marked as SOP^D (Stochastic oscillation point) in Figure 5.6. SOP^D corresponds to the point at which oscillations arise in cell 2. It is clear from Figure 5.6 that SOP^D occurs before oscillations arise in the deterministic system (marked TB), indicating that noise moves to the left the point in parameter space at which oscillations arise.

From Figure 5.6 it can be seen that the maximum average Cyclin D concentration in both cells for the stochastic system far exceeds that of the deterministic system. Although there are many other 'rogue' stochastic solutions (many of which are torus like solutions) where the average Cyclin D concentration does not exceed that of the deterministic model, it appears that by and large noise increases the average Cyclin D concentration in both cells, in a similar fashion to the single cell case.

Shown in Figure 5.7 are bifurcation diagrams where the variance of the additive noise is 0.005, ten times more than that of the results displayed in Figure 5.6. The increased variance results in the point at which oscillations in the second cell arise (SOP^D in Figure 5.7) being shifted even more dramatically. Indeed SOP^D occurs at $a'_{d2} = 0.2750$ when

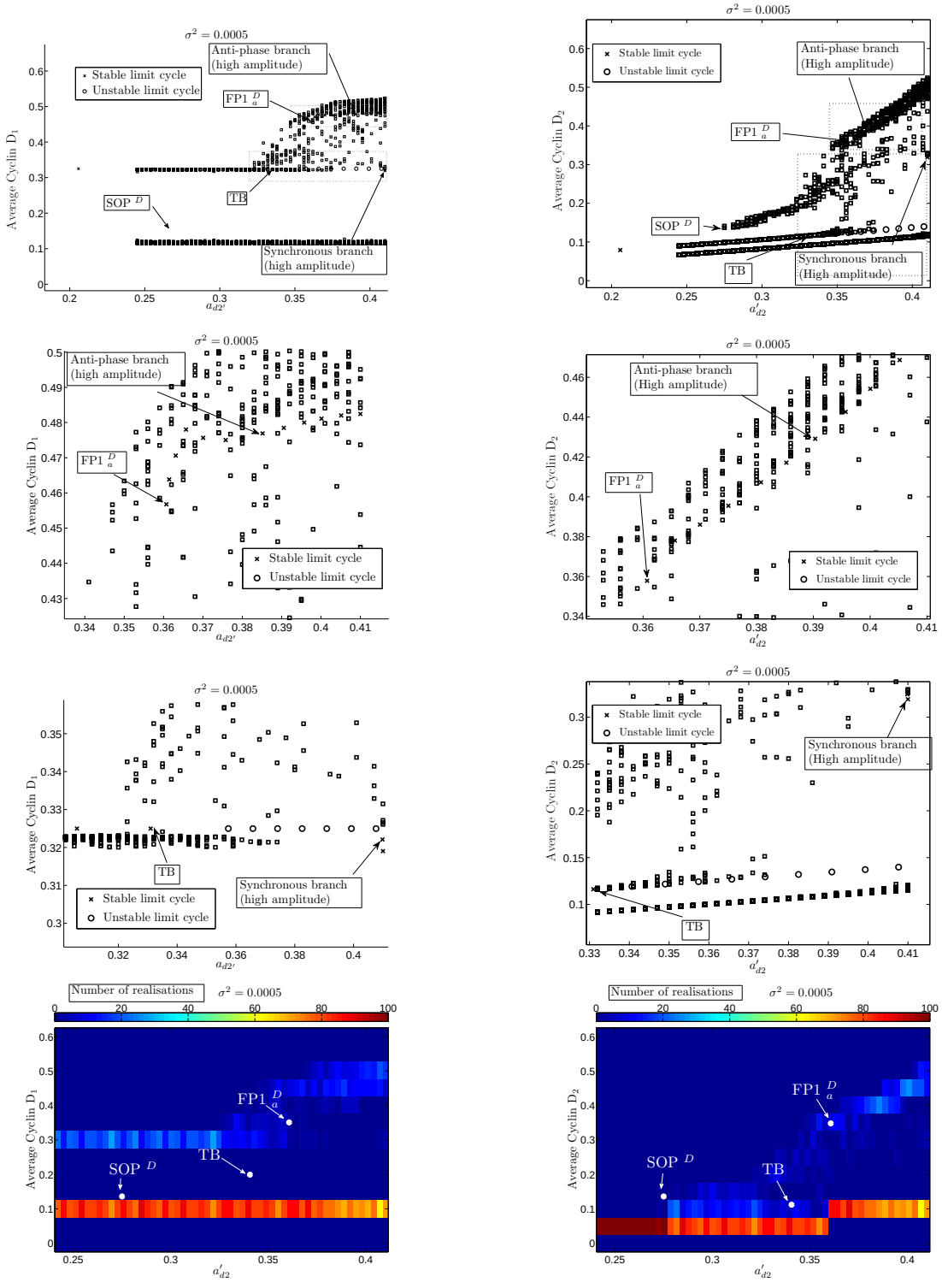
Cell 1
Cell 2
$\sigma^2 = 0.0005$
Anti-phase branch (high amplitude)
Stable limit cycle
Unstable limit cycle
FP1 ^D_a
SOP ^{D}
TB
Synchronous branch (high amplitude)
Average Cyclin D1
Average Cyclin D2
$a_{d2'}$
a'_{d2}
Number of realisations

Figure 5.6

Figure 5.6: Bifurcation diagrams of system (3.1)-(3.14) for $\sigma^2 = 0$ (the deterministic system) and and for $\sigma^2 = 0.0005$ (the stochastic system) for two cells in the Cyclin D dependent ATP release model ($(H_i, H_c) = (D_i, D_c + \xi(t, \mu, \sigma^2))$). The diagrams show that noise moves the point at which oscillatory type solutions arise to the left and suggest that the average Cyclin D concentration of the oscillations in cells 1 and 2 increases with noise. TB corresponds to a torus bifurcation point, SOP^D corresponds to the point at which oscillations arise in cell 2 in the stochastic system, while FP1_a^D corresponds to the point at which limit cycle solutions arise in the deterministic system. Each stochastic realisation is indicated by a square in the first six plots. The X's, O's and straight lines in these plots correspond to the deterministic system. The dotted boxes in the first row of plots correspond to the areas that we have zoomed in on in subsequent plots. The bottom row of plots are colour plots with average Cyclin D within each of a set of bins (ranging from -0.025 - 0.625 at intervals of 0.05) for each value of a'_{d2} (ranging from 0.24-0.41 at intervals of 0.0003). The deterministic bifurcation diagram was produced using AUTO, and the stochastic bifurcation diagrams were produced as outlined in Section 5.3.2 with an ensemble of 100 initial conditions for each value of a'_{d2} considered. Parameter values as in Table 5.1 unless otherwise indicated.

$\sigma^2 = 0.0005$, while it occurs at $a'_{d2} = 0.2480$ when $\sigma^2 = 0.005$.

In Figure 5.8 are shown bifurcation diagrams for our two cell stochastic system, but this time for a different value of a'_{d1} (the Cyclin D synthesis rate of cell 1). Up until this point we have considered values for a'_{d1} of 0.41. However in Figure 5.8 we set a'_{d1} to 0.38. The reason we did this was because we wanted to explore variation in a'_{d2} for different characteristic situations in cell 1. Interestingly, it appears that in this case additive noise fails to move to the left the point at which oscillatory type solutions arise. In fact it appears that the noise shifts it to the right. We suspect, however, that the shifting of the point leading to oscillatory type solutions in this manner is an artifact of having too small an ensemble of initial conditions. For such a small value of the variance (0.0005), the system's dynamics are unlikely to be as severely affected as they would be for a larger value of the variance and it would therefore be more difficult to pick up any change in these dynamics. This argument is supported by the results in Figure 5.8, where it can clearly be seen that for a larger value of the variance (0.005), noise does shift the onset of oscillatory solutions to the left.

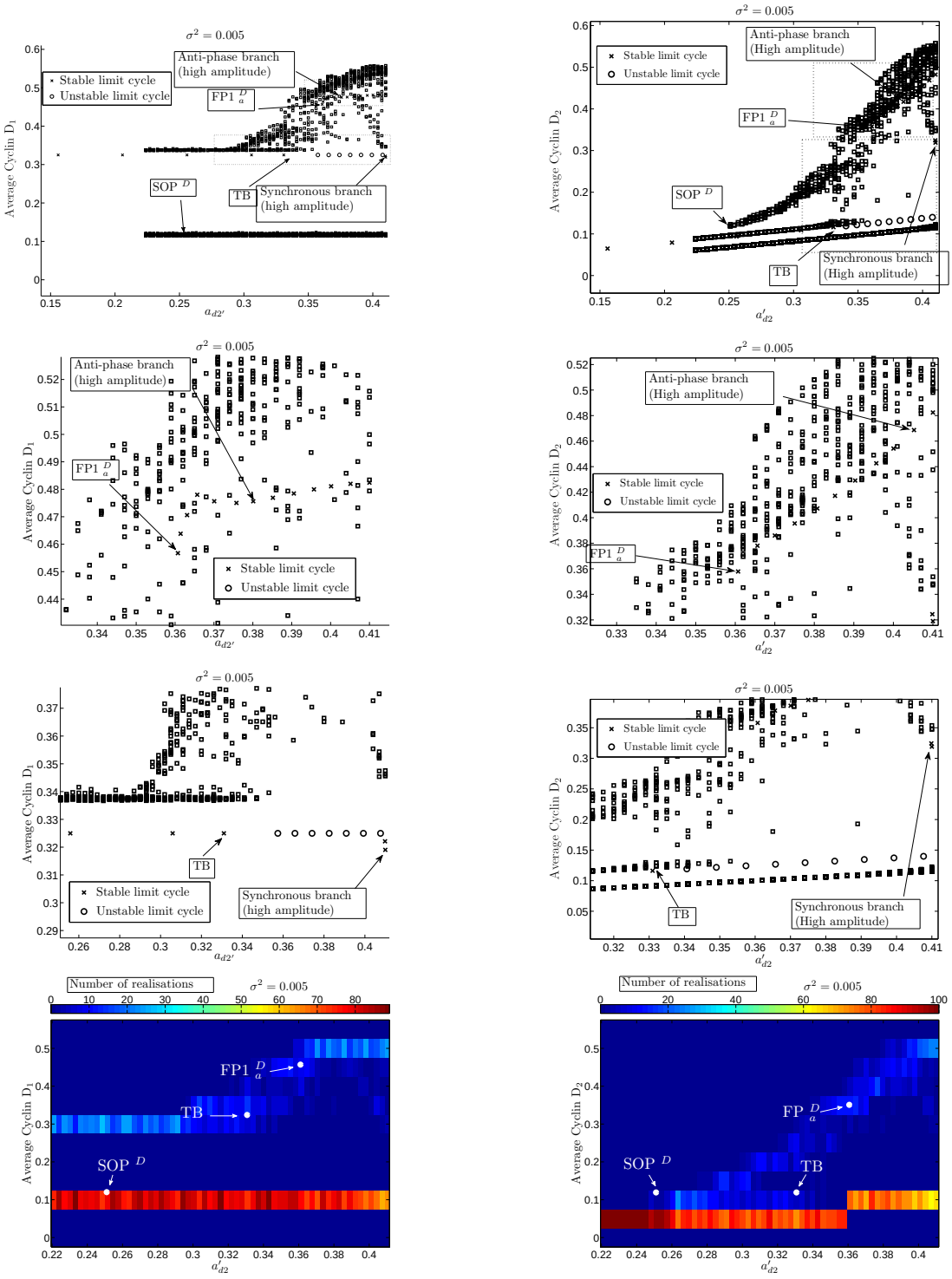
Cell 1
Cell 2
$\sigma^2 = 0.005$
Anti-phase branch (high amplitude)
Stable limit cycle
Unstable limit cycle
FP1 ^D_a
SOP ^{D}
TB
Synchronous branch (high amplitude)
Average Cyclin D$_1$
Average Cyclin D$_2$
$a_{d2'}$
a'_{d2}
Number of realisations
FP ^D_a

Figure 5.7

Figure 5.7: Bifurcation diagrams of system (3.1)-(3.14) for $\sigma^2 = 0$ (the deterministic system) and $\sigma^2 = 0.005$ (the stochastic system) for two cells in Cyclin D dependent ATP release model ($(H_i, H_c) = (D_i, D_c + \xi(t, \mu, \sigma^2))$). By comparing the diagrams to the results displayed in Figure 5.6, it can be seen that increasing the variance of the noise further shifts to the left the point at which oscillations arise in cell 2. The diagrams also suggest that the average Cyclin D concentration of the the oscillations in cell 1 and cell 2 increases further still when the variance of the noise is increased. Parameter values as in Table 5.1 unless otherwise indicated.

Figure 5.10 shows 2 cell bifurcation diagrams which confirm the general theme of this section, i.e. the greater the variance of the additive noise, the greater the shift in the point at which oscillations arise in our system and the greater the average Cyclin D concentration of the oscillatory type solutions. In the first column of this figure we plot two parameter bifurcation diagrams where σ^2 and the Cyclin D synthesis rate of cell 2, a'_{d2} are the control parameters for three different values of the Cyclin D synthesis rate of cell 1 a'_{d1} (0.41, 0.38 and 0.35). In all cases, noise of a sufficient variance shifts the point at which oscillatory type solutions arise such that they arise for lower values of a'_{d2} than in the deterministic case. Increasing the variance shifts the point at which stochastic oscillations arise further away from where they arise deterministically. Furthermore, in the second column of plots are shown bifurcation diagrams for three different values of the Cyclin D synthesis rate of cell 1 a'_{d1} (0.41, 0.38 and 0.35), which indicate that noise acts to increase the average Cyclin D concentration of the system.

These results support the notion that noise in ATP mediated coupling may increase the collective rate of radial glial proliferation. As for the single cell case, in the two cell case the noise is filtered in a non-linear manner and acts to advance the onset of oscillatory type solutions. This keeps the possibility very much alive that a system with noise may be able to recruit quiescent cells more quickly and/or recruit cells beyond the reach of a deterministic system.

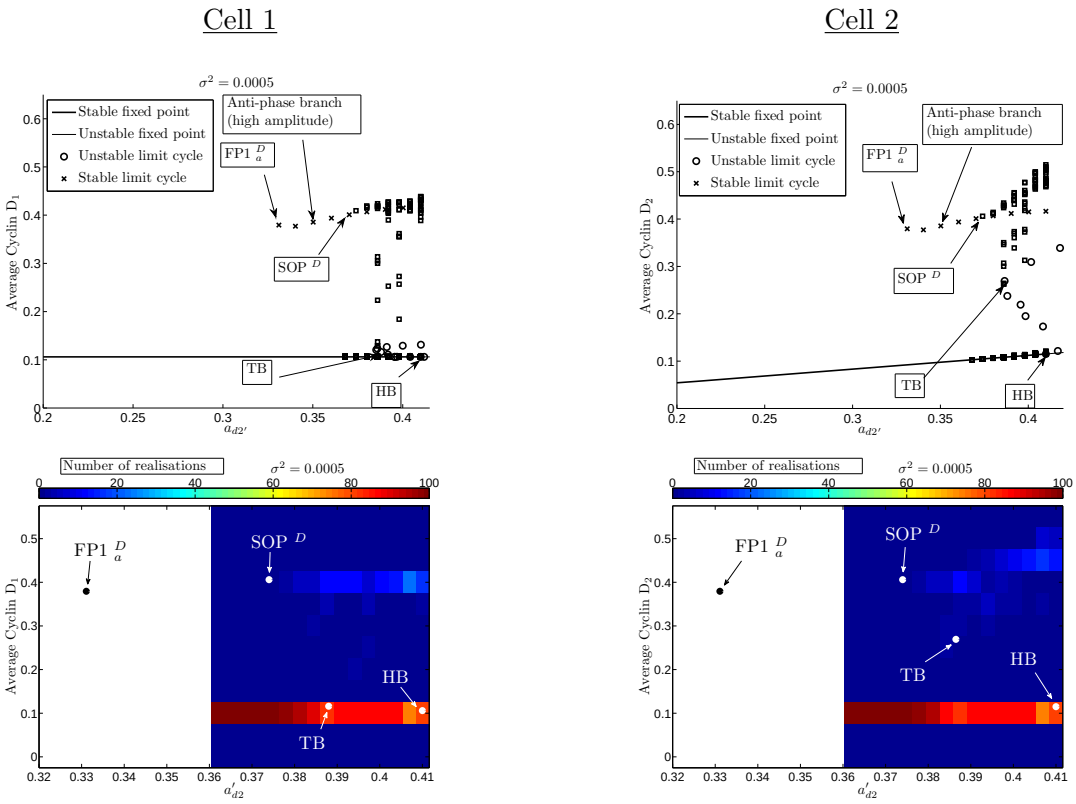

Figure 5.8: Bifurcation diagrams of system (3.1)-(3.14) for $\sigma^2 = 0$ (the deterministic system) and for $\sigma^2 = 0.0005$ (the stochastic system) for two cells in the Cyclin D dependent ATP release model ($(H_i, H_c) = (D_i, D_c + \xi(t, \mu, \sigma^2))$). The diagrams show that for a value of a'_{d1} of 0.38, noise shifts to the right the point at which oscillations arise, although it appears to increases the average Cyclin D concentrations of the oscillatory type solutions. Parameter values as in Table 5.1 except for $a'_{d1} = 0.38$.

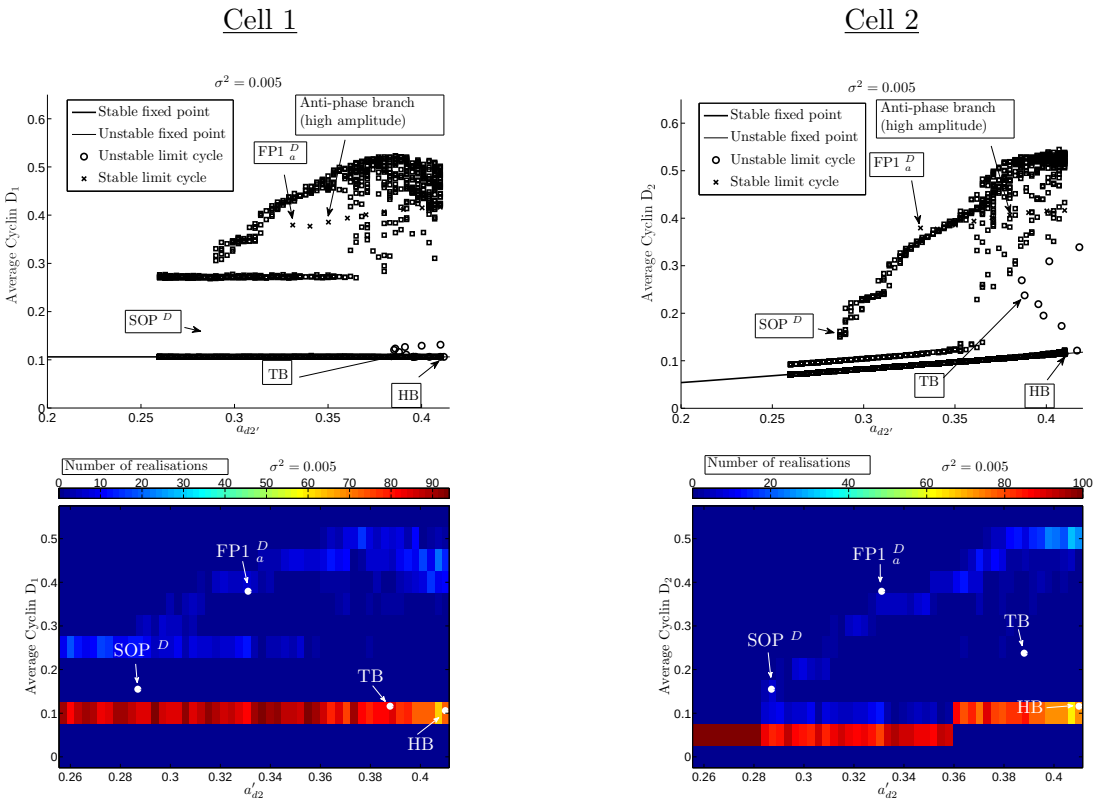

Figure 5.9: Bifurcation diagrams of system (3.1)-(3.14) for $\sigma^2 = 0$ (the deterministic system) and for $\sigma^2 = 0.005$ (the stochastic system) for two cells in the Cyclin D dependent ATP release model ($(H_i, H_c) = (D_i, D_c + \xi(t, \mu, \sigma^2))$). The diagrams show that even for a value of a'_{d1} of 0.38, noise of a high enough intensity shifts to the left the point at which oscillations arise. It can also be seen that it increases the average Cyclin D concentrations of the oscillatory type solutions. Parameter values as in Table 5.1 except for $a'_{d1} = 0.38$.

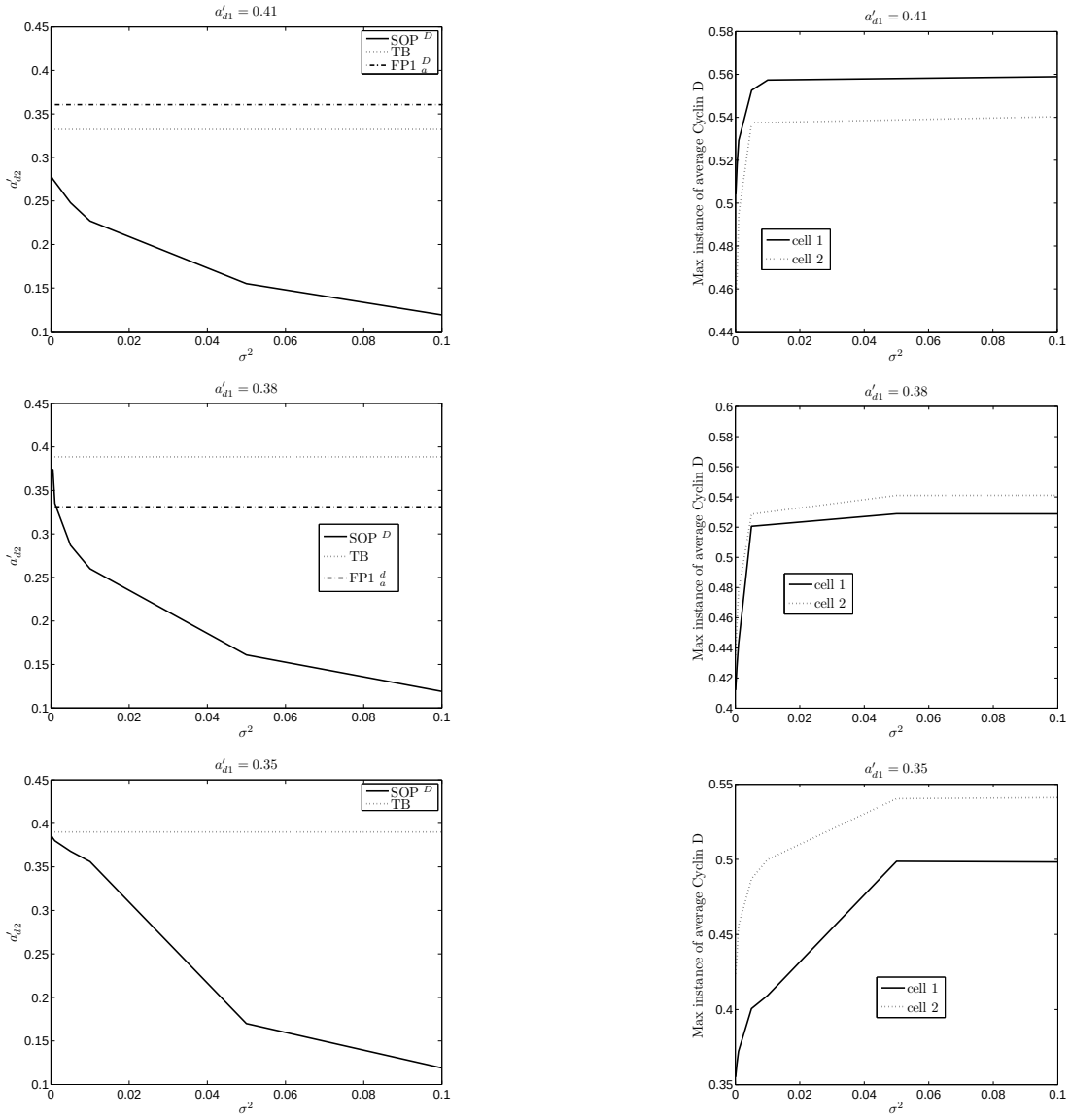

Figure 5.10: The first column shows two parameter bifurcation diagrams which indicate that increasing the variance of the noise further shifts the point at which oscillations occur away from FP1_a^D for the 3 values of a'_{d1} considered. The plots in the second column show that, at $a'_{d2} = 0.392$, increasing the variance of the noise increases the average Cyclin D concentrations of the oscillatory type solutions. Note that limit cycle solutions do not exist for the deterministic model when $a'_{d1} = 0.35$, which explains the absence of FP1_a^D in the bottom left hand corner plot.

5.5.2 R_s Dependent ATP Release

We next focused upon our R_s dependent model (system (3.1)-(3.14), with $(H_i, H_c) = (R_{sc} + \xi(t, \mu, \sigma^2), R_{si})$). The qualitative results of our two cell bifurcation analysis here are much the same as for the Cyclin D dependent model. Figure 5.11 shows the results for a variance of 0.0005, where it can be seen from the locations of TB and SOP^{Rs} that noise acts to shift the point at which oscillations arise to the left. Interestingly, the behaviour of our stochastic system appears more regular in the left hand area of parameter space in Figure 5.11 than in the right hand area. Between $a'_{d2} \approx 0.22$ and ≈ 0.28 oscillatory type solution trajectories of the stochastic system are very closely grouped around one of two curves (marked group 1 and group 2). In the bifurcation diagram of Cyclin D in cell 2 (the top right hand plot) there is a third curve beneath group 2, these are steady state type solutions. The curves in groups 1 and 2 are very regular and reminiscent of the branches of limit cycle solutions we encountered in deterministic two cell bifurcation diagrams in Section 4.2 of chapter 4. Towards the right hand area of the parameter space shown in Figure 5.11 this regularity is lost, with the data points almost having a 'scatter gun' effect, with many of the solutions being torus type solutions that we first discovered in Section 4.2 of chapter 4. Interestingly, the scatter gun effect only appears at $a'_{d2} \approx 0.28$, just before the torus bifurcation point of the deterministic system (marked TB). The regular behaviour seen in group 1 occurs well before the point at which limit cycle solutions arise in the deterministic system (marked FP_s^{Rs}), however. This suggests that the noise has a far greater effect upon moving the saddle node bifurcation point (FP_s^{Rs}) than it does the torus bifurcation point (TB). In effect it moves FP_s^{Rs} past TB, so that limit cycle type solutions arise before torus type solutions in the stochastic system, the converse to the deterministic system. In this instance therefore, noise in the R_s dependent ATP release model appears to 'regulate' the behaviour of the system by seemingly allowing the limit cycle type solutions to dominate the torus type solutions. This is a phenomenon that could have biological implications and is something that we did not encounter when studying the Cyclin D dependent ATP release model. It also appears that, generally speaking and especially where cell 2 is concerned, noise has the effect of increasing the average Cyclin D concentration of the oscillatory type solutions of our system.

As we have seen before, the effect of noise on the system is intensified when the variance is increased. For a value of σ^2 of 0.0005, SOP^{Rs} occurs at $a'_{d2} = 0.238$, while for $\sigma^2 = 0.005$

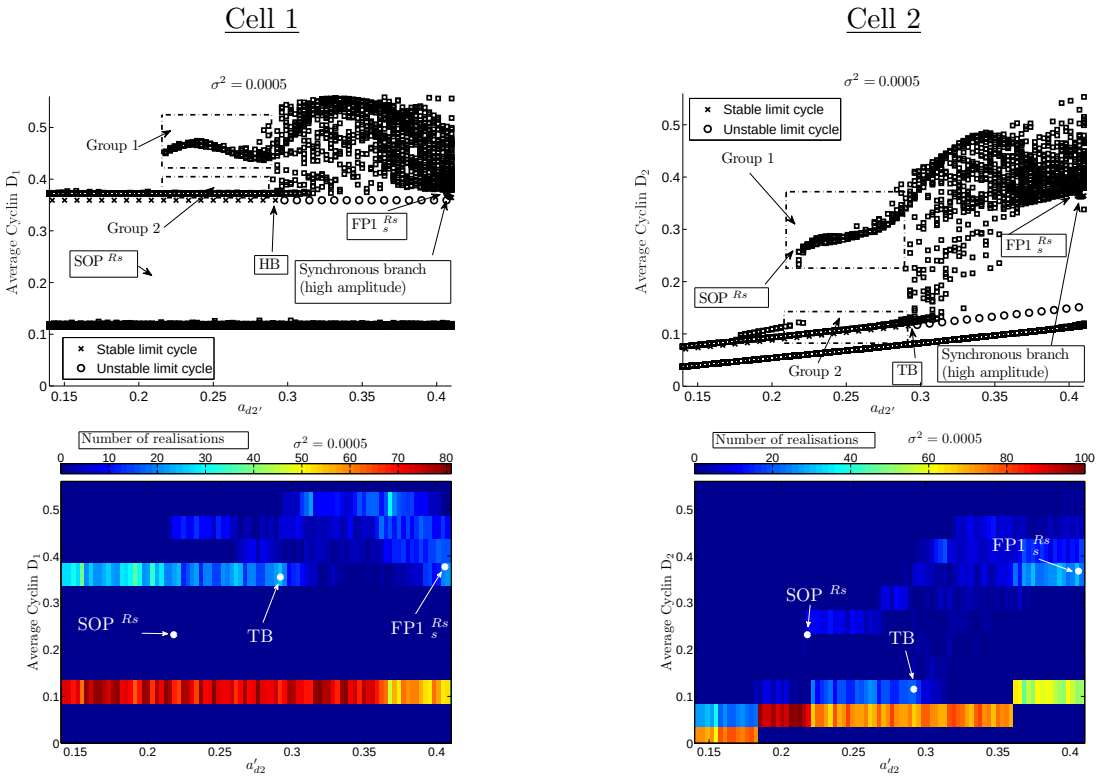

Figure 5.11: Bifurcation diagrams of system (3.1)-(3.14) for $\sigma^2 = 0$ (the deterministic system) and $\sigma^2 = 0.0005$ (the stochastic system) for two cells in the R_s dependent ATP release model ($(H_i, H_c) = (R_{sc} + \xi(t, \mu, \sigma^2), R_{si})$). The diagrams show that noise acts to shift to the left the point at which oscillatory type solutions arise and suggest that the average Cyclin D concentration of the oscillations in cells 1 and 2 increases with noise. TB corresponds to a torus bifurcation point, SOP^{Rs} corresponds to the point at which oscillations arise in cell 2 in the stochastic system, while FP1$^{Rs}_{s}$ corresponds to the point at which limit cycle solutions arise in the deterministic system. Each stochastic realisation is indicated by a square in the two plots. The X's, O's and straight lines in these plots correspond to the deterministic system. The dashed boxes in the first row of plots correspond to the groupings referred to in the text. The bottom row of plots are colour plots with average Cyclin D within each of a set of bins (ranging from -0.025 - 0.575 at intervals of 0.05) for each value of a'_{d2} (ranging from 0.15-0.41 at intervals of 0.0003). The deterministic bifurcation diagram was produced using AUTO, and the stochastic bifurcation diagrams were produced as outlined in Section 5.3.2 with an ensemble of 100 initial conditions for each value of a'_{d2} considered. Parameter values as in Table 5.1 unless otherwise indicated.

(Figure 5.12), SOP^{Rs} occurs at $a'_{d2} = 0.161$. Figure 5.12 shows that, as for the results displayed in Figure 5.11, there is an area in parameter space where limit cycle type solutions fall into one of two groups (between $a'_{d2} \approx 0.161$ and ≈ 0.25, marked groups 1 and 2). Furthermore, torus type solutions, which give the scatter gun effect seen in the right hand side of Figure 5.12, do not seem to appear until $a'_{d2} \approx 0.25$, just before the torus bifurcation point of the deterministic system (TB). It therefore appears that, in this example as well, noise acts to move the point at which limit cycle solutions arise in the deterministic system ($FP1_s^{Rs}$) to a far greater degree than it moves the point at which torus type solutions arise (TB). This reinforces the notion that noise in the R_s dependent ATP release model effects the torus bifurcation point and fold point $FP1_a^{Rs}$ in a quantitatively different manner (although in both cases noise appears to move the bifurcation points to the left relative to the deterministic case). This effect is even more pronounced in the results in Figure 5.12 than it is in those shown in Figure 5.11, due to the increased variance of the noise in Figure 5.12.

When the system of two cells is considered, but for a value of $a'_{d1} = 0.38$, the story is much the same. It can be seen from Figure 5.13 that oscillatory type behaviour in the second cell arises for lower values of the control parameter a'_{d2} than is the case in the deterministic system, for a value of the variance of 0.0005. Interestingly, in this case as well the noise appears to regulate the behaviour of the system in the left hand area of parameter space, with torus type solutions not arising until just before the torus bifurcation point of the deterministic system, as was the case for the results displayed in Figures 5.11 and 5.12. This behaviour can also be seen for the larger variance of $\sigma^2 = 0.005$ (Figure 5.14). These results also support the notion that increasing the variance of the noise further shifts the point at which oscillatory type solutions arise, as for $\sigma^2 = 0.0005$ (Figure 5.13), SOP^{Rs} occurs at ≈ 0.194, while for $\sigma^2 = 0.005$ (Figure 5.14), SOP^{Rs} occurs at ≈ 0.167.

The 2 parameter stochastic bifurcation diagrams shown in the left hand column of Figure 5.15 augment the results we have seen so far in this section. The diagrams reveal that as the variance of the noise is increased the point at which the oscillatory type solutions arise (SOP^{Rs}) moves away from the point they arise in the deterministic system (TB). Furthermore, by and large, as the variance of the noise is increased, so is the average concentration of Cyclin D of the oscillatory type solutions.

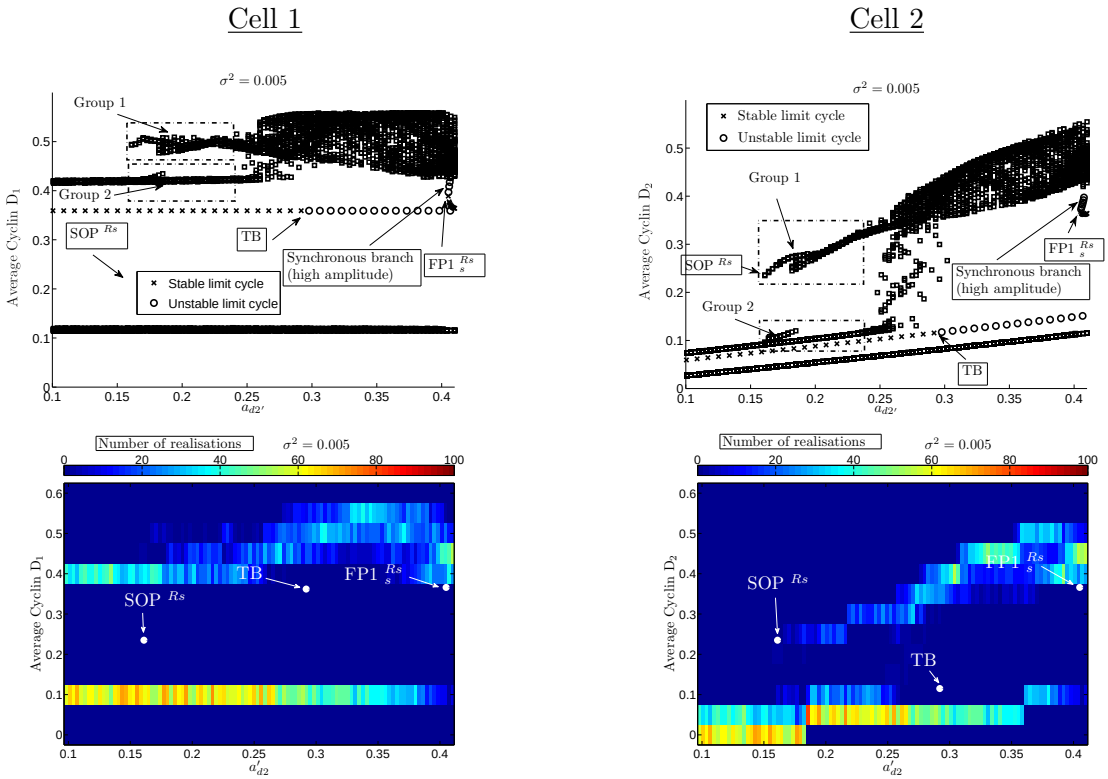

Figure 5.12: Bifurcation diagrams of system (3.1)-(3.14) for $\sigma^2 = 0$ (the deterministic system) and for $\sigma^2 = 0.005$ (the stochastic system) for two cells in the R_s dependent ATP release model ($(H_i, H_c) = (R_{sc} + \xi(t, \mu, \sigma^2), R_{si})$). The diagrams suggest that increasing the variance of the noise further moves to the left the point at which oscillatory type solutions arise. They also support the notion that noise shifts the point at which limit cycle solutions arise (FP1^{Rs}_{a}) far more severely than the point at which torus solutions arise (TB). It can also be seen that noise acts to increase the average Cyclin D concentrations of the oscillatory type solutions. Parameter values as in Table 5.1.

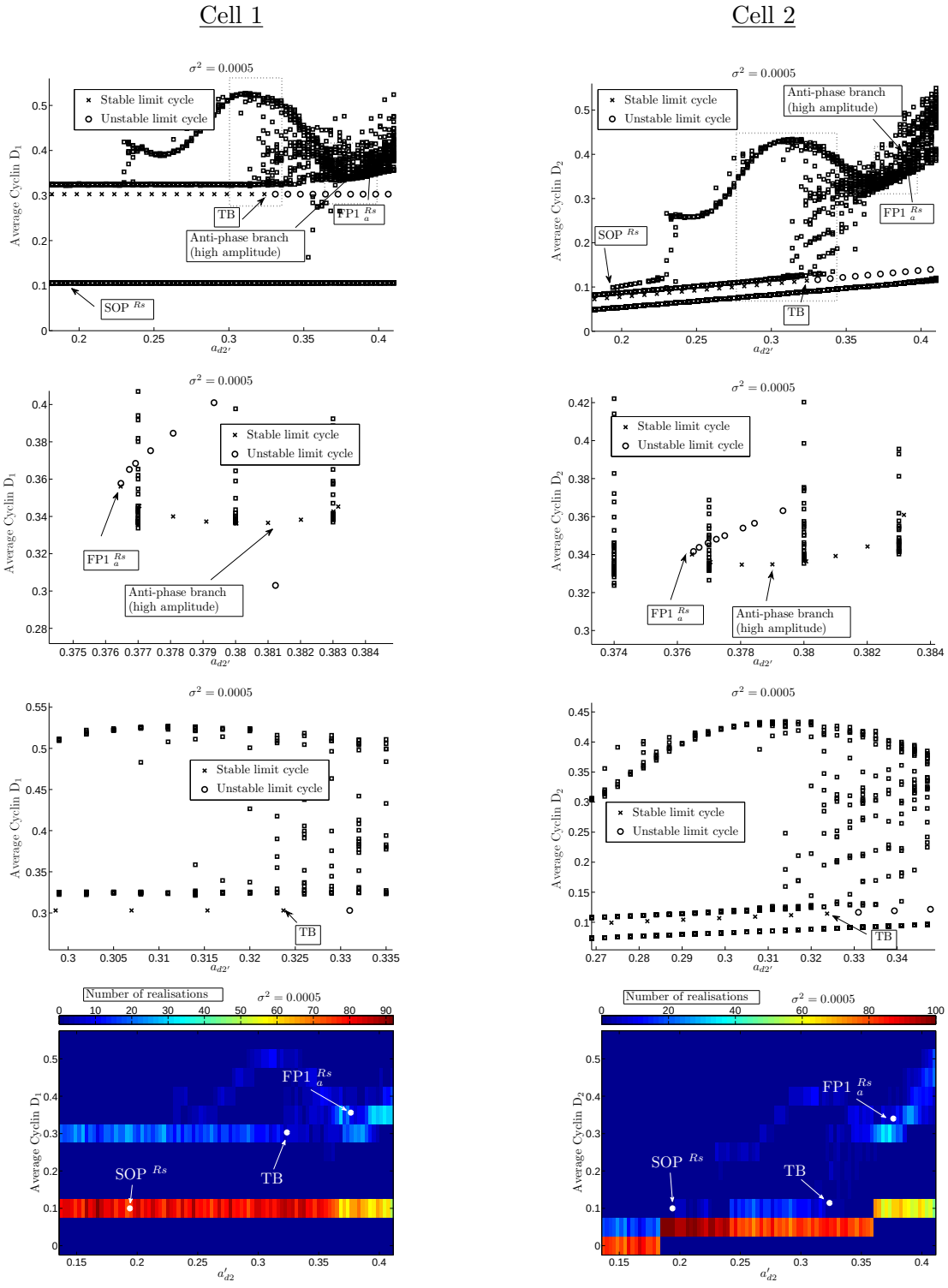
Cell 1
Cell 2
$\sigma^2 = 0.0005$
Stable limit cycle
Unstable limit cycle
Anti-phase branch (high amplitude)
TB
FP1 $^{Rs}_{a}$
SOP ^{Rs}
Average Cyclin D$_1$
Average Cyclin D$_2$
$a_{d2'}$
Number of realisations
a'_{d2}

Figure 5.13

Figure 5.13: Bifurcation diagrams of system (3.1)-(3.14) for $\sigma^2 = 0$ (the deterministic system) and $\sigma^2 = 0.0005$ (the stochastic system) for two cells in the R_s dependent ATP release model ($(H_i, H_c) = (R_{sc} + \xi(t, \mu, \sigma^2), R_{si})$). The dotted boxes indicate the areas that have been zoomed in on in subsequent plots. The diagrams show that even when a'_{d1}=0.38, noise acts to move the bifurcation point leading to oscillatory type solutions and appears to regulate the behaviour of the stochastic system in the left hand area of parameter space (top row of plots) in a similar fashion to the results displayed in Figures 5.11 and 5.12 . Furthermore, it acts to increase the average Cyclin D concentration of the oscillatory type solutions in both cells. Parameter values as in Table 5.1 except for $a'_{d1} = 0.38$.

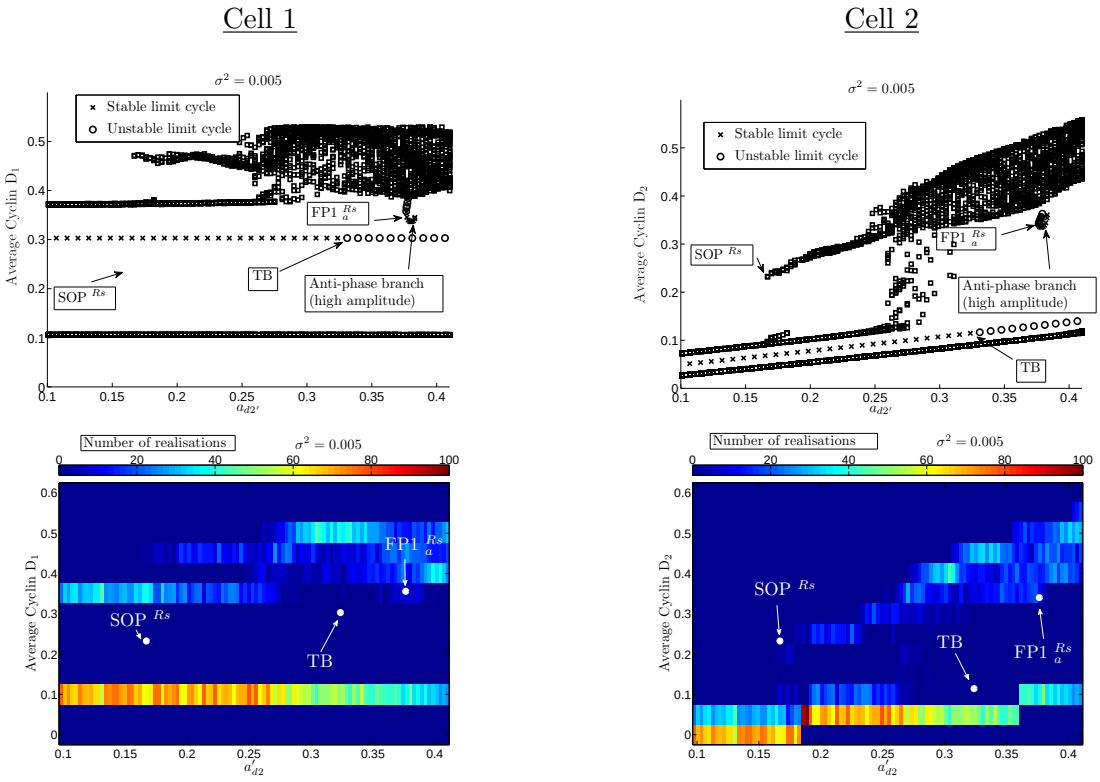

Figure 5.14: Bifurcation diagrams of system (3.1)-(3.14) for $\sigma^2 = 0$ (the deterministic system) and $\sigma^2 = 0.005$ (the stochastic system) for two cells in the R_s dependent ATP release model ($(H_i, H_c) = (R_{sc} + \xi(t, \mu, \sigma^2), R_{si})$). Comparing these results to those displayed in Figure 5.13 suggests that increasing the variance of the noise further shifts the point at which oscillatory type solutions arise even for a value of $a'_{d1} = 0.38$. Parameter values as in Table 5.1 except for $a'_{d1} = 0.38$.

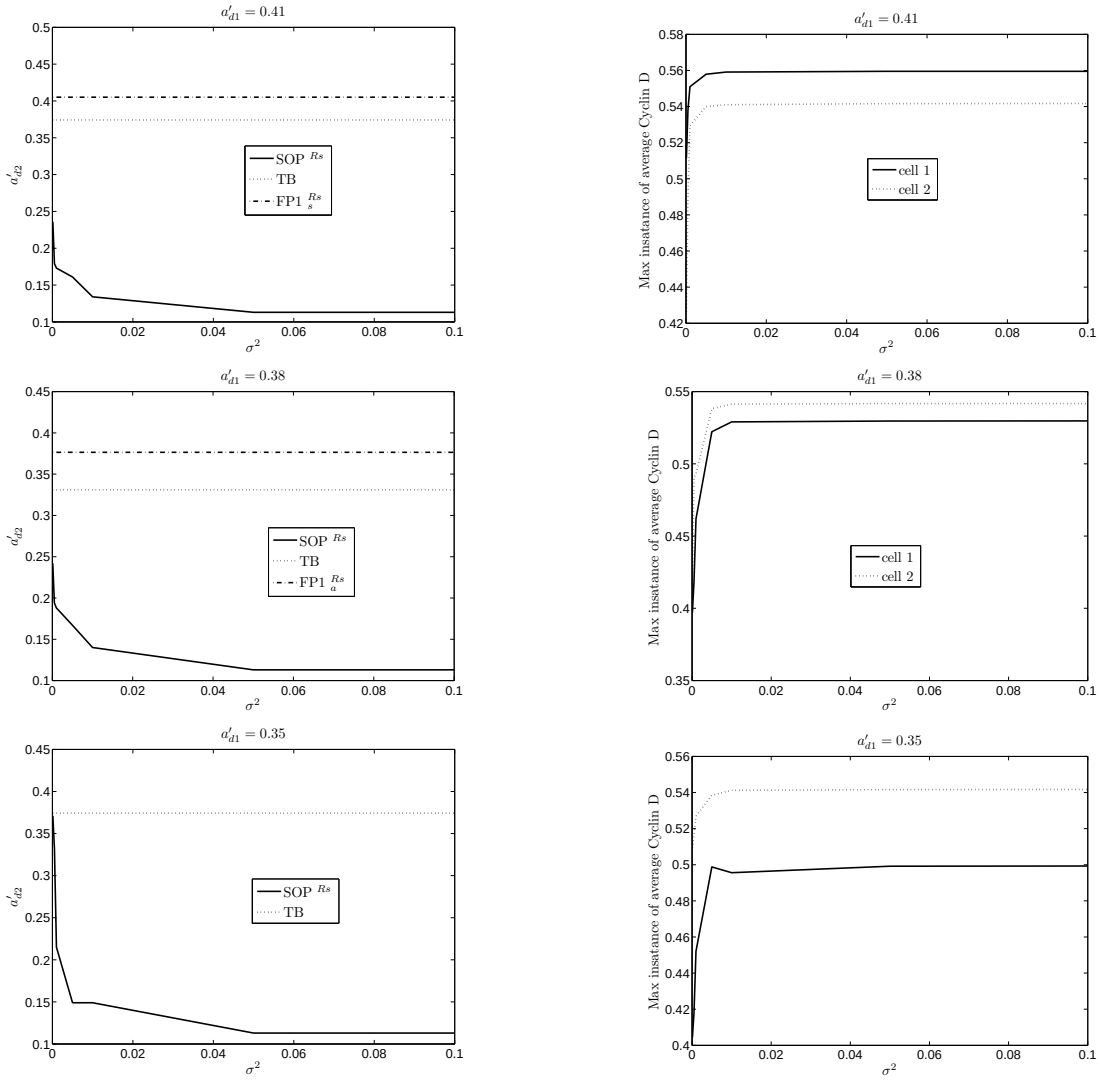

Figure 5.15: In the first column are shown two parameter bifurcation diagrams for three different values of a'_{d1} which indicate that increasing the variance of the noise further advances the point at which oscillatory type solutions arise. The plots in the second column show that at, $a'_{d2} = 0.392$, increasing the variance of the noise appears to increase the average Cyclin D concentrations of the oscillatory type solutions. Note that limit cycle solutions do not exist for the deterministic model when $a'_{d1} = 0.35$, which explains the absence of FP1^{Rs} in the bottom left hand corner plot.

It appears therefore that, as in the Cyclin D dependent model, noise in the R_s dependent ATP release model moves the point at which oscillatory type solutions arise, and hence may allow for the enhancement of a driving cell's ability to recruit quiescent cells, in turn leading to an increase in overall proliferation.

5.6 Simulations of Larger Systems

In this section we consider, as a 'proof of concept', a small number of simulations to investigate if noise enhances a driving cell's ability to recruit quiescent cells onto the cell cycle in 10 cell systems. In order to model the non-identical nature of the radial glial cells, we sampled a'_{di} from a normal distribution of mean 0.381 and variance 0.035, using Matlab's pseudo-random number generator drawn from the normal distribution `randn`. We chose these values for the mean and variance so that we were very unlikely to get very low or negative values for a'_{di}, whilst ensuring that our values for a'_{di} were sufficiently disparate that the intrinsic frequency of oscillation of all cells differed.

The system was initialised with each cell such that it sat on the branch of stable steady state type solutions which model the quiescent G_0 state, except for the cell which had the largest value of a_d. This cell's initial conditions were such that the cell initially exhibited oscillatory type behaviour. We believe that in a noisy system, over a sufficiently long period of time, the noise should act to enable initially dormant cells to exit this state and begin to oscillate. We also believe that in a system of quiescent cells, the cell likely to exit the steady state type solution first is the cell with the largest values for a'_d. This assumption is in keeping with some preliminary work (not shown), which suggested that noise can lift initially dormant cells out of quiescence and that cells with a larger value for a'_d are more likely to exit this state, and would begin to oscillate more quickly, than cells with a lower value for a'_d. This is why we chose the cell with the largest value for a'_d to be the cell that initially exhibits oscillatory type solutions. In effect, when simulating our system in this manner, we are modelling a state whereby the first quiescent cell has just exited the steady state like solution.

We simulated our stochastic system 10 times and obtained an average number of cell

cycles over the period of integration in order to measure the rate of proliferation.

5.6.1 Cyclin D Dependent ATP Release

In Figure 5.16 we simulate the deterministic system. The results of one realisation of our stochastic Cyclin D dependent ATP release model from the same initial conditions and under the same parameter regime are shown in Figure 5.17. Figure 5.17 reveals that initially quiescent cells are recruited onto the cell cycle relatively quickly, although it is not clear if the cells are entrained in a synchronous manner. Over 10 realisations, the average number of cell cycles during the period of integration (1600 hours) for the stochastic system was 266. In the deterministic case all cells are recruited by $t \approx 1430$ hours, while for the stochastic case all cells have been recruited far earlier than this at $t \approx 1100$ hours. Not surprisingly therefore the total number of cell cycles that occur during the period of integration in the deterministic case (165) is lower than that of the stochastic model (266). This corresponds to an increase in proliferation brought about by the noise of 61.2 %. If we take cell 2 from Figures 5.17 and 5.16 and compare the trajectories of the Cyclin D concentrations of each, a driving cell's enhanced ability to recruit quiescent cells in noisy systems becomes even clearer. By referring to Figure 5.18 it can be seen that cell 2 is recruited at $t \approx 890$ hours in the stochastic model, while it is not until $t \approx 1085$ that it is recruited in the deterministic model. These preliminary results suggest that noisy hemichannels may be responsible for increased radial glia proliferation during neurogenesis.

5.6.2 R_s Dependent ATP Release

In Figure 5.19 we plot the results of a simulation of the deterministic R_s dependent ATP release model. By comparing the results shown in Figure 5.19 to Figure 5.20, which contains one realisation for the stochastic system, it becomes clear that in the noisy system quiescent cells are recruited far more quickly, with all cells recruited by $t \approx 130$ hours. Only cell 2 is recruited onto the cell cycle within the period of integration in the deterministic case, with cells 3-10 remaining quiescent. If the period of integration is increased in the deterministic example, eventually all of the cells will be recruited (results not shown). In the deterministic case the total number of cell cycles is 62, while in the stochastic case the average number of cell cycles was 587. This corresponds to an increase brought about by

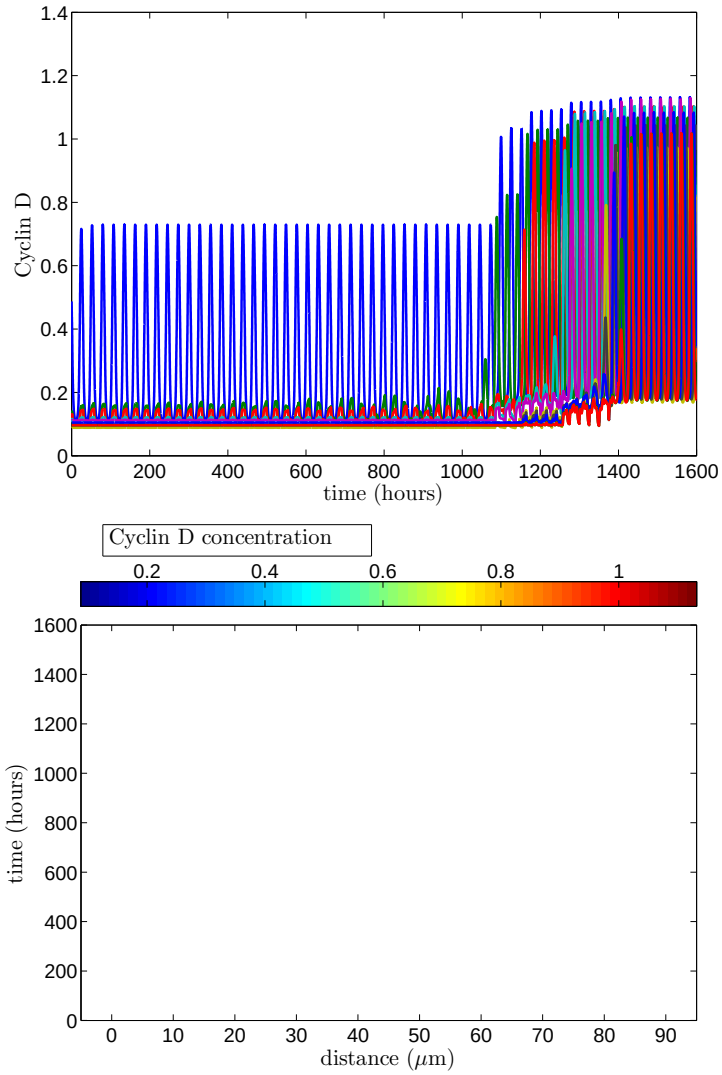

Figure 5.16: Simulation of system (3.1)-(3.14) for $\sigma^2 = 0$ (the deterministic system) for the Cyclin D dependent ATP release model ($(H_i, H_c) = (D_i, D_c + \xi(t, \mu, \sigma^2))$) with zero flux boundary conditions. The results give us some indication as to the the ability of a driving cell to recruit quiescent cells onto the cell cycle in the deterministic system. The upper panel shows the Cyclin D concentrations in all cells. The lower panel shows the distribution of Cyclin D throughout the spatial mesh. Parameter values as in Table 5.1 except for $a'_{d1,2,\ldots 10}$=[0.3991 0.3677 0.3856 0.3852 0.3983 0.3205 0.3551 0.3760 0.3448 0.3471] which were sampled from a normal distribution as outlined in this section. Parameter values as for Figure 5.17. Initial conditions were such that all cells sat on the branch of steady state solutions, except for cell 1, which initially sat on the branch of limit cycle solutions.

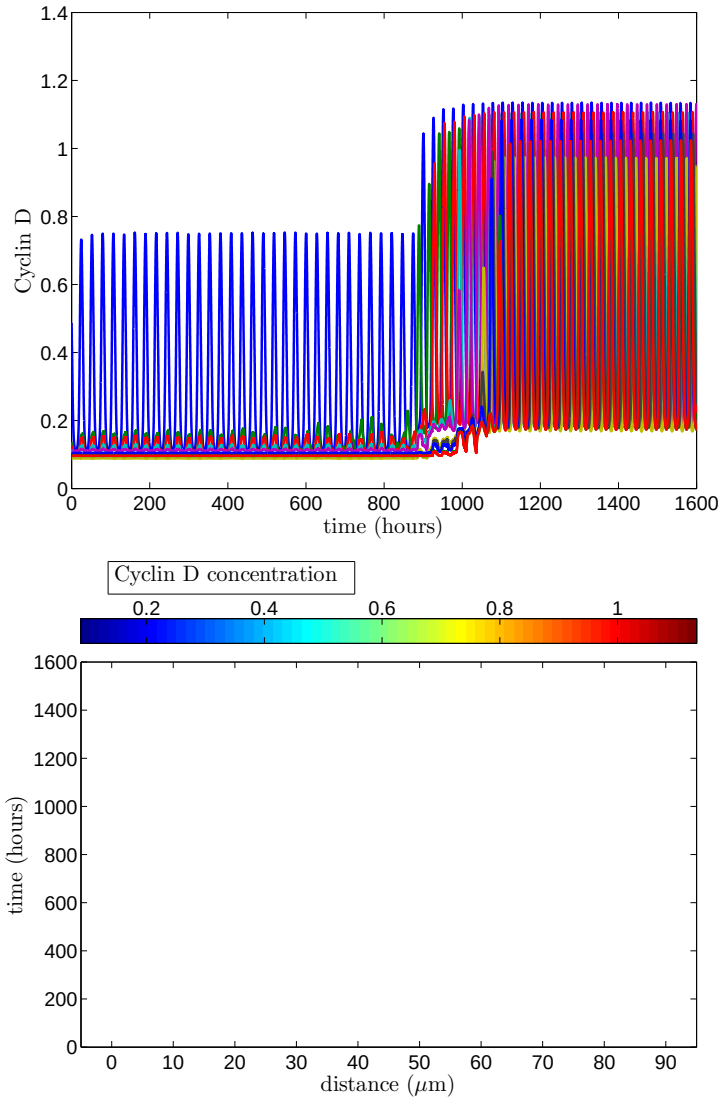

Figure 5.17: Simulation of system (3.1)-(3.14) for the stochastic Cyclin D dependent ATP release model ($(H_i, H_c) = (D_i, D_c + \xi(t, \mu, \sigma^2))$) with zero flux boundary conditions. The results give us some indication as to the enhanced ability of a driving cell to recruit quiescent cells onto the cell cycle in a noisy system. Parameter values as in Figure 5.16 except for $\sigma^2 = 0.01$. Initial conditions were such that all cells sat on the branch of steady state solutions of the deterministic system, except for cell 1, whose initial conditions were such that it exhibited oscillatory type solutions.

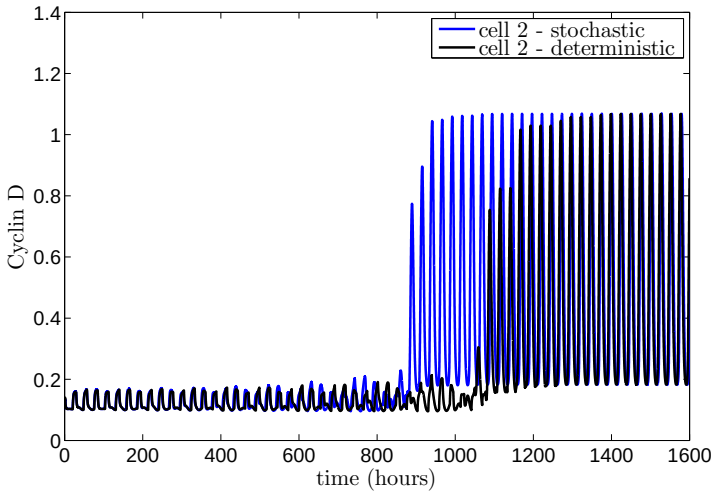

Figure 5.18: Plot of cell 2 from the stochastic system (Figure 5.17) and the deterministic system (Figure 5.16) which illustrate the enhanced ability of a driving cell to recruit quiescent cells in a noisy system.

the noise of 946.77 %, reflecting the enhanced ability of a driving cell to recruit quiescent cells in the stochastic system. This enhancement becomes clearer still if one refers to Figure 5.21, where plots of cell 2 from the stochastic model (Figure 5.20) and deterministic model (Figure 5.19) are shown. Cell 2 is recruited at $t \approx 100$ hours, while it is not until $t \approx 1475$ hours that it is recruited in the deterministic model.

5.7 Conclusions and Further Work

The results in this chapter suggest that noise may have an important role to play with regard to radial glia proliferation during neurogenesis. Our one and two cell bifurcation analysis revealed that additive Gaussian noise in the switch, which models the opening of hemichannels and subsequent release of ATP, is filtered by both models in such a way that the bifurcation point which gives rise to oscillatory solutions is shifted, resulting in oscillatory type solutions arising for lower values of a'_d than for the deterministic case. Furthermore, this effect is augmented as the variance of the noise is increased. We also discovered, in Section 5.5.2, that in the stochastic R_s dependent ATP release model the noise appeared to act to regulate the dynamics of the system. It seemed that the noise shifted the point at which limit cycle solutions arose in the deterministic system far more than it moved the

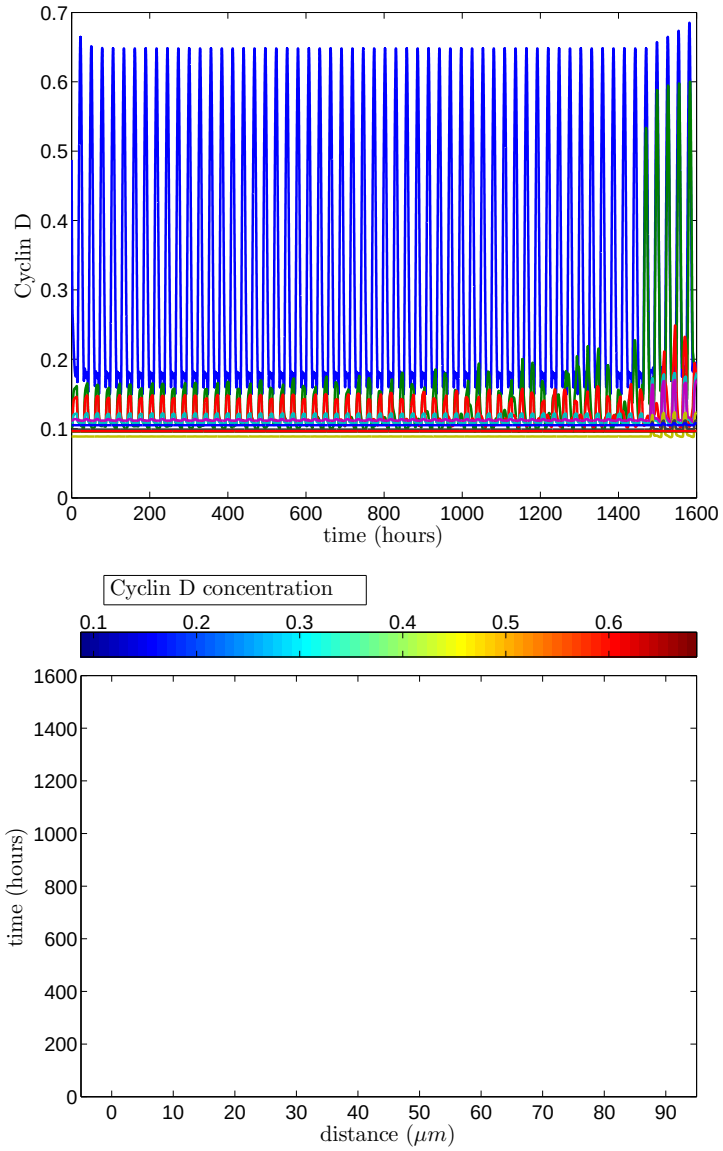

Figure 5.19: Simulation of system (3.1)-(3.14) for $\sigma^2 = 0$ (the deterministic system) for the R_s dependent ATP release model ($(H_i, H_c) = (R_{sc} + \xi(t, \mu, \sigma^2), R_{si})$) with zero flux boundary conditions. It can be seen that only cell 2 is recruited for the deterministic system. Parameter values as in Table 5.1 except for $a'_{d1,2,...10}$=[0.3991 0.3677 0.3856 0.3852 0.3983 0.3205 0.3551 0.3760 0.3448 0.3471]. Initial conditions were such that all cells sat on the branch of steady state solutions, except for cell 1, which initially sat on the branch of limit cycle solutions.

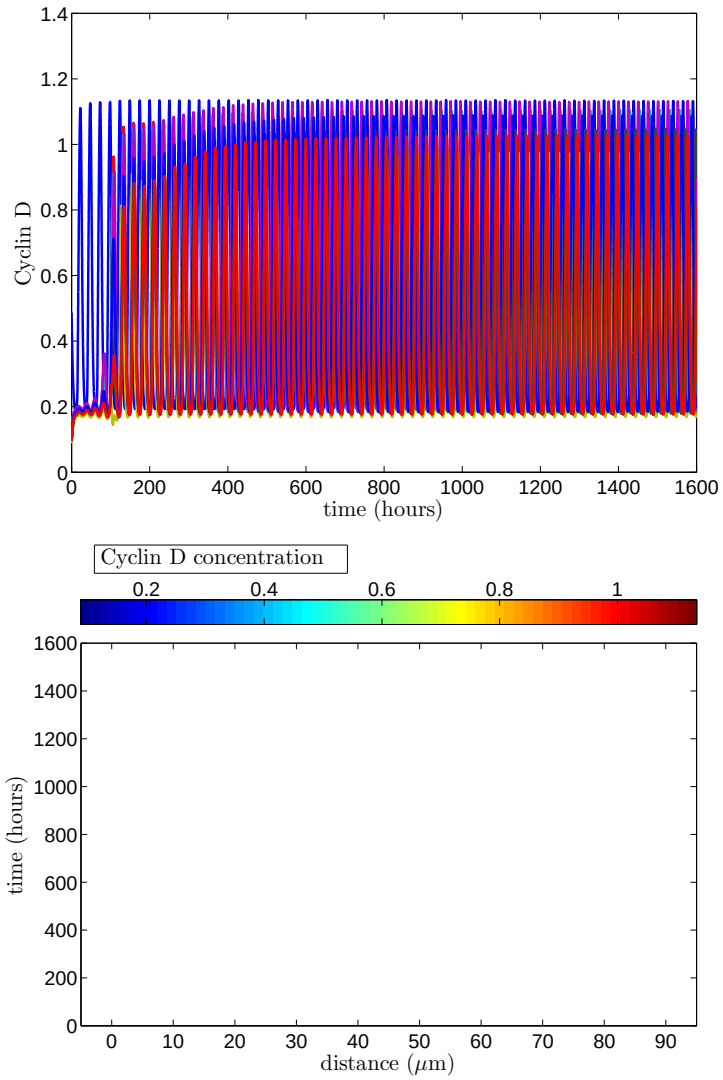

Figure 5.20: Simulation of system (3.1)-(3.14) for the stochastic R_s dependent ATP release model ($(H_i, H_c) = (R_{sc} + \xi(t, \mu, \sigma^2), R_{si})$) with zero flux boundary conditions. The results give us some indication as to the enhanced ability of a driving cell to recruit quiescent cells onto the cell cycle for a noisy system. It is clear that all cells are recruited by $t \approx 150$ hours (c.f Figure 5.19, the deterministic case where only cell 2 is recruited). Parameter values as in Figure 5.19 except for $\sigma^2 = 0.01$. Initial conditions were such that all cells sat on the branch of steady state solutions of the deterministic model, except for cell 1, whose initial conditions were such that it exhibited oscillatory type solutions.

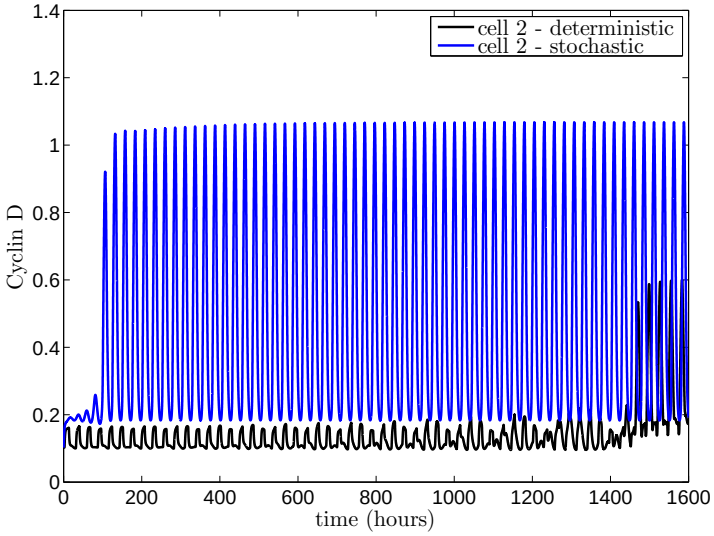

Figure 5.21: Plot of cell 2 from the stochastic system (Figure 5.20) and the deterministic system (Figure 5.19) which illustrate the enhanced ability of driving cells in the the noisy system to recruit quiescent cells onto the cell cycle.

point at which torus solutions arose, to such an extent that limit cycle type solutions arose well before torus type solutions in the stochastic system (this was the other way around in the deterministic system) and began to dominate large areas of parameter space. This result could have important implications with regard to phase locked solutions, with noise possibly acting to promote phase locked solutions in the R_s dependent ATP release model. This would need to be investigated further through running many more simulations for different numbers of cells and for different parameter sets.

As mentioned in Section 5.3.2, where we outlined our numerical method for producing stochastic bifurcation diagrams, the size of our initial condition ensemble was 100. Using a far larger ensemble, where the initial condition of every variable is varied, rather than Cyclin D, would provide us with a fuller picture as to the dynamics of our stochastic system. This would prove to be a hugely computationally expensive task however and would most likely require the use of High Performance Computing (HPC) facilities.

We then showed, for a small number of examples, that noise, in shifting the point at which oscillatory type solutions arise, allows a driving cell to recruit quiescent cells onto

the cell cycle far more quickly than is the case for the deterministic system. The increase in proliferation this brings about in both models can be large, especially so for the R_s dependent model for the parameter values considered. This suggests that noisy hemichannel opening may contribute to the increase in the proliferation of radial glia during neurogenesis. To build upon these results it would be interesting to study larger systems in one and two spatial dimensions under several different parameter regimes, in order to ascertain the degree to which noisy hemichannel opening can lead to increased radial glia proliferation. Furthermore, it would be interesting to investigate how noise affects cell cycle synchronisation. This may require the development of a synchrony measure which could be applied to stochastic system, if a suitable existing measure can not be found.

In Section 5.6 we mentioned that we believe that noise may also play a role in initiating the process of neurogenesis. We envisaged a scenario where all cells would lay dormant but subject to stochastic fluctuations. Eventually these fluctuations would allow one cell to exit quiescence and begin cycling, at which point it would begin to recruit the other quiescent cells onto the cell cycle. This would lift the constraint we have so far placed on the initial conditions of the system when investigating entrainment, where we have ensured that at least one cell is initially oscillating. In doing so it could provide us with a possible mechanism for the onset of neurogenesis in the developing mammalian neocortex. However, it is important to note that neurogenesis starts at a fairly well defined time during embryonic development and any of the results would have to agree with this timing. Single cell and multiple cell systems would need to be considered and the ability of noise of different magnitudes to lift quiescent cells on the cell cycle would need to be studied. We did study this to an extent during the course of this project, but only for single cell systems by calculating the 'exit times' (the times at which initially quiescent cells exited this state and began to oscillate) of cells for different values of a'_{d1}. Our results demonstrated that noise can indeed provide a mechanism for the spontaneous lifting of cells from quiescence, signalling the onset of neurogenesis (results not shown).

Table 5.1: Parameter values

Parameter	Value	Parameter	Value
r_h^*	0.6 μMs^{-1}	a'_{d1}	0.41
a_E	0.16	a_X	0.08
k	0.054	q_D	0.6
q_E	0.6	q_X	0.8
f	0.2	g	0.528
p_s	0.6	p_D	0.48
p_E	0.096	p_X	0.48
d_D	0.4	d_E	0.2
d_X	1.04	a_f	0.9
R_T	2.5	$\ominus$	1.5
GF	6.3	t_s	3600
V_{deg}	2 μMs^{-1}	$[ATP_I]_{max}$	500 μM
V_{ATP}	0.8 s^{-1}	$[IP_3]_{min}$	0.013 μM
D_c	0.5	$[IP_3]_c$	0.012 μM
ϱ	0.01 μM^{-1}	γ	1
D_{ATP}	10 μm^{2}s^{-1}	Δx	10 μm
$p1$	0.0159835 μM	$p2$	0.514987
$p3$	1.31319	$p4$	0.332195
$p5$	0.787902	m	24.1946
n	9.79183	α	0.083 s^{-1}
K_{deg}	50 μM	$[Ca^{2+}]_b$	0.0159835 μM
k_{deg}	0.0625 s^{-1}	R_{sc}	1

Chapter 6

Discussion

ATP mediated calcium waves are thought to be the primary means by which radial glial cells communicate in the developing neocortex [93]. Calcium waves increase radial glia proliferation, in turn leading to an increase in neural production. It has also been speculated that they are responsible for the synchronisation of the cell cycles of clusters of radial glia. This synchronisation may be involved in the shedding of cells in uniform sheets, and could therefore play an important role in the development of the brain architecture. We have investigated whether a calcium signalling mechanism can increase radial glia proliferation and enable cell cycle synchronisation.

The precise timing of the release of ATP by radial glial cells has not been discovered, although it occurs sometime between the G_1 and S phases of the cell cycle. In chapter 2 we presented two models for the coupling between the cell cycle dynamics and calcium dynamics in radial glial cells. In the first model, we modelled ATP release as predominantly occurring during mid G_1 phase and in the second occurring predominantly during the G_1/S phase transition. Through bifurcation analysis, weakly coupled oscillator theory and direct numerical simulation we showed that two cell systems of both models displayed a rich variety of behaviour. For both models, under certain parameter regimes, stable synchronous solutions existed. Under the Cyclin D dependent ATP release model, where ATP release was modelled as occurring in the middle of G_1 phase, stable anti-phase phase locked solutions were also detected. The R_s dependent model, which modelled ATP release as occurring during the G_1/S transition, displayed stable asynchronous solutions for two cells in addition to the stable synchronous solutions.

In chapter 3 we built upon this work and, via weakly coupled oscillator theory and direct numerical simulation, investigated cell cycle synchronisation in systems of several cells in one and two spatial dimensions for both models. The pitfalls of the theory of weakly coupled oscillators, which we first encountered in chapter 2, re-appeared in chapter 3. The theory relies on the strength of the coupling between oscillators to be weak, such that the coupling does not lead to amplitude effects in the resulting limit cycle solutions. In our system the coupling was so strong that the analytic results from the theory of weakly coupled oscillators became unreliable. This meant that, in order to gain an insight into the behaviour of the two models for systems of several cells, it was necessary to run many numerical simulations. However, there is the possibility that we can obtain an analytical insight into the behaviour of the models by another method. One possibility is to study a simplified system where the high dimensional cell cycle model is replaced with a linear oscillator which is periodically forced by a linear piecewise function, which models ATP mediated calcium release. We could then consider systems of many such oscillators which are coupled via this linear piecewise function which we could solve to obtain analytic results. One approach to obtaining a simplified model, would be to calculate the phase response curve of the full model in order to ascertain by how much perturbations advance or retard the phase of oscillation. A piecewise linear oscillator model could then be formed which captures this behaviour (or at least an approximation to it). With this achieved, one could then study populations of coupled oscillators, where the coupling acts to perturb the phase of oscillation of neighbouring oscillators (mimicking the ATP coupling of the full model). Rhouma and Frigui take a similar approach in order to investigate synchronisation in systems of coupled oscillators [75]. They consider systems of integrate and fire oscillators which are globally coupled to all other oscillators via a linear function. This then allows them to derive analytical results regarding the conditions under which networks of integrate and fire oscillators synchronise. It may be possible for us to use a similar technique to this.

Despite this, through the numerical simulations conducted in chapter 3, a rich variety of behaviour was discovered for both models for systems of several cells with often more than one stable solution existing under the same parameter regime. However, the R_s dependent ATP release model proved more successful at generating synchronous or near synchronous behaviour under the parameter regimes considered. This formed the first major result of our work, i.e that ATP release occurring predominantly during the G_1/S transition was more likely to lead to cell cycle synchronisation than during mid G_1 phase. Furthermore, showing

that the timing of ATP release is crucial for cell cycle synchronisation in our models raised the possibility that some neural malfunctions during neurogenesis may be the result of a malfunction in the timing of ATP release. There is the possibility that this result may be an artifact of the parameter regimes chosen, rather than purely due to the intrinsic difference in the timing of ATP release. It is possible that we sampled the parameter space unfairly, and that, by considering even more diverse parameter regimes, our conclusion may need to be revised. In order to investigate if this is the case, we would need to run many more simulations under different parameter regimes. Nevertheless, we would be very interested in experimentally testing whether the timing of ATP release affects neural development in this manner, as we are not aware of any experiments which have focussed upon this. Conducting such experiments may prove problematic however, as although it is relatively straightforward to block ATP release by blocking hemichannel opening throughout the duration of the cell cycle, it would be more difficult to block hemichannel opening only at certain points during the cell cycle.

Our models incorporated Obeyesekere *et al*'s cell cycle model [66]. As mentioned in chapter 1, several other cell cycle models exist, some of which include a term for Cyclin D [85, 90], the cell cycle protein affected by calcium. It would be interesting to study the effect on our system if one of these models was used to model the cell cycle instead of Obeyesekere *et al*'s model. If it was discovered that with these alternative models, modelling ATP release as occurring predominantly during the G_1/S transition was still more likely to lead to synchronous or near synchronous behaviour than release occurring predominantly during mid G_1 phase, then this would add more weight to the conclusions drawn from the results of chapters 2 and 3. If, however it was shown that the dynamics with a different cell cycle model behaved radically differently to the dynamics of our current system then our conclusions may have to be revised. The various shortcomings mentioned in chapter 1 in the cell cycle models which include a term for Cyclin D would have to be overcome for this to be achieved, however. For example Swat *et al* only model G_1 phase of the cell cycle [85], and their model, although including a term for Cyclin D, is not continuous and does not exhibit limit cycle solutions. It would need to be modified so that it models the whole of the cell cycle and displays limit cycle behaviour for it to be incorporated into our models. Tyson and Novak's high dimensional model [90] is so complex that large scale simulations will become very computationally expensive if it were to be used. It would need to be simplified significantly, perhaps by assuming quasi-steady state approximations for some

state variables, for it to become a viable option. However, this approach is only likely to be valid if the time scales of the state variables differ by a significant degree.

Towards the end of our project, Seward *et al* identified the signal transduction pathway by which calcium promotes Cyclin D activity [79]. They discovered that in NIH/3T3 fibroblasts (an embryonic mouse cell line) calcium activated CaMK-II acts to promote Cyclin D activity. They found that when calcium transients subside, CaMK-II becomes less active at which point a protein called Flightless-I begins to disassociate from CaMK-II. Flightless-I then migrates into the nucleus of the cell where it acts to suppress the transcription of Cyclin D. Consequently, calcium activated CaMK-II which sequesters Flightless-I and prevents its migration into the nucleus of the cell acts to enable the transcription of Cyclin D. Modelling this signal transduction pathway and incorporating it into our model would certainly result in a more detailed model. If, when studying this more detailed model we are able to confirm the main results contained within this thesis, then this would re-enforce the conclusions drawn from these results. Alternatively, if the results from the more detailed model conflict with the results contained within this thesis, then we may have to revise the main conclusions contained within this thesis.

Until chapter 4, the increase in proliferation of the cells in our models was relatively modest. This formed our motivation for investigating the ability of a driving cell to recruit a quiescent cell onto the cell cycle in chapter 4. We exploited the area of multistability in our system to model scenarios where one cell was initially quiescent and one initially oscillating. After showing that under a number of parameter regimes the quiescent cell could be recruited we turned our attention to the matter of synchronous entrainment. Under all of the parameter regimes considered, the R_s dependent ATP release model proved to be superior to the Cyclin D dependent model at entraining a quiescent cell synchronously. As a 'proof of concept', we considered larger systems and showed that our results from two cell systems scaled up to these larger systems. The increase in the proliferation brought about by calcium signalling in these larger systems was very similar to the increase indicated in the experimental literature. This suggests that the increase in proliferation brought about by calcium signalling may be as a result of a driving cell's ability, through ATP mediated calcium waves, to recruit quiescent cells. The superiority of the R_s dependent ATP release model in facilitating synchronous entrainment added weight to the argument that ATP release occurring during the G_1/S transition is more likely to lead to synchronous

behaviour than release at other times. More simulations of larger systems in one and two spatial dimensions, with each cell under a different parameter regime, would prove useful in extending these results.

In chapter 5, we investigated the effect noisy hemichannel opening had on the dynamics of our system. By conducting a numerical exploration of one and two cell systems, using a similar method to Hutt [42], we discovered that additive Gaussian noise was filtered in a non-linear manner. This resulted in the shifting of the bifurcation point that lead to oscillatory type solutions, increasing the area within parameter space that gives rise to oscillatory type solutions. Furthermore, we showed that the movement of the bifurcation point became more dramatic as the intensity of the noise was increased. This result augments the other examples in the literature where additive noise has acted to move bifurcation points. For example, Hutt discovered that additive noise could move saddle node bifurcation points in a system that displayed hysteresis behaviour [42]. Gudowska-Nowak demonstrated that noise can advance the onset of limit cycle type solutions by moving Hopf bifurcation points [37]. We then showed, via numerical simulation, that the shifting of bifurcation points in this manner allowed driving cells to recruit quiescent cells more quickly and/or recruit cells that the deterministic system could not. This raised the possibility that noise may play an important role in the increased radial glia proliferation seen during neurogenesis. More numerically intensive work would need to be carried out on larger systems in one and two spatial dimensions under different parameter regimes and for different variances of the noise to confirm this. It would also be intersting to investigate if and by how much noise effects cell cycle synchronisation. To achieve this, a synchrony measure which can be effectively applied to stochastic systems would have to be utilised. If a suitable measure can not be found, it may be necessary to develop one. Comparing these results with the results of our deterministic system would allow us to judge whether noise influences cell cycle synchronisation. Additionally it may be possible to apply some of the analytical techniques that Hutt employs [42] to our stochastic models in order to derive some more general results. These techniques may even help to explain the behaviour we saw in Section 5.5.2 of chapter 5, in the two cell stochastic system for the R_s dependent ATP release model. In this section, our numerical explorations suggested that, although noise acted to shift the bifurcation points of the system, the degree to which different bifurcation points moved differed. In the left hand area of parameter space the dynamics of the system were very regular, reminiscent of the limit cycle solutions we encountered when studying the deterministic model. In the

adjacent right hand area of parameter space, torus solutions appeared to dominate. We noticed that torus type solutions arose just before they did in the deterministic system. This led us to speculate that noise acted to move the bifurcation point that led to limit cycle solutions ($FP1_s^{Rs}$) far more than the point that lead to torus type solutions (TB), to the extent that limit cycle solutions began to dominate.

In chapter 5 we mentioned that we believed that noise was capable of lifting initially dormant cells into the oscillatory domain. If this proved to be the case, it would lift the constraints we placed on the initial conditions in our simulation in chapters 4 and 5 and in doing so provide us with a possible mechanism by which neurogenesis is initiated, a very interesting result indeed. To investigate the feasibility of this however, many computationally expensive simulations would need to carried out on one and multiple cell systems under different parameter regimes in order to see if noise is sufficient to lift quiescent cells on to the cell cycle and the resultant effect (if any) this would have on the dynamics of the system. We would also need to check that the initiation was regular and occurred at the right time during embryonic development.

In this thesis, we have laid the foundations for the mathematical investigation into the mechanisms by which radial glia cells communicate. Our work has yielded a number of interesting results, many of which merit further investigation. We hope this body of work will prove useful to mathematical biologists and experimental biologists with an interest in embryonic neurogenesis.

References

[1] R. Baserga. Biochemistry of the cell cycle: a review. *Cell Proliferation*, 1(2):167–191, 2008.

[2] S.A. Bayer, J. Altman, R.J. Russo, and Xin Zhang. Timetables of neurogenesis in the human brain based on experimentally determined patterns in the rat. *Neurotoxicology*, 14(1):83–144, 1993.

[3] S.R. Beauman, B. Campos, M.A. Kaetzel, and J.R. Dedman. Cyclin B1 expression is elevated and mitosis is delayed in HeLa cells expressing autonomous CaMKII. *Cellular Signalling*, 15(11):1049–1057, 2003.

[4] Y. Ben-Ari. Neuro-archaeology: pre-symptomatic architecture and signature of neurological disorders. *Trends in Neurosciences*, 31(12):626–636, 2008.

[5] M.R. Bennett, L. Farnell, and W.G. Gibson. A quantitative model of purinergic junctional transmission of calcium waves in astrocyte networks. *Biophysical Journal*, 89(4):2235–2250, 2005.

[6] M.R. Bennett, L. Farnell, W.G. Gibson, and S. Karunanithi. Quantal transmission at purinergic junctions: stochastic interaction between ATP and its receptors. *Biophysical Journal*, 68(3):925–935, 1995.

[7] M.J. Berridge. Calcium signalling and cell proliferation. *Bioessays*, 17(6), 1995.

[8] M.J. Berridge. Inositol trisphosphate and calcium signaling. *Annals of the New York Academy of Sciences*, 766(1):31–43, 1995.

[9] M.J. Berridge, P. Lipp, and M.D. Bootman. The versatility and universality of calcium signalling. *Nature Reviews Molecular Cell Biology*, 1(1):11–21, 2000.

[10] K.S. Bittman and J.J. LoTurco. Differential Regulation of Connexin 26 and 43 in Murine Neocortical Precursors. *Cerebral Cortex*, 9(2):188–195, 1999.

[11] P.C. Bressloff and S. Coombes. A dynamical theory of spike train transitions in networks of integrate-and-fire oscillators. *SIAM Journal on Applied Mathematics*, pages 820–841, 2000.

[12] V.S. Caviness, T. Takahashi, and R.S. Nowakowski. Numbers, time and neocortical neuronogenesis: a general developmental and evolutionary model. *Trends in Neurosciences*, 18(9):379–383, 1995.

[13] Z. Chen, R.S. Duan, Y. Zhu, R. Folkesson, C. Albanese, B. Winblad, and J. Zhu. Increased Cyclin E expression may obviate the role of Cyclin D1 during brain development in Cyclin D1 knockout mice. *Journal of Neurochemistry*, 92(5):1281, 2005.

[14] A. Chenn and S.K. McConnell. Cleavage orientation and the asymmetric inheritance of Notch1 immunoreactivity in mammalian neurogenesis. *Cell*, 82(4):631–642, 1995.

[15] S. Coombes and Y. Timofeeva. Sparks and waves in a stochastic fire-diffuse-fire model of Ca2+ release. *Physical Review E*, 68(2):21915, 2003.

[16] P. Coti Bertrand, J.R. O'Kusky, and S.M. Innis. Maternal dietary(n-3) fatty acid deficiency alters neurogenesis in the embryonic rat brain. *The Journal of Nutrition*, 136(6):1570–1575, 2006.

[17] R.A. de Graaf, A. van Kranenburg, and K. Nicolay. In vivo 31P-NMR diffusion spectroscopy of ATP and phosphocreatine in rat skeletal muscle. *Biophysical Journal*, 78(4):1657–1664, 2000.

[18] G. Dupont. Link between fertilization-induced Ca2+ oscillations and relief from metaphase II arrest in mammalian eggs: a model based on calmodulin-dependent kinase II activation. *Biophysical Chemistry*, 72(1-2):153–167, 1998.

[19] A. dOnofrio. Mathematical analysis of the Tyson model of the regulation of the cell division cycle. *Nonlinear Analysis*, 62(5):817–831, 2005.

[20] F. Erlandsson, HS Martinsson-Ahlzén, KL Wallin, AC Hellstrom, S. Andersson, and A. Zetterberg. Parallel Cyclin E and Cyclin A expression in neoplastic lesions of the uterine cervix. *British Journal of Cancer*, 94(7):1045–1050, 2006.

[21] Bard Ermentrout. *Simulating, Analyzing, and Animating Dnynamical Systems. A Guide to XPPAUT for Researchers and Students.* SIAM, 2002.

[22] G.B. Ermentrout. Stable periodic solutions to discrete and continuum arrays of weakly coupled nonlinear oscillators. *SIAM Journal on Applied Mathematics*, 52(6):1665–1687, 1992.

[23] G.B. Ermentrout and N. Kopell. Frequency Plateaus in a Chain of Weakly Coupled Oscillators, I. *SIAM Journal on Mathematical Analysis*, 15:215, 1984.

[24] G.B. Ermentrout and N. Kopell. Oscillator death in systems of coupled neural oscillators. *SIAM Journal on Applied Mathematics*, pages 125–146, 1990.

[25] G.B. Ermentrout and N. Kopell. Multiple pulse interactions and averaging in systems of coupled neural oscillators. *Journal of Mathematical Biology*, pages 195–217, 1991.

[26] P. Fatt and B. Katz. Some observations on biological noise. *Nature*, 166:597–598, 1950.

[27] C.C. Fink, B. Slepchenko, and L.M. Loew. Determination of time-dependent inositol-1, 4, 5-trisphosphate concentrations during calcium release in a smooth muscle cell. *Biophysical journal*, 77(1):617–628, 1999.

[28] N. Gaiano, J.S. Nye, and G. Fishell. Radial glial identity is promoted by Notch1 signaling in the murine forebrain. *Neuron*, 26(2):395–404, 2000.

[29] L. Gammaitoni, P. Hanggi, P. Jung, and F. Marchesoni. Stochastic resonance. *Reviews of Modern Physics*, 70(1):223–287, 1998.

[30] A Goldbeter. Comments. *Journal of Theoretical Biology*, 3:75, 1993.

[31] D. Golomb and J. Rinzel. Dynamics of globally coupled inhibitory neurons with heterogeneity. *Physical Review E*, 48(6):4810–4814, 1993.

[32] EL Gordon, JD Pearson, and LL Slakey. The hydrolysis of extracellular adenine nucleotides by cultured endothelial cells from pig aorta. Feed-forward inhibition of adenosine production at the cell surface. *Journal of Biological Chemistry*, 261(33):15496–15507, 1986.

[33] Ellen L. Gordon, Jeremy D. Pearson, Ellen S. Dickinson, Deborah Moreau, and Linda L. Slakey. The Hydrolysis of Extracellular Adenine Nucleotides by Arterial Smooth Muscle Cells. *Journal of Biological Chemistry*, pages 18986–18995, March 1989.

[34] T. Goto, T. Takahashi, S. Miyama, R.S. Nowakowski, P.G. Bhide, and V.S. Caviness. Developmental regulation of the effects of fibroblast growth factor-2 and 1-octanol on neuronogenesis: Implications for a hypothesis relating to mitogen-antimitogen opposition. *Journal of Neuroscience Research*, 69(6):714–722, 2002.

[35] M. Gotz and Y.A. Barde. Radial Glial Cells Defined and Major Intermediates between Embryonic Stem Cells and CNS Neurons. *Neuron*, 46(3):369–372, 2005.

[36] L. Grandbarbe, J. Bouissac, M. Rand, M. Hrabe de Angelis, S. Artavanis-Tsakonas, and E. Mohier. Delta-Notch signaling controls the generation of neurons/glia from neural stem cells in a stepwise process. *Development*, 130(7):1391, 2003.

[37] E. Gudowska-Nowak and P.P. Szczesny. Effect of a shot-noise generator on oscillations in a Salnikov model of an exothermal chemical reaction. *Acta Physica Polonica. B*, 23(1):3–14, 1992.

[38] P. Hanggi. Stochastic Resonance in Biology. How Noise can Enhance Detection of Weak Signals and help Improve Biological Information Processing. *Journal of Chemical Physics and Physical Chemistry*, 3(3):285–290, 2002.

[39] D. Hansel, G. Mato, and C. Meunier. Synchrony in excitatory neural networks. *Neural Computation*, 7(2):307–337, 1995.

[40] W. Haubensak, A. Attardo, W. Denk, and W.B. Huttner. Neurons arise in the basal neuroepithelium of the early mammalian telencephalon: a major site of neurogenesis. *Proceedings of the National Academy of Sciences*, 101(9):3196–3201, 2004.

[41] Frank C. Hoppensteadt and Eugene M. Izhikevich. *Weakly Coupled Neural Networks*. Springer, 1997.

[42] A. Hutt. Additive noise may change the stability of nonlinear systems. *EPL (Europhysics Letters)*, 84:34003, 2008.

[43] S.M. Joseph, M.A. Pifer, R.J. Przybylski, and G.R. Dubyak. Methylene ATP analogs as modulators of extracellular ATP metabolism and accumulation. *British Journal of Pharmacology*, 142(6):1002, 2004.

[44] G. Juan and C. Cordon-Cardo. Intranuclear Compartmentalization of Cyclin E during the Cell Cycle: Disruption of the Nucleoplasm-Nucleolar Shuttling of Cyclin E in Bladder Cancer 1. *Cancer Research*, 61(3):1220–1226, 2001.

[45] C.R. Kahl and A.R. Means. Regulation of cell cycle progression by calcium/calmodulin-dependent pathways. *Endocrine Reviews*, 24(6):719–736, 2003.

[46] C.R. Kahl and A.R. Means. Regulation of Cyclin D1/Cdk 4 Complexes by Calcium/Calmodulin-dependent Protein Kinase I. *Journal of Biological Chemistry*, 279(15):15411–15419, 2004.

[47] M. Koike, T. Kashiwagura, and N. Takeguchi. Gluconeogenesis stimulated by extracellular ATP is triggered by the initial increase in the intracellular Ca 2+ concentration of the periphery of hepatocytes. *Biochemical Journal*, 283:265–272, 1992.

[48] N. Kopell and G.B. Ermentrout. Symmetry and phaselocking in chains of weakly coupled oscillators. *Communications on Pure and Applied Mathematics*, 39(5):623–660, 1986.

[49] N. Kopell and G.B. Ermentrout. Phase transitions and other phenomena in chains of coupled oscillators. *SIAM Journal on Applied Mathematics*, 50(4):1014–1052, 1990.

[50] N. Kopell, W. Zhang, and G.B. Ermentrout. Multiple Coupling in Chains of Oscillators. *SIAM Journal on Mathematical Analysis*, 21:935, 1990.

[51] T. Kreuz, F. Mormann, R.G. Andrzejak, A. Kraskov, K. Lehnertz, and P. Grassberger. Measuring synchronization in coupled model systems: A comparison of different approaches. *Physica D: Nonlinear Phenomena*, 225(1):29–42, 2007.

[52] Y. Kuramato. *Chemical Oscillations, Waves, and Turbulence*. Springer, 1984.

[53] T.J. Lewis and J. Rinzel. Dynamics of spiking neurons connected by both inhibitory and electrical coupling. *Journal of Computational Neuroscience*, 14(3):283–309, 2003.

[54] Y. Li and J. Rinzel. Equations for inositol-triphosphate receptor-mediated calcium oscillations derived from a detailed kinetic model: A Hodgkin-Huxley like formalism. *Journal of Theoretical Biology*, 166:461–473, 1994.

[55] JJ Liu, JR Chao, MC Jiang, SY Ng, JJ Yen, and HF Yang-Yen. Ras transformation results in an elevated level of Cyclin D1 and acceleration of G1 progression in NIH 3T3 cells. *Molecular and Cellular Biology*, 15(7):3654–3663, 1995.

[56] P. Malatesta, E. Hartfuss, and M. Gotz. Isolation of radial glial cells by fluorescent-activated cell sorting reveals a neuronal lineage. *Development*, 127(24):5253–5263, 2000.

[57] D.W. Marquardt. An algorithm for least-squares estimation of nonlinear parameters. *Journal of the Society for Industrial and Applied Mathematics*, pages 431–441, 1963.

[58] M.R. Metea and E.A. Newman. Calcium signaling in specialized glial cells. *Glia*, 54(7):650, 2006.

[59] V. Moll, M. Weick, I. Milenkovic, H. Kodal, A. Reichenbach, and A. Bringmann. P2Y receptor-mediated stimulation of Muller glial DNA synthesis. *Investigative Ophthalmology & Visual Science*, 43(3):766–773, 2002.

[60] T.A. Morris, R.J. DeLorenzo, and R.M. Tombes. CaMK-II inhibition reduces Cyclin D1 levels and enhances the association of p27kip1 with Cdk2 to cause G1 arrest in NIH 3T3 cells. *Experimental Cell Research*, 240(2):218, 1998.

[61] J.D. Murray. *Mathematical Biology.* Number 19 in Biomathematics Texts. Springer-Verlag, second, corrected edition, 1993.

[62] C. Nicholson and E. Syková. Extracellular space structure revealed by diffusion analysis. *Trends in Neurosciences*, 21(5):207–215, 1998.

[63] S.C. Noctor, A.C. Flint, T.A. Weissman, R.S. Dammerman, and A.R. Kriegstein. Neurons derived from radial glial cells establish radial units in neocortex. *Nature*, 409(6821):714–720, 2001.

[64] B. Novak and J.J. Tyson. A model for restriction point control of the mammalian cell cycle. *Journal of Theoretical Biology*, 230(4):563–579, 2004.

[65] M.N. Obeyesekere, E.S. Knudsen, J.Y.J. Wang, and S.O. Zimmerman. A mathematical model of the regulation of the G1 phase of Rb+/+ and Rb-/-mouse embryonic fibroblasts and an osteosarcoma cell line. *Cell Proliferation*, 30(3-4):171–194, 1997.

[66] M.N. Obeyesekere, S.O. Zimmerman, E.S. Tecarro, and G. Auchmuty. A model of cell cycle behavior dominated by kinetics of a pathway stimulated by growth factors. *Bulletin of Mathematical Biology*, 61(5):917–934, 1999.

[67] R. Patel, M. Holt, R. Philipova, S. Moss, H. Schulman, H. Hidaka, and M. Whitaker. Calcium/calmodulin-dependent phosphorylation and activation of human Cdc25-C at the G2/M phase transition in HeLa cells. *Journal of Biological Chemistry*, 274(12):7958–7968, 1999.

[68] J.D. Pearson, J.S. Carelton, and J.L. Gordon. Metabolism of adenine nucleotides by ectoenzymes of vascular endothelial and smooth-muscle cells in culture. *Biochemical Journal*, 190(429):421, 1979.

[69] P.F. Pinsky and J. Rinzel. Synchrony measures for biological neural networks. *Biological Cybernetics*, 73(2):129–137, 1995.

[70] Y. Piontkewitz, Y. Assaf, and I. Weiner. Clozapine Administration in Adolescence Prevents Postpubertal Emergence of Brain Structural Pathology in an Animal Model of Schizophrenia. *Biological Psychiatry*, 2009.

[71] D. Postnov, S.K. Han, and H. Kook. Synchronization of diffusively coupled oscillators near the homoclinic bifurcation. *Physical Review E*, 60(3):2799–2807, 1999.

[72] D.E. Quelle, R.A. Ashmun, S.A. Shurtleff, J.Y. Kato, D. Bar-Sagi, M.F. Roussel, and C.J. Sherr. Overexpression of mouse D-type Cyclins accelerates G1 phase in rodent fibroblasts. *Genes & Development*, 7(8):1559–1571, 1993.

[73] D. Reigada, W. Lu, X. Zhang, C. Friedman, K. Pendrak, A. McGlinn, R.A. Stone, A.M. Laties, and C.H. Mitchell. Degradation of extracellular ATP by the retinal pigment epithelium. *American Journal of Physiology- Cell Physiology*, 289(3):617–624, 2005.

[74] D. Resnitzky, M. Gossen, H. Bujard, and SI Reed. Acceleration of the G1/S phase transition by expression of Cyclins D1 and E with an inducible system. *Molecular and Cellular Biology*, 14(3):1669–1679, 1994.

[75] M.B.H. Rhouma and H. Frigui. Self-organization of pulse-coupled oscillators with application to clustering. *IEEE Transactions on Pattern Analysis and Machine Intelligence*, 23(2):180–195, 2001.

[76] D.A. Rusakov and D.M. Kullmann. Geometric and viscous components of the tortuosity of the extracellular space in the brain. *Proceedings of the National Academy of Sciences*, 95(15):8975–8980, 1998.

[77] E. Scemes, N. Duval, and P. Meda. Reduced expression of P2Y1 receptors in connexin43-null mice alters calcium signaling and migration of neural progenitor cells. *Journal of Neuroscience*, 23(36):11444–11452, 2003.

[78] E. Schneidman, B. Freedman, and I. Segev. Ion channel stochasticity may be critical in determining the reliability and precision of spike timing. *Neural Computation*, 10(7):1679–1703, 1998.

[79] M.E. Seward, C.A. Easley, J.J. McLeod, A.L. Myers, and R.M. Tombes. Flightless-I, a gelsolin family member and transcriptional regulator, preferentially binds directly to activated cytosolic CaMK-II. *FEBS letters*, 582(17):2489–2495, 2008.

[80] H.W. Spurr Jr. Adenosine Triphosphate Quantification as Related to Cryptobiosis, Nematode Eggs, and Larvae. *Journal of Nematology*, 8(2):152, 1976.

[81] D.W. Stacey. Cyclin D1 serves as a cell cycle regulatory switch in actively proliferating cells. *Current Opinion in Cell Biology*, 15(2):158–163, 2003.

[82] M. Stamatakis and N.V. Mantzaris. Astrocyte signaling in the presence of spatial inhomogeneities. *Chaos: An Interdisciplinary Journal of Nonlinear Science*, 17:033123, 2007.

[83] S.H. Strogatz and R.E. Mirollo. Stability of incoherence in a population of coupled oscillators. *Journal of Statistical Physics*, 63(3):613–635, 1991.

[84] A. Sveiczer, J.J. Tyson, and B. Novak. A stochastic, molecular model of the fission yeast cell cycle: role of the nucleocytoplasmic ratio in cycle time regulation. *Biophysical Chemistry*, 92(1-2):1–15, 2001.

[85] M. Swat, A. Kel, and H. Herzel. Bifurcation analysis of the regulatory modules of the mammalian G1/S transition. *Bioinformatics*, 20(10):1506–1511, 2004.

[86] T. Takahashi, R.S. Nowakowski, and V.S. Caviness. The leaving or Q fraction of the murine cerebral proliferative epithelium: a general model of neocortical neuronogenesis. *Journal of Neuroscience*, 16(19):6183–6196, 1996.

[87] R.W. Tsien and R.Y. Tsien. Calcium channels, stores, and oscillations. *Annual Review of Cell Biology*, 6(1):715–760, 1990.

[88] Y. Tsunoda. Oscillatory Ca2+ signaling and its cellular function. *The New Biologist*, 3(1):3, 1991.

[89] J.J. Tyson and B. Novak. Regulation of the eukaryotic cell cycle: molecular antagonism, hysteresis, and irreversible transitions. *Journal of Theoretical Biology*, 210(2):249, 2001.

[90] J.J. Tyson and Bela Novak. *Computational Cell Biology*. Springer, Febuary 2005.

[91] O. Uckermann, J. Grosche, A. Reichenbach, and A. Bringmann. ATP-evoked calcium responses of radial glial (Muller) cells in the postnatal rabbit retina. *Journal of Neuroscience Research*, 70(2), 2002.

[92] X.J. Wang and G. Buzsaki. Gamma Oscillation by Synaptic Inhibition in a Hippocampal Interneuronal Network Model. *Journal of Neuroscience*, 16(20):6402, 1996.

[93] T.A. Weissman, P.A. Riquelme, L. Ivic, A.C. Flint, and A.R. Kriegstein. Calcium Waves Propagate through Radial Glial Cells and Modulate Proliferation in the Developing Neocortex. *Neuron*, 43:647–661, September 2004.

[94] J.A. White, R. Klink, A. Alonso, and A.R. Kay. Noise from voltage-gated ion channels may influence neuronal dynamics in the entorhinal cortex. *Journal of Neurophysiology*, 80(1):262–269, 1998.

[95] J.F. Whitefield, A.L. Boynton, J.P. Macmanus, R.H. Rixon, M. Sikorska, B. Tsang, and P.R. Walker. The roles of calcium and cyclic AMP in cell proliferation. *Annals of the New York Academy of Sciences*, pages 216–240, 1980.

[96] Ke Yang, Masahiro Hitomi, and Dennis W. Stacey. Variations in Cyclin D1 levels during the cell cycle determine the proliferative fate of a cell. *Cell Division*, 2006.

[97] G.W.D. Young and J. Keizer. A single-pool inositol 1, 4, 5-trisphosphate-receptor-based model for agonist-stimulated oscillations in Ca2+ concentration. *Proceedings of the National Academy of Sciences*, 89(20):9895–9899, 1992.

[98] Y. Zhang, M. Qian, Q. Ouyang, M. Deng, F. Li, and C. Tang. Stochastic model of yeast cell-cycle network. *Physica D: Nonlinear Phenomena*, 219(1):35–39, 2006.